International Journal of Navigation and Observation

Modeling and Processing of Radar Signals for Earth Observation

Guest Editors: Maria Greco and Simon Watts

Modeling and Processing of Radar Signals for Earth Observation

International Journal of Navigation and Observation

Modeling and Processing of Radar Signals for Earth Observation

Guest Editors: Maria Greco and Simon Watts

Contents

Hindawi Publishing Corporation
International Journal of Navigation and Observation
Volume 2008, Article ID 463741, 2 pages
doi:10.1155/2008/463741

Editorial

Modeling and Processing of Radar Signals for Earth Observation

Maria Greco[1] and Simon Watts[2]

[1] *Dipartimento di Ingegneria dell'Informazione, Università di Pisa, 56122 Pisa, Italy*
[2] *Thales Aerospace Division, Manor Royal, Crawley, West Sussex RH10 9HA, UK*

Correspondence should be addressed to Maria Greco, m.greco@iet.unipi.it

Received 14 October 2008; Accepted 14 October 2008

The rapidly growing number of real aperture and synthetic aperture radars (SARs) devoted to Earth observation provides today a very broad coverage across space, time, and the electromagnetic spectrum. Very large quantities of data and images are being systematically collected, processed, and stored. The all-weather, day, and night capabilities of these radar sensors permit acquisition of information under conditions that are not possible with EO sensors. Radars can monitor iceberg position, movement, and age to improve safety at sea. They can provide useful information on oceans and their currents. Radars can also explore vast areas of the Earth, providing an inventory of potential mineral resources, new transportation routes, freshwater supplies, sites for agriculture, and so on.

The papers in this special issue reflect some of the many varied applications of radar that are being researched today.

Synthetic aperture radar, whether from space or airborne platforms, continues to attract much attention. Spatial resolutions of the order of 1 m are currently available from space-based SAR systems such as TerraSAR-X, whilst airborne spotlight SAR systems can achieve resolutions of the order of 10 cm. Many space-based radars are now fully polarimetric, and there is considerable scope for interferometric SAR operation, either using repeat-pass methods or tandem platforms. In their paper entitled "Scattering-based model of the SAR signatures of complex targets for classification applications," G. Margarit and J. J. Mallorqui present a method for analysing SAR imagery and the scattering from complex targets. This has led to a proposed method for classifying targets such as ships and urban buildings, using features obtained from polarimetric and interferometric SAR images.

Interferometric techniques can also be applied to analyse the movement of targets in an SAR image. A. Budillon et al. describe a technique for detecting radially moving targets in an SAR image in their paper "Multi-channel along-track interferometric SAR systems: Moving targets detection and velocity estimation." They consider the performance of multichannel AT-InSAR systems in terms of moving target detection and the accuracy of radial velocity estimation.

Polarimetric data can also be successfully used for classification purposes in inverse synthetic aperture radar (ISAR) images, as described by M. Martorella et el. in "CLEAN technique for polarimetric ISAR." This paper addresses the problem of estimating the position and the scattering vector of target scattering centres from polarimetric ISAR images. The CLEAN techniques are used for reducing the data size of the images without losing useful information, with the aim of classifying and recognizing objects on the Earth surface.

A very interesting area of research in the last few years concerns the applications of passive SAR bistatic systems. In the paper entitled "Experiences gained during the development of a passive BSAR with GNSS transmitters of opportunity," M. Cherniakov et al. present an overview of the research conducted at the University of Birmingham in the area of space-surface bistatic synthetic aperture radar (SSB-SAR) since 2003. The main aim of the research is to experimentally demonstrate the feasibility and performance of airborne SS-BSAR, utilizing the Global Navigation Satellite System (GNSS) as the transmitter of opportunity. The paper highlights and briefly discusses the various factors that determine image quality, including various systems

parameters (related to resolution, power budget, etc.), signal processing algorithms (for imaging, synchronization, etc.), and specific problems to be addressed (such as interference and motion compensation).

The problem of the correct reconstruction of an image is also the topic of the paper by Y. Shkvarko et al. "Enhanced radar imaging in uncertain environment: A descriptive experiment design regularization approach." A new robust technique is developed by the authors for high-resolution reconstructive imaging, applied to enhanced remote sensing (RS) with an imaging array radar and/or a synthetic aperture radar (SAR), operating in an uncertain RS environment. The operational scenario uncertainties are associated with the unknown statistics of perturbations of the signal formation operator (SFO) in a turbulent medium, imperfect array calibration, finite dimensionality of measurements, uncontrolled antenna vibrations and, in the case of SAR, random platform trajectory deviations. In that paper, the authors propose new descriptive experiment design regularization (DEDR) approach to treat the uncertain radar image enhancement/reconstruction problems.

Another important research area for remote sensing is the application of satellite imagery for damage assessment. G. Trianni and P. Gamba, in "Damage detection from SAR imagery: application to the 2003 Algeria and 2007 Peru earthquakes," describe a method for fusing remotely sensed radar imagery with geographic databases. The method is illustrated by analysis of real radar imagery. It can provide rapid assessment of earthquake damage although further work is needed to improve the accuracy that can be achieved.

Real aperture radar also continues to play a fundamental role in remote sensing of the environment. P. L. Herselman et al. in "An analysis of X-band calibrated sea clutter and small boat reflectivity at medium to low grazing angles" show how accurate empirical modeling of sea clutter can provide the basis for inference of local sea conditions from remote low-grazing-angle radar returns. They have also analysed the coherent signatures of small boats, which interact in a complex way with the local clutter returns, and show how this information can be used to provide improved target detection methods.

The modeling of sea clutter is also the topic of the paper "Non-linear dynamics of sea clutter," by T. Field and S. Haykin. In their paper, the authors expand on the characterization of sea clutter as a nonlinear dynamic process, using the stochastic differential equation (SDE) theory. The stochastic dynamics of radar sea scattering are derived in terms of a pair of coupled stochastic differential equations for the received envelope and the radar cross-section (RCS). The analysis presented by the authors leads to the conclusion that, from both experimental and theoretical points of view, the dynamics of sea clutter are nonlinear with a consistent degree of nonlinearity that is determined by the sea state.

This special issue represents a small selection of current research. Nevertheless, this issue hascollected an interesting cross-section of papers representing work from 7 different countries. We would like to thank all the authors who contributed to this special issue and, in particular, the many anonymous referees who played such an important part.

Maria Greco
Simon Watts

Hindawi Publishing Corporation
International Journal of Navigation and Observation
Volume 2008, Article ID 426267, 11 pages
doi:10.1155/2008/426267

Research Article

Scattering-Based Model of the SAR Signatures of Complex Targets for Classification Applications

Gerard Margarit and Jordi J. Mallorqui

Remote Sensing Laboratory, Department Signal Theory and Communications, Universitat Politècnica de Catalunya, Jordi Girona 1-3, 08034 Barcelona, Spain

Correspondence should be addressed to Jordi J. Mallorqui, mallorqui@tsc.upc.edu

Received 5 February 2008; Accepted 14 May 2008

Recommended by Simon Watts

The modeling of complex target response in SAR imagery is the main subject of this paper. The analysis of a large database of SAR images with polarimetric and interferometric capabilities is used to accurately establish how the different structural parts of targets interact with the incident signal. This allows to relate the reflectivity information provided by SAR images with specific geometries and to fix variation reflectivity patterns in terms of different imaging parameters such as image resolution, incidence angle, or operating frequency. Most of the used images have been obtained from the SAR simulator of complex targets developed at UPC, which is able to generate realistic data for a wide range of observation and environmental conditions. The result is a precise scattering-based SAR model that opens the door, among others, to an alternative way for reliable geometry retrieval. Under this approach, a novel SAR classification method for ships has been proposed. The preliminary evaluation in simulated scenarios shows a notable classification capability even under strong clutter and ship motion conditions. Due to these promising results, the same methodology is intended to be applied to urban areas. Concerns about possible model limitations and required improvements are preliminarily treated.

1. INTRODUCTION

The proliferation of new SAR sensors with improved capabilities in terms of system resolution and information channels (polarimetry and interferometry) has increased the range of products that can be obtained from SAR imagery [1]. Examples are characterization and classification of man-made structures like ships or urban targets [2–5]. In the past, the limitations of sensors' performance have made it almost impossible to precisely retrieve those physical and geometrical parameters related with the imaged targets. This trend is currently changing with the new generation of airborne and orbital sensors.

Now, real data have higher diversity, as polarimetric channels are available, and increased revisiting times. Their adequate interpretation requires the development of new models, where the SAR signatures of complex targets become related with their geometries. The development of such models with real imagery is difficult and arduous because the required amount of data with the related ground-truth is not always available and can be too expensive to generate. A feasible alternative lies in the usage of realistic simulators, where flexibility and reduced cost can overcome previous limitations allowing to rapidly increase the knowledge in target scattering.

In this context, the current paper provides a new methodology for modeling the response of complex targets in SAR imagery based on the analysis of large stacks of simulated scattering maps [6]. By using an accurate and realistic SAR simulator, the response of each structural part of a target can be described in terms of the three-dimensional position, the scattering properties (reflectivity intensity and polarimetric behavior), and the dependence of these properties with respect to key imaging parameters (incidence angle and target orientation, resolution, operating frequency, etc.). All this information can help to predict the expected real SAR response for a given set of observation conditions and, hence, geometrical and physical information may be retrieved by simply inverting the relations established within simulation environments. As a result, a new target

model emerges, which can be exploited in a large number of applications.

The previous modeling methodology has been applied to ships [7] and urban targets [8]. This has been done with GRECOSAR [9], a simulator able to realistically simulate SAR images of complex targets within flexible and controlled scenarios. It works with 3D high-frequency ElectroMagnetic (EM) calculations using physical optics (PO) and physical theory of diffraction (PTD) [10, 11]. In a first step, a large number of fully polarimetric scattering maps (inverse SAR, ISAR) with resolution around centimeters have been used to study the dispersion behavior of targets in terms of their geometries and observation conditions. This has allowed to observe a specific scattering pattern from which the dispersion information can be linked with target geometry for a large range of views. In a second step, the signatures of targets have been analyzed in simulated SAR images. For an adequate image resolution, it follows that the previous scattering patterns can be related with the observed structures or, in other words, targets' geometry can be inferred from the scattering patterns.

As a result, the proposed scattering-based model of complex targets appears to be feasible for practical applications. Its usefulness in real scenarios has been evaluated by testing its potentialities for basing new classification/identification approaches. Special attention is placed on ships where the availability of robust algorithms is mandatory for complementing new ship monitoring techniques devoted to SAR platforms (see European IMPAST [12], DECLIMS [13], and LIMES [14] projects). In this sense, the vessel classification algorithm (VCA) working with polarimetric interferometric SAR (PolInSAR) imagery is presented [6]. Its operating principle is briefly described and some tests are carried out within simulated scenarios for the analyzed real-like observation conditions. The results show notable classification ratios even under adverse observation conditions, mainly manifested by sea clutter and ship motions [7]. Regarding urban environments, the conclusions derived from the model are used to improve real-data interpretation and the performance of interferometric-related applications such as subsidence.

This paper is structured as follows. Section 2 describes the modeling methodology stressing its advantages and limitations with respect to classical approaches. Section 3 presents samples of the scattering maps used to relate the model scattering behavior with its geometry. The reliability of the derived scattering patterns in SAR images is assessed in Section 4. They are exploited in Section 5, where the VCA algorithm and new guidelines for helping to improve the interpretation of urban data are introduced.

2. MODELING METHODOLOGY

Modeling the dispersion response of complex targets should take into account what follows: (1) the measuring variables (*model inputs*, i.e., polarimetric and interferometric data), (2) the parameters to be inverted (*model outputs*), and (3) the main application for which target modeling is sought. In our context, complex target modeling is conceived for characterization and classification and, hence, the retrieval of key geometrical information is the main goal (*model output*). To successfully do this process, accurate geometry-scattering relations are mandatory so that the reflectivity information of SAR images can be connected with specific geometrical shapes. For such purpose, large datasets have to be analyzed for the largest possible scenario diversity. In real scenarios, this task is extremely complex as, besides the long and costly measurement campaigns, the coordination between the sensor and testing scenarios should be almost perfect for reaching the planned observation conditions and acquiring accurate ground-truth. In most situations, for instance, with vessels at sea, this is almost impossible.

Recent works have suggested the possibility to exploit numerical tools for carrying out, in a first stage, the previous studies [7, 9]. Simulation presents two advantages: (1) the capability to quickly process a wide range of scenarios for which target models can be developed, and (2) the possibility to plan measurement campaigns, where observation conditions allow to efficiently test, improve, and/or validate the proposed model. The combination of both can lead to better models.

In this study, simulated images have been used. They have been obtained from the GRECOSAR numerical tool [9], which is able to reproduce in simple PC realistic SAR images of complex targets. It is based on UPC's GRaphical Electromagnetic COmputing (GRECO) solver [10] that estimates, for each single frequency, the radar cross-section (RCS) of 3D targets via high-frequency methods (PO, PTD). Targets are modeled with the CAD package GiD of the International Center of Numerical Methods for Engineering (CIMNE) [15]. Computer efficiency and scenario flexibility are the main advantages of the simulator. This allows to simulate any sensor for any operating band, mode, and resolution with polarimetric and/or interferometric capabilities. Target environment is configurable with dielectric materials, relative sensor-to-target orientation, incidence angle, and, in the case of vessels, speed, motion dynamics, and dynamic sea surfaces [16, 17]. Exhaustive tests performed with both canonical and complex targets have validated the code. Its potentialities for complex target studies have been shown in previous works devoted to ships [6, 7].

2.1. Model outputs

For classification applications, the parameters to be inverted have to be related with target's geometry. It would be desirable to obtain from data the three-dimensional position of all points defining the structure. However, this is not possible with radars as only a reduced group of geometrical shapes with high RCS is present in the image [2, 7, 18]. The remaining scatterers are either cluttered by the stronger ones due to the limited system resolution or have an RCS below the noise floor.

In this framework, the model is focused to find the 3D position of a set of significant scatterers that summarize the macroscale geometry of the different types of targets, like those obtained from polarimetric decompositions. Such scatterers are termed as *permanent polarimetric*

scatterers (PePSs) in the sense that they present similar scattering properties within a wide range of observation conditions. For each target model, particular combinations of PePSs are selected according to the analysis of simulated scattering maps derived for different observation conditions. Mathematically, the feature vector for target j can be denoted by

$$\Theta^j = \{\Theta_i^j\} \quad \text{for } 1 < i < N_{\text{PePS}}, \tag{1}$$

where N_{PePS} points to the number of PePSs for that target and

$$\Theta_i^j = \{a_i, \text{gr}_i, h_i, p_i\}^j \tag{2}$$

gathers the azimuth (a_i) and ground-range (gr_i) locations of scatter i, jointly with its height (h_i) and related scattering mechanism (p_i). *Scattering mechanisms* are defined according to the basic Pauli mechanisms [19], namely, "trihedral" for those mechanisms with odd number of reflections (sphere, flat planes, 3D corners, etc.), "dihedral" for those mechanisms with even number of reflections (2D corners), and "antisymmetric" for those mechanisms without the symmetry property. All three follow the orthogonality property and have appeared to be indispensable for increasing the discrimination capability among different PePS configurations [6]. This explains the importance of the polarimetric term p_i in (2). Other polarimetric decompositions could also be used, but orthogonality helps to better discriminate the interferometric phase information related to each mechanism.

2.2. Model inputs

The retrieval of the previous information needs from *polarimetric interferometric SAR* (PolInSAR) imagery. Certainly, SAR imagery provides information about azimuth (a_i) and ground-range (gr_i) scatter locations, SAR interferometry (InSAR) [20] about the relative height among scatterers (h_i), and, finally, SAR polarimetry (PolSAR) [19, 21, 22] about the associated scattering mechanisms (p_i). These relations are valid if each resolution cell does not contain more than one PePS with the same scattering mechanism. This implies that (1) it is possible to discriminate a maximum of three scatterers with different scattering mechanisms within the same resolution cell, and (2) a minimum of resolution is required for an adequate PePS discrimination. Different tests have shown that a resolution around 3 m seems to be enough for ship classification applications [6, 7].

The sensor requirements that imply the usage of PolInSAR with high resolution are quite demanding [17]. Certainly, the management of six information channels in the time slot of one synthetic aperture position increases the hardware complexity and, even worst, imposes important restrictions on the coverage (swath is severely limited if compared with single-pol SAR). By now, this can only be assumed by airborne sensors, despite the fact that the new operating modes of TerraSAR-X and Radarsat-2 are close to this goal if single-pass interferometry is not considered. In order to make an efficient usage of the available information, some alternatives are now under consideration, such as *alternate polarimetric* (AP) modes or *partial polarimetry* (PP) [23–25]. They allow to reduce the number of polarimetric channels but at the expense of some model approximations that in some cases cannot be applied, as in the case of ships against strong clutter conditions [17].

2.3. Modeling scheme

The scheme of the adopted modeling methodology can be summarized in the following points.

(i) Select a set of targets that can be considered as representatives of the different types that can be found.

(ii) Generate a large number of scattering maps with numerical tools that help to fix the scattering behavior of the different parts of targets' structure. These data have to be derived for a particular set of observation conditions (Φ^k) and should evaluate the impact of the surrounding environment. In a first approach, Φ^k is defined for the incidence angle ($\phi[^\circ]$), relative target-to-sensor orientation ($\beta[^\circ]$), and operating frequency (f[Ghz]) taking different values within a fixed range.

(iii) For a given set of observation conditions $\Phi^k = \{\phi, \beta, f\}^k$, define a particular feature set Θ^j for the type of target j. PePSs are selected by those scatterers presenting an RCS 10 dB higher than that of the surrounding scatterers and a stable polarimetric behavior within a solid angle of at least $\pi/3$ steradian (this is the solid angle subtended by a cone of 30° of aperture). Three issues are important in this definition: (1) stable polarimetric behavior for PePS i means to take the same value of p_i^j within the selected aspect angle (see (4) and (5)); (2) PePS 3D positions are expressed with respect to a local coordinate system within the target from which the migration to SAR location parameters (a_i^j and gr_i^j) is performed according to the particular imaging geometry (see Figure 1); (3) the threshold in the angular aperture is selected by the response of typical canonical scatterers, like trihedrals and dihedrals. This implies that the modeling methodology is focused to locate those structures with the closest scattering behavior to canonical targets.

2.4. Inversion scheme

Model inversion implies basically to retrieve the information of Θ_i^j for all the potential candidates of PePS. It assumes that target signature has been previously isolated from the environment with any of the currently available detection methods (see [26, 27] for ships and [5, 28, 29] for urban areas). In a first iteration, all local maxima present in target's signature for all polarimetric channels are selected (N_{lm}) (see Section 5.1). For each one, $\langle\Theta_n^j\rangle$ is estimated according to (1)

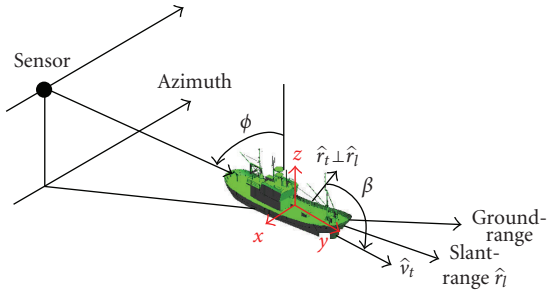

Figure 1: Local coordinate system used to define PePS within targets. The center is located at target's center of mass.

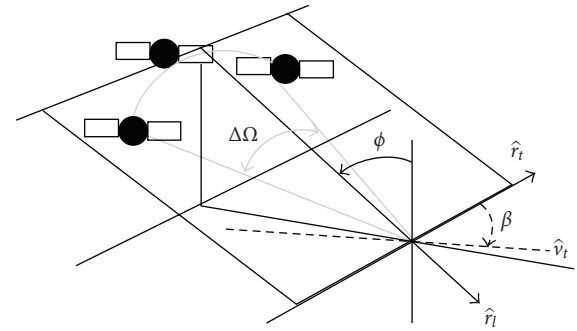

Figure 2: ISAR imaging geometry of GRECOSAR.

with $1 < n < N_{\text{lm}}$. The formulae required for this process are listed as follows. Regarding height,

$$\langle h_n^j \rangle = \sin\phi \left[\frac{cr_o}{4\pi f B^{\perp}} \Delta\psi - \frac{\Delta r}{\tan\phi} \right], \tag{3}$$

where $\Delta\psi$ and Δr fix the interferometric phase and slant-range difference of scatter n with respect to a fixed reference. r_o is the range, and $B^{\perp}$ is the perpendicular baseline, both known as radar parameters [20, 30]. Interferometric phase corresponds to the phase of the pixel of the interferogram related to scatter n. The interferogram is built by multiplying the master image with the complex conjugate of the slave for a particular polarimetric channel [20].

The polarimetric term p_i is estimated according to the significance of the Pauli scattering mechanism associated with the analyzed scatter n. This implies the following relations:

$$\begin{aligned}
\langle p_n^j \rangle &= 0 \quad \text{if } |p_{n,0}^j| > |p_{n,1}^j|, |p_{n,2}^j|, \\
\langle p_n^j \rangle &= 1 \quad \text{if } |p_{n,1}^j| > |p_{n,0}^j|, |p_{n,2}^j|, \\
\langle p_n^j \rangle &= 2 \quad \text{if } |p_{n,2}^j| > |p_{n,0}^j|, |p_{n,1}^j|,
\end{aligned} \tag{4}$$

where $|p_{n,xx}^j| = p_{n,xx}^j / \max\{p_{n,0}^j, p_{n,1}^j, p_{n,2}^j\}$ defines the normalized significance of the three Pauli mechanisms:

$$\begin{aligned}
p_{n,0}^j &= \frac{1}{\sqrt{2}} \frac{S_{hh}^n + S_{vv}^n}{2}, \\
p_{n,1}^j &= \frac{1}{\sqrt{2}} \frac{S_{hh}^n - S_{vv}^n}{2}, \\
p_{n,2}^j &= \frac{1}{\sqrt{2}} S_{hv}^n
\end{aligned} \tag{5}$$

for the elements of the monostatic master scattering matrix $[S]^n$ measured in the pixel of scatter n :

$$[S]^n = \begin{bmatrix} S_{hh} & S_{hv} \\ S_{hv} & S_{vv} \end{bmatrix}^n. \tag{6}$$

The term $xx = \{0, 1, 2\}$ is related to the "trihedral," "dihedral," and "antisymmetric" Pauli mechanisms. Finally, azimuth and ground-range locations are obtained from the azimuth ($a_{n,\text{SAR}}^j$) and slant-range ($\text{sr}_{n,\text{SAR}}^j$) positions of scatter n in the SAR image:

$$\begin{aligned}
\langle a_n^j \rangle &= a_{n,\text{SAR}}^j, \\
\langle \text{gr}_n^j \rangle &= \frac{\text{sr}_{n,\text{SAR}}^j + \langle h_n^j \rangle \cos\phi}{\sin\phi}.
\end{aligned} \tag{7}$$

The inversion process ends by selecting those PePSs whose combination better matches the list defined by Θ^j.

3. SCATTERING MAPS

The modeling methodology starts with the generation of stacks of scattering maps (Ω_j^k) defined for particular sets of observation conditions (Φ^k) and targets' types (j). This step has been done with GRECOSAR following the inverse SAR imaging geometry shown in Figure 2. Some samples are presented in this section for two different classes of targets: ships and buildings. The intrinsic geometries of both raise some particular scattering properties that can help to make the modeling process more efficient. For instance, the symmetric distribution of scatters in the normal direction to the line of sight (LOS) [18] induces a higher scattering stability within a wide range of views, and allows to use a unique feature vector (Θ^j) for characterizing the target. This normally happens with symmetric targets like ships, which appear to be specially suited for the modeling methodology [7, 16].

All the presented scattering maps are fully polarimetric and depict the normalized Pauli significance ($|p_{n,xx}^j|$) with an RGB-based color code: red→$|p_{n,0}^j|$ (first Pauli mechanism), green→$|p_{n,1}^j|$ (second Pauli mechanism), and blue→$|p_{n,2}^j|$ (third Pauli mechanism). They show the most representative cases of all those generated (see [6] for further details).

3.1. Modeling ship responses

Figure 3 provides scattering maps at X, C, and L bands for an incidence angle of $\phi = 20^\circ$ and three different target orientations, $\beta = \{295, 315, 335\}^\circ$. Three types of ships have been considered: a Spanish fishing vessel of 30 m long and 7 m wide (target $j = S0$), an Icelandic fishing vessel of 70 m long and 15 m wide (target $j = S1$), and a passenger ferry

Table 1: Feature vectors for targets $j = S0$, $j = S1$, and $j = S2$ and $\Phi^{SO1} = \{10-30^\circ, 280-350^\circ, 5.3-9.65\,\text{GHz}\}^{SO1}$. Heights ($z$) are normalized with respect to the lowest value in order to match interferometric height conventions.

Θ^{S0}					Θ^{S1}				
Θ_i^{S0}	x_i	y_i	z_i	p_i	Θ_i^{S1}	x_i	y_i	h_i	p_i
1	3.5	−10	0	0	1	3	−2	0	1
2	3.5	−5	0	0	2	−6	−14	6.5	1
3	−0.5	−8	2.5	1	3	−1	1	6.5	1
4	−0.5	−2	4.5	1	—	—	—	—	—
Θ^{S2}							—		
Θ_i^{S2}	x_i	y_i	z_i	p_i			—		
1	12	−25	0	0			—		
2	10	−25	0.5	1			—		
3	9	8	2.5	1			—		
4	9	−8	2.5	1			—		

Table 2: Feature vectors for $\Phi^{UO1} = \{20^\circ, 190^\circ, 9.65\,\text{GHz}\}^{SO1}$ and targets $j = U0$ and $j = U1$. Heights (z) are normalized with respect to the lowest value in order to match interferometric height conventions.

Θ^{U0}					Θ^{U1}				
Θ_i^{U0}	x_i	y_i	z_i	p_i	Θ_i^{U1}	x_i	y_i	h_i	p_i
1	−8	2	5.5	0	1	−4	2	0	0
2	−7	−3	2.2	0	2	4	−8	9.5	0
3	−6	−8	0	0	3	8	−1	12.5	0

of 200 m long and 30 m wide (target $j = S2$). As observed, each type of ship presents a particular distribution of strong scatters, PePS candidates, which appear to be stable within a specific range of views.

The selection criteria described in Section 2.3 have been applied to these datasets and have confirmed that each ship presents different PePS combination that leads to the feature vectors summarized in Table 1. They mainly correspond to dihedral interactions of cylindric structures (like masts and funnels) and trihedral behaviors due to corner geometries (like buttresses). Such vectors are valid for the set of simulated observation conditions $\Phi^{SO1} = \{10-30^\circ, 280-350^\circ, 5.3-9.65\,\text{GHz}\}^{SO1}$ that cover different range of values for incidence, target orientation, and operating frequency. The margin of validity in terms of incidence angle and target orientation is notably large and opens the door for characterizing a vessel with a reduced set of feature vectors. In Table 1, PePS 3D positions are expressed in the local coordinate system shown in Figure 3, from which SAR location parameters are derived according to the incidence and target orientation angles. Such conversion needs the knowledge of vessels' bearing that can be extracted from any of the currently available methods [31, 32]. Note also in Table 1 that the defined PePSs are valid for the complementary range of orientation values owned to the symmetry of the vessels' structure.

3.2. Modeling urban responses

The same procedure is now being conducted for urban areas. The presented results should be considered preliminarily as the work is still in progress and the amount of simulated images is not comparable with that currently available for ships. In this sense, Figure 4 presents some scattering maps similar to those introduced previously, but related to two different classes of buildings ($j = U0$ for the upper one and $j = U1$ for the lower one). The structures of both buildings are clearly depicted in Figure 6. They correspond to two structures within a test site, where ground-based SAR (GB-SAR) measurements were carried out by UPC [33, 34]. This has provided accurate ground-truth about building structure as well as external elements that may interfere. The images have been obtained for $\phi = 60^\circ$ and $\beta = \{190, 200\}^\circ$ at X band in order to reproduce the observation conditions of the GB-SAR sensor.

In the light of the obtained results, it follows that the response of these targets can be also described by a set of PePSs. The related feature vectors are summarized in Table 2 for which point positions are expressed in terms of the coordinate system depicted in Figure 4. Such scatterers are mainly related to frame points located in doors and windows (trihedral) and punctual wall-street interactions (dihedral). But now the scattering maps are not as stable as those obtained from vessels. In general terms, the whole response is appreciably modified (even by eye inspection) from one orientation to another, despite the fact that some particular PePSs can still be identified. The causes are the extremely complex environments that make most of the details to be able to contribute to the scattering map depending on the incidence conditions.

Therefore, it appears that building discrimination via target scattering is more difficult as the number of feature vectors demanded for covering target dispersion increases notably. However, due to the high realism achieved by GRECOSAR in reproducing the scattering information of real scenarios [8], other areas can take profit of these results. Examples may be the development of differential interferometry- (DInSAR-) related applications for subsidence monitoring [5] and the inclusion of polarimetric data provided by the new sensors, like TerraSAR-X or Radarsat-2.

4. MODEL ANALYSIS IN SAR IMAGES

This section tests the performance of the first model version generated in the previous section for SAR images. For such purpose, some of the previous simulations have been rerun for the SAR imaging geometry of Figure 1. A PolInSAR X band sensor covering the previously indicated incidences and providing a resolution of 2.3 m in azimuth and 1.3 m in range has been used.

4.1. Ship targets

Some ship samples are presented first in Figure 5 by expressing the significance of each Pauli mechanism in gray scale. The scenario does not take target environment into account

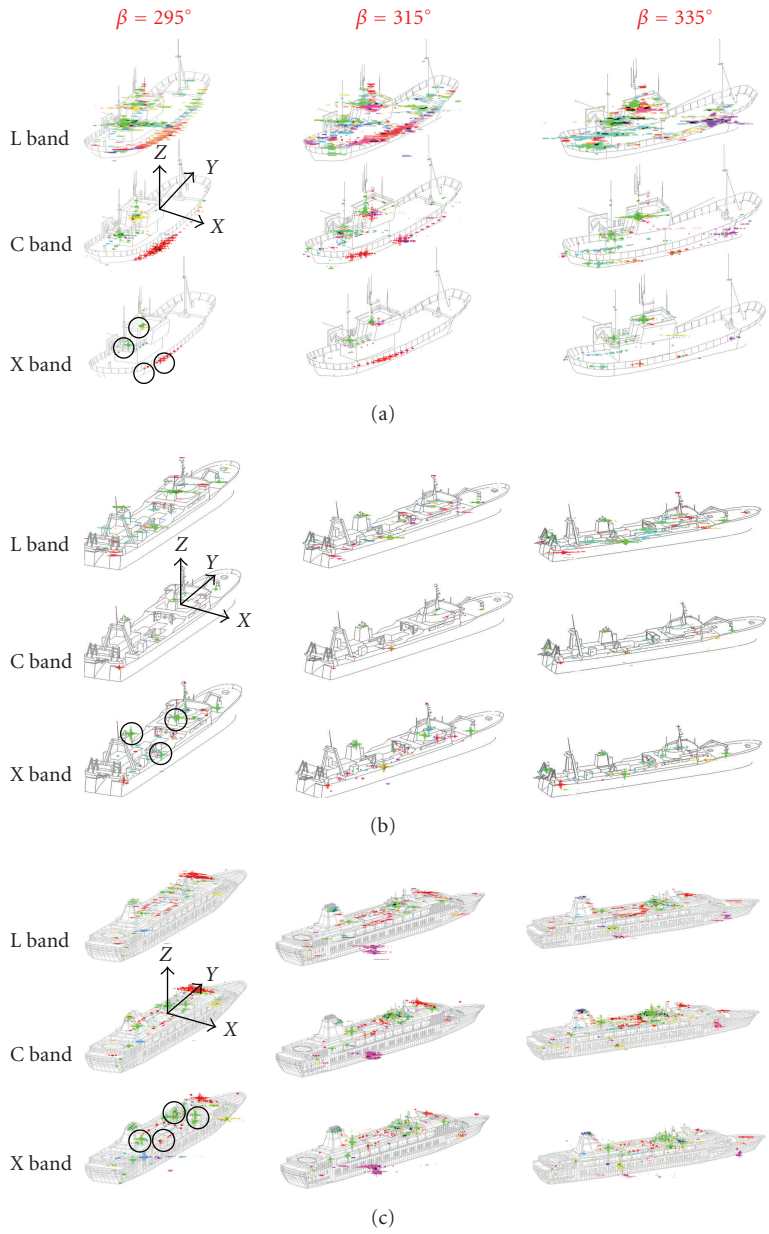

Figure 3: Scattering maps obtained for the SPA (a), ICE (b), and FER (c) vessels at L, C, and X bands with $\beta \in \{295, 315, 335\}^\circ$ and $\phi = 20^\circ$. They have been analyzed with the Pauli CTD theorem for a dynamic range of 25 dB. The lengths of the SPA, ICE, and FER ships are 30, 70, and 200 meters. Circles isolate the PePSs used in the feature vectors of Table 1.

so that qualitative data interpretation can be done. From all the contemplated bearings ($\beta = [295 : 10 : 355]$), Figure 5 only presents two of them, $\beta = 295, 315^\circ$ ($\phi = 20^\circ$), which can be considered as representatives of the remaining ones.

The inspection of these images shows that the isolation of those PePSs conforming the feature vectors is possible. They are imaged with the same scattering properties found in the scattering maps relative to polarimetric behavior, RCS, and spatial distribution. This implies that the proposed model can be inverted and, thus, valuable geometrical information is retrieved. In fact, this process has been done following the explanation of Section 2.4 and a confidence estimation of around 80% has been found.

However, the previous case is ideal and, normally, real scenes do not present such level of isolation between sea clutter and target response. Their interaction is higher and this leads to image corruption that can put PePS isolation at risk [7, 17]. Next section will further treat this point showing that a proper image post-processing can assure reliable model inversion even under adverse observation conditions.

4.2. Urban targets

Something similar has been done for the two building targets. In this case, PePS analysis is not performed while

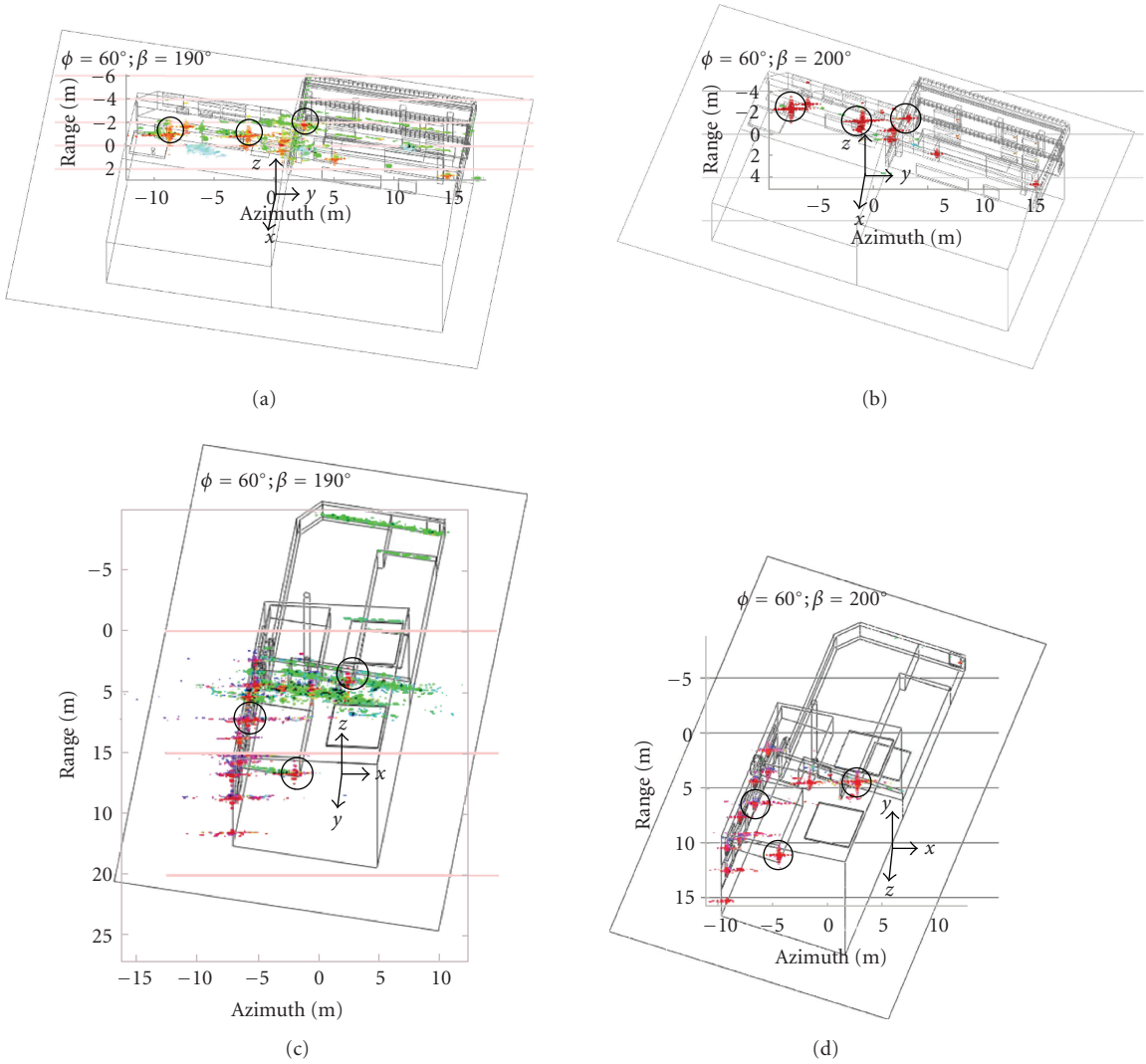

FIGURE 4: Scattering maps obtained for two building models at X band with $\beta \in \{190, 200\}^\circ$ and $\phi = 20^\circ$. They have been analyzed with the Pauli CTD theorem for a dynamic range of 25 dB. The models cover a maximum area of 50 square meters. Circles isolate the PePSs used in the feature vectors of Table 2.

thinking in classification (according to previous scattering analysis), but in other applications, such as subsidence, monitoring via PolInSAR is performed. There, the isolation of a set of guide scatterers with stable scattering properties is essential to retrieve accurate estimations of terrain deformation velocities along slant-range. So, the higher the scattering characterization is, the better the confidence is achieved. In single polarimetric SAR, this technique is mature, and now it is being successfully exploited in real scenarios [35, 36]. However, it has not migrated yet to PolInSAR, and so the current work would be helpful.

In contrast to the case with ships, SAR simulations are presented in terms of a 3D scattering map, where the relative scatter height is displayed jointly with the value of $|p^j_{n,xx}|$ (the previous RGB color code is also adopted here). These maps are shown in Figure 6 ($\phi = 60^\circ$, $\beta = 190^\circ$) and allow the isolation of almost all the PePSs identified in Section 3.2 with a confidence of ~75%. With these maps, a type of product similar to the ISAR one, but with less sensor requirements, can be obtained for scattering analysis [7]. One main advantage is the possibility to isolate different scatterers within the same resolution cell. This is advanced in Section 2.2 and related to the increased discrimination capability supplied by polarimetric channels. This permits to increase the accuracy in subsidence measurements due to the subpixel resolution that may be reached in some cells (in fact, those having PePSs, which can be considered as good candidates for use as subsidence guide scatterers).

5. MODEL EXPLOITATION

Once it has been shown that the proposed model of complex targets can be feasibly inverted in SAR images, the exploration of what applications can benefit is useful. In the case of ships, the application of this model can be considered mature, from which the novel VCA method resulted [7]. For

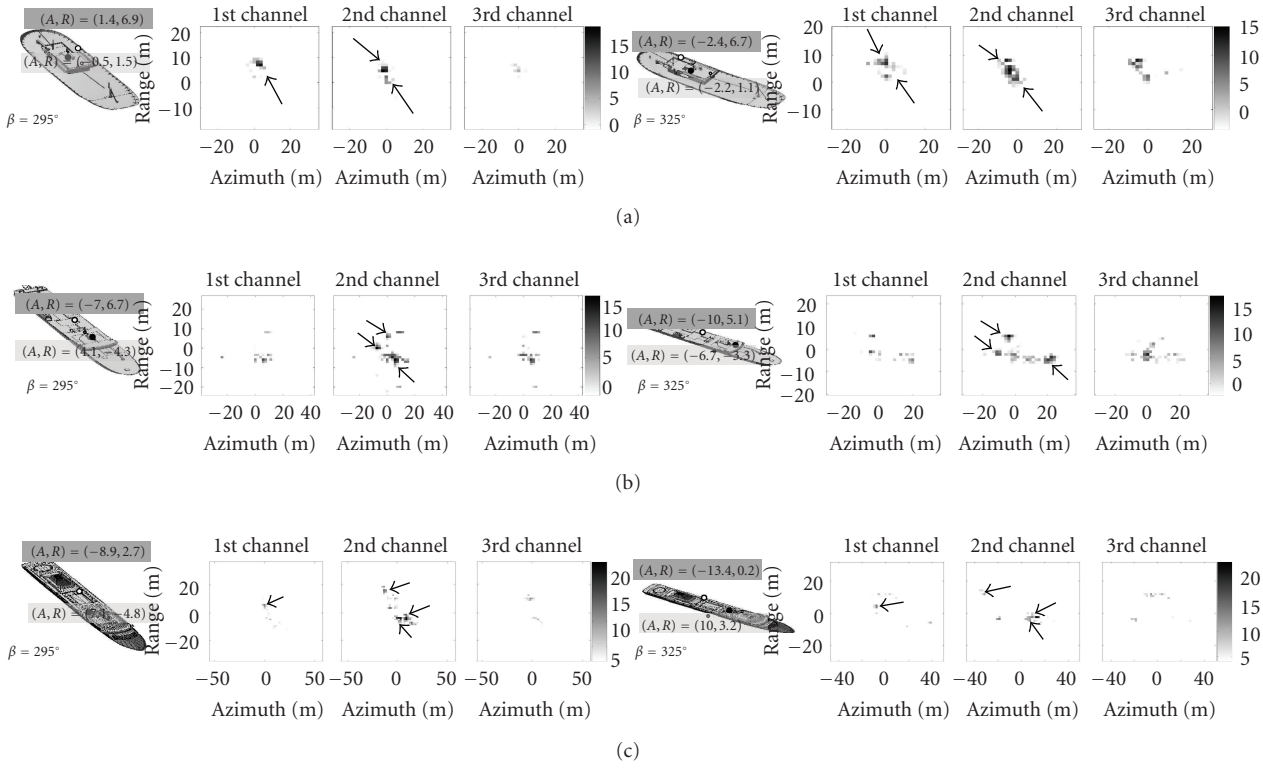

FIGURE 5: Pauli gray images showing the weight of each Pauli channel for the X band PolInSAR simulations of ships. The targets are $j = S0$ (a), $j = S1$ (b), and $j = S2$ (c) taking the bearing values of $\beta = 295, 325^{\circ}$. The arrows locate the reference PePSs gathered in the feature vectors of Table 1, where positions are transformed into the SAR azimuth slant-range grid according to the user incidence and bearing angles.

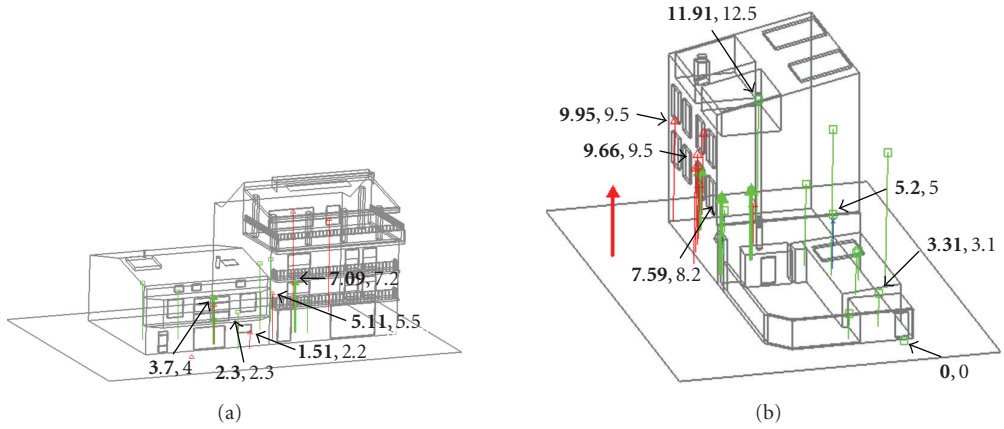

FIGURE 6: 3D scattering maps retrieved with PolInSAR for urban simulations ($\phi = 60^{\circ}$, $\beta = 190^{\circ}$). Bold and normal numbers indicate measured and expected heights for the highlighted scatterers. Model and data coregistration is made with a set of reference model points and imaging geometry.

urban targets, the study is in a preliminary stage and some guidelines for specific applications can be only provided.

5.1. Ship targets: VCA algorithm

The operating principle of VCA lies in analyzing the input PolInSAR dataset with the quad-pol Pauli vector (due to the fact that Pauli decomposition is a complete representation, the same simple mechanisms are isolated in any basis, e.g., linear or circular). This leads to three different interferograms (one per each Pauli mechanism), from which local maxima are isolated. All of them are combined in all possible permutations building estimated feature vectors with different lengths. These vectors are then correlated with the reference ones associated with specific ships, whose relative distance is quantified by a similarity parameter, S,

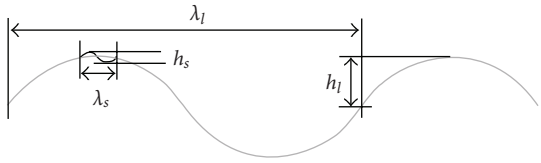

Figure 7: Scheme of the two-scale sea surface model.

Table 3: Scenario configurations for simulations in Section 4. Sea parameters are $h_l = 1.5$ m, $h_s = 0.1$ m, $\lambda_l = 100$ m, $\lambda_s = \lambda/(2\sin\phi)$.

Scenario	Bearings	Motions	Sea surface
0	$[295 : 10 : 355]^\circ$	No	No
1	$[295 : 10 : 355]^\circ$	Table 4	No
2	$[295 : 10 : 355]^\circ$	No	Two-scale
3	$[295 : 10 : 355]^\circ$	Table 4	Two-scale

Table 4: Rotational motions in the scenarios defined in Table 3. First-order angular velocities are expressed in rad/s.

β	$\dot{\delta}_{\text{roll}}$	$\dot{\delta}_{\text{pitch}}$	β	$\dot{\delta}_{\text{roll}}$	$\dot{\delta}_{\text{pitch}}$
295	−1.56	−0.26	335	−0.98	−1.16
305	−1.43	−0.52	345	−0.76	−1.32
315	−1.32	−0.76	355	−0.52	−1.43
325	−1.16	−0.98	—	—	—

based on an Euclidean norm [7]. The result is a quantitative manner for identifying the imaged ship with one of those within the available pattern base.

VCA performance is evaluated with a set of simulations similar to those of Figure 5. The same X band sensor has been used for a perpendicular baseline of $B^\perp = 30$ m and $\phi = 20^\circ$, and a resolution of 2.3 m in azimuth and 1.3 m in range [7]. The scenario considers the three types of ships for bearings ranging from 295 to 355 in steps of 10 degrees, surrounded by sea surface and experimenting ship motions. On the one hand, sea clutter is modeled with a two-scale approach for which a specific height profile is applied to the points of a dielectric discrete surface [17, 37–39]. The adopted complex dielectric permittivity is $\epsilon = 75 - j\cdot 27$, which corresponds to sea water with salinity of 35 psu and temperature of 25C [40, 41]. On the other hand, rotational and translational motions during image acquisition are considered by rotating the CAD model at each azimuth position. In real scenarios, ship motions can lead to important image distortions that are characterized by azimuth shifts. They normally cause notable geolocation errors and signature shape distortions [9, 42]. All environmental conditions are summarized in Tables 3 and 4. Sea main parameters are described in Figure 7, and pitching and rolling angular velocities are defined counterclockwise with respect to the rotation axis [9]. In all cases, ocean waves travel parallel to the ship from stern to bow.

Table 5 shows the similarity table for the specified bearings (the remaining ones provide similar results). They gather the similarity values related to each feature vector

Table 5: VCA similarity values, $0 < S < 1$, retrieved for the X band PolInSAR simulations with sea and ship motions.

$\beta = 295^\circ \mid \beta = 315^\circ$	SPA_{pat}	ICE_{pat}	FER_{pat}
Processing SPA	**0.57**|**0.44**	0.15|0	0|0.25
Processing ICE	0.1|**0.7**	**0.8**|0.44	0.1|0.25
Processing FER	0.21|0	0.3|0	**0.69**|**0.56**

when each ship is processed in the given observation conditions. As observed, all ships are well identified in almost all situations preserving a reasonable identification confidence against strong clutter. Two items are important: (1) the azimuth shifts help in some cases to improve the identification capability; (2) sea clutter appears to be the most adverse factor dropping the identification confidence. Specially adverse is for target $j = S1$whose lack of PePSs in the first Pauli channel makes the presence of the sea, with dominating sphere-like behaviors, increase the confusion with respect to the remaining ships. In general terms, VCA appears to be reliable enough as to consider its application in real scenarios. Further simulation studies give confidence to these asseveration and future measurement campaigns, which should try to provide the required framework for making the proper tests.

5.2. Urban targets: data interpretation

Section 4.2 has shown that the proposed model of complex targets may be useful for complementing single-pol subsidence studies, and may help in their possible migration to PolSAR systems (rather than developing classification). In this sense, the main advantage is the possibility to predict for which situations and geometries PePSs can be observed and considered as reliable guide scatterers for deformation studies.

Historically, urban applications have been related to orbital monitoring, because the velocity of changes can be assumed by the revisiting time of satellites, and historical databases for almost the same imaging geometry can be built. As a result, most geometries are expected to be imaged for a specific set of well-defined observation parameters and, hence, target model can be defined in urban environments as in ships. The only consideration is that feature vectors should meet the imaging geometries of current sensors rather than being expressed in terms of solid or radar aspect angles. In this context, feature vectors take sense, which may help, for example, to predict where the guide scatterers may be located. Such result would give a complementary reliability estimation of subsidence measurements, as well as refining and making the searching criteria more efficient.

6. CONCLUSION

This paper has presented a new modeling methodology for the SAR signatures of complex targets. The analysis of stacks of simulated images related to diversified scenarios, sensors, and types of targets is used to look for certain

reference scatterers (PePSs). Such scatterers accomplish a set of conditions focused to assure the discrimination among different types of geometries. Their 3D position and polarimetric scattering mechanism conform the bases of the model feature vectors, which allows to link the reflectivity information of SAR images with the macroscale structure of targets.

One of the main advantages of the proposed modeling approach is the minimization of the amount of real images required for testing the model. Certainly, simulated images can allow, in a first stage, the generation of preliminary version of models with reduced costs. Following this, these results would be used to define adequate measurement campaigns and model tests, which can lead to more refined solutions. In the current work, the first step has been tackled with the SAR simulator GRECOSAR, which has appeared to be an efficient tool for such scattering analysis.

GRECOSAR has been used to generate scattering maps for three types of ships and two types of buildings. The images have shown that PePS isolation is possible, but with different scattering sensitivity in both types of targets. While the same feature vector is valid for ships along a large set of observation conditions, buildings have to be identified with different vectors. The reason is their higher structure complexity and lack of symmetry.

The analysis of these results in SAR images has confirmed that the current model can be useful for different applications. In the case of ships, classification techniques may benefit as target discrimination can be reached via a quantitative and robust manner. This has been shown by presenting the novel VCA method, which allows, according to tests performed in simulated scenarios, high identification ratios even against sea clutter and ship motions. In the past, these items have become important limitations for classical methods. For urban scenarios, the current model is useful for fixing structures which are potential candidates for use in subsidence applications. Improved interpretation of interferometric data is also an important item, which may benefit the development of height profiles or better real-data analysis.

Therefore, the scattering-based model seems viable for ships and urban-like targets. Its exploitation in SAR imagery needs, however, from PolInSAR sensors with recommended resolutions lower than 3 m so that PePSs can be properly isolated. In the case of ships, single-pass modes are very demanding as it is not clear whether satellite-based solutions could be someday available. On the contrary, just launched designs as TerraSAR-X and Radarsat-2 can provide repeat-pass capabilities useful for urban applications. Future works should devote efforts for evaluating the model in real images so that definitive confidence to the model and related applications can be reached.

ACKNOWLEDGMENTS

This work was supported by Spanish Ministerio de Educación y Ciencia (MEC) and EU Fondos Europeos para el Desarrollo Regional (FEDER) funds under Project no. TEC2005-06863-C02-01.

REFERENCES

[1] A. Roth and R. Werninghaus, "Status of the TerraSAR-X mission," in *Proceedings of the International Geoscience and Remote Sensing Symposium (IGARSS '06)*, pp. 1918–1920, Denver, Colo, USA, July-August 2006.

[2] R. Touzi, R. K. Raney, and F. Charbonneau, "On the use of permanent symmetric scatterers for ship characterization," *IEEE Transactions on Geoscience and Remote Sensing*, vol. 42, no. 10, pp. 2039–2045, 2004.

[3] S. Guillaso, L. Ferro-Famil, A. Reigber, and E. Pottier, "Building characterization using L-band polarimetric interferometric SAR data," *IEEE Geoscience and Remote Sensing Letters*, vol. 2, no. 3, pp. 347–351, 2005.

[4] R. Z. Schneider, K. P. Papathanassiou, I. Hajnsek, and A. Moreira, "Polarimetric and interferometric characterization of coherent scatterers in urban areas," *IEEE Transactions on Geoscience and Remote Sensing*, vol. 44, no. 4, pp. 971–983, 2006.

[5] D. Perissin and A. Ferretti, "Urban-target recognition by means of repeated spaceborne SAR images," *IEEE Transactions on Geoscience and Remote Sensing*, vol. 45, no. 12, pp. 4043–4058, 2007.

[6] G. Margarit, *Marine applications of SAR polarimetry*, Ph.D. dissertation, Remote Sensing Laboratory (RSLab), Universitat Politècnica de Catalunya, Barcelona, Spain, July 2007.

[7] G. Margarit, J. J. Mallorqui, and X. Fàbregas, "Single-pass polarimetrie SAR interferometry for vessel classification," *IEEE Transactions on Geoscience and Remote Sensing*, vol. 45, no. 11, pp. 3494–3502, 2007.

[8] G. Margarit, J. Mallorqui, I. Corney, L. Pipia, C. López, and F. X. Fàbregas, "Analysis of urban areas scattering with simulated SAR imagery," in *Proceedings of ESA Fringe Workshop*, Frascati, Italy, November 2007.

[9] G. Margarit, J. J. Mallorqui, J. M. Rius, and J. Sanz-Marcos, "On the usage of GRECOSAR, an orbital polarimetric SAR simulator of complex targets, to vessel classification studies," *IEEE Transactions on Geoscience and Remote Sensing*, vol. 44, no. 12, pp. 3517–3526, 2006.

[10] J. M. Rius, M. Ferrando, and L. Jofre, "High-frequency RCS of complex radar targets in real-time," *IEEE Transactions on Antennas and Propagation*, vol. 41, no. 9, pp. 1308–1319, 1993.

[11] J. M. Rius, M. Vall-llossera, and A. Cardama, "GRECO: graphical processing methods for high frequency RCS prediction," *Annals of Telecommunications*, vol. 50, no. 5-6, pp. 551–556, 1995.

[12] *IMPAST project final report with reference (IMPAST/D 1.4/2.0) and under contract nr: Q5RS-2001-02266*, IMPAST consortium, DG-FISH.

[13] *DECLIMS project*, Joint Research Center (JRC), European Comission, https://declims.jrc.ec.europa.eu/1.

[14] *Land and Sea Integrated Monitoring for European Security (LIMES) project*, European Comission, 6th Framework Programme.

[15] *GID*, Manual of; International Center for Numerical Methods in Engineering (CIMNE).

[16] G. Margarit, J. J. Mallorqui, C. López-Martínez, and J. Fortuny-Guasch, "Phenomenological vessel scattering study based on simulated inverse SAR imagery," submitted to *IEEE Transactions on Geoscience and Remote Sensing*.

[17] G. Margarit, J. J. Mallorqui, C. López-Martínez, and J. Fortuny-Guasch, "Exploitation of Ship Scattering in Polarimetric SAR for an Improved Classification under High Clutter

Conditions," accepted for publication at *IEEE Transactions of Geoscience and Remote Sensing*.

[18] R. Touzi and F. Charbonneau, "Characterization of target symmetric scattering using polarimetric SARs," *IEEE Transactions on Geoscience and Remote Sensing*, vol. 40, no. 11, pp. 2507–2516, 2002.

[19] S. R. Cloude and E. Pettier, "A review of target decomposition theorems in radar polarimetry," *IEEE Transactions on Geoscience and Remote Sensing*, vol. 34, no. 2, pp. 498–518, 1996.

[20] P. A. Rosen, S. Hensley, I. R. Joughin, et al., "Synthetic aperture radar interferometry," *Proceedings of the IEEE*, vol. 88, no. 3, pp. 333–382, 2000.

[21] W.-M. Boerner, S. R. Cloude, and E. Poitier, "Radar polarimetry and interferometry," Tech. Rep. RTO-EN-SET-081, NATO Research & Technology Organisation, Paris, France, 2004.

[22] W.-M. Boerner, L. A. Cram, W. A. Holm, et al., *Direct and Inverse Methods in Radar Polarimetry*, NATO ASI Series C: Mathematical and Physical Sciences, Kluwer Academic Publishers, Dordrecht, The Netherlands, 1985.

[23] R. K. Raney, "Dual-polarized SAR and stokes parameters," *IEEE Geoscience and Remote Sensing Letters*, vol. 3, no. 3, pp. 317–319, 2006.

[24] R. K. Raney, "Hybrid-polarity SAR architecture," *IEEE Transactions on Geoscience and Remote Sensing*, vol. 45, no. 11, pp. 3397–3404, 2007.

[25] J.-C. Souyris, P. Imbo, R. Fjørtoft, S. Mingot, and J.-S. Lee, "Compact polarimetry based on symmetry properties of geophysical media: the $\pi/4$ mode," *IEEE Transactions on Geoscience and Remote Sensing*, vol. 43, no. 3, pp. 634–645, 2005.

[26] M. Tello, C. López-Martínez, and J. J. Mallorqui, "A novel algorithm for ship detection in SAR imagery based on the wavelet transform," *IEEE Geoscience and Remote Sensing Letters*, vol. 2, no. 2, pp. 201–205, 2005.

[27] D. J. Crisp, "The state-of-the-art in ship detection in synthetic aperture radar imagery," Public Release Document DSTO-RR-0272, Defence Science and Technology Organization (DSTO), Department of Defence, Australian Government, Canberra, Australia, 2004.

[28] D. Perissin, C. Prati, and F. Rocca, "ASAR parallel-track PS analysis in urban sites," in *Proceedings of the International Geoscience and Remote Sensing Symposium (IGARSS '07)*, pp. 1167–1170, Barcelona, Spain, June 2007.

[29] F. Cao, W. Hong, Y. Wu, and E. Pottier, "An unsupervised segmentation with an adaptive number of clusters using the SPAN/H/α/A space and the complex Wishart clustering for fully polarimetrie SAR data analysis," *IEEE Transactions on Geoscience and Remote Sensing*, vol. 45, no. 11, pp. 3454–3467, 2007.

[30] S. N. Madsen, *Syntehtic Aperture Radar Interferometry: Principles and Applications*, Artech House, Boston, Mass, USA, 1999.

[31] S. Musman, D. Kerr, and C. Bachmann, "Automatic recognition of ISAR ship images," *IEEE Transactions on Aerospace and Electronic Systems*, vol. 32, no. 4, pp. 1392–1404, 1996.

[32] G. Zilman, A. Zapolski, and M. Marom, "The speed and beam of a ship from its wake's SAR images," *IEEE Transactions on Geoscience and Remote Sensing*, vol. 42, no. 10, pp. 2335–2343, 2004.

[33] L. Pipia, X. Fabregas, A. Aguasca, C. López-Martínez, J. J. Mallorqui, and O. Moraline, "Polarimetric temporal information for urban deformation map retrieval," in *Proceedings of the International Geoscience and Remote Sensing Symposium (IGARSS '07)*, pp. 192–195, Barcelona, Spain, June 2007.

[34] L. Pipia, X. Fàbregas, A. Aguasca, and C. López-Martínez, "Atmospheric artifact compensation in ground-based DInSAR applications," *IEEE Geoscience and Remote Sensing Letters*, vol. 5, no. 1, pp. 88–92, 2008.

[35] A. Ferretti, C. Prati, and F. Rocca, "Permanent scatterers in SAR interferometry," *IEEE Transactions on Geoscience and Remote Sensing*, vol. 39, no. 1, pp. 8–20, 2001.

[36] O. Mora, *Advanced differential interferometric SAR techniques for detection of terrain and building displacements*, Ph.D. dissertation, Remote Sensing Laboratory (RSLab), Universitat Politècnica de Catalunya, Barcelona, Spain, April 2004.

[37] W. J. Plant, W. C. Keller, and K. Hayes, "Measurement of river surface currents with coherent microwave systems," *IEEE Transactions on Geoscience and Remote Sensing*, vol. 43, no. 6, pp. 1242–1257, 2005.

[38] R. O. Harger, "A sea surface height estimator using synthetic aperture radar complex imagery," *IEEE Journal of Oceanic Engineering*, vol. 8, no. 2, pp. 71–78, 1983.

[39] G. Margarit and J. J. Mallorqui, "Discretization effects in sea surface simulation applied to ship classification studies," in *Proceedings of the 2nd International SAR Oceanography Workshop (SEASAR '08)*, Frascati, Italy, January 2008.

[40] V. Hesany, W. J. Plant, and W. C. Keller, "The normalized radar cross section of the sea at 10° incidence," *IEEE Transactions on Geoscience and Remote Sensing*, vol. 38, no. 1, pp. 64–72, 2000.

[41] S. Blanch and A. Aguasca, "Dielectric permittivity measurements of sea water at L band," in *Proceedings of the 1st Results Workshop on EuroSTARRS, WISE, LOSAC Campaigns*, pp. 137–141, Toulouse, France, November 2002.

[42] K. Ouchi, M. Iehara, K. Morimura, S. Kumano, and I. Takami, "Nonuniform azimuth image shift observed in the Radarsat images of ships in motion," *IEEE Transactions on Geoscience and Remote Sensing*, vol. 40, no. 10, pp. 2188–2195, 2002.

Hindawi Publishing Corporation
International Journal of Navigation and Observation
Volume 2008, Article ID 310656, 16 pages
doi:10.1155/2008/310656

Review Article

Multichannel Along-Track Interferometric SAR Systems: Moving Targets Detection and Velocity Estimation

Alessandra Budillon, Vito Pascazio, and Gilda Schirinzi

Dipartimento per le Tecnologie, Università di Napoli "Parthenope", Centro Direzionale di Napoli, Isola C4, 80143 Napoli, Italy

Correspondence should be addressed to Vito Pascazio, vito.pascazio@uniparthenope.it

Received 19 February 2008; Revised 31 July 2008; Accepted 25 September 2008

Recommended by Simon Watts

Along-track interferometric synthetic aperture radar (AT-InSAR) systems are used to estimate the radial velocity of targets moving on the ground, starting from the interferometric phases, obtained by the combinations of two complex SAR images acquired by two antennas spatially separated along the platform moving direction. Since the radial velocity estimation obtained from a single-phase interferogram (single-channel) suffers from ambiguities, multichannel AT-InSAR systems using more than one interferogram can be used. In this paper, we first analyze the moving target detection problem, evaluating the systems performance in terms of probability of detection and probability of false alarm obtained with different values of target radial velocity, signal-to-clutter ratio, and clutter-to-thermal noise ratio. Then, we analyze the radial velocity estimation accuracy in terms of Cramer-Rao lower bounds and of mean square error values, obtained by using a maximum likelihood estimation technique. We consider the cases of single-baseline and dual-baseline satellite systems, and we evaluate the detection and estimation performance improvement obtained in the dual-baseline case with respect to the single-baseline one. Sensitivity of the presented method with respect to the involved target and system parameters is also discussed.

1. INTRODUCTION

In this paper, we review the problem of detecting the presence of a ground moving target and estimating its radial velocity by means of along-track inteferometric synthetic aperture radar (AT-InSAR) systems, mounted on moving platforms. This kind of systems can be used, for example, for continuous (day and night and with any weather condition) traffic monitoring [1, 2].

The detection of moving targets on the ground by means of radar systems is addressed in literature as ground moving target indication (GMTI). GMTI is a very difficult problem due to the difficulty of separating the signal returned from a moving target from the stationary background (clutter) [3, 4]. Several methods, based on very different approaches, have been proposed in literature. In some of them, radar detection of moving targets on the ground is accomplished by enhancing the target Doppler signature against the competing ground clutter returns. Recent clutter suppression techniques use space-time adaptive processing (STAP) [5–7], requiring more than two channels, and time-frequency processing [8], requiring high pulse repetition frequency (PRF) values. While these techniques are effective in improving the detection of fast targets, for slowly moving targets the signal from clutter separation is more critical. In particular, clutter reduction becomes more critical when the Doppler frequency shift due to the target radial velocity falls inside the clutter azimuth bandwidth. Since such bandwidth increases with the ratio between the platform velocity and the azimuth antenna dimension, which in satellite-borne case is high, the range of target velocities values which are critical to be estimated can be wide in the case of satellite systems. Moreover, spectral separation requires increased PRF values, which are not desirable for the very high data rates and PRF ambiguity problems [9].

Other systems that can be used to detect ground moving target are the AT-InSAR systems, initially introduced to study ocean currents [10, 11], and then used to detect slow moving objects (ships, ground vehicles) [12–15] and to estimate their radial velocity. AT-InSAR systems use more than one SAR antenna (typically two), mounted on the same platform and displaced along the platform moving direction. The information about the radial velocity of the moving target is estimated from the interferometric phase of the images.

The accuracy obtained for the estimation of ocean currents velocity using airborne AT-InSAR sensors can be of the order of few centimeters per second [10]. These very satisfactory results can be obtained since the two images acquired with a negligible time delay are very highly correlated and all the scatterers within a resolution cell move with the same velocity. In this case, the moving target is an extended one (the sea surface), while the stationary clutter is absent. The only disturbing signal to be considered is the additive thermal noise.

Differently from the case of ocean currents estimation, when AT-InSAR techniques are applied to the detection and tracking of small targets, such as vehicles, the presence of stationary clutter has to be considered. This heavily affects the interferometric phase values and their statistical distribution, thus degrading the performance of the moving target detection and of the radial velocity estimation.

For the application of statistical techniques to the detection and estimation steps, it is necessary to compute the statistical distribution of the measured interferometric phases. In the stationary image pixels, the interferometric phase reduces to only phase noise, whose statistical distribution is well known and depends on the interferometric signals correlation (the coherence) [16]. In the image pixels where a moving target is present, the phase statistical distribution diverges from that of stationary pixels, and strongly depends on the target velocity and on the statistical model assumed for the target radar cross-section (RCS). The higher the velocity, the larger the deviation, with respect to the stationary case. Different models can be assumed for the radar response of the target. In the following we will adopt two different RCS models: a deterministic model [13], and a zero mean Gaussian model [12], underlying differences and analogies.

Another problem to be taken into account is that the interferometric phase is measured in the interval $(-\pi, \pi]$, then a *phase unwrapping* (PhU) operation is required to retrieve the target radial velocity. The PhU operation presents solution ambiguities when only one phase interferogram (single-channel) is used. It has already been shown in [13, 15] that the joint use of multichannel configurations (derived from the use of more than two interferometric images acquired with different baselines or at different working frequencies) and of classical statistical estimation techniques allows to obtain very accurate solutions and to overcome the limitations due to the presence of ambiguous solutions, intrinsic in the single-channel configurations.

In this paper, we show that AT-InSAR systems based on the use of more interferograms (multichannel) acquired with frequency or baseline diversity outperform conventional AT-InSAR systems using a single interferogram. In particular, we show that even a dual-baseline system allows achieving detection and estimation performance much better than the one obtained by a single-baseline system. The results obtained in the estimation process are partially a review of what we have presented in [15]. The analysis, in terms of moving target detection and radial velocity estimation accuracy, is carried out varying the main AT-InSAR system and target parameters, such as velocity values, signal-to-clutter ratio (SCR), defined as the ratio between the power received from the moving target and the background clutter power, and clutter-to-noise ratio (CNR), defined as the ratio between the power received from the background clutter and the additive thermal noise power in the receiver. The performances presented in the following sections have been obtained considering two RCS models: deterministic and Gaussian. Finally, a discussion about robustness of the proposed model with respect to uncertainty on system parameters has been also included.

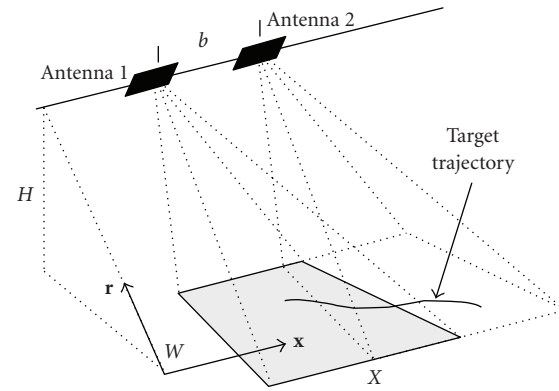

Figure 1: Along-track interferometry system geometry.

2. ALONG-TRACK INTERFEROMETRIC SAR SYSTEMS

Consider an AT-InSAR system constituted by two antennas moving along the direction x (azimuth) (see Figure 1), and suppose that the two antennas are separated by the baseline b along the azimuth direction x, such that $b \ll H$, where H is the platform height. Assume a target on the ground moving with a constant velocity $\mathbf{v}_T = v_{Tx}\mathbf{x} + v_{Tr}\mathbf{r}$, where v_{Tx} and v_{Tr} are the velocity components along the azimuth and the line of sight direction (range) $\mathbf{r}$, respectively.

Both azimuth and range velocity components change the Doppler history of the moving target (but in different ways) in comparison to the stationary background. In order to show this behavior, we have simulated an SAR image of a stationary target shown in Figure 2(a) (the horizontal axis represents azimuth and the vertical axis represents range). In Figures 2(b) and 2(c), the images of a target moving with only radial velocity and with only azimuth velocity are shown, respectively. Finally, the image in Figure 2(d) is related to a target moving with both radial and azimuth velocity components. We can observe that the radial velocity component v_{Tr} produces an azimuth displacement of the target, due to a Doppler offset (see Figures 2(b) and 2(d)). The azimuth velocity component v_{Tx}, instead, produces a Doppler slope change [3, 5] causing a defocusing in the moving target image (see Figures 2(c) and 2(d)) that can be compensated by using autofocusing techniques [17]. These effects can be exploited to separate moving target from stationary background by means of Doppler filtering [4]. However, Doppler filtering is effective for fast moving targets

and requires PRF values much higher than the Doppler bandwidth for making available a certain visibility region in the frequency domain and to achieve a consistent clutter reduction.

To avoid excessive data rates and the PRF ambiguity problem [9], it is desirable to work with low PRF values. In this case, along-track interferometric systems allow the radial velocity estimation exploiting phase information.

Suppose that $|v_{Tx}|,\ |v_{Tr}| \ll |v_P|$, where $\mathbf{v}_P = v_P\mathbf{x}$ is the velocity of the flying platform and $H \gg X$ and $H \gg W$, where X and W are the antenna footprint dimensions. Let Z_1 the complex SAR image be acquired by the first antenna and let Z_2 the complex SAR image of the same ground region be acquired by the second antenna (we understand the dependence on the pixel coordinates).

The two SAR complex images can be modeled as follows:

$$Z_1 = \begin{cases} Z_{c1} + N_1 + Z_{T1} & \text{in presence of moving target,} \\ Z_{c1} + N_1 & \text{in absence of moving target,} \end{cases}$$
$$Z_2 = \begin{cases} Z_{c2} + N_2 + Z_{T2} & \text{in presence of moving target,} \\ Z_{c2} + N_2 & \text{in absence of moving target,} \end{cases} \tag{1}$$

where Z_{c1} and Z_{c2} are the clutter signals acquired by the two antennas, N_1 and N_2 represent the thermal noise at the receivers, and Z_{T1} and Z_{T2} denote the SAR images of the moving target produced by the two interferometric antennas. The SAR target images will exhibit a phase factor related to the radial velocity [10]:

$$\mathrm{Z}_{T1} = A_1, \qquad \mathrm{Z}_{T2} = A_2 e^{-j\phi_v}, \tag{2}$$

where A_1 and A_2 are the target complex images and ϕ_v is the nominal ATI phase which in the above-mentioned assumptions is given by

$$\phi_v = \left\langle \frac{4\pi b}{\lambda} \frac{v_r}{|v_P|} \right\rangle_{2\pi} = \left\langle \frac{4\pi b}{\lambda} u_r \right\rangle_{2\pi}, \tag{3}$$

where $\langle\cdot\rangle_{2\pi}$ is the modulo 2π operation, λ is the wavelength corresponding to the working frequency $f = c/\lambda$ of the SAR system, and $u_r = v_r/|v_P|$ is the normalized radial velocity, where the moving target is present $v_r \neq 0$ and $\phi_v \neq 0$. From (3), it follows that there are several velocity values which produce the same nominal ATI phase. The difference between two velocity values that produce the same nominal ATI phase is $2ku_{r,\mathrm{amb}}$, where k is an integer and $u_{r,\mathrm{amb}} = \pm\lambda/(4b)$ is the ambiguity velocity value corresponding to a nominal ATI phase equal to $\pm\pi$.

The SAR interferometric phase signal Φ is

$$\Phi = \angle Z_1 Z_2^*, \tag{4}$$

where $\angle$ denotes the principal phase value and $*$ denotes the conjugate.

Note that the measured interferometric phase ϕ differs from the nominal ATI phase ϕ_v due to the presence of clutter and noise signals.

It is well known that the SAR clutter signals Z_{c1} and Z_{c2} can be assumed as random processes, whose real and imaginary parts are mutually uncorrelated Gaussian signals, with zero mean and same variance, since they are resulting from the superposition of the signals backscattered from many scattering centers lying in the resolution cell. N_1 and N_2 can be modeled as two additive (to the clutter) zero mean Gaussian complex processes independent of each other, and independent on the clutter.

Then, when the moving target is absent, the two processes Z_1 and Z_2 are Gaussian with zero mean and correlation coefficient γ given by [18]

$$\begin{aligned} \gamma &= \frac{E[(Z_1 - E[Z_1])(Z_2 - E[Z_2])^*]}{\sqrt{\mathrm{var}[Z_1]\mathrm{var}[Z_2]}} \\ &= \frac{E[(Z_{c1} + N_1)(Z_{c2} + N_2)^*]}{\sqrt{E[|Z_{c1} + N_1|^2]E[|Z_{c2} + N_2|^2]}} \\ &= \frac{\gamma_c}{(1 + \sigma_n^2/\sigma_c^2)} = \frac{\gamma_c}{(1 + 1/\mathrm{CNR})}, \end{aligned} \tag{5}$$

where $E[\,]$ denotes the expectation operation, γ_c is the clutter coherence, representing the correlation between images Z_{c1} and Z_{c2}, and CNR is given by

$$\mathrm{CNR} = \frac{\sigma_c^2}{\sigma_n^2}, \tag{6}$$

where $2\sigma_c^2$ and $2\sigma_n^2$ are the clutter and thermal noise powers (the factor 2 is due to the sum of the powers of the real and imaginary parts).

In ATI-InSAR space applications, γ_c is usually assumed to be equal to one [12], since the two images are acquired from the same antenna position with a time lag lower than 1 millisecond. In the case of bistatic systems, as next generation satellite clusters, clutter coherence can, instead, assume values smaller than 1. Moreover, a parasitic cross-track baseline may introduce a height-induced interferometric phase that needs to be taken into account. Anyway, it can be partly compensated by exploiting a priori DEM knowledge.

In absence of targets, the pdf of the interferometric phase can be expressed in closed form as [16]

$$\begin{aligned} &f_\Phi(\phi; \phi_0, \gamma) \\ &= \frac{1}{2\pi} \frac{1 - |\gamma|^2}{1 - |\gamma|^2 \cos^2(\phi - \phi_0)} \\ &\quad \times \left\{ 1 + \frac{|\gamma| \cos(\phi - \phi_0) \cos^{-1}[-|\gamma| \cos(\phi - \phi_0)]}{[1 - |\gamma|^2 \cos^2(\phi - \phi_0)]^{1/2}} \right\}, \\ &\qquad \phi \in (-\pi, \pi], \end{aligned} \tag{7}$$

where ϕ_0 is the phase of γ, that in this case is equal to zero, being the coherence given by (5) real-valued since the real and imaginary parts of the clutter signal are uncorrelated.

When the moving target is present, two different statistical models for Z_{T1} and Z_{T2} can be considered as follows:

(1) *deterministic model:* the target RCS is assumed to be deterministic;

(2) *Gaussian model:* the target RCS is assumed to be Gaussian distributed with zero mean.

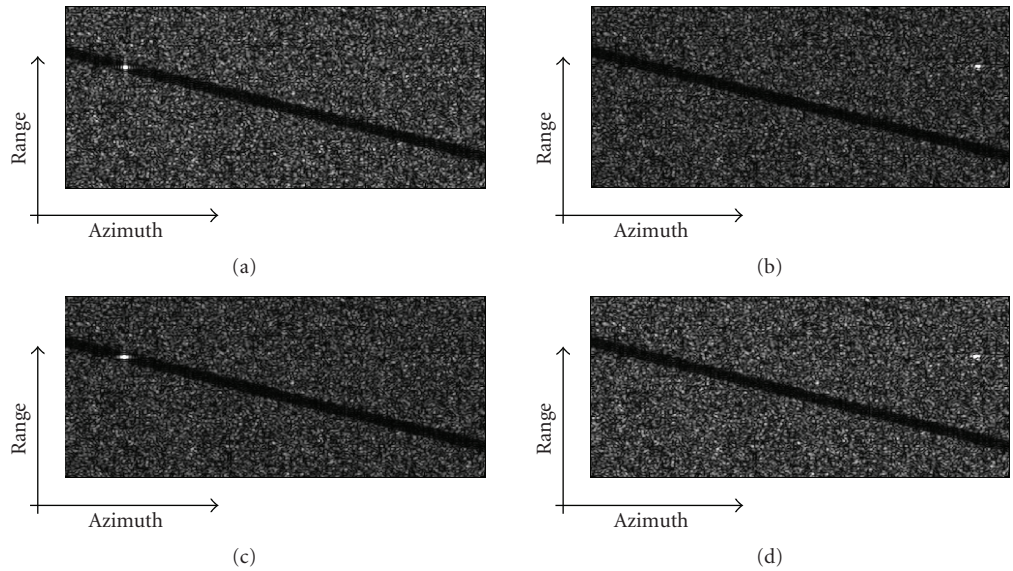

Figure 2: (a) Stationary target, (b) target moving with radial velocity ($v_{Tr} = 27.4$ Km/h), (c) target moving with azimuth velocity ($v_{Tx} = -109.6$ Km/h), and (d) target moving with both radial and azimuth velocities ($\mathbf{v}_T = v_{Tx}\mathbf{x} + v_{Tr}\mathbf{r}$).

2.1. Statistical distribution of AT-InSAR phase for deterministic RCS

A deterministic model is applicable to the case of a target whose RCS can be expressed by a deterministic function of the incidenceangle. This model applies to canonical scattering objects (such as corner reflectors, spheres), and to complex or extended targets whose RCS does not rapidly change between the interferometric acquisitions. Since the RCS value of a given target mainly depends on incidence angle and target aspect angle, which does not change in the small time required to the SAR antenna to cover the baseline length, the target RCS can be usually assumed to be constant in the interferometric images. Such value influences the signal-to-clutter ratio, and is not a priori known. This is the model to be used in the interferograms simulation. It can be adopted also in the velocity estimation procedure if a precise knowledge of the RCS value is available. An accurate knowledge of the average RCS values can be available only for accurately characterized targets [19]. Moreover, this case provides the reference pdfs of the interferometric phases produced by a given complex target of known RCS. In this assumption, we can put in (2) $A_1 = A_2 = A$, with A a deterministic constant. Then, the two processes Z_1 and Z_2 are Gaussian, with nonzero mean (due to the presence of the target) and the target RCS can be described in terms of $|A|^2$.

The first-order probability density function (pdf) of the interferometric phase Φ can be, in this case, numerically computed via Monte Carlo techniques, since no closed form, so far, has been found. The pdf depends on the clutter coherence coefficient γ_c, on the target radial velocity (as shown by (2) and (3)) and on CNR and SCR, where CNR is given by (6) and SCR is given by

$$\mathrm{SCR} = \frac{|A|^2}{2\sigma_c^2}, \tag{8}$$

Table 1: Main parameters of TerraSAR-X system.

TerraSAR-X	
Height	514.8 Km
Platform velocity	7.6 Km/s
Along-track antenna dimension	4.8 m
Across-track antenna dimension	0.8 m
Along-track baseline	1.2 m
Working frequency	X band—9.65 GHz
Wavelength	3.12 cm
Range bandwidth	150 MHz

where $|A|^2$ is the signal power. In this case, the SCR values do not affect the coherence γ between the signals Z_1 and Z_2, which is still expressed by (5), but affect the shape of the pdf, which cannot be expressed by (7). Figure 3 shows the dependence of the pdf $f_\Phi(\phi)$ on SCR, CNR, and u_r in the case of a deterministic target, evaluated for $\gamma_c = 1$ and using the TerraSAR-X parameters [20] of Table 1. In Figure 3(a), the pdf shape is reported for the values CNR = 10 dB and SCR = 0, 10, and 20 dB and a radial normalized velocity $u_r = 3.25 \times 10^{-3}$, corresponding to the nominal ATI phase value $\phi_v = \pi/2$. Figure 3(b) is related to the values SCR = 10 dB and CNR = 0, 10, and 20 dB and to the same value of u_r. In Figure 3(c), the pdfs are plotted for SCR = 10 dB and CNR = 10 dB and by varying the normalized velocity u_r.

Figure 3 shows that the measured phase pdfs are strongly dependent on SCR values and assume a peak value in a position which, for low SCR, is different from the nominal ATI phase value (3), that in this case is given by $\pi/2$ and is highlighted with a dot. The dependence on CNR is, instead, less pronounced. The sensitivity of the pdfs shape with respect to u_r is significant, and the corresponding variances gradually increase by increasing u_r.

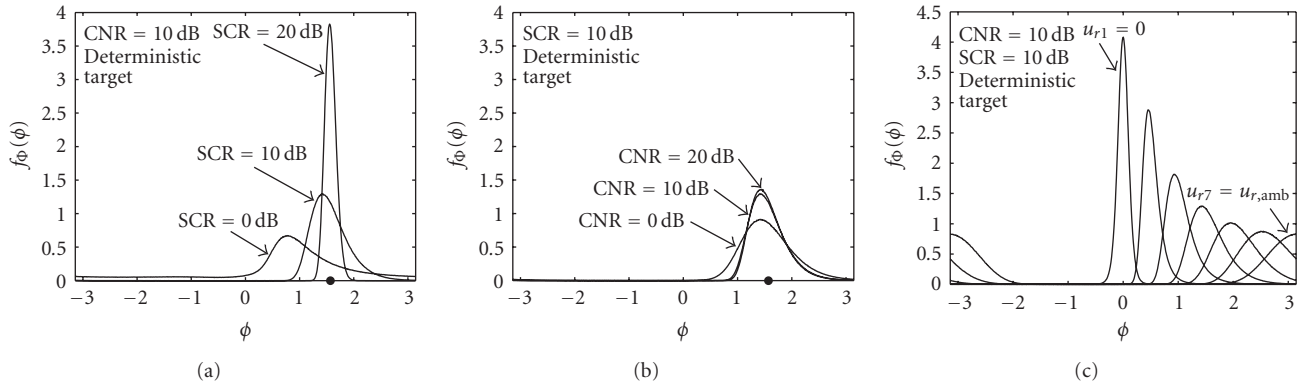

FIGURE 3: (a) Pdf of the interferometric phase in presence of a deterministic target moving with a radial velocity such that $\phi_v = \pi/2$ (the dot on the ϕ axis), for $\gamma_c = 1$, CNR = 10 dB, and SCR = 0, 10, 20 dB, (b) SCR = 10 dB and CNR = 0, 10, 20 dB, and (c) SCR = 10 dB, CNR = 10 dB, for seven radial velocities ($u_{rk} = (k-1)/6\ u_{r,\text{amb}}, k = 1, \ldots, 7$).

2.2. Statistical distribution of AT-InSAR phase for Gaussian RCS

A Gaussian model is applicable when the RCS of the targets A_1 and A_2 and then the signals Z_{T1} and Z_{T2} are assumed to be zero mean (complex) Gaussian processes, as in [12]. This model allows to take into account the lack of knowledge of the target RCS values (that can be described in terms of variance σ_T^2) and then of the SCR. It applies to complex or extended targets which can be considered to consist of a large number of isotropic scattering elements, randomly distributed in a region whose dimensions are large compared to the wavelength of the illuminating radiation, and all contributing to the overall signal with the same weight [21]. When the number of the elementary scatterers in which the target can be decomposed is small and/or some of them are dominant with respect to the others, the pdf of the backscattered signal is not zero mean Gaussian and is difficult to derive [22]. However, even if this model could not be always appropriate for the description of the signal intensity distribution, it has the advantage of providing an analytical form for the interferometric phase pdf, which in many cases well approximates the true distribution. Moreover, as it will be shown in the next section, the adoption of a Gaussian model for the moving target RCS instead of the actual deterministic model will not impair significantly the GMTI performance.

Since the signals Z_1 and Z_2 acquired by the two interferometric antennas are still zero mean Gaussian signals, as happens when the target is absent, the pdf of the interferometric phase can be expressed in the closed form given by (7), where γ is the coherence coefficient between the images Z_1 and Z_2, and ϕ_0 is the phase of γ. Now, the expression of γ is changed with respect to (5) and is given by [12]

$$\gamma = \frac{E\left[\left(Z_{c1} + N_1 + Z_{T1}\right)\left(Z_{c2} + N_2 + Z_{T2}\right)^*\right]}{\sqrt{E\left[\left|Z_{c1} + N_1 + Z_{T1}\right|^2\right]E\left[\left|Z_{c2} + N_2 + Z_{T2}\right|^2\right]}} = \frac{\gamma_c\sigma_c^2 + \sigma_T^2\gamma_T}{\sigma_c^2 + \sigma_n^2 + \sigma_T^2} = \frac{\gamma_c + \gamma_T \text{SCR}}{1 + 1/\text{CNR} + \text{SCR}}, \tag{9}$$

where $\text{SCR} = \sigma_T^2/\sigma_c^2$, and γ_T is the target (complex) coherence and depends on the target velocity through the nominal phase (1):

$$\gamma_T = \frac{E[Z_{T1}Z_{T2}^*]}{\sqrt{E\left[\left|Z_{T1}\right|^2\right]E\left[\left|Z_{T2}\right|^2\right]}} = \frac{E[A_1A_2^*]}{\sqrt{E\left[\left|A_1\right|^2\right]E\left[\left|A_2\right|^2\right]}}e^{j\phi_v} = \gamma_{T0}e^{j\phi_v}, \tag{10}$$

where γ_{T0} is the target coherence for zero radial velocity, equal to one. It has to be noted that ϕ_0, the phase of γ, is different from ϕ_v.

Figure 4 shows the dependence of the pdf $f_\Phi(\phi)$ on SCR, CNR, and u_r in the case of a Gaussian distributed target, evaluated for $\gamma_c = \gamma_{T0} = 1$ and using the TerraSAR-X parameters [20] of Table 1. In Figure 4(a), the pdf shape is reported for the values CNR = 10 dB and SCR = 0, 10, and 20 dB and a radial normalized velocity $u_r = 3.25 \times 10^{-3}$, corresponding to the nominal ATI phase value $\phi_v = \pi/2$. Figure 4(b) is related to the values SCR = 10 dB and CNR = 0, 10, and 20 dB and to the same value of u_r. In Figure 4(c), the pdfs are plotted for SCR = 10 dB and CNR = 10 dB and by varying the normalized velocity u_r.

Figure 4 shows that also in this case the measured phase pdfs are not centered on the noise-free value highlighted with a dot and given by (3), and that their shape strongly depends on SCR and weakly on CNR. Moreover, we note that now the pdfs have always a behavior that is symmetrical around the phase ϕ_0, contrarily to what happened in the deterministic case (see Figure 3). The sensitivity of pdfs shape with respect to u_r is similar to the deterministic case and also in this case the corresponding variances gradually increase by increasing u_r.

However, for high SCR (strongly reflective target), the pdfs derived in the two cases are quite similar, as shown in Figure 5, where we have reported the pdfs related to the two models, (a) with SCR = 0 dB, (b) SCR = 10 dB, and (c) SCR = 20 dB.

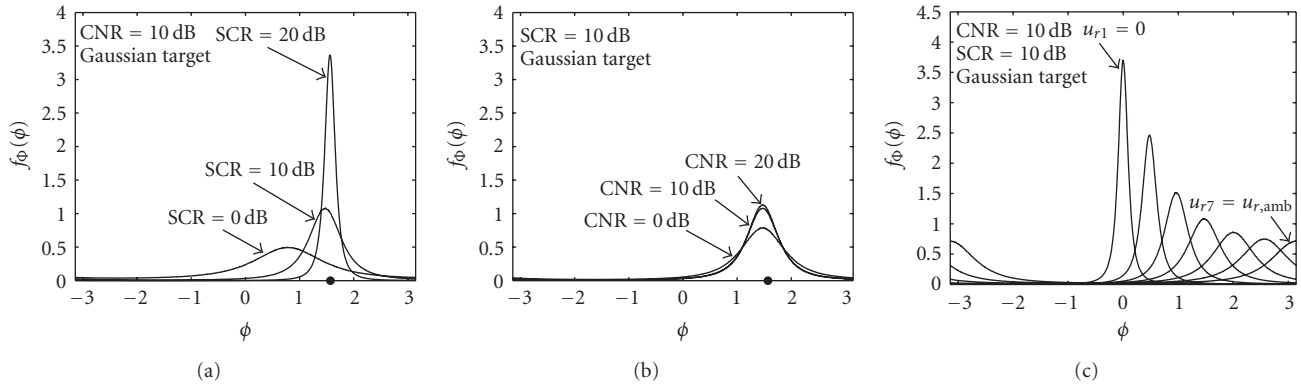

FIGURE 4: (a) Pdf of the interferometric phase in presence of Gaussian target moving with a radial velocity such that $\phi_v = \pi/2$ (the dot on the ϕ axis), for $\gamma_c = 1$, CNR = 10 dB and SCR = 0, 10, 20 dB, (b) SCR = 10 dB and CNR = 0, 10, 20 dB, and (c) SCR = 10 dB, CNR = 10 dB, for seven radial velocities ($u_{rk} = (k-1)/6\ u_{r,\mathrm{amb}}, k = 1, \ldots, 7$).

Moreover, the availability of an analytical expression for the pdf and for the coherence (see (7) and (10)) allows to easily discuss the effects that CNR, SCR, and radial velocity variations have on the interferometric measured phase distribution. First of all, we note that the pdf behavior changes according to the changes of $|\gamma|$ and ϕ_0. In particular, when $|\gamma|$ decreases, the spreading of the measured phase values around ϕ_0 increases, while the changes in the values of ϕ_0 determine a simple circular shift of the curves. The first effect affects the velocity estimation accuracy, while the latter introduces a phase polarization ϕ_0-ϕ_v, which, if known, can be implicitly taken into account and compensated in the velocity estimation procedure.

We can easily analyze the pdf dependence on the system and target parameters in three limit cases.

(i) Strong targets

SCR $\gg 1$ and CNR $\gg 1$; then, from (9) and (10), $|\gamma| \cong |\gamma_{T0}|$ is independent on the velocity value and $\phi_0 \cong \phi_v$, that is, the pdf maximum position does not depend on SCR and CNR. For high SCR values we expect that the velocity estimation accuracy does not depend on the velocity value.

(ii) Camouflaged targets

SCR $\cong 1$, CNR $\gg$ SCR, and assume $\gamma_c \cong \gamma_{T0}$; then, from (9) and (10), $\gamma \cong \gamma_c(1 + \exp(j\phi_v))/2 = \gamma_c \exp(j\phi_v/2)\cos(\phi_v/2)$. Consequently, $|\gamma| \cong |\gamma_c \cos(\phi_v/2)|$ and $\phi_0 \cong \phi_v/2$. In this case, the pdf spreading and the phase polarization are strongly dependent on the velocity value.

(iii) Weak targets

SCR $\ll 1$; then, from (9) and (10), $\gamma \cong \gamma_c/(1 + \mathrm{CNR})$. In this case $\phi_0 \cong 0$, the clutter term is dominant, and the pdf of the phase is in practice independent on the velocity value. As expected, the velocity estimation problem cannot be solved for very low SCR values.

The behavior of $|\gamma|$ and ϕ_0 versus SCR using the TerraSAR-X parameters, with $\phi_v = \pi/2$ and CNR values of 10, 20, and 30 dB, is shown in Figure 6. Note that ϕ_0 is independent on CNR for the considered values of SCR, while $|\gamma|$ is practically independent on CNR for SCR values larger than 0 dB. Then, we expect that for SCR values greater than 0 dB, measurement errors on CNR will not influence significantly the velocity estimation accuracy.

Note further that, for small changes of SCR around the value SCR = 0 dB (SCR = 1), the curves exhibit strong variations. This implies that small errors in the knowledge of the SCR can affect the velocity estimation accuracy.

For the deterministic model the pdf is not given by (6), and there is not a direct relation between $|\gamma|$ and the pdf spreading, and between ϕ_0 and the position of the pdf maximum. Even so, the general qualitative behavior of $|\gamma|$ and ϕ_0 with respect to changes of SCR, CNR, γ_c, and γ_{T0} is similar to the one obtained in the Gaussian case.

3. MULTICHANNEL ALONG-TRACK SAR INTERFEROMETRY

The along-track interferometric phase depends on radial velocity, baseline, and wavelength as shown in (3). Phase values outside interval $(-\pi, \pi)$ wrap mod(2π), so that such values are indistinguishable from the ones differing for 2π multiples. The same holds for the corresponding radial velocity values. The radial velocity ambiguity value $u_{r,\mathrm{amb}} = \pm\lambda/(4b)$, corresponding to the interferometric phase $\pm\pi$, is then the maximum velocity value that can be unambiguously detected. Moreover, in the realistic case of noisy data, this ambiguity problem can be present also for normalized radial velocities smaller than $u_{r,\mathrm{amb}}$. Such effect can be particularly critical either for detection applications or for velocity estimation ones.

A method for overcoming these limitations, restoring the solution uniqueness, consists in exploiting different datasets acquired with different baselines, or with frequency diversity [13, 15].

Different baseline datasets (at least two) can be generated when the AT-InSAR system is constituted by more than two antennas (at least three). Different frequency datasets

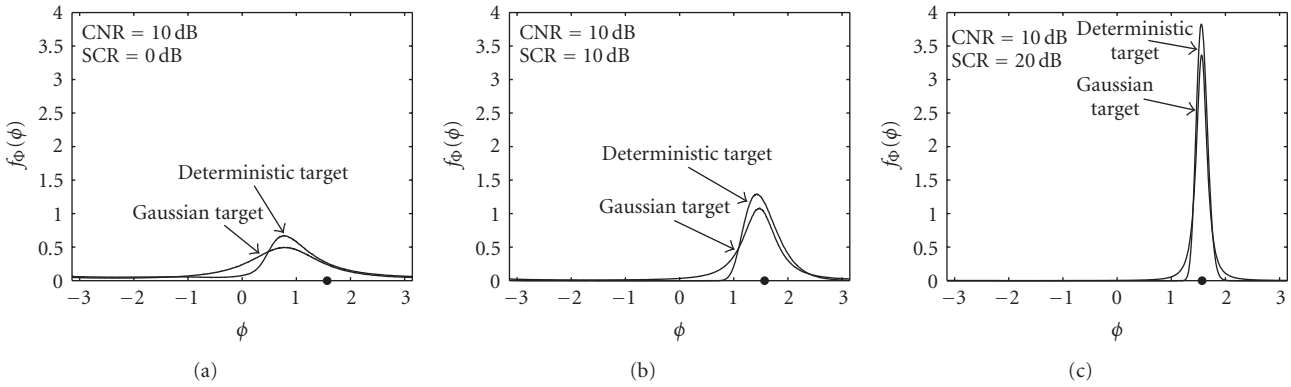

FIGURE 5: Pdfs of the interferometric phase in presence of a deterministic and a Gaussian target moving with a radial velocity such that $\phi_v = \pi/2$ (the dot on the ϕ axis), for $\gamma_c = 1$CNR $= 10$ dB and (a) SCR $= 0$ dB, (b) SCR $= 10$ dB, and (c) SCR $= 20$ dB.

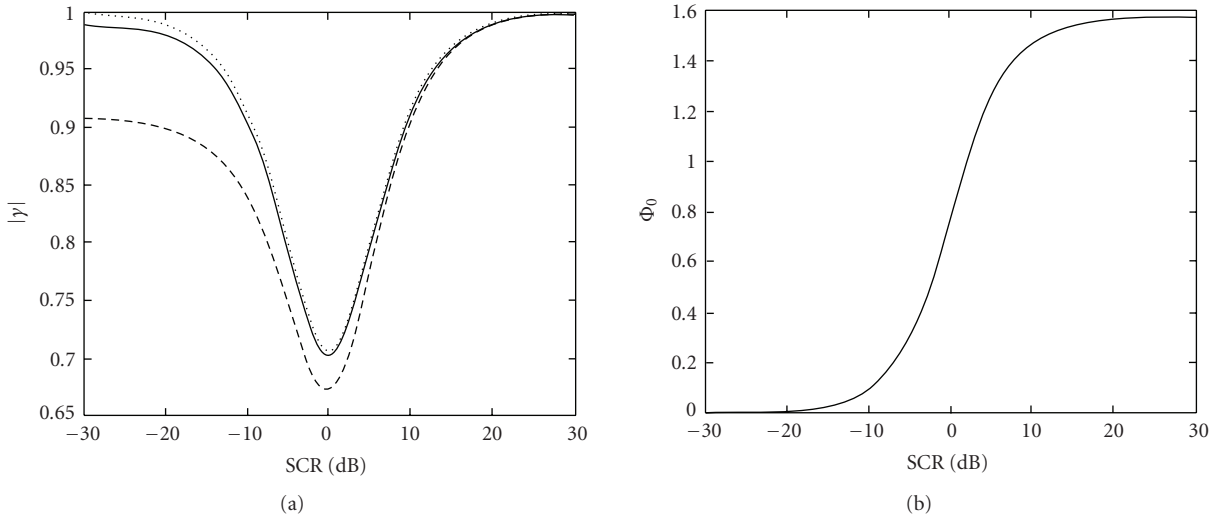

FIGURE 6: TerraSAR-X parameters and Gaussian target model: (a) $|\gamma|$ versus SCR, and (b) ϕ_0 versus SCR, with CNR = 10 dB (dashed line), CNR = 20 dB (solid line), CNR = 30 dB (dotted line), and $\gamma_c = \gamma_{T0} = 1$. Note that the ϕ_0 curves obtained for different values of CNR are coincident.

can be generated in two ways. In the first, we can suppose that the SAR sensors can operate at different working frequencies, for instance in X and C bands simultaneously. In the second, the multifrequency interferograms can be obtained by subband filtering of the interferometric images splitting the overall bandwidth as shown in Figure 7. Azimuth band partition produces the conventional azimuth looks, while range band partition produces different range looks. Note that this second partition generates looks with a small frequency diversity. Their generation is finalized to phase noise suppression as in conventional multilook procedure.

We will refer in the following to multifrequency and/or multibaseline configuration as multichannel configuration. The moving target detection and the radial velocity estimation are performed from the knowledge of such multiple wrapped interferometric phase (statistically independent) signals obtained with different baselines or with different working frequencies. It has to be noted that when the channels originate by band partition, the multichannel approach has a drawback, as the SCR is reduced, as we will show in the following.

The CNR is given, in the case of a single-look SAR image, by

$$\begin{aligned} \mathrm{CNR}_{\mathrm{SLook}} &= \frac{P_{\mathrm{Clutter}}}{P_{\mathrm{Noise}}} \\ &= \frac{(K_a K_r)^2 (P_{Tx} G_A \lambda^2/(4\pi)^3 R^4)(\delta x \delta r \sigma_0)}{K_a K_r P_{\mathrm{Noise}}}, \end{aligned} \tag{11}$$

where K_a and K_r are the *integratio* samples along the azimuth and the range direction, respectively, P_{Tx} is the power transmitted by the SAR antenna, G_A is the radar antenna gain, R is the distance between the SAR antenna and the ground region where this ratio is evaluated, σ_0 is the normalized radar cross-section relative to the background (the clutter), δx and δr are the spatial resolutions of the images, and P_{Noise} is the thermal power at the receiver. Note that the product $(\delta x \delta r \sigma_0)$ represents the RCS of a clutter resolution cell.

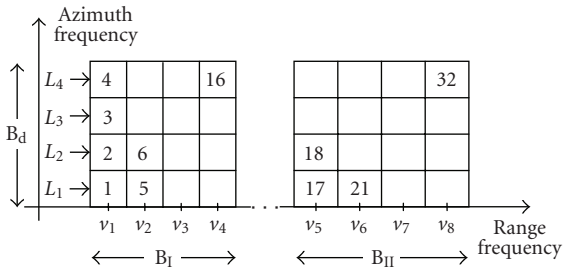

Figure 7: Partition of the dual-band spectrum of a hypothetical SAR interferometric system. The two bands B_I and B_{II} are subband filtered into $N_r = 8$ range subband (central frequencies $\nu_1, \nu_2, \ldots, \nu_8$), and the Doppler band B_d into $N_a = 4$ azimuth looks (L_1, L_2, L_3, L_4). Each $(n = 1, \ldots, N = N_a \times N_r = 32)$ identifies a portion of the 2D frequency domain not overlapping with the others. Absence of overlapping guarantees the statistical independence of interferograms.

The SCR is given, in the case of a single-look radar image, by

$$\begin{aligned}\mathrm{SCR}_{\mathrm{SLook}} &= \frac{P_{\mathrm{Target}}}{P_{\mathrm{Clutter}}} = \frac{(K_a K_r)^2 (P_{Tx} G_A \lambda^2/(4\pi)^3 R^4)\sigma_{\mathrm{Target}}}{(K_a K_r)^2 (P_{Tx} G_A \lambda^2/(4\pi)^3 R^4)(\delta x \delta r \sigma_0)} \\ &= \frac{\sigma_{\mathrm{Target}}}{(\delta x \delta r \sigma_0)},\end{aligned} \tag{12}$$

where σ_{Target} is the moving target RCS.

In the case of a multichannel system, two cases have to be distinguished: the case where more antennas (multibaseline) or more working frequencies are used, and the case where the overall system bandwidth is partitioned into different subbands (multilook). In the first case, the spatial resolution does not change, and supposing that the integration samples are the same for each channel, the CNR and the SCR values do not change. In the latter case, as the band partition reduces the spatial resolution, and supposing that N_a and N_r are the number of azimuth looks and range looks, respectively, the CNR and the SCR values change in

$$\begin{aligned}&\mathrm{CNR}_{\mathrm{MLook}} \\ &\quad= \frac{(K_a K_r / N_a N_r)^2 (P_{Tx} G_A \lambda^2/(4\pi)^3 R^4)(N_a \delta x N_r \delta r \sigma_0)}{(K_a K_r / N_a N_r) P_{\mathrm{Noise}}} \\ &\quad= \mathrm{CNR}_{\mathrm{SLook}},\end{aligned} \tag{13}$$

$$\mathrm{SCR}_{\mathrm{MLook}} = \frac{\sigma_{\mathrm{Target}}}{(N_a \delta x N_r \delta r \sigma_0)} = \frac{1}{(N_a N_r)} \mathrm{SCR}_{\mathrm{SLook}}. \tag{14}$$

The multichannel (derived by band partition) along-track SAR interferometry system scheme is depicted in Figure 8.

4. MULTICHANNEL AT-InSAR MOVING TARGET DETECTION

The interferometric phase Φ is distributed according to a pdf depending on several parameters:

$$f_\Phi(\phi \mid u_r; \lambda, b, \gamma_c, \mathrm{SCR}, \mathrm{CNR}). \tag{15}$$

Of course, in the absence of a moving target ($u_r = 0$, and $\mathrm{SCR} = 0$), Φ reduces to pure phase noise.

A moving target can be detected by comparing the interferometric phase Φ with a threshold ϕ_T in the interval $(-\pi, \pi]$. We can evaluate the detection probability (P_D) and false alarm probability (P_{FA}) in the following way:

$$\begin{aligned}P_D &= \int_{-\pi}^{-\phi_T} f_\Phi(\phi \mid u_r; \lambda, b, \gamma_c, \mathrm{SCR}, \mathrm{CNR})\, d\phi \\ &\quad + \int_{\phi_T}^{\pi} f_\Phi(\phi \mid u_r; \lambda, b, \gamma_c, \mathrm{SCR}, \mathrm{CNR})\, d\phi, \\ P_{\mathrm{FA}} &= 2\int_{\phi_T}^{\pi} f_\Phi(\phi \mid 0; \lambda, b, \gamma_c, \mathrm{CNR})\, d\phi.\end{aligned} \tag{16}$$

The performance of the detection process is, as expected, better for high values of SCR, that is, when the moving targets power is significantly larger than the clutter power. For moving targets mingling with the background clutter, the detection capability worsens, so that if one wants low values of P_{FA}, the P_D can decrease to very low values, not consistent with the applications [23]. This approach, based on a single interferogram value, does not provide the desired results in terms of simultaneous low values of P_{FA} and high values of P_D. An alternative improved detection strategy is based on the use of multichannel interferograms. After the application of the threshold to each channel, a binary integration procedure can be adopted to combine single-channel decisions.

We use a hypothetical dual-baseline system working at the frequency $f = 9.65\,\mathrm{GHz}$, with three antennas separated by the two baselines $b_1 = 1.2\,\mathrm{m}$ and $b_2 = 1.8 b_1\,\mathrm{m}$. Both interferometric signals are partitioned into 4 azimuth looks, for a total of $N = 8$ channels. Note that the same effect could be obtained with a dual frequency system, with a first working frequency f_1 and a second working frequency equal to $f_2 = 1.8 f_1$ (e.g., C band and X band).

Suppose that the detection probability of one of the channels corresponding to the first baseline (or first frequency) is equal to P_{D1}, and that the detection probability of one of the channels corresponding to the second baseline (or second frequency) is equal to P_{D2}; we can evaluate the probability that the target is detected from $(N/2 + j)$ channels ($j = 1, \ldots, N/2$) on a total of N channels:

$$\begin{aligned}P_j = \sum_{k=j}^{N/2} &\left[\binom{N}{k} P_{D1}^k (1 - P_{D1})^{N/2-k} \right] \\ &\times \left[\binom{\frac{N}{2}}{\frac{N}{2} - k + j} P_{D2}^{N/2-k+j} (1 - P_{D2})^{k-j} \right].\end{aligned} \tag{17}$$

We have developed two possible strategies and compared them with the one based on a single interferogram. Strategy 1 consists in considering present the moving target when the majority of the interferogram values are above prefixed

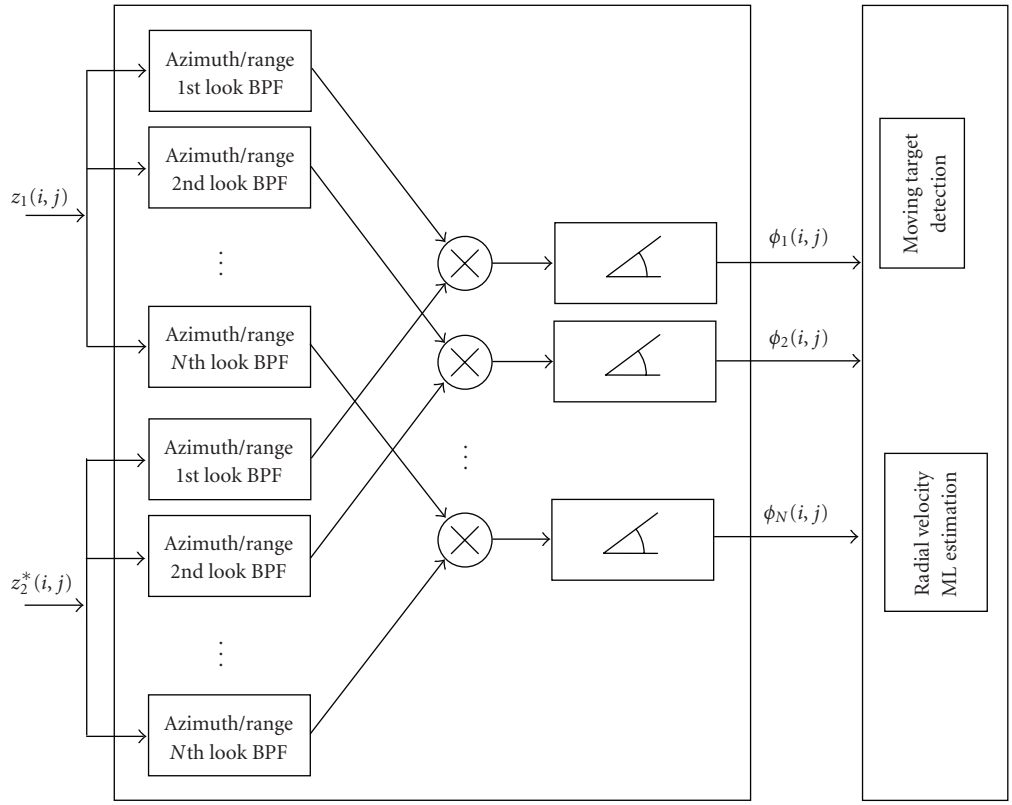

Figure 8: Multichannel along-track SAR interferometry system scheme.

thresholds. We obtain the following estimated detection probability:

$$P_{D>N/2} = \sum_{j=1}^{N/2} P_j. \tag{18}$$

For the estimation of the false alarm probability, we have used the same reasoning, using the single-channel false alarm probabilities P_{FA1} and P_{FA2} in place of P_{D1} and P_{D2} in (17).

Strategy 2 consists in considering present the moving target when more than 3/4 of the total interferogram values are above prefixed thresholds. We obtain

$$P_{D>3N/4} = \sum_{j=n/4+1}^{N/2} P_j. \tag{19}$$

In Figure 9, we have reported all the P_D's corresponding to different operating conditions and in the case of the deterministic model (the Gaussian model provides similar results). We have reported also the estimation of P_D adopting Strategy 1 (dashed line) and Strategy 2 (solid line). The single-channel detection probabilities are depicted with dash-dotted and dotted lines. All the results refer to a moving target with $u_r = 1 \times 10^{-3}$, SCR = 10 dB, CNR = 10 dB, and $\gamma_c = 1$. The P_D's have been plotted versus the velocity values $u_{r,T}$ corresponding to the thresholds ϕ_T.

In Figure 10, we have reported all the P_{FA}'s corresponding to the same operating conditions, adopting Strategy 1 (dashed line) and Strategy 2 (solid line). All the results are evaluated in absence of a moving target and for CNR = 10 dB and $\gamma_c = 1$.

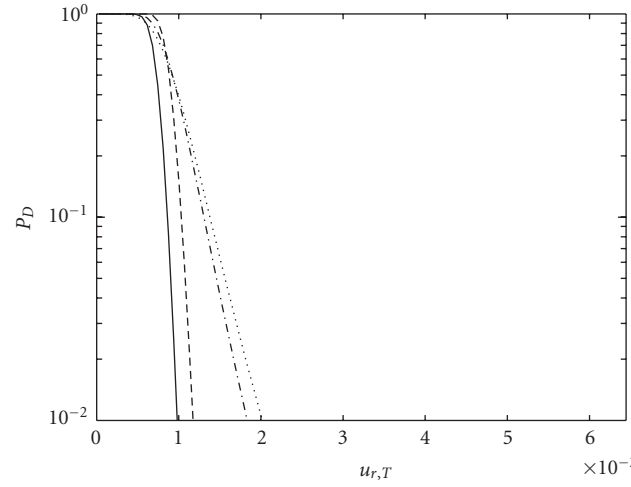

Figure 9: P_D's adopting Strategy 1 (dashed line) and Strategy 2 (solid line), in presence of a moving target with $u_r = 0.001$, SCR = CNR = 10 dB, and $\gamma_c = 1$. Single-channel P_D's are depicted with dash-dotted line (first baseline) and dotted line (second baseline).

In Figure 11, Strategies 1 and 2 are compared in terms of P_{FA} and P_D. Following Strategy 2, it can be found that a

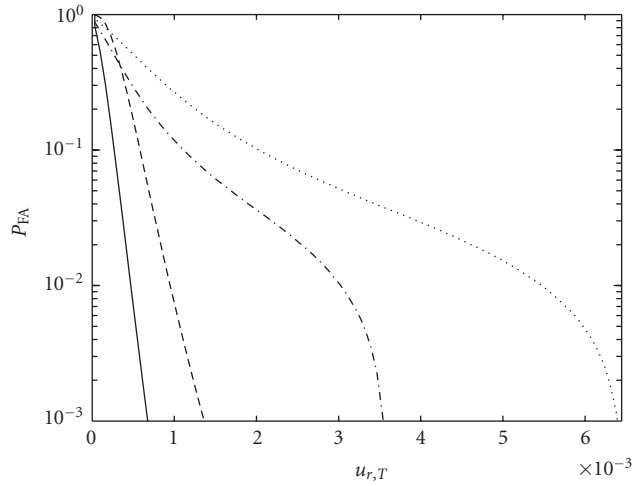

FIGURE 10: P_{FA}'s adopting Strategy 1 (dashed line) and Strategy 2 (solid line), in absence of moving targets, CNR = 10 dB, γ_c = 1. Single-channel P_{FA}'s are depicted with dash-dotted line (first baseline) and dotted line (second baseline).

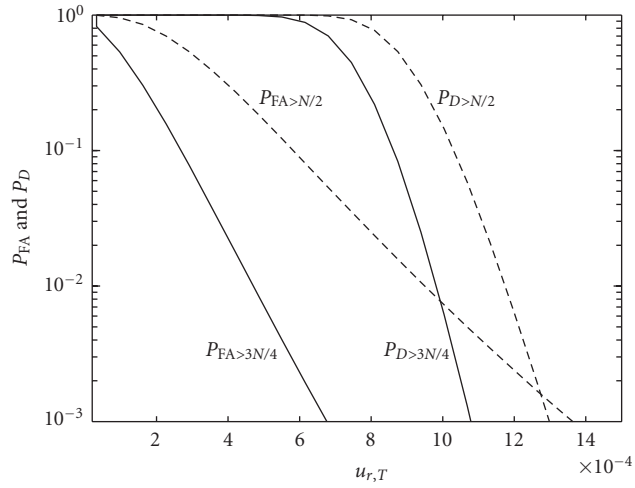

FIGURE 11: P_{FA} and P_D adopting Strategy 1 (dashed line) and Strategy 2 (solid line). $u_r = 1 \times 10^{-3}$, SCR = CNR = 10 dB, and $\gamma_c = 1$.

threshold exists where performances are quite good with P_D approaching 1 and P_{FA} approaching 0.

Figure 11 has been plotted for a fixed velocity value ($u_r = 1 \times 10^{-3}$). When the velocity value changes, the detection probability changes, while the false alarm probability remains unchanged. In particular, considering Strategy 2, in Figures 12(a) and 12(b) it can be appreciated that, as expected, by increasing the velocity the detection probability increases.

To better show this effect, the detection probability versus velocity at fixed values of false alarm probability is shown in Figures 13(a) and 13(b) for CNR = 10, $\gamma_c = 1$, with SCR = 10 (Figure 13(a)) and SCR = 20 (Figure 13(b)) for two different fixed values of P_{FA}(10^{-2} and 10^{-3}).

It can be observed that in these examples a target can be detected with probability approaching 1 starting from normalized velocity values approximately equal to $u_r = 10^{-3}$, also for $P_{FA} = 10^{-3}$. In this case, the phase thresholds corresponding to $u_r = 10^{-3}$ and that guarantee $P_{FA} = 10^{-3}$ and $P_D \cong 1$ are $\phi_{T1} = 4\pi b_1 10^{-3}/\lambda = 0.49$ and $\phi_{T2} = 4\pi b_2 10^{-3}/\lambda = 0.88$. In general, the phase thresholds depend on the minimum detectable velocity according to (3). The velocities values that can be detected reduce significantly when P_{FA} increases, or when the target RCS increases.

5. MULTICHANNEL AT-InSAR MOVING TARGET RADIAL VELOCITY ESTIMATION

As discussed in Section 2, the accuracy of the velocity estimation, obtainable with a given AT-InSAR system configuration, depends on the statistical model assumed for the target image, on the target radial velocity, and on the following parameters: SCR, CNR, γ_c, and γ_{T0}.

We have already presented the multichannel system (multifrequency and/or multibaseline) configuration, providing the different phase measurements which are required to find a reliable solution for the detection and estimation problems [13, 15].

The ML estimation of the normalized radial velocity from multichannel data is given by

$$\hat{u}_r = \arg\max_{u_r} L(u_r),$$
$$L(u_r) = \prod_{\substack{n=1,\ldots,N \\ m=1,\ldots,M}} \underbrace{f_\Phi(\phi_{n,m} \mid u_r; \lambda_n, b_m, \gamma_c, \gamma_{T0}, \mathrm{SCR}, \mathrm{CNR})}_{\text{single channel likelihood function}}, \tag{20}$$

where $L(\cdot)$ is the multichannel likelihood function, obtained by multiplying the likelihood functions corresponding to the central frequency of the subbands and/or to the different baselines, and $\phi_{n,m}$ represent the wrapped phase values relative to the N frequencies c/λ_n and to the M baselines b_m. The factorization (20) comes from the assumed statistical independence of the multichannel interferograms.

We evaluate numerically the Cramer-Rao lower bound (CRLB) of the estimated (normalized) velocity for the two different target statistical models considered above, and we estimate the target radial velocity using (20). We compare the CRLB with the root mean square error (RMSE) values. It has to be reminded that the CRLB represents the lower bound for the variance of the estimated parameter (the normalized radial velocity, in this case), whatever unbiased estimator working on the available set of data (the wrapped phases) may be considered [24].

We use the TerraSAR-X parameters introduced in Table 1 for the numerical simulation, and we consider a single-baseline system and a dual-baseline system (b_1 = 1.2 m and $b_2 = 1.8 b_1$ m), as in Section 4. For each baseline we considered 2 subbands and 2 azimuth looks, in total 4 different channels [23]. For baseline b_1 the maximum radial velocity value that can be unambiguously detected is $|u_{r,\mathrm{amb1}}| = \lambda/(4b_1) = 6.5 \times 10^{-3}$ and for baseline b_2 is

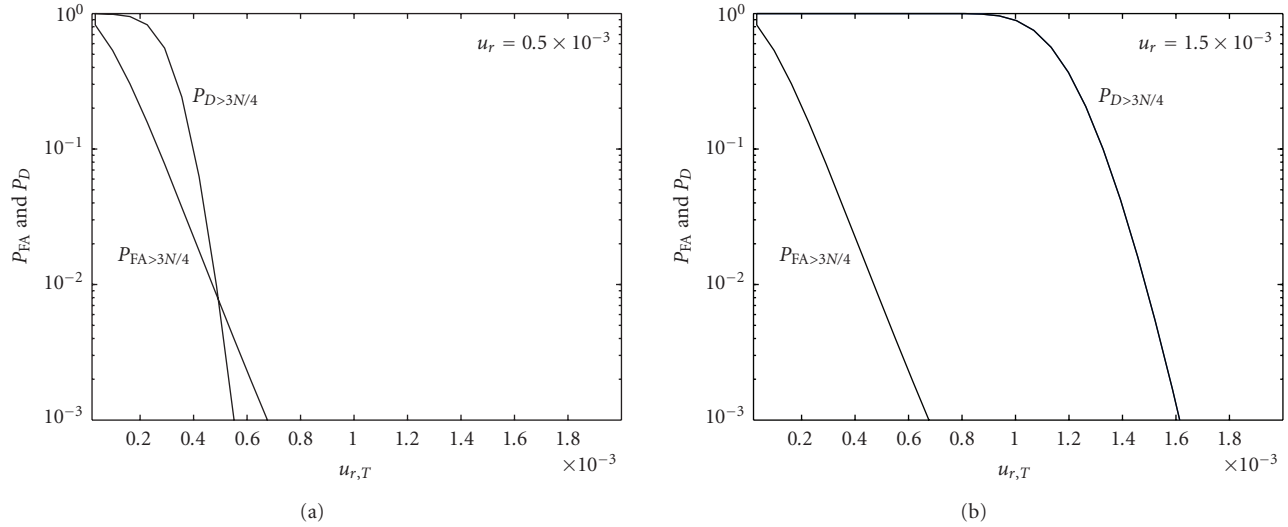

FIGURE 12: P_{FA} and P_D adopting Strategy 2 for SCR = CNR = 10 dB, $\gamma_c = 1, 0$; (a) $u_r = 0.5 \times 10^{-3}$ and (b) $u_r = 1.5 \times 10^{-3}$.

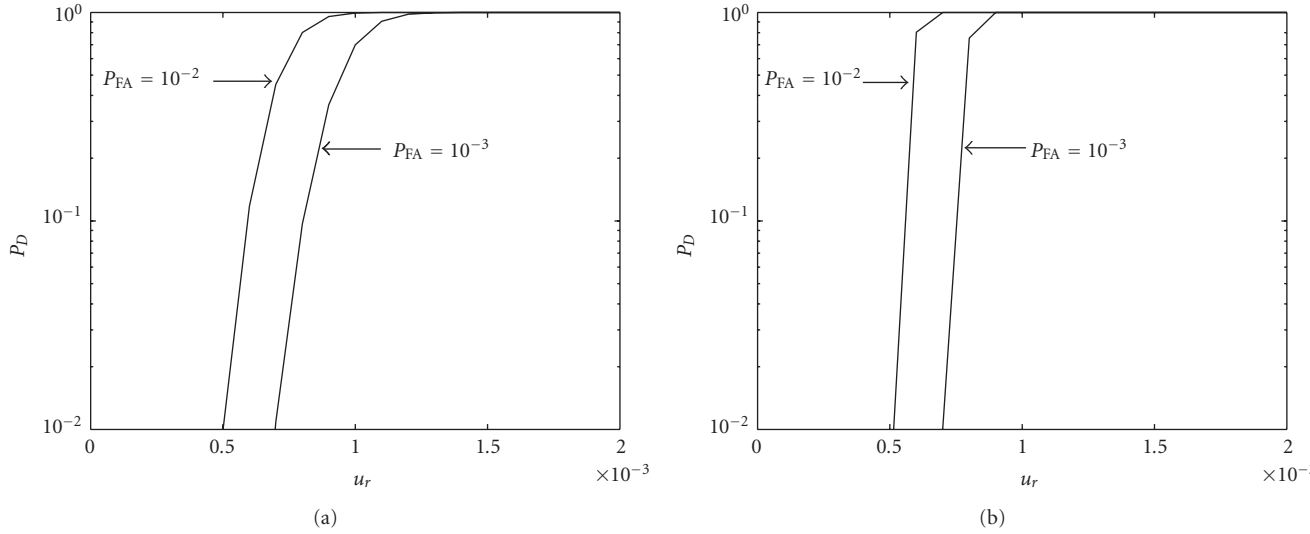

FIGURE 13: P_D versus velocity for fixed values of $P_{FA}(10^{-2}$ and $10^{-3})$ for CNR = 10, $\gamma_c = 1$; (a) SCR = 10 and (b) SCR = 20.

$|u_{r,amb2}| = \lambda/(4b_2) = 3.6 \times 10^{-3}$. A correspondence table between normalized and true radial velocity values in the TerraSAR-X case is reported in Table 2.

The CRLB$^{1/2}$ and RMSE values (in logarithmic scale) for the deterministic case and for the Gaussian case, with $\gamma_c = 1$, SCR = 0, 10, and 20 dB, CNR = 10 dB, and $b_1 = 1.2$ m, are reported in Figure 14. Of course, the SCR values are the ones obtained after the subband filtering (14).

The CRLB values vary with the normalized velocity u_r to be estimated since the pdfs of the interferometric phase change with it (see Figures 3(c) and 4(c)), as shown in Section 2. In particular, in all cases considered, the CRLB values increase with the increasing of velocity. Estimation of velocity values is more accurate for small values of velocity (the CRLB are lower), and less accurate when velocity increases.

We observe also that, with the same SCR, CNR, and γ_c values, the deterministic target model exhibits lower CRLB values than the Gaussian model. This effect is due to the different variance values corresponding to the deterministic and Gaussian cases for the same SCR, CNR, and γ_c values (see Figures 3(c) and 4(c)). The larger the variance (the larger the phase noise), the larger the corresponding CRLB.

We observe further that in all considered cases the CRLB values decrease by increasing SCR under the same CNR and γ_c values. Then, as expected, velocity estimation is more accurate when signal-to-clutter ratio is larger. It can be noted that the RMSE values for velocities far from the ambiguity value are only "slightly" larger than the CRLB$^{1/2}$ ones and the RMSE values obtained using the deterministic model, likewise the CRLB$^{1/2}$, are lower than the RMSE in the Gaussian case, as expected. This means that 4 channels

Table 2: Correspondence between normalized and true velocity values in the TerraSAR-X case.

u_r	1×10^{-4}	4×10^{-4}	7×10^{-4}	1×10^{-3}	2×10^{-3}	3×10^{-3}	4×10^{-3}	5×10^{-3}	6×10^{-3}
v_r [m/s]	0.76	3.04	5.32	7.60	15.2	22.8	30.4	38.0	45.6
v_r [km/h]	2.74	10.9	13.7	27.4	54.7	82.1	109.4	137.0	164.4

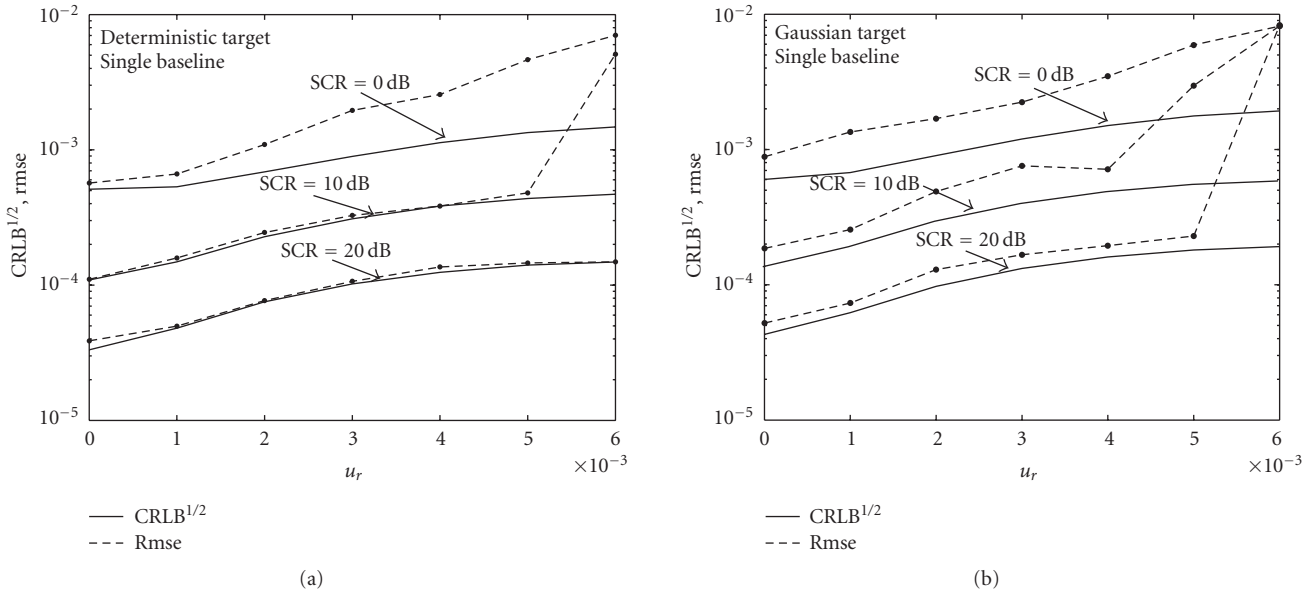

Figure 14: CRLB$^{1/2}$ (solid line) and RMSE (dashed line) values (in log scale) of the estimated target radial normalized velocity, with CNR = 10 dB, SCR = 0, 10, 20 dB, $\gamma_c = 1$, for a single-baseline system ($b_1 = 1.2$ m) for (a) a deterministic modeled moving target and (b) a Gaussian modeled moving target.

are sufficient, for the chosen values of CNR, SCR, and γ_c, to obtain quality performance very close to the best theoretical results when there are no ambiguity problems. Instead, it can be noted that the RMSE for velocities approaching the ambiguity value (from 4×10^{-3} to 6×10^{-3}) and for low SCR tends to deviate from the CRLB values. This behavior is more pronounced in the Gaussian case.

In case we consider two baselines, we can obtain CRLB and RMSE values less variable with velocity and less sensitive to ambiguity problems. In particular, considering $b_1 = 1.2$ m and $b_2 = 1.8b_1$ m, $\gamma_c = 1$, SCR = 0, 10, and 20 dB, CNR = 10 dB, we get the CRLB$^{1/2}$ and RMSE curves (in logarithmic scale) shown in Figure 15, for the deterministic and Gaussian cases.

It can be appreciated that the CRLBs are reduced with respect to the single-baseline case, and that they are less variable with the velocity. Differently from the single-baseline system, in the dual-baseline system the RMSE values for all the velocities considered are very close to the CRLBs at least for high SCR values. Only for SCR = 0 dB it can be observed that a degradation of the estimation performances exists. The performance analysis shows that the considered AT-InSAR system allows to estimate normalized radial velocity with RMSE of the order of 10^{-4} (using two baselines and 4 channels for baseline) even for SCR = 10 dB. In traffic monitoring applications, when the moving targets are cars and trucks, the RCS can be of the order of, or larger than, 100 m^2. In this case, the SCR can be significantly larger than 10 dB, allowing the application of this kind of sensors to practical situations.

5.1. Multichannel ML velocity estimation algorithm robustness

5.1.1. Robustness with respect to the target model

As discussed in Section 2, the deterministic target model is less tractable because, so far, no analytical statistical description has been obtained, but it is more realistic (targets of interest—cars, trucks—exhibit RCSs that do not vary significantly with the radar observation angles [19]). The Gaussian target model is less realistic (it is rare that cars and trucks response is a zero mean Gaussian signal which varies significantly inside the synthetic aperture), but it allows to perform the velocity estimation using analytical likelihood functions, since an analytical expression for the interferometric phase pdf is available with great advantages in terms of the computational efficiency. For this reason, we present the performance results in terms of RMSE values obtained using data generated with deterministic RCS, processed with the likelihood functions derived from the Gaussian model. In other words, we process the AT-InSAR data with a model different from the actual one used to simulate them. We compare again the single-baseline system

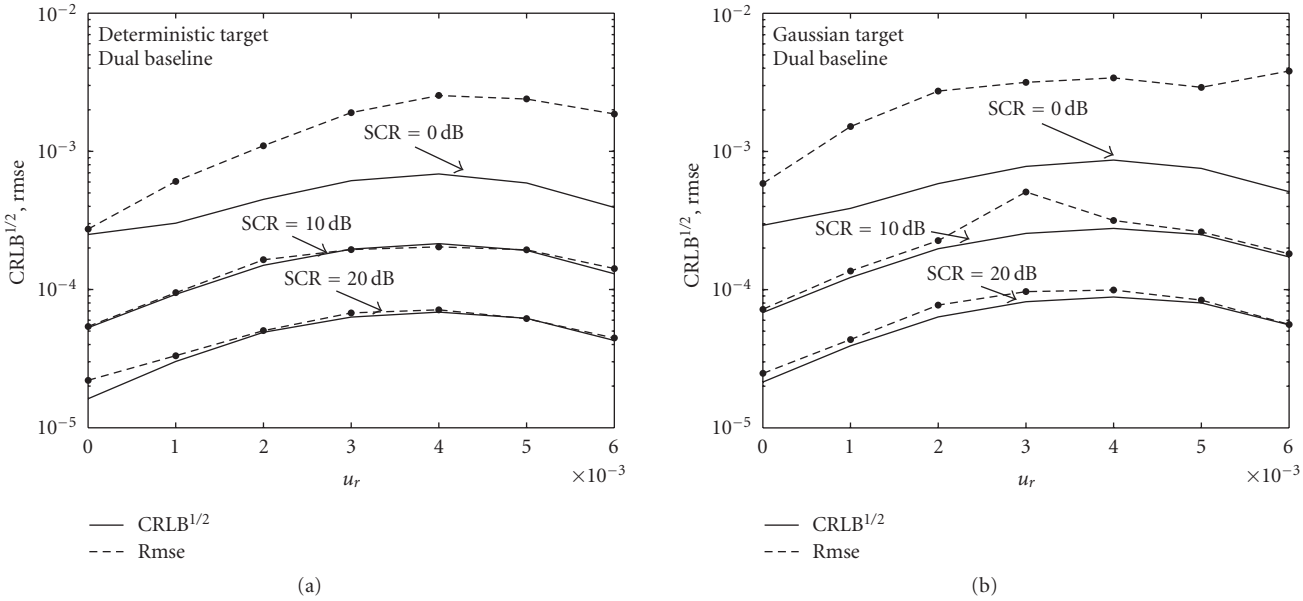

FIGURE 15: CRLB$^{1/2}$ (solid line) and RMSE (dashed line) values (in log scale) of the estimated target radial normalized velocity, with CNR = 10 dB, SCR = 0, 10, 20 dB, $\gamma_c = 1$, for a dual-baseline system ($b_1 = 1.2$ m, $b_2 = 1.8\, b_1$ m) for (a) a deterministic modeled moving target and (b) a Gaussian modeled moving target.

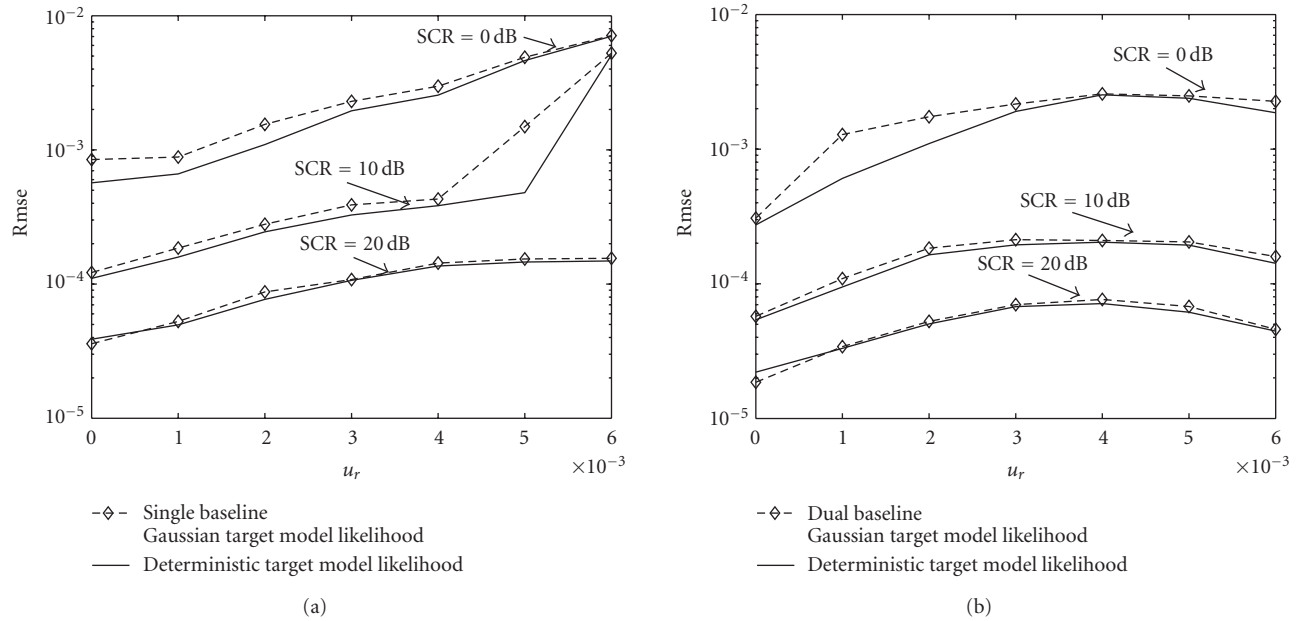

FIGURE 16: RMSE values of the estimated target radial normalized velocity, for a deterministic target likelihood (solid line) and RMSE values for a Gaussian target likelihood (dashed line), in log scale, with CNR = 10 dB, SCR = 0, 10, 20 dB, $\gamma_c = 1$ and for (a) a single-baseline system ($b_1 = 1.2$ m) and (b) for a dual-baseline system ($b_1 = 1.2$ m, $b_2 = 1.8 b_1$ m).

with the dual-baseline one. The RMSE values for CNR = 10 dB, SCR = 0, 10, 20 dB, and $\gamma_c = 1$ for a deterministic modeled moving target obtained using a likelihood function derived from the deterministic and the Gaussian models are reported in Figure 16, for (a) the single-baseline system ($b_1 = 1.2$ m) and (b) the dual-baseline system ($b_1 = 1.2$ m, $b_2 = 1.8\, b_1$ m).

It can be noted, quite surprisingly, that the RMSE values processed with the likelihood functions derived from the Gaussian model are very close to the ones relative to the deterministic case. In such a way it is possible to process efficiently actual data with a tractable estimation algorithm without impairing significantly the estimation performance.

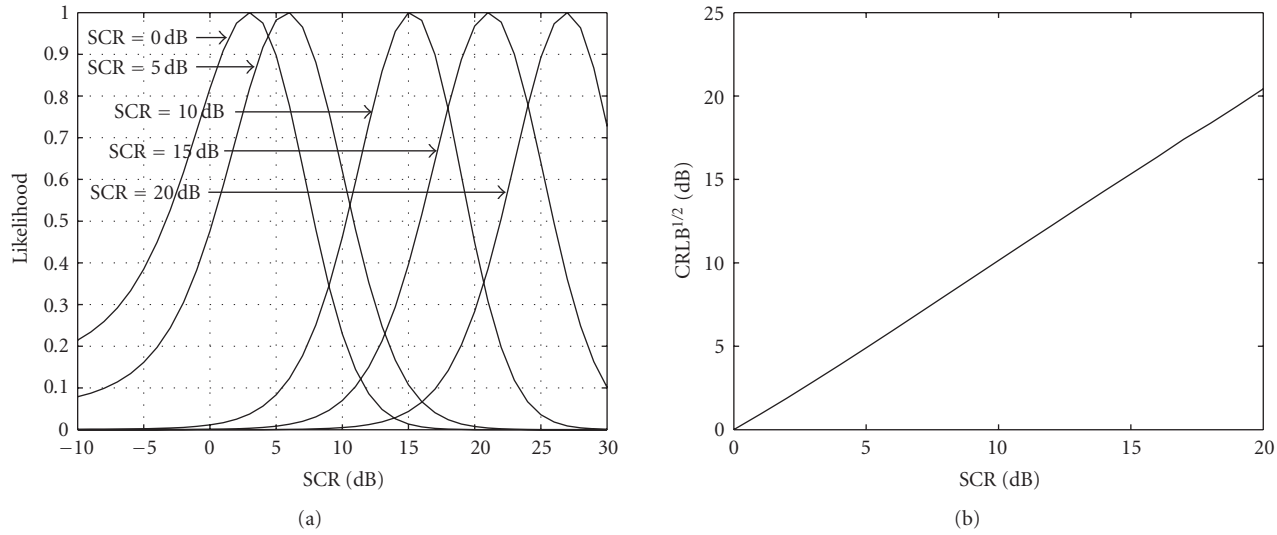

Figure 17: (a) Likelihood functions (21) versus SCR for a fixed radial velocity value; (b) square root of the CRLB for SCR.

Table 3: RMSE values of the estimated radial velocity relative to data generated with different values of SCR using the target deterministic RCS model processed with Gaussian RCS-derived likelihood functions, using, respectively, the nominal value of SCR (SCR_n), the estimated (by (9)) value of SCR (SCR_e), and a fixed value of SCR = 30 dB (SCR_f). All other parameters (CNR = 10 dB, $\gamma_c = 1$, etc.) are fixed.

	SCR = 5 dB			SCR = 10 dB			SCR = 15 dB			SCR = 20 dB		
u_r	SCR_n	SCR_e	SCR_f	SCR_n	SCR_e	SCR_f	SCR_n	SCR_e	SCR_f	SCR_n	SCR_e	SCR_f
$1e^{-3}$	$3.77e^{-4}$	$4.24e^{-4}$	$4.14e^{-4}$	$1.73e^{-4}$	$1.82e^{-4}$	$2.26e^{-4}$	$9.45e^{-5}$	$9.68e^{-5}$	$1.23e^{-4}$	$5.07e^{-5}$	$5.23e^{-5}$	$6.33e^{-5}$
$2e^{-3}$	$5.37e^{-4}$	$5.55e^{-4}$	$6.48e^{-4}$	$2.97e^{-4}$	$2.99e^{-4}$	$3.54e^{-4}$	$1.46e^{-4}$	$1.51e^{-4}$	$1.93e^{-4}$	$8.62e^{-5}$	$8.98e^{-5}$	$1.08e^{-4}$
$3e^{-3}$	$1.30e^{-3}$	$1.15e^{-3}$	$1.21e^{-3}$	$3.58e^{-4}$	$3.73e^{-4}$	$4.75e^{-4}$	$1.96e^{-4}$	$1.97e^{-4}$	$2.71e^{-4}$	$1.05e^{-4}$	$1.08e^{-4}$	$1.42e^{-4}$

5.1.2. Robustness with respect to the system parameters

A further experiment directed to test robustness consists in varying the parameters of the model that are not perfectly known. In particular, while CNR and γ_c can be easily obtained from the system characteristics (noise power of the SAR sensor) and from the processed SAR images (clutter power and coherence), the SCR value is unknown until the target is unknown (we do not a priori know its position or its RCS). Note also that it is not necessary to test robustness against CNR since, as highlighted in the comments to Figures 3 and 4, errors on it do not influence significantly the velocity estimation accuracy. Instead the role of SCR is quite determinant in the target velocity estimation procedure with respect to the other parameters, as shown by the pdf shapes and in the CRLB and RMSE behaviors. For this reason, we test the performance algorithm when the target RCS value is not a priori known.

First of all, we note that the SCR can be estimated from the data and the final estimation can be casted as a joint estimation of velocity and SCR:

$$[\hat{u}_r, \widehat{\mathrm{SCR}}] = \arg\max_{u_r,\mathrm{SCR}} L(u_r, \mathrm{SCR}),$$
$$L(u_r, \mathrm{SCR}) = \prod_{\substack{n=1,\ldots,N \\ m=1,\ldots,M}} \underbrace{f_\Phi(\phi_{n,m} \mid u_r, \mathrm{SCR}; \vartheta)}_{\text{single channel likelihood function}}, \quad (21)$$

where ϑ denotes the following parameters $\lambda_n, b_m, \gamma_c = 1$, $\gamma_{T0} = 1$, CNR_0 is computed from the data. We assume a Gaussian target model to derive the likelihood since it allows to perform the velocity estimation using analytical likelihood function and it does not degrade the estimation performance, as previously seen, even if the data are generated using a deterministic target model.

As far as the accuracy of the estimation of SCR is concerned, we show in Figure 17(a) some cuts (relative to different SCR values) of the likelihood function (21) versus SCR for a fixed radial velocity value. Note that the curves exhibit a similar shape since the axis of abscissas is in log scale, while in linear scale they would appear very different from each other, and their spreading increases by increasing SCR. Consequently, as the best theoretical obtainable accuracy (the Cramer-Rao lower bound (CRLB)) is directly connected to the spreading of the likelihood function, the accuracy worsens increasing the SCR. The complete behavior of the square root of the CRLB for SCR is presented in Figure 17(b) and confirms the mentioned trend.

We analyze also the system performance in terms of RMSE in the three following cases: (1) the estimation is performed by adopting for SCR the nominal value SCR_n; (2) SCR is estimated in conjunction with the normalized radial velocity; (3) the estimation is performed by adopting for SCR a fixed value SCR_f different from the true one. In

Table 3, we report the RMSE values of the estimated radial velocity using AT-InSAR images simulated with the system parameters reported in Table 1, with CNR = 10 dB, SCR = 10 dB, $\gamma_c = 1$, and with normalized target velocities $u_r = 1 \times 10^{-3}$, $u_r = 2 \times 10^{-3}$, $u_r = 3 \times 10^{-3}$. The multichannel MLE algorithm (21) adopts a single baseline ($b_1 = 1.2$ m) and 4 different channels (the 2 subbands and 2 azimuth looks used for the CRLB evaluation).

The best performance has been (of course) obtained using the nominal SCR values (SCR_n column) but the adoption of the estimated SCR values through (21) (SCR_e column) or the fixed one (SCR_f column) do not impair significantly the velocity estimation performance, showing that there is a weak sensitivity of the velocity estimation from the SCR values. We have tested the robustness of the ML algorithm with respect to an unknown SCR in the single-baseline system but we expect a similar behavior in the dual-baseline system.

6. CONCLUSIONS

In this paper, we presented the performance evaluation of multichannel AT-InSAR systems in terms of moving target detection ability and target radial velocity estimation accuracy. The analysis has been performed with different target statistical model and system parameters, such as radial velocity, SCR, CNR, and number of system channels. In particular, we compared a single-baseline system with a dual-baseline system. Regarding the detection process, the use of multichannel interferograms, after the application of a threshold stage to each channel, allows to adopt a binary integration to combine single-channel decisions. Such a strategy, compared with the one based on a single interferogram, provides better results in terms of simultaneous low values of P_{FA} and high values of P_D.

With reference to the target radial velocity estimation, two target models have been considered: deterministic target response and Gaussian target response. The first model is more realistic and applies to well-characterized targets, while the latter applies when the target RCS is not accurately known. The use of the Gaussian model in the velocity estimation procedure has proved to be particularly appropriate to the case of realistic datasets, since it allows to take into account the uncertainty on the knowledge of the target RCS. The mean square errors obtained using the Gaussian model are not very different from the lower bounds which are obtained using a deterministic model exploiting a very accurate knowledge of the target RCS. The estimation errors obtained using the Gaussian model exhibit a low sensitivity to the errors on the knowledge of the SCR value, which is a parameter difficult to be estimated in the absence of an accurate target characterization.

The analysis of performance which has been presented evidences that a single-baseline AT-InSAR system allows to obtain accurate radial velocity estimations approaching the CRLB also in the case of a small number of channels (only four, in the presented case) for velocities far from the ambiguity value, while to solve ambiguities at least a dual-baseline AT-InSAR system is required.

The present paper is focused on detection and estimation of interferometric phase data in order to highlight the performance improvement derived by the use of more than one channel (baseline). The use of more than two baselines would allow further performance improvement at the expenses of growing system complexity and cost.

REFERENCES

[1] H. Breit, M. Eineder, J. Holzner, H. Runge, and R. Bamler, "Traffic monitoring using SRTM along-track interferometry," in *Proceedings of IEEE International Geoscience and Remote Sensing Symposium (IGARSS '03)*, vol. 2, pp. 1187–1189, Toulouse, France, July 2003.

[2] S. Hinz, F. Meyer, A. Laika, and R. Bamler, "Spaceborne traffic monitoring with dual channel synthetic aperture radar theory and experiments," in *Proceedings of IEEE Computer Society Conference on Computer Vision and Pattern Recognition (CVPR '05)*, vol. 3, p. 7, San Diego, Calif, USA, June 2005.

[3] R. K. Raney, "Synthetic aperture imaging radar and moving targets," *IEEE Transactions on Aerospace and Electronic Systems*, vol. 7, no. 3, pp. 499–505, 1971.

[4] S. Barbarossa, "Detection and imaging of moving objects with synthetic aperture radar—part I: optimal detection and parameter estimation theory," *IEE Proceedings of Radar and Signal Processing*, vol. 139, no. 1, pp. 79–88, 1992.

[5] J. H. G. Ender, "Space-time processing for multichannel synthetic aperture radar," *Electronics & Communication Engineering Journal*, vol. 11, no. 1, pp. 29–38, 1999.

[6] S. Barbarossa and A. Farina, "Space-time-frequency processing of synthetic aperture radar signals," *IEEE Transactions on Aerospace and Electronic Systems*, vol. 30, no. 2, pp. 341–358, 1994.

[7] J. H. G. Ender and D. Cerutti-Maori, "Position estimation of moving vehicles for space based multi-channel SAR/MTI systems," in *Proceedings of the 6th European Conference on Synthetic Aperture Radar (EUSAR '06)*, pp. 1–4, Dresden, Germany, May 2006.

[8] S. Chiu, "Clutter effects on ground moving target velocity estimation with SAR along-track interferometry," in *Proceedings of IEEE International Geoscience and Remote Sensing Symposium (IGARSS '03)*, vol. 2, pp. 1314–1319, Toulouse, France, July 2003.

[9] C. Elachi, *Spaceborne Radar Remote Sensing: Applications and Techniques*, IEEE Press, New York, NY, USA, 1988.

[10] R. M. Goldstein and H. A. Zebker, "Interferometric radar measurement of ocean surface currents," *Nature*, vol. 328, no. 6132, pp. 707–709, 1987.

[11] R. E. Carande, "Dual baseline and frequency along-track interferometry," in *Proceedings of IEEE International Geoscience and Remote Sensing Symposium (IGARSS '92)*, pp. 1585–1588, Houston, Tex, USA, May 1992.

[12] C. W. Chen, "Performance assessment of along-track interferometry for detecting ground moving targets," in *Proceedings of IEEE Radar Conference*, pp. 99–104, Philadelphia, Pa, USA, April 2004.

[13] A. Budillon, V. Pascazio, and G. Schirinzi, "Multi-channel along track interferometry," in *Proceedings of IEEE International Geoscience and Remote Sensing Symposium (IGARSS '04)*, vol. 4, pp. 2601–2603, Anchorage, Alaska, USA, September 2004.

[14] C. H. Gierull, "Statistical analysis of multilook SAR interferograms for CFAR detection of ground moving targets," *IEEE*

Transactions on Geoscience and Remote Sensing, vol. 42, no. 4, pp. 691–701, 2004.

[15] A. Budillon, V. Pascazio, and G. Schirinzi, "Estimation of radial velocity of moving targets by along-track interferometric SAR systems," *IEEE Geoscience and Remote Sensing Letters*, vol. 5, no. 3, pp. 349–353, 2008.

[16] R. Bamler and P. Hartl, "Synthetic aperture radar interferometry," *Inverse Problems*, vol. 14, no. 4, pp. R1–R54, 1998.

[17] C. V. J. Jakowatz, D. E. Wahl, P. H. Eichel, D. C. Ghiglia, and P. A. Thompson, *Spotlight-Mode Synthetic Aperture Radar: A Signal Processing Approach*, Springer, Berlin, Germany, 1996.

[18] V. Pascazio, G. Schirinzi, and A. Farina, "Moving target detection by along-track interferometry," in *Proceedings of IEEE International Geoscience and Remote Sensing Symposium (IGARSS '01)*, vol. 7, pp. 3024–3026, Sydney, Australia, July 2001.

[19] G. Palubinskas, H. Runge, and P. Reinartz, "Radar signatures of road vehicles," in *Proceedings of IEEE International Geoscience and Remote Sensing Symposium (IGARSS '04)*, vol. 2, pp. 1498–1501, Anchorage, Alaska, USA, September 2004.

[20] J. Mittermayer and H. Runge, "Conceptual studies for exploiting the TerraSAR-X dual receive antenna," in *Proceedings of IEEE International Geoscience and Remote Sensing Symposium (IGARSS '03)*, vol. 3, pp. 2140–2142, Toulouse, France, July 2003.

[21] R. V. Ostrovityanov and F. A. Basalov, *Statistical Theory of extended Radar Targets*, Artech House, Dedham, Mass, USA, 1985.

[22] J. S. Daba and M. R. Bell, "Statistics of the scattering cross-section of a small number of random scatterers," *IEEE Transactions on Antennas and Propagation*, vol. 43, no. 8, pp. 773–783, 1995.

[23] A. Budillon, G. Ferraiuolo, V. Pascazio, and G. Schirinzi, "Multichannel SAR interferometry via classical and Bayesian estimation techniques," *Eurasip Journal on Applied Signal Processing*, vol. 2005, no. 20, pp. 3180–3193, 2005.

[24] S. M. Kay, *Fundamentals of Statistical Signal Processing: Estimation Theory*, Prentice-Hall, Upper Saddle River, NJ, USA, 1993.

Hindawi Publishing Corporation
International Journal of Navigation and Observation
Volume 2008, Article ID 325279, 12 pages
doi:10.1155/2008/325279

Research Article

CLEAN Technique for Polarimetric ISAR

M. Martorella,[1] A. Cacciamano,[1] E. Giusti,[1] F. Berizzi,[1] B. Haywood,[2] and B. Bates[2,3]

[1] *Department of Information Engineering, University of Pisa, via Caruso 16, 56122 Pisa, Italy*
[2] *Defence Science & Technology Organisation, Edinburgh, SA 5111, Australia*
[3] *School of Electrical & Electronic Engineering, University of Adelaide, SA 5005, Adelaide, Australia*

Correspondence should be addressed to A. Cacciamano, andrea.cacciamano@iet.unipi.it

Received 19 February 2008; Accepted 3 June 2008

Recommended by M. Greco

Inverse synthetic aperture radar (ISAR) images are often used for classifying and recognising targets. To reduce the amount of data processed by the classifier, scattering centres are extracted from the ISAR image and used for classifying and recognising targets. This paper addresses the problem of estimating the position and the scattering vector of target scattering centres from polarimetric ISAR images. The proposed technique is obtained by extending the CLEAN technique, which was introduced in radar imaging for extracting scattering centres from single-polarisation ISAR images. The effectiveness of the proposed algorithm, namely, the Polarimetric CLEAN (Pol-CLEAN) is tested on simulated and real data.

1. INTRODUCTION

The CLEAN algorithm was introduced in radio astronomy to reduce sidelobe-induced artefacts. In [1], the authors use the CLEAN technique to alleviate two types of artefacts introduced by the point spread function (PSF) sidelobes in real aperture radar images. Such a technique iteratively estimates the PSF of the brightest scatterer and removes it from the formed image.The CLEAN technique was applied later to inverse synthetic aperture radar (ISAR) imaging with interesting results [2]. Recently, fully polarimetric radars have been largely used for synthetic aperture radar (SAR) application [3, 4] as well as, although less extensively, for ISAR applications [5]. The advantage of fully polarimetric data is due to the fact that scattering mechanisms and target properties can be identified by measuring scattering matrices [6–9]. Inverse synthetic aperture radar (ISAR) images prove useful when used for classifying and recognising targets [10, 11]. Nevertheless, the image data size is often too large to implement real time classifiers. For this reason, algorithms such as the CLEAN technique can be employed for reducing the data size significantly without losing useful information. The problem of reducing the amount of data without losing useful information is even more critical when dealing with polarimetric ISAR images, since the data size is three to four times larger. An algorithm for scattering centre extraction from polarimetric SAR (PolSAR) images was proposed in [12]. In [12], the signal model was strongly based on the SAR geometry, which is known a priori. In the ISAR case, the non-cooperativity of the target does not allow using any such knowledge. So a parametric model is introduced to account for unknown target motions. Therefore, the problem of estimating the model parameters and the scattering centre extraction problem must be solved jointly. Moreover, in typical ISAR scenarios, only the received radar echo is presumed to be available (no ancillary data is used). In this paper, a polarimetric CLEAN (Pol-CLEAN) technique is proposed by extending the CLEAN technique in [2] in order to extract target features such as the position of the scattering centres and their scattering matrix. It is worth pointing out that the novelty of the proposed Pol-CLEAN technique, with respect to the CLEAN technique, lies on the extension to polarimetric ISAR images and on a new method for estimating the scattering centre point spread function.

The signal model is introduced in Section 2 whereas the Pol-CLEAN technique is detailed in Section 3. The effectiveness of the proposed algorithm is tested on simulated and real data and presented in Section 4.

2. SIGNAL MODEL

The polarimetric matrix of the received signal, in free space conditions, can be written in a time-frequency domain by

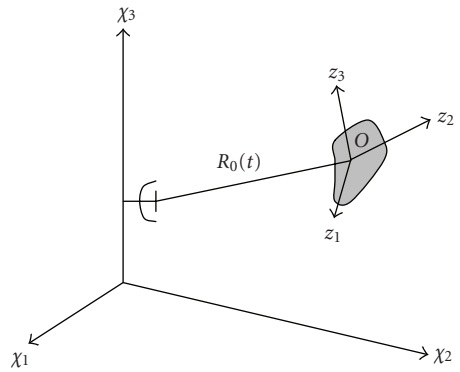

Figure 1: Radar-target geometry.

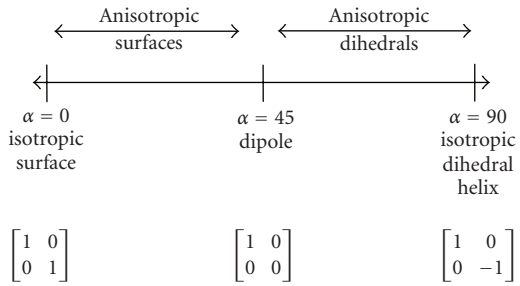

Figure 2: Interpretation of the internal degree of freedom α.

extending the signal model defined in [13]

$$\mathbf{S}_R(f,t) = W(f,t)\exp\left[-j\frac{4\pi f}{c}R_0(t)\right] \cdot \int_V \boldsymbol{\zeta}(\mathbf{z})\exp\left\{-j\frac{4\pi f}{c}\left[\mathbf{z}^T\cdot\mathbf{i}_{R_0}^{(\mathbf{z})}(t)\right]\right\}d\mathbf{z} + \mathbf{N}(f,t), \quad (1)$$

where $\mathbf{S}_R(f,t) = \begin{bmatrix} S_R^{HH}(f,t) & S_R^{HV}(f,t) \\ S_R^{VH}(f,t) & S_R^{VV}(f,t) \end{bmatrix}$ is expressed by means of a polarimetric matrix, $W(f,t) = \text{rect}[t/T_{\text{obs}}]\text{rect}[(f-f_0)/B]$ represents a rectangular window in the time-frequency domain (t,f), f_0 is the carrier frequency, B is the transmitted signal bandwidth, T_{obs} is the observation time, V is the spatial domain where the scattering matrix $\boldsymbol{\zeta}(\mathbf{z}) = \begin{bmatrix} \zeta^{HH}(\mathbf{z}) & \zeta^{HV}(\mathbf{z}) \\ \zeta^{VH}(\mathbf{z}) & \zeta^{VV}(\mathbf{z}) \end{bmatrix}$ is defined, and $\mathbf{N}(f,t) = \begin{bmatrix} N^{HH}(f,t) & N^{HV}(f,t) \\ N^{VH}(f,t) & N^{VV}(f,t) \end{bmatrix}$ is the polarimetric matrix containing the noise. With reference to Figure 1, $\mathbf{z}$ is the vector that locates a generic scatterer, $R_0(t)$ is the modulus of vector $\mathbf{R}_0(t)$, which locates the focusing point O and $\mathbf{i}_{R_0}^{(z)}(t)$ the unit vector of $\mathbf{R}_0(t)$. The function rect(x) is equal to 1 for $|x| < 0.5$, 0 otherwise.

Before proceeding, it is convenient to use a different notation, as detailed in [7], and exploit the characteristic of isotropic media that are encountered in ISAR applications. Therefore, the polarimetric data that represents the received signal can be written according to Pauli's decomposition as follows:

$$\mathbf{S}_R = \frac{1}{\sqrt{2}}\left[S_R^{VV}+S_R^{HH}, S_R^{VV}-S_R^{HH}, 2S_R^{HV}\right]^T = A\mathbf{k}, \quad (2)$$

where $A = |\mathbf{k}|$ and where the dependence on (f,t) is omitted for notation simplicity. The polarimetric unit vector $\mathbf{k}$ is defined as follows:

$$\mathbf{k} = \left[\cos\alpha e^{j\delta}, \sin\alpha\cos\beta e^{j\gamma}, \sin\alpha\sin\beta e^{j\varphi}\right], \quad (3)$$

where β represents the physical rotation of the scatterer about the radar line of sight (LoS), δ, γ, and φ are the scatterer phases in the three polarimetric channels, and α is a scatterer internal degree of freedom, which ranges in the interval $[0°, 90°]$. It must be pointed out that the angle α is rotation invariant and therefore it is decoupled from β. An interpretation of the internal degree of freedom α is given in Figure 2.

It is worth noting that such a representation is meant to highlight the physical properties of the scattering mechanism induced by a given scatterer. Therefore, by defining the unit vector $\mathbf{k}$, it is possible to define a specific polarisation that resonates with a scatterer with given physical properties. It must also be pointed out that the same decomposition applies for the target scattering matrix. Therefore, the scattering vector obtained from the scattering matrix is $\boldsymbol{\zeta}(\mathbf{z}) = [\zeta^{VV}(\mathbf{z})+\zeta^{HH}(\mathbf{z}), \zeta^{VV}(\mathbf{z})-\zeta^{HH}(\mathbf{z}), 2\zeta^{HV}(\mathbf{z})]$.

2.1. Signal separation

The Range-Doppler technique is based on an approximation that allows considering a rectangular support for the received signal in the Fourier domain. Such an approximation also leads to the separation of the domain in two independent one-dimensional domains: a time and a frequency component. Therefore, the received signal, relative to a single point-like scatterer, can be written in terms of the product of a time and a frequency component as follows:

$$s_R^{(i)}(t,f) = s_1^{(i)}(t)s_2^{(i)}(f), \quad (4)$$

where

$$s_1^{(i)}(t) = B_i\exp\left(j2\pi\left(\eta + f_d t + \frac{\mu}{2}t^2\right)\right)\text{rect}\left(\frac{t}{T_{\text{ob}}}\right), \quad (5)$$

$$s_2^{(i)}(f) = A_i\exp\left(j2\pi f\tau_0\right)\text{rect}\left(\frac{f-f_o}{B}\right), \quad (6)$$

where the product A_iB_i represents the complex amplitude in the ith Pauli channel, f_d is the Doppler frequency, μ is the chirp rate, and τ_0 is the time delay associated with the scattering centre. It is worth pointing out that the parameter μ is related to the signal model, which accounts for a quadratic radial motion, that is, it includes Doppler acceleration. Therefore, it should not be confused with the transmitted signal chirp rate if any is employed.

3. POL-CLEAN

The Pol-CLEAN technique is derived from the CLEAN technique proposed in [2]. Specifically, the Pol-CLEAN works iteratively by

(1) locating the brightest scattering centre in the polarimetric ISAR image and therefore by finding its coordinates in the delay-Doppler image plane (τ^*, ν^*),

(2) extracting its polarimetric vector $\mathbf{k}_s$, and

(3) removing it from the ISAR image in order to extract the next brightest scattering centre.

In order to eliminate a scattering centre from an ISAR image, the scattering centre point spread function (PSF) must be estimated and subtracted from the ISAR image. Let $S^{(1)}(f,t)$, $S^{(2)}(f,t)$ and $S^{(3)}(f,t)$ be the received signal in the three Pauli channels. After motion compensation, three ISAR images, namely, $I^{(1)}(\tau,\nu)$, $I^{(2)}(\tau,\nu)$ and $I^{(3)}(\tau,\nu)$ are obtained by means of a 2D Fourier Transform. The brightest scattering centre (dominant scatterer) is found within the three images. The range and cross-range indexes τ^* and ν^* and the Pauli's channel i^*, which corresponds to the polarimetric channel that contains the brightest scattering centre, are extracted by means of (7)

$$(\tau^*,\nu^*,i^*) = \arg\max_{(\tau,\nu,i)}\{\,|I^{(i)}(\tau,\nu)|\,\}, \tag{7}$$

with $i \in \{1,2,3\}$, $\tau \in \{1,2,\ldots,M\}$, $\nu \in \{1,2,\ldots,N\}$ and where M and N are the number of range and cross-range bins. The estimation of the PSF is performed by minimising the image energy after scattering centre removal. In order to find an efficient solution of the nonlinear optimisation problem stated in (7), the received signal separation is exploited.

3.1. Time component

By referring to (5), B_i ($i \in \{1,2,3\}$), f_d, and μ are the parameters to be estimated. The constant η can be neglected, because it does not affect the shape of the PSF. The signal $s_1^{(i)}(t)$, which is an N-dimensional row vector, is Fourier transformed to obtain a cross-range profile. A cost function is defined by means of the energy remaining in the range bin after scattering centre deletion. In order to treat the optimisation problem in a real domain, the scattering centre deletion is performed by considering the absolute value of the range profile. Such an operation can be performed in a single channel and then applied to the remaining channels by adjusting the corresponding B_i parameter. It must be pointed out that only the magnitude $\widetilde{B}$ of B must be estimated at this stage whereas the phase component is estimated separately and directly from the image. In summary, the following optimisation problem can be stated:

$$\left\{\hat{f}_d,\hat{\mu},\widehat{\widetilde{B}}_{i^*}\right\} = \arg\min_{(f_d,\mu,\widetilde{B}_{i^*})}\{E_{d_{i^*}}(f_d,\mu,\widetilde{B}_{i^*})\}, \tag{8}$$

where $E_{d_{i^*}} = \int |d_{i^*}(\nu)|^2 d\nu$ is the energy of a Doppler section in the i^*th Pauli channel, with $d_{i^*}(\nu) = |I^{(i^*)}(\tau^*,\nu)| - |S_1^{(i^*)}(\nu)|$ and $S_1^{(i^*)}(\nu)$ the Fourier Transform of $s_1^{(i^*)}(t)$. The estimates $\hat{f}_d$ and $\hat{\mu}$ are then used in the remaining Pauli channels for estimating the complex amplitudes B_i (with $i \neq i^*$). The latter estimation problem is transformed into an optimisation problem as follows:

$$\left\{\widehat{\widetilde{B}}_i\right\} = \arg\min_{\widetilde{B}_i}\{E_{d_i}(\hat{f}_d,\hat{\mu},\widetilde{B}_i) \text{ with } i \neq i^*\}, \tag{9}$$

where $E_{d_i} = \int |d_i(\nu)|^2 d\nu$ is the energy of a Doppler section in the ith Pauli channel ($i \neq i^*$) with $d_i(\nu) = |I^{(i)}(\tau^*,\nu)| - |S_1^{(i)}(\nu)|$.

3.2. Frequency component

A similar procedure is followed to estimate the frequency component of the PSF. The signal component in (6) is an M-dimensional column vector. After selecting a Doppler bin and range compressing via the Fourier Transform, a section of the ith channel ISAR image $I^{(i)}(\tau,\nu^*)$ can be obtained. Then, the delay τ_0 is jointly estimated with the magnitude $\widetilde{A}_{i^*}$ (in the i^*th Pauli channel) as follows:

$$\{\hat{\tau}_0,\widehat{\widetilde{A}}_{i^*}\} = \arg\min_{(\tau_0,\widetilde{A}_{i^*})}\{E_{g_{i^*}}(\tau_0,\widetilde{A}_{i^*})\}, \tag{10}$$

where $E_{g_{i^*}} = \int |d_{g_{i^*}}(\nu)|^2 d\nu$ is the energy of a delay section in the i^*th Pauli channel, with $g_{i^*}(\nu) = |I^{(i^*)}(\tau,\nu^*)| - |S_2^{(i^*)}(\tau)|$ and $S_2^{(i^*)}(\tau)$ the inverse fourier transform of $s_2^{(i^*)}(f)$.

The remaining two complex amplitudes are separately estimated by solving two separate one-dimensional optimisation problems:

$$\widetilde{A}_i = \arg\min_{\widetilde{A}_i}\{E_{g_i}(\hat{\tau}_0,\widetilde{A}_i)\} \quad \text{with } i \neq i^*, \tag{11}$$

where $E_{g_i} = \int |d_{g_i}(\nu)|^2 d\nu$ is the energy of a delay section in the ith Pauli channel ($i \neq i^*$) with $g_i(\nu) = |I^{(i)}(\tau,\nu^*)| - |S_2^{(i)}(\tau)|$.

3.3. Scattering centre PSF

The scattering centre PSF in the ith Pauli channel is obtained by calculating the two dimensional Fourier Transform of the product of the time and frequency components multiplied by the phase extracted from the ISAR image, as analytically detailed in

$$I_{\mathrm{PSF}}^{(i)}(\tau,\nu) = \left|\mathrm{FT}^2\left\{\hat{s}_1^{(i)}(t)\hat{s}_2^{(i)}(f)\right\}\right| \cdot \angle(I^{(i)}(\tau,\nu)). \tag{12}$$

The scattering vector $\mathbf{k}_s(\tau^*,\nu^*)$ relative to the considered scattering centre is therefore available by calculating the three scattering centre PSF centred in (τ^*,ν^*). Then, at the generic kth iteration, the scattering centre must be eliminated from the ISAR image via (13) in order to extract the following brightest scatterer:

$$I_{k+1}^{(i)}(\tau,\nu) = I_k^{(i)}(\tau,\nu) - I_{\mathrm{PSF}_k}^{(i)}(\tau,\nu). \tag{13}$$

The algorithm stops when the energy of the signal component in the ISAR image at the kth iteration is lower than a given threshold, λ. Such a threshold is typically set to 5% of the initial energy, that is, the total energy of the polarimetric ISAR image before any component removal. In mathematical detail, the preset threshold depends on the energy content and on the SNR of the initial ISAR image, as detailed in (14)

$$\lambda = K \cdot E\frac{\mathrm{SNR}}{\mathrm{SNR}+1}, \tag{14}$$

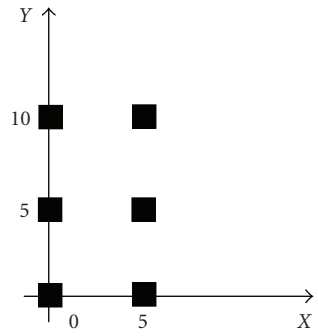

Figure 3: Six-point target geometry.

where $E^{(\mathbf{I}(\tau,\nu))} = \sum_{i=1}^{3} E^{(I^{(i)}(\tau,\nu))}$, with $E^{(I^{(i)}(\tau,\nu))} = \iint |I^{(i)}(\tau, \nu)|^2 d\tau\, d\nu$. It is worth pointing out that a coefficient SNR/(SNR + 1) is used in order to account for the energy of the signal component (noiseless image). Moreover, the SNR can be estimated in the image domain by selecting image areas where no target is present. It must also be noted that the energy of the signal component of the ISAR image at each iteration has to be compared to the energy threshold in (14). Therefore, the iterations stop when $E_k^{(\mathbf{I}(\tau,\nu))}(\text{SNR}/(\text{SNR} + 1)) < \lambda$.

4. RESULTS

The algorithm performance is tested both by using simulated and real data. The simulation test highlights the algorithm effectiveness when extracting ideal point-like scatterers, whereas the real data test shows an example of the output when the Pol-CLEAN is applied to "real-world" data.

4.1. Simulation

The analysis of simulated data aims at testing the Pol-CLEAN effectiveness when the target is composed of a number of ideal point-like scatterers with different polarimetric properties. Two separate tests are run. The first concerns a six-point target with scatterers placed at a distance of 5 resolution cells from each other. The second experiment is proposed to test the Pol-CLEAN robustness when the point-like scatterers distance drops down to one resolution cell.

4.1.1. Six-point target

An X-band radar and a six-point target are considered for the generation of the received signal. Each point is located at a distance of 5 resolution cells from the others (as shown in Figure 3). The scattering matrices relative to each point are shown in Table 1, whereas the main radar parameters are shown in Table 2.

The simulation is repeated by changing the zero padding in order to test the algorithm robustness with respect to the image oversampling. Specifically, zero padding factor (ZPF) of 1, 2, 4, and 8 are considered (note that ZPF = 1 means "no zero padding"). Gaussian noise has been added to the raw data in order to have an SNR = −10 dB (in the data domain).

Table 1: Scattering centre characteristics.

Type	Scattering matrix
S_1 Surface ($\alpha = 0°$)	$\begin{bmatrix} 1 & 0 \\ 0 & 1 \end{bmatrix}$
S_2 Dihedral ($\alpha = 90°, \beta = 0°$)	$\begin{bmatrix} 1 & 0 \\ 0 & -1 \end{bmatrix}$
S_3 Dipole ($\alpha = 45°, \beta = 45°$)	$\begin{bmatrix} 1+\frac{\sqrt{2}}{2} & \frac{\sqrt{2}}{2} \\ \frac{\sqrt{2}}{2} & 1-\frac{\sqrt{2}}{2} \end{bmatrix}$
S_4 Dihedral ($\alpha = 90°, \beta = 30°$)	$\begin{bmatrix} \frac{\sqrt{3}}{2} & \frac{1}{2} \\ \frac{1}{2} & -\sqrt{\frac{3}{2}} \end{bmatrix}$
S_5 Surface ($\alpha = 0°$)	$\begin{bmatrix} 1 & 0 \\ 0 & 1 \end{bmatrix}$
S_6 Dipole ($\alpha = 45°, \beta = 60°$)	$\begin{bmatrix} \frac{3}{2} & \frac{\sqrt{3}}{2} \\ \frac{\sqrt{3}}{2} & \frac{1}{2} \end{bmatrix}$

The estimated scattering vectors are decomposed according to (2) and (3) (only parameters α and β are shown). The estimated type of scattering (α) matches the true values as well as the estimated orientation angle (β), as shown in Table 3, where the mean value of the couple of parameters (α, β), obtained by generating 25 noise realisations, is shown. It is worth noting that the estimated mean values are weakly affected by the ZPF whereas the standard deviation decreases when the zero padding increases, as shown in Figure 4, where the root mean square error (RMSE) of α and β is plotted as a function of the ZPF.

The original ISAR images and the ISAR images after the first and the last scattering centre elimination are shown in Figures 5, 6, and 7 for the three Pauli channels, respectively. All ISAR images are obtained by using ZPF = 8. It is worth noting that the first component removal only affects the first Pauli channel (HH+VV) since the extracted scatterer has zero-components in the other two Pauli channels (VV-HH and 2HV) It can be pointed out that, after the last elimination, the scatterer's contribution is significantly suppressed.

4.1.2. Robustness analysis with respect to scatterer's distance

An algorithm performance loss is expected when the distance between the scatterers reduces. With the present experiment,

Table 2: Radar parameters.

Central freq. (f_0)	10 GHz	No. of radar sweeps (N)	96
Bandwidth (B)	400 MHz	Cross-range res.	0.68 m
Freq. step (Δf)	3.15 MHz	Range res.	0.375 m
No. of tx freq. (M)	128	SNR (data domain)	−10 dB

Table 3: Estimated scattering parameters.

ZP		S_1	S_2	S_3	S_4	S_5	S_6
1	α	55.5°	85.99°	45.53°	86.73°	6.55°	45.40°
	β	—	0.07°	45.12°	29.88°	—	61.39°
2	α	5.02°	86.64°	45.43°	86.91°	5.64°	45.08°
	β	—	0.23°	45.16°	29.51°	—	61.44°
4	α	5.06°	86.56°	45.20°	86.74°	5.52°	45.22°
	β	—	−0.13°	45.13°	29.47°	—	61.52°
8	α	4.97°	86.71°	45.37°	86.96°	5.44°	45.15°
	β	—	−0.09°	45.19°	29.71°	—	61.43°

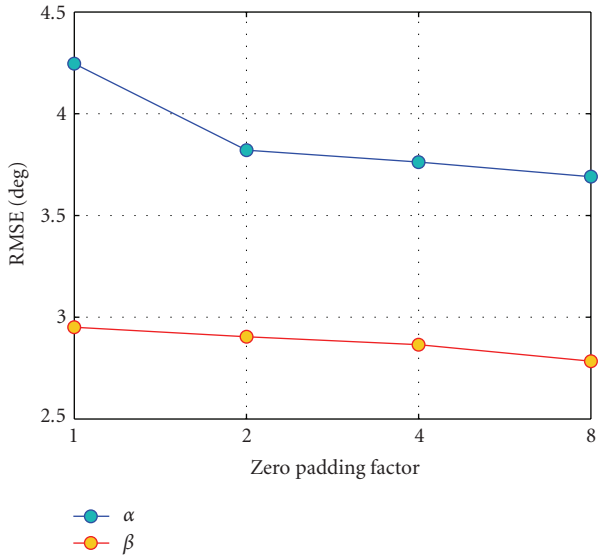

Figure 4: Standard deviation versus zero padding factor.

the algorithm robustness with respect to the interference caused by the vicinity of other scatterers is tested. Specifically, two scatterers close to each other are considered in order to create such an interference. The scatterers chosen are $S1$ and $S4$ (from the previous experiment) and their scattering matrices are shown in Table 1. Gaussian noise is added to the generated data in order to obtain a SNR = −10 dB (in the data domain). Both the vicinity along the range and cross-range coordinate is tested. In particular, the scatterer's distance is varied within one to five range cells, first along the range direction and then along the cross-range direction. Figure 8 shows the results in terms of estimation error for the parameters α and β against the distance in range (as in the number of range resolution cells), whereas Figure 9 shows the similar results against the distance in cross-range (as in number of cross-range resolution cells). The results are shown in terms of the RMSE and they are obtained by using a ZPF = 8.

As predicted, the performance of the algorithm decreases when the distance between scatterers reduces. It can also be pointed out that the same conclusions are reached when considering range and cross-range directions. This effect is mainly due to two reasons.

(1) Scatterers interfere with each other because of their sidelobes. Although it would be tempting to use a window in order to reduce the sidelobe level, the inconvenient effect of widening the main lobe would negatively affect the performance when the distance is equal to one resolution cell.

(2) The cancellation of the scatterer under test is a non-linear operation that affects the estimated scattering matrix of the nearest scatterers.

4.2. Real data

The analysis of real data provides a clear example of the results achievable when using the Pol-CLEAN. Since no accurate target model is available, a direct error analysis is not viable for this kind of experiment. Nevertheless, the results are visually readable by comparing the extracted scatterers with the Pol-ISAR image.

4.2.1. Data set description

The data used for this test is collected during a real turn-table experiment. The data is obtained from the GTRI publicly releasable data set. The experiment is run by using a stepped-frequency fully polarimetric radar system arranged on a tower and looking down to a turn-table. The illuminated target is a T72 tank. The data file contains 79 radar sweeps for a fixed elevation angle (θ_{el} = 29.9994°). After each radar sweep, the turn table is rotated by 0.05°. Therefore, a total azimuth angle variation of 3.9° is spanned about

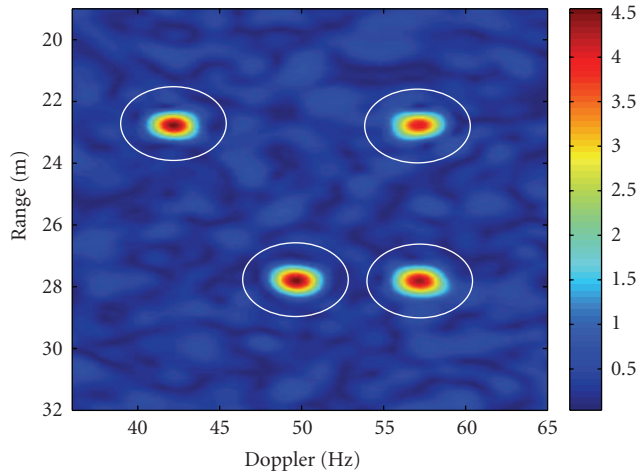

(a)

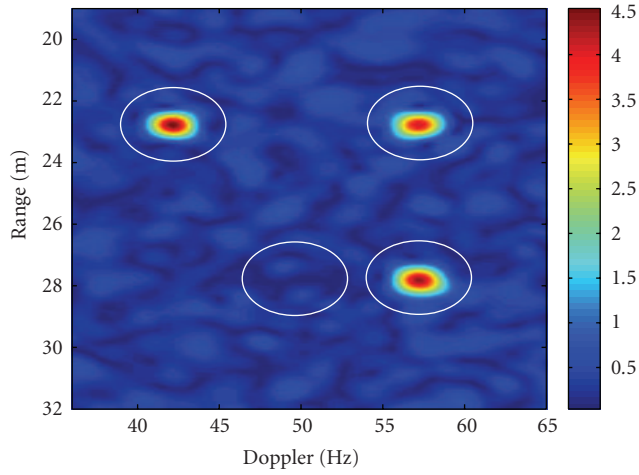

(b)

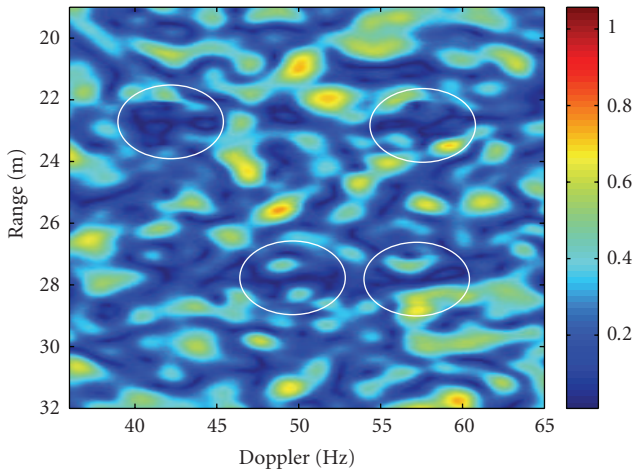

(c)

Figure 5: ISAR image on channel HH+VV before any cancellation (a), after the first cancellation (b), and after the last cancellation (c).

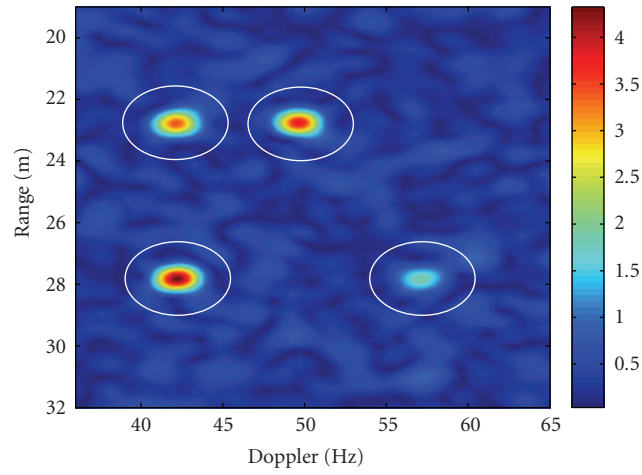

(a)

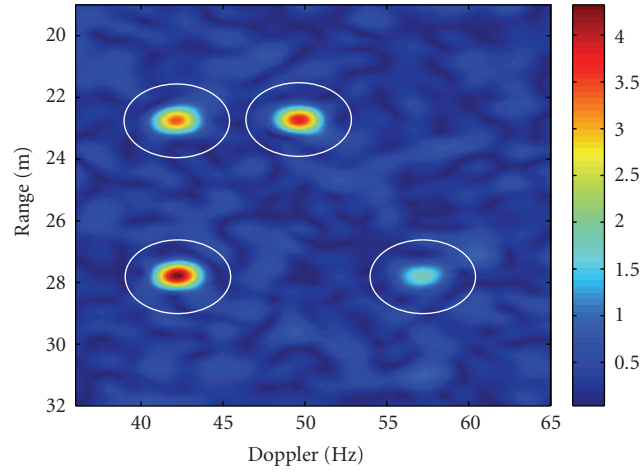

(b)

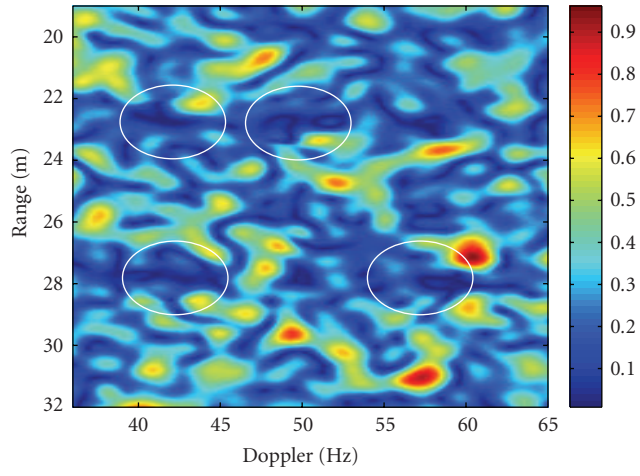

(c)

Figure 6: ISAR image on channel VV-HH before any cancellation (a), after the first cancellation (b), and after the last cancellation (c).

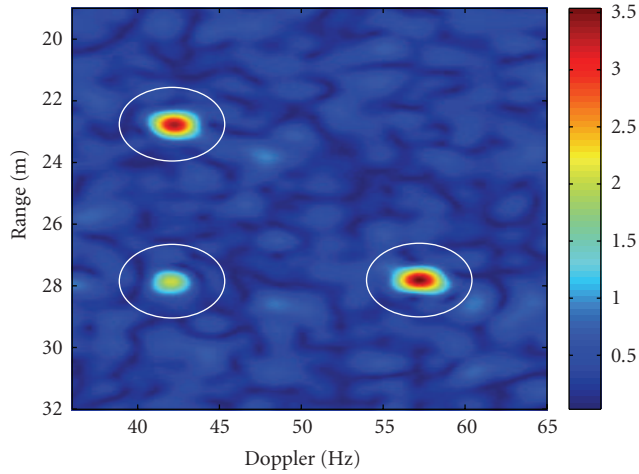

(a)

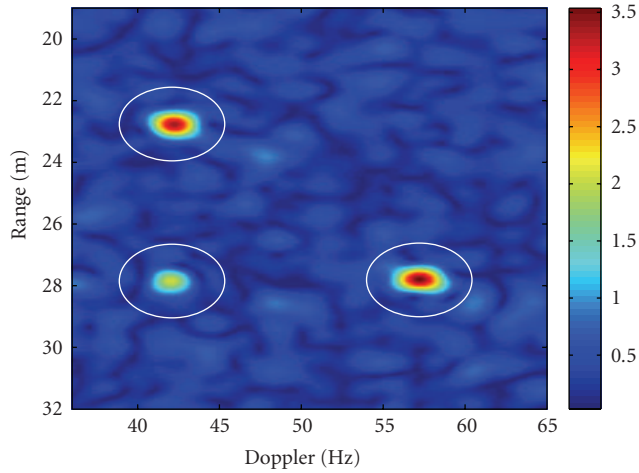

(b)

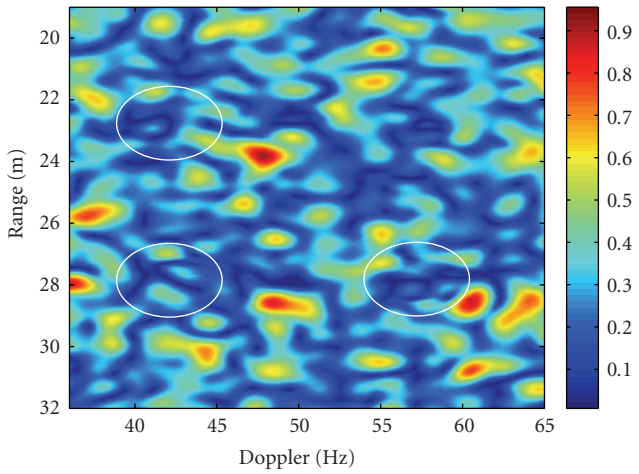

(c)

Figure 7: ISAR image on channel HV before any cancellation (a), after the first cancellation (b), and after the last cancellation (c).

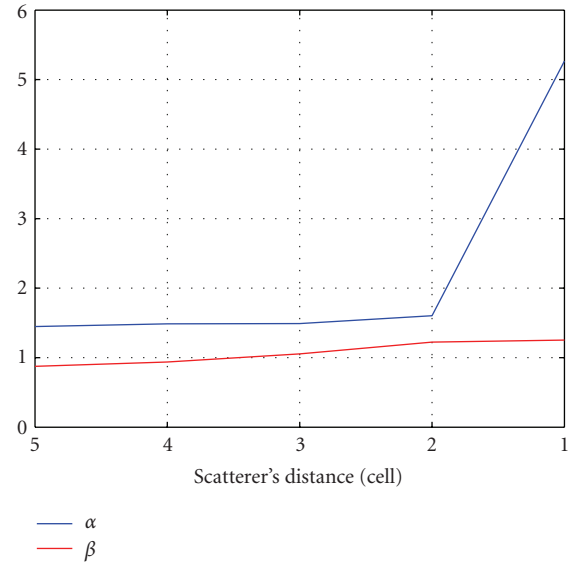

Figure 8: RMSE against the distance in range.

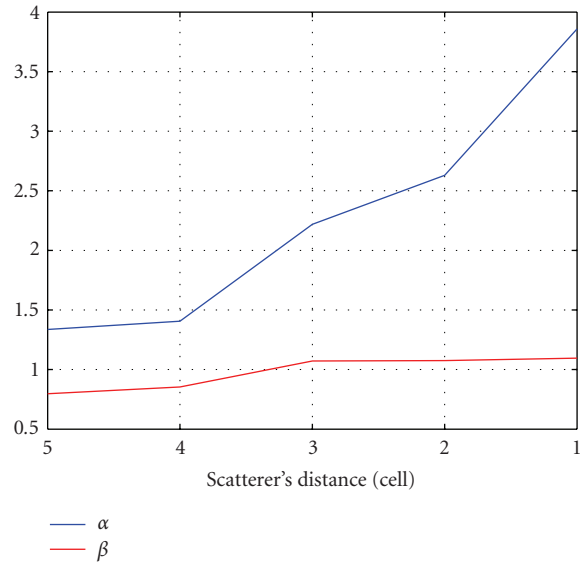

Figure 9: RMSE against the distance in cross range.

the central azimuth angle ($\theta_{az} = 89.231°$). The central frequency is equal to $f_0 = 9.6$ GHz whereas the number of transmitted frequencies is equal to 221, equally spaced by 3 MHz. The resultant bandwidth is equal to 660 MHz and both the nominal range and cross-range resolutions are equal to 0.3048 m.

The radar-target geometry is depicted in Figure 10, whereas the target is shown in Figure 11. The radar parameters are shown in Table 4.

4.2.2. Real data results

The image cross-range section cut across the scattering centre peak (in blue) and the estimated cross-range section of the

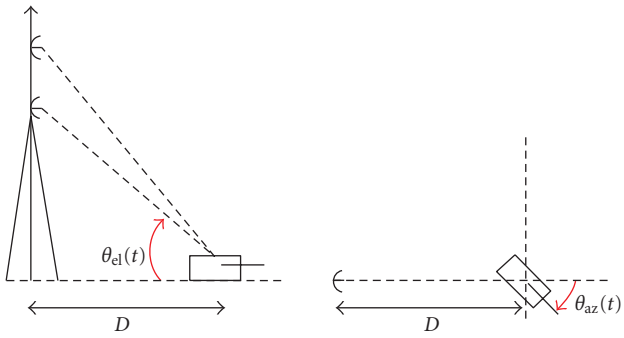

Figure 10: Radar target geometry.

Figure 11: Target T72.

Table 4: Radar parameters.

Parameters	Value
f_0	9.6 Ghz
Frequency step	3 Mhz
N° transmitted frequencies	221
N° sweeps	79
Azimutal sampling rate	0.05°
Total aspect angle for each file	3.9°
Nominal range resolution	1 foot
Nominal cross-range resolution	1 foot

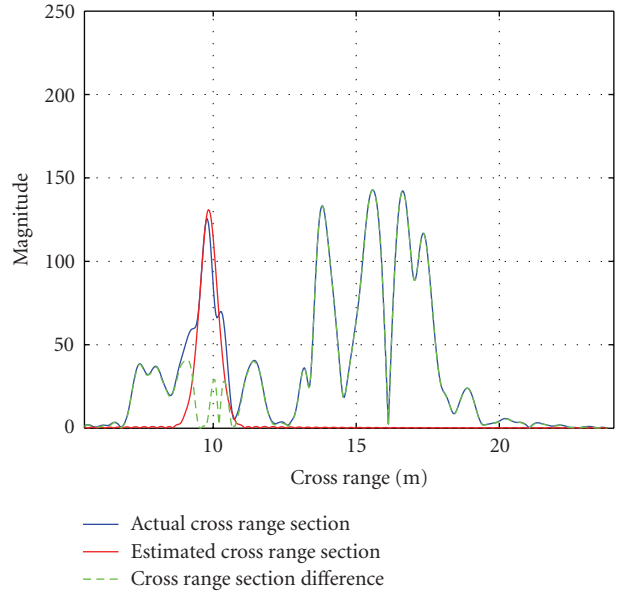

Figure 12: Polarimetric channel HH+VV.

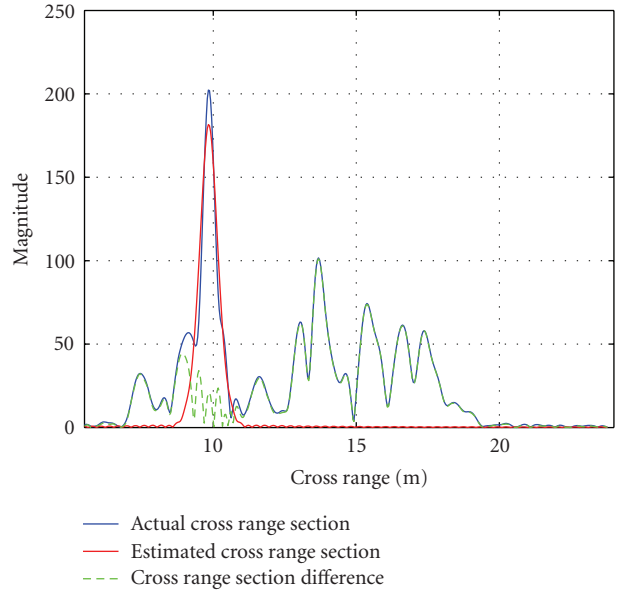

Figure 13: Polarimetric channel VV-HH.

scattering centre PSF (in red) are shown, for all polarimetric channels, in Figures 12, 13, and 14. Moreover, the cross-range section after the scattering centre removal is shown in green colour. It is worth noting that the estimated PSF cross-range section is estimated quite accurately, and therefore the scattering centre is removed from the image. The range section of the same scattering centre, as well as the range section of the estimated PSF, is shown in Figures 15, 16, and 17. It can be noted that the results along the range direction are similar to those along the cross-range direction. Figures 18, 19, 21, 22, 24 and 25 show the ISAR image before and after the cancellation of the first scatterer, for all three polarimetric channel. Figures **??**, 23, 26 how the ISAR images after the cancellation of the last scatterer. By setting the energy threshold defined in (14) to $K = 0.05$, a number of 43 scatterers are extracted. The RGB ISAR image of the target is also shown in Figure 27. The colored dots represent the scattering centres extracted by means of the Pol-CLEAN. The colour of each dot represents the polarimetric signature of the extracted scattering centre in the Pauli basis. It should be noted that the colour of the extracted dot is very close to the colour of the underlying ISAR image, especially in the case of bright scatterers. Weaker extracted scatterers do not match perfectly the colour of the underlying ISAR image. This can be explained by considering that

(1) weaker scatterers are partially masked by stronger scatterer's sidelobes (it can be read as an interference problem);

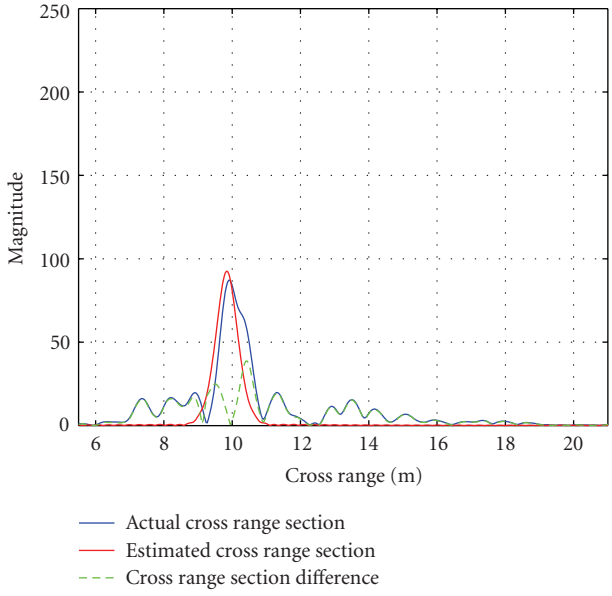

Figure 14: Polarimetric channel 2HV.

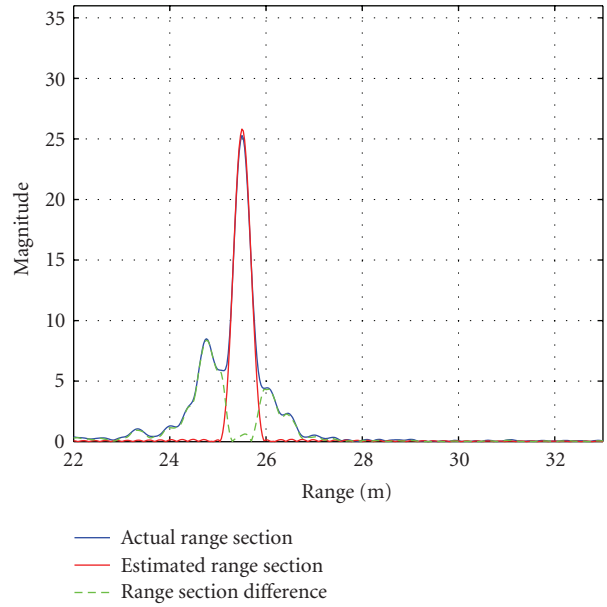

Figure 16: Polarimetric channel VV-HH.

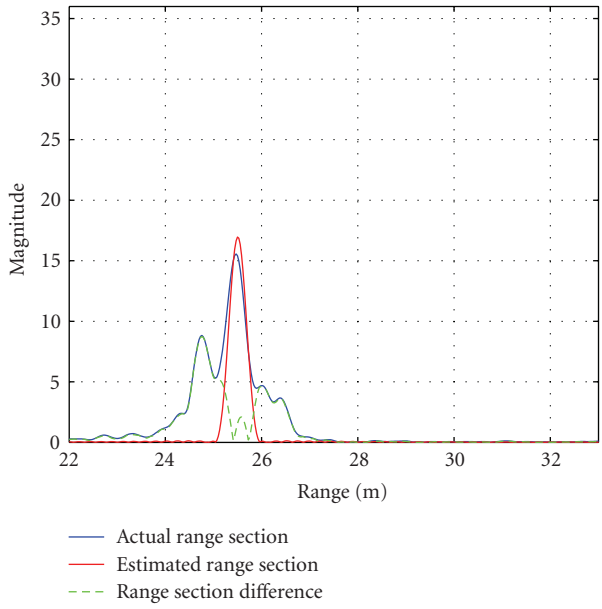

Figure 15: Polarimetric channel HH+VV.

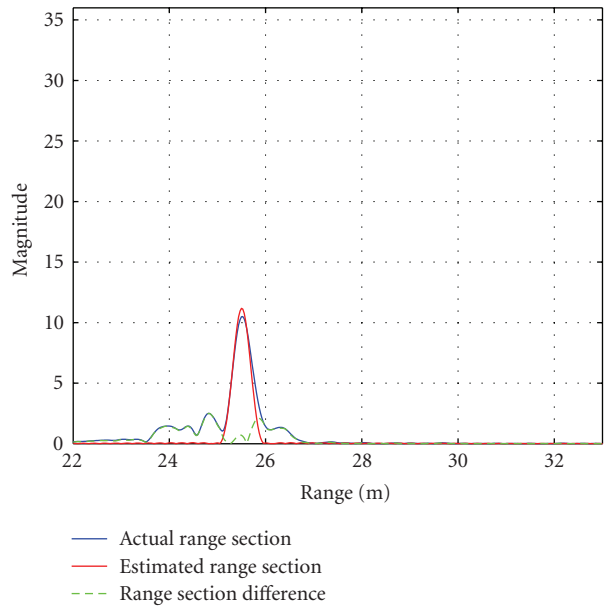

Figure 17: Polarimetric channel 2HV.

(2) even after stronger scatterers are removed, some residuals remain that affect the extraction of weaker scatterers and therefore lead to larger estimation errors.

Nevertheless, classifiers would weight bright scatterers more than weak scatterers and therefore such an effect would not affect the classification performances significantly.

5. CONCLUSIONS

Scattering centre extraction from polarimetric ISAR images can be achieved by extending the CLEAN technique, which was designed to perform scattering centre extraction from single polarization ISAR images. The extension of the CLEAN technique, namely, the Pol-CLEAN technique has been first proposed in this paper and then tested on simulated and real data. The results have shown that the Pol-CLEAN technique is able to extract scattering centres from noisy ISAR images and estimate their locations and polarisation vectors. A table with essential information is then obtained that contains only the positions and polarimetric vectors of the extracted scatterers, which can be used as a feature set for automated target classification and recognition.

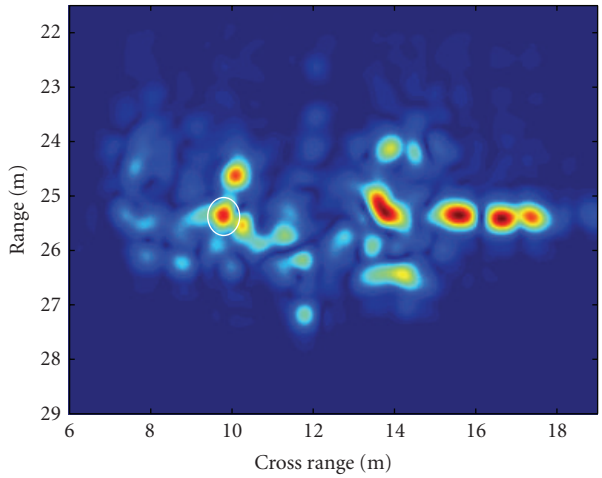

Figure 18: Original ISAR image—polarimetric channel HH+VV.

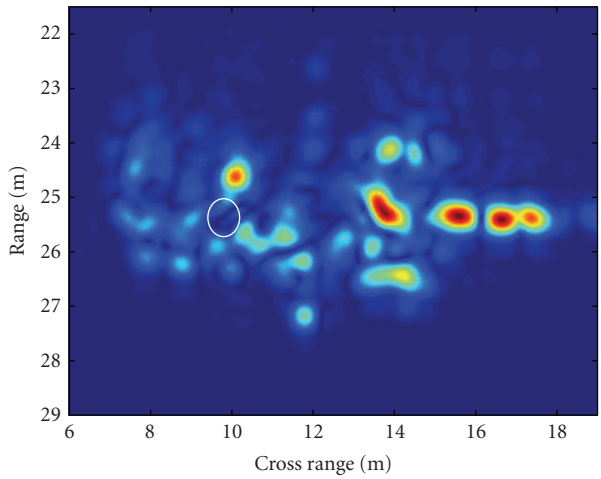

Figure 19: ISAR image after removing the first scattering centre—polarimetric channel HH+VV.

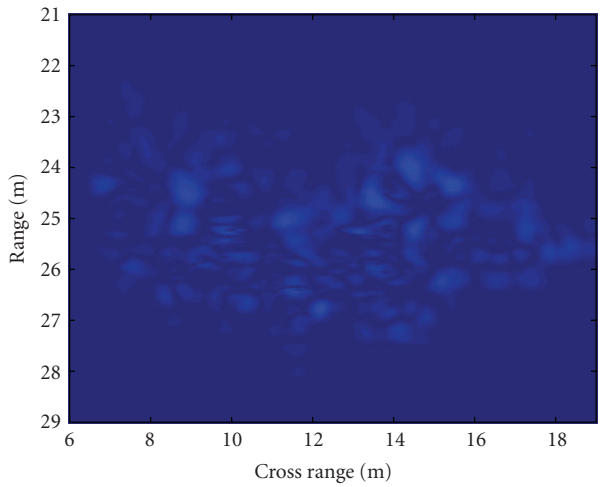

Figure 20: ISAR image after removing the last scattering centre—Polarimetric channel HH+VV.

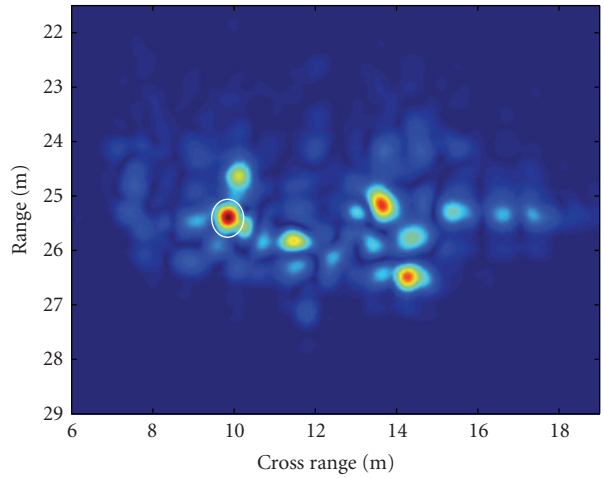

Figure 21: Original ISAR image—polarimetric channel VV-HH.

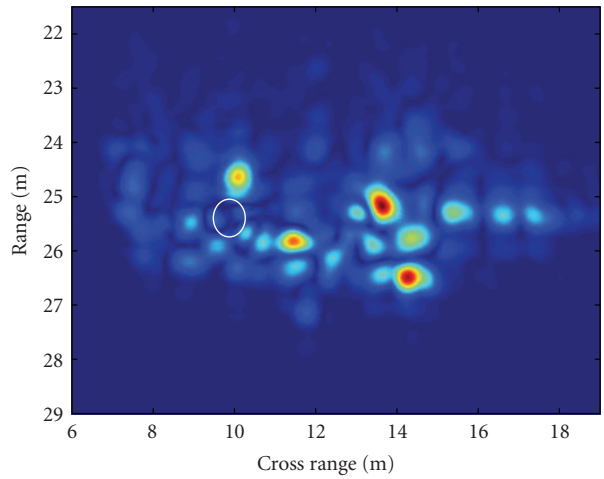

Figure 22: ISAR image after removing the first scattering centre—polarimetric channel VV-HH.

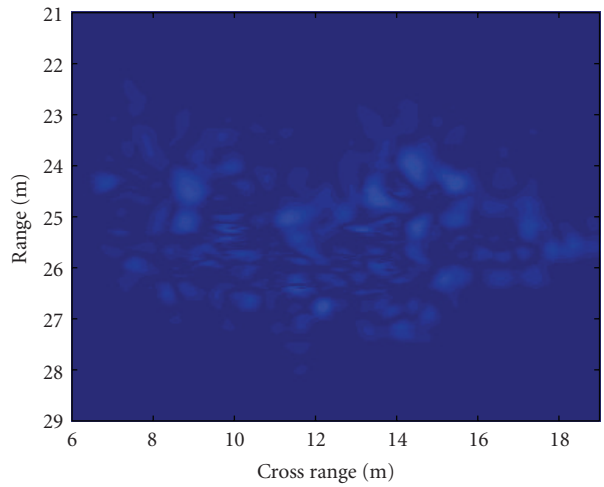

Figure 23: ISAR image after removing the last scattering centre—Polarimetric channel VV-HH.

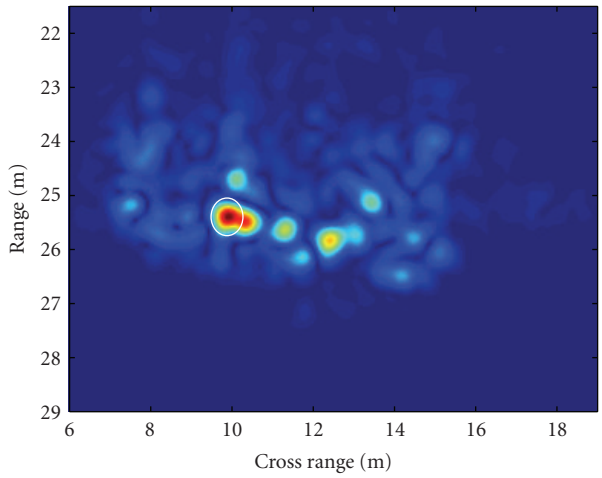

Figure 24: Original ISAR image—Polarimetric channel 2HV.

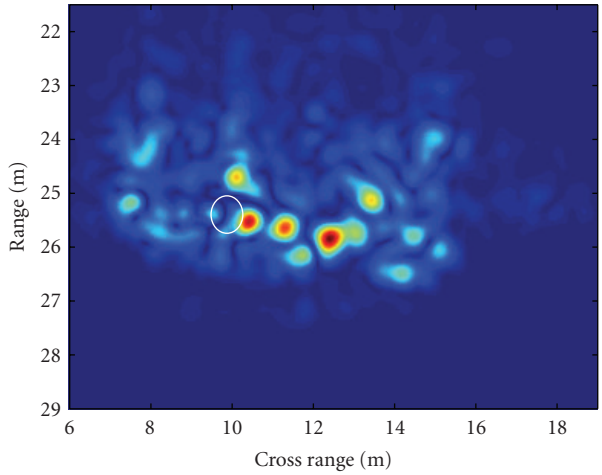

Figure 25: ISAR image after removing the first scattering centre—polarimetric channel 2VH.

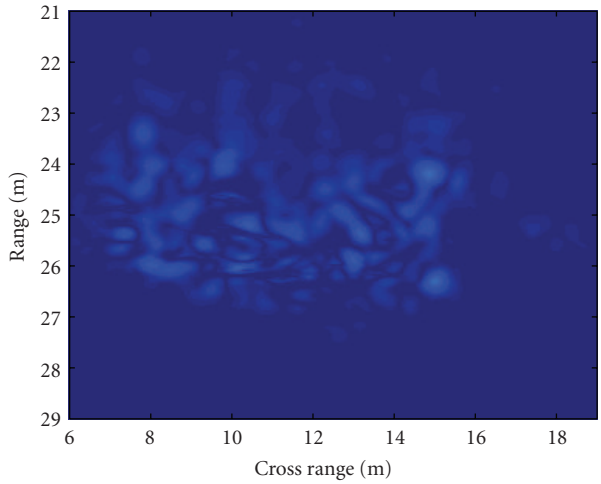

Figure 26: ISAR image after removing the last scattering centre—Polarimetric channel 2HV.

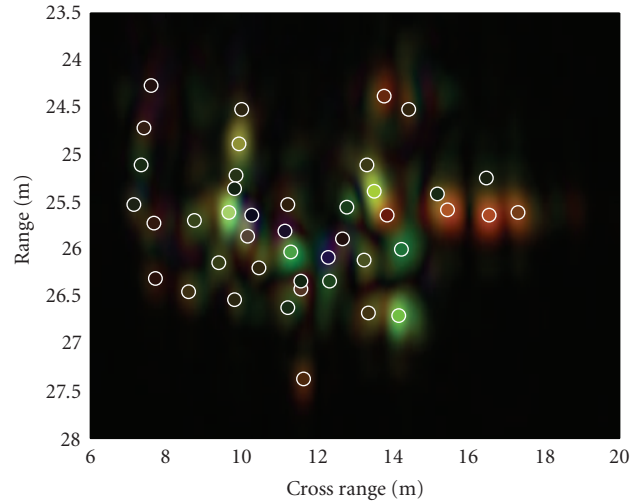

Figure 27: RGB ISAR of the target—the colored spots represent the scatterer extracted by the algorithm.

ACKNOWLEDGMENTS

The authors would like to thank The Sensor ATR Technology Division of the US Air Force Research Laboratory (AFRL) for releasing real data and the Australian Defence Science and Technology Organisation (DSTO) for partially funding this work. The views and conclusions contained in this document are those of the authors and should not be interpreted as representing the official policies, either expressed or implied, of the Defense Advanced Research Projects Agency, the United States Air Force, the Department of Defense, or the US Government.

REFERENCES

[1] J. Tsao and B. D. Steinberg, "Reduction of sidelobe and speckle artifacts in microwave imaging: the CLEAN technique," *IEEE Transactions on Antennas and Propagation*, vol. 36, no. 4, pp. 543–556, 1988.

[2] Y. Sun and P. Lin, "An improved method of ISAR image processing," in *Proceedings of the 35th Midwest Symposium on Circuits and System*, vol. 2, pp. 983–986, Washington, DC, USA, August 1992.

[3] S. R. Cloude and K. P. Papathanassiou, "Polarimetric SAR interferometry," *IEEE Transactions on Geoscience and Remote Sensing*, vol. 36, no. 5, part 1, pp. 1551–1565, 1998.

[4] R. Touzi and F. Charbonneau, "Characterization of target symmetric scattering using polarimetric SARs," *IEEE Transactions on Geoscience and Remote Sensing*, vol. 40, no. 11, pp. 2507–2516, 2002.

[5] M. Martorella, J. Palmer, B. D. Bates, F. Berizzi, and B. Haywood, "Polarimetric hot spot processing for ISAR image autofocusing," in *Proceedings of the IET International Conference on Radar Systems (RADAR '07)*, Edimburgh, UK, October 2007.

[6] W. L. Cameron, N. N. Youssef, and L. K. Leung, "Simulated polarimetric signatures of primitive geometrical shapes," *IEEE Transactions on Geoscience and Remote Sensing*, vol. 34, no. 3, pp. 793–803, 1996.

[7] S. R. Cloude and E. Pottier, "A review of target decomposition theorems in radar polarimetry," *IEEE Transactions on Geoscience and Remote Sensing*, vol. 34, no. 2, pp. 498–518, 1996.
[8] J. R. Huynen, "Measurement of the target scattering matrix," *Proceedings of IEEE*, vol. 53, no. 8, pp. 936–946, 1965.
[9] E. Krogager, "New decomposition of the radar target scattering matrix," *Electronics Letters*, vol. 26, no. 18, pp. 1525–1527, 1990.
[10] T. Cooke, M. Martorella, B. Haywood, and D. Gibbins, "Use of 3D ship scatterer models from ISAR image sequences for target recognition," *Digital Signal Processing*, vol. 16, no. 5, pp. 523–532, 2006.
[11] K.-T. Kim, D.-K. Seo, and H.-T. Kim, "Efficient classification of ISAR images," *IEEE Transactions on Antennas and Propagation*, vol. 53, no. 5, pp. 1611–1621, 2005.
[12] L. Vignaud, "Robust polarimetric scatterers extraction for SAR ATR," in *Proceedings of the RTO-SET Symposium on Target Identification and Recognition Using RF Systems*, Oslo, Norway, October 2004.
[13] M. Martorella, F. Berizzi, and B. Haywood, "Contrast maximisation based technique for 2-D ISAR autofocusing," *IEE Proceedings: Radar, Sonar and Navigation*, vol. 152, no. 4, pp. 253–262, 2005.

Hindawi Publishing Corporation
International Journal of Navigation and Observation
Volume 2008, Article ID 807958, 12 pages
doi:10.1155/2008/807958

Research Article

Experiences Gained during the Development of a Passive BSAR with GNSS Transmitters of Opportunity

M. Cherniakov, Rajesh Saini, Michael Antoniou, Rui Zuo, and Eleftherios Plakidis

Microwave Integrated Systems Laboratory (MISL), Department of Electronic, Electrical and Computer Engineering, University of Birmingham, Edgbaston, Birmingham B15 2TT, UK

Correspondence should be addressed to M. Cherniakov, m.cherniakov@bham.ac.uk

Received 18 February 2008; Accepted 14 May 2008

Recommended by M. Greco

This paper presents an overview of the research conducted at University of Birmingham. It highlights and briefly discusses various systems parameters (e.g., resolution, power budget), problems (e.g., interference, heterodyne channel Doppler compensation), and signal processing algorithms (imaging, synchronization) required for successfully obtaining an image. The GLONASS satellite is used for experiential confirmation of the main results. All these results are presented and briefly discussed.

1. INTRODUCTION

Synthetic aperture radar (SAR) works by collecting the echo returns from many pulses along the flight path and processing them into a single high-resolution radar image. In a monostatic SAR, the transmitter and receiver are on the same platform, whereas in a bistatic SAR (BSAR) the transmitter and receiver are separated by a distance that is comparable to the expected target distance. Examples of BSAR include airborne systems, where the transmitter and receiver are located on different aircrafts [1, 2]. In a space-borne system, the transmitter and receiver are based on two or more satellites [3, 4]. There is another subclass of bisatic SAR known as space-surface bistatic synthetic aperture radar (SS-BSAR). The SS-BSAR consists of a spaceborne transmitter and a receiver mounted on or near the earth's surface, see Figure 1. The receiver could be airborne, mounted on a ground vehicle, onboard a ship, or even in a stationary position on the surface. For the stationary receiver, a nongeostationary satellite should be used to provide aperture synthesis.

The core of SS-BSAR systems is their asymmetric topology [5]. This is in contrast to a more usual bistatic SAR configuration, where the transmitter and the receiver are moving along collinear trajectories. The basic operation of SS-BSAR systems is much the same as the operation of other BSAR systems, the differences being introduced mainly as a consequence of the geometry employed.

University of Birmingham (UoB) has been carrying out active research in the area of SS-BSAR since 2003. The main aim of this research is to experimentally demonstrate the feasibility and performance of airborne SS-BSAR, utilising Global Navigation Satellite System (GNSS) as the transmitter of opportunity.

The goal of this paper is to give the reader an overview of the research conducted at the UoB. It highlights and briefly discusses various systems parameters (for resolution, power budget), problems (e.g., interference, motion compensation), and signal processing algorithms (imaging, synchronisation) required for successfully obtaining an image. The GLONASS satellite is used for experiential confirmation of the main results. All these results are presented and briefly discussed.

It should be noted that although we are using a particular satellite system, the structure and main parameters of the radar system are generic and could be used with different GNSS transmitters.

2. RESOLUTION

The GLONASS satellite was selected as the transmitter of opportunity for experimentation, despite its rather poor potential slant range resolution (30 m). This was due to the fact that it was the only one available at the time of experimentation. Another GNSS system (GPS) has a navigation signal with twice the spectral width, and hence 15 m

Table 1: The main parameters of different GNSS signals.

GNSS	GLONASS		GPS			Galileo	
Channels (code)	L1(P)	L2 (P)	L1(P/M)	L2 (P/M)	L5	E5a/b	E5 (E5a+E5b)
Central frequency (MHz)	1602–1615	1246–1257	1575.4	1227.6	1176	1191.79	1191.795
Minimum power (dBW)	−161	−167	−158 (global beam) −138 (spot beam)		−154.9	−157	−154
Chip rate (Mcps)	5.11	5.11	10.23/5.11	10.23/5.11	10.23	10.23	10.23
Aggregated bandwidth (MHz)	—	—	20–30	20–30	—	—	20–50
Range resolution (m)	30	30	5–8	5–8	15	15	3–8

Table 2: Potential target detection range for different GNSS signals.

Transmitter	λ(cm)	V_a(m/s)	η	A_e(m^2)	Δ_{az}(m)	T_s(K)
Galileo E5	25.2	200	0.5	0.5	1	410
GPS L5	25.5					
GPS spot beam	19					
GLONASS L1	18.8					

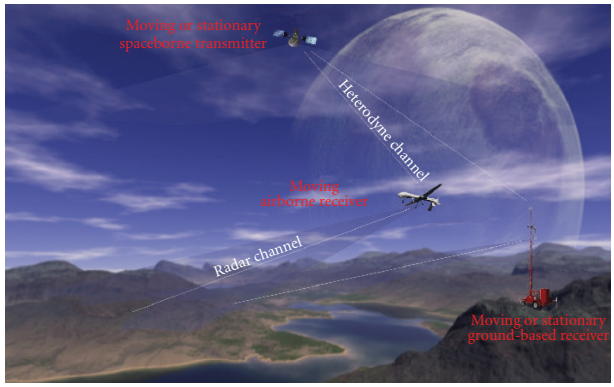

Figure 1: SS-BSAR concept for imaging.

potential range resolution, but this is a coded signal and can be used only with special authorisation. The most promising GNSS for the considered purposes are the EU Galileo system and the new proposed GPS signal structure [6]. Figure 2(a) shows the signal spectrum of Galileo E5 signal. Two signal components (E5a and E5b) in the E5 band are modulated as a single wideband signal generated following the AltBOC (15, 10) modulation. This wideband signal is centred at the frequency of 1191.795 MHz and has a bandwidth of at least 50 MHz. Since the E5a and E5b signals transmit independent information from each other, it is possible in theory to develop a signal processing technique that combines the received E5a and E5b signals in such a way to give a resolution of 3–8 m. Similarly, the different signals (P-code and M-code) of the modernised GPS L1/L2 channel can be combined to achieve 20–30 MHz bandwidth or 5–8 m range resolution. This makes GNSS (Galileo, GPS) based SS-BSAR a prospective candidate for many practical applications.

Table 1 summarises some GNSS signal parameters and their potential slant range resolution. The stated resolution is for a quasimonostatic configuration. However, for other configurations the resolution is dependent upon the geometry of the system, that is, satellite-receiver-target positions not relative to each other. The effect of the system's geometry on the resolution is comprehensively discussed in [7].

It should be noted that one of the key advantages of using a GNSS satellite compared to other satellites (e.g., Geostationary TV satellite) is that the user can choose the desired bistatic topology (low bistatic angle, i.e., negligible resolution loss). This is due to the fact that 4 to 10 GNSS satellites are simultaneously visible at any point on the earth. As a result, a particular satellite in the best (or at least suitable) position can be selected and there is no need for a very specific aircraft trajectory to allow the observation of an area. On the other hand, geostationary satellites are fundamentally positioned above the equator and this requires a specific aircraft trajectory for mapping a particular area and, in many or even most situations, a vital loss in ground resolution may take place.

3. POWER BUDGET

The receiving part of the SS-BSAR consists of two channels: the heterodyne channel (pointed directly towards the satellite) is used for synchronisation and the radar channel is used for receiving reflected signal from the target area. The power budget of the radar channel is a determining parameter for target detection, which is calculated for the time of aperture synthesis and considering only targets that have RCS independent of frequency and angle. For bistatic SAR, the expression for SNR after range and azimuth compression can be written as [8]

$$\frac{S}{N} = \frac{\rho A_e \sigma \lambda \eta}{4\pi R_R K T_S V_a \Delta_{az}}, \quad (1)$$

where ρ is power flux density of the transmitting signal in target area, σ is the radar cross-section of the target, η is a general loss factor, R_R is the receiver-target range, V_a is the receiver velocity, Δ_{az} is the potential azimuth resolution.

Table 1 shows the minimum received signal power by 0 dB omnidirectional antenna on the ground for different

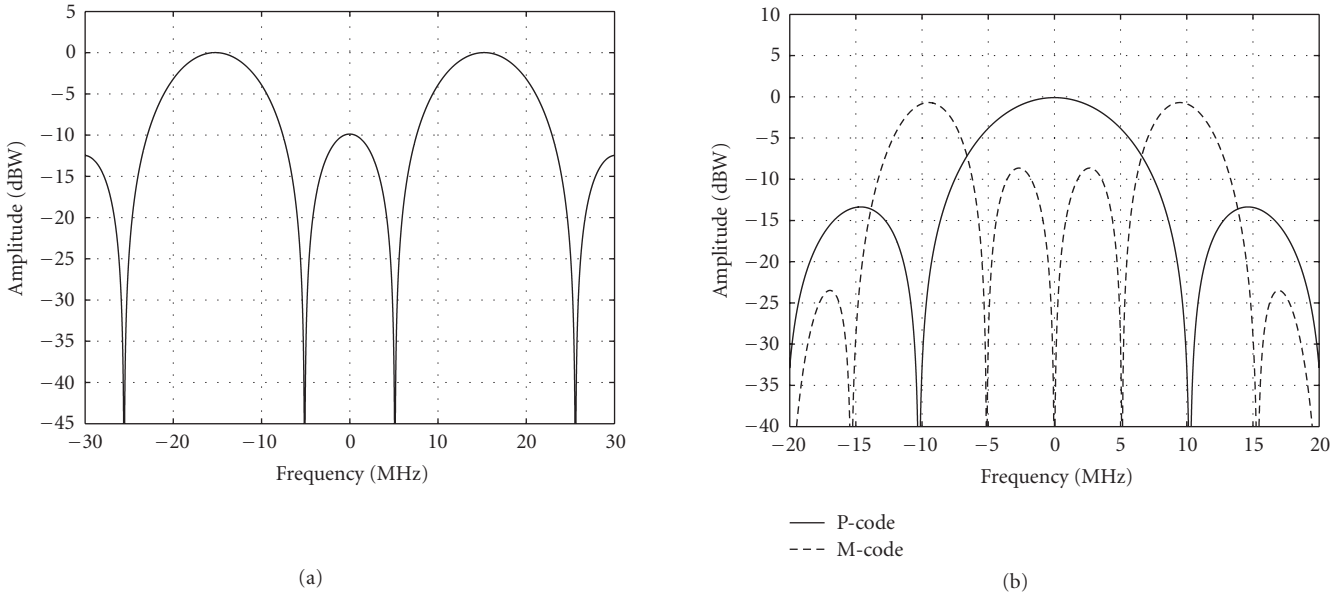

Figure 2: (a) Galileo E5 channel Spectrum, (b) GPS L1 or L2 channel Spectrum.

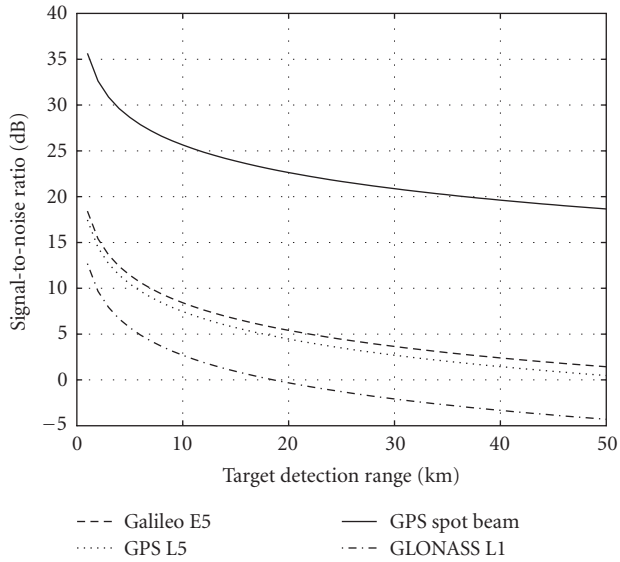

Figure 3: Detection range for 50 m^2 RCS target.

GNSS signals. It can be noted that the Galileo E5 signal and new GPS L5 signal provide at least 6 dB more power compared to GLONASS L1 channel. In addition GPS after modernisation will broadcast the signal from a high-gain directional antenna, termed as spot beam, which generates 20 dB more power than its global beam and covers the ground area of 1200 km × 1200 km that is enough for our application.

Using the parameters provided in Tables 1, 2, and (1), Figure 3 shows the potential range of SS-BSAR for different GNSS signals. If we consider 10–13 dB SNR as the radar detection threshold, targets with 50 m^2 RCS can be detected at the range of approximately 5 km using Galileo E5 or GPS L5 signal. By using GPS spot beam (available in 2013), the detection range can be extended to more than 50 km for target with 50 m^2 RCS.

It also should be noted that all the above range calculations were done using the minimum power received for each signal. The minimum power level is received when the satellite is near the horizon and the maximum when the satellite is at an elevation of approximately 45°. On average, the difference between the minimum and maximum power level is around 6 dB. Hence, one can expect four times more improvement in the maximum range when a satellite at an elevation of about 45°.

4. INTERFERENCE

Using GNSS as an illuminator in SS-BSAR presents a specific problem in signal detection. In addition to the desired target echo, a number of interference signals are present in the system. GNSS signals are modulated continuous waves and the desired reflected signal has to be detected against a continuous interference background. The first type of such interference is direct path interference (DPI), which is the signal received directly by the radar antenna from the illuminating satellite. The second type is adjacent channel interference (API) coming from another GNSS satellite operating in the same frequency band. These interference sources discussed in [8, 9] showed that the signal-to-interference ratio (SIR) is high enough to detect the desired signal. It was shown that the interference and the desired signal are essentially the same process, and at the output of the matched filter the interference level is specified by the cross-correlation side-lobes. In addition, the SAR algorithm itself acts as a spatial filter to these interference sources. The fact that the interference signals are coherent to the desired signal introduces some low-level false targets,

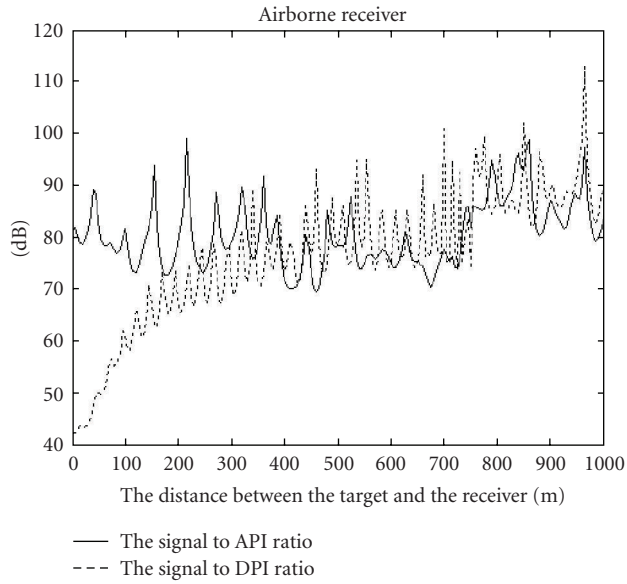

Figure 4: Signal-to-interference ratio [9] (zoomed).

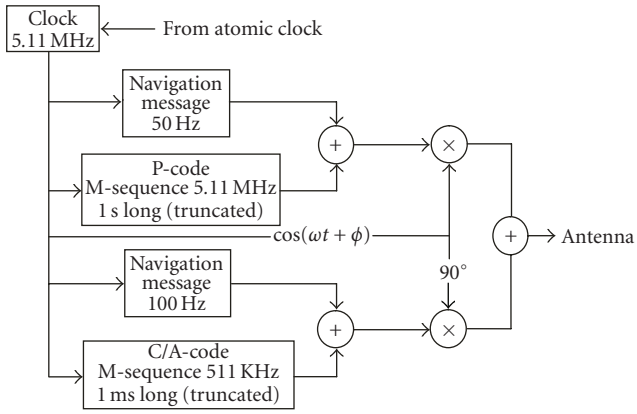

Figure 5: Simplified block diagram of the L1 GLONASS signal structure.

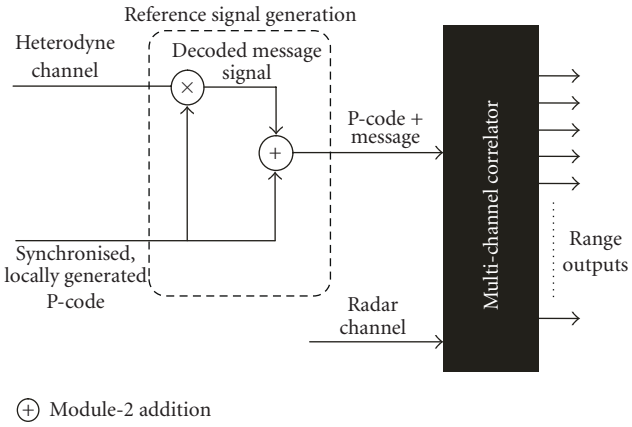

Figure 6: Range compression algorithm.

but these false targets will be outside the observation area. Figure 4 shows the SIR evaluated for a practical situation [9].

5. GLONASS SIGNAL STRUCTURE AND SYNCHRONISATION

Figure 5 shows a simplified block diagram of the structure of GLONASS signals transmitted in the L1 frequency band [10]. The C/A and P-code signals are in phase quadrature. The C/A code rate is 511 KHz and the code period is 1 millisecond. The C/A code sequence is added (mod 2) to a 100 Hz navigation message. The P-code has a chip rate of 5.11 MHz and is a truncated M-sequence repeated every 1 second. The navigation message on the P-code has a clock rate of 50 Hz.

Mathematically the transmitted signal can be written as

$$Y = A_p P(t) D_p(t) \cos(\omega_c t + \phi) + A_C C(t) D_c(t) \cos(\omega_c t + \phi), \quad (2)$$

where Y is the signal at L1 frequency, $A_p(t)$ is the amplitude of the P-code, $P(t)$ represents the polarity (± 1) of the P-code, $D_p(t)$ is the binary (± 1) P-code navigation message, ω_c is the L1 frequency, ϕ is the initial phase, $A_c(t)$ is the amplitude of the C/A code, $C(t)$ represents the polarity (± 1) of the C/A code, $D_c(t)$ is the binary (± 1) C/A navigation message.

The P-code will be used for the purpose of imaging, as it provides a reasonable range resolution of about 30 m (quasimonostatic case) and is no longer encrypted. Usually, in a radar signal processor, the range compression consists of a correlation of the radar channel signal with the heterodyne channel signal delayed for each range resolution cell in the multichannel correlator. In our previous publication [7], it was demonstrated that for GLONASS signal it is not possible to directly correlate the heterodyne channel with the radar channel. For a quick reminder, we briefly discuss the reason below.

The signal received from the GLONASS satellite is a superposition of the C/A code and P-code signals, the spectra of which overlap; the P-code (5.11 MHz bandwidth) is used for the purpose of imaging, as mentioned earlier. If the heterodyne channel is directly correlated with the radar channel, the P-code will be masked by the C/A code at the output of the correlator. The bandwidth of the C/A code is only one-tenth that of the P-code but even if the C/A code of the desired satellite signal is filtered out in the heterodyne channel, the signal correlation properties are degraded by the C/A codes of interfering satellites (It should be noted that this is a peculiarity of only GLONASS signal. In GPS, C/A codes are transmitted on the same carrier frequencies by different satellites. Therefore, the C/A code can be filtered out for all the satellites in the heterodyne channel). It was also demonstrated that, if the radar channel signal is correlated with a locally generated signal containing only the P-code, the effect of the C/A code could be suppressed. However, this technique needs navigation message decoding which, in turn, requires P-code synchronisation. Figure 6 shows the principles of the proposed range compression algorithm.

The synchronisation compromises of tracking the satellite in delay, Doppler, and phase in order to fully decode the

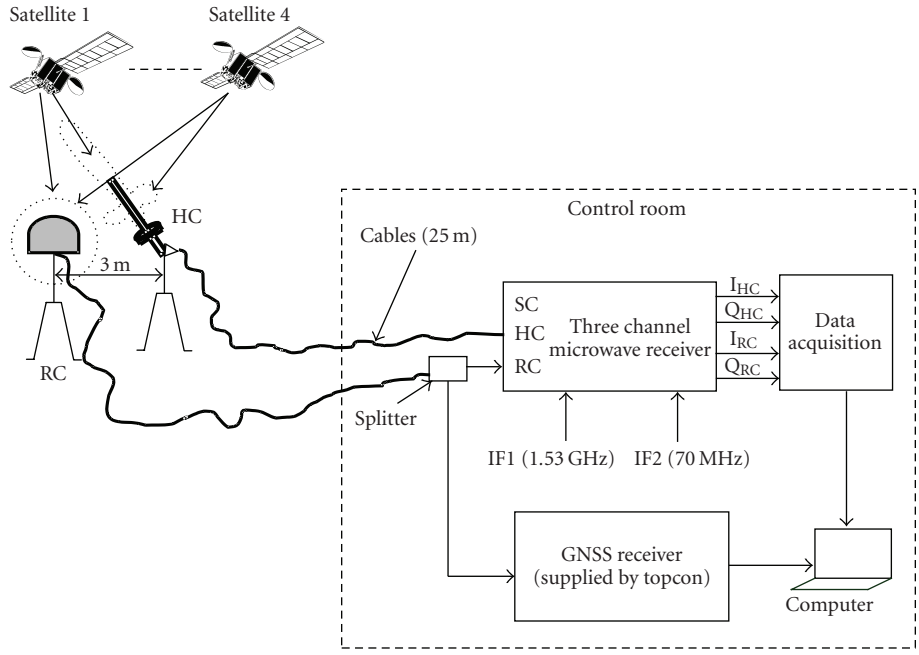

Figure 7: Experimental setup for confirming synchronisation.

navigation message. The "block adjustment of synchronising signal (BASS)" algorithm for Doppler extraction was used. This algorithm is used in software GPS receivers and is comprehensively discussed in [11]. For delay tracking and algorithm based on conventional delayed-locked loop was used [11]. It should be noted that a detailed discussion of the synchronisation algorithms is outside the scope of this paper. Here, we only present the experiment results.

Figure 7 shows the experimental setup for collecting data from the satellite to verify the range compression and synchronisation algorithms. The signal from the satellite was directly received on two channels (radar and heterodyne channels). The radar channel antenna was a stationary omnidirectional antenna (6 dBi gain) and was separated by some 3 m from the heterodyne channel antenna. This topology corresponds to a target at "zero range." For the heterodyne channel, a directional spiral antenna with a gain of 16 dBi was pointed towards the satellite. A satellite transmitting on channel 10 (1607.625 MHz) was used.

Figures 8(a) and 8(b) shows the estimated frequency and delay variation of the satellite. From Figure 8(b), it is seen that the rate of frequency variation is around 0.4 Hz/sec. Figure 8(c) shows the decoded message signal from the P-code after phase tracking. These results confirm the proper functioning of our algorithm. Figure 8(d) represents the correlation obtained from the proposed range compression algorithm shown in Figure 6. It is seen that the algorithm gives a good correlation and confirms our computer modelling result. As expected, the width (first null) of the main lobe is 0.2 microsecond and the RMS sidelobe level of −60 dB for 45 seconds integration time.

6. HETERODYNE CHANNEL DOPPLER COMPENSATION

Figure 9 shows the experimental setups used to verify the imaging algorithm (discussed in the next section). The first setup consisted of stationary heterodyne channel and moving radar channel (for antenna synthesis). The second experiment represents a more practical scenario, where both the heterodyne and radar antennas are moving. It is obvious that the only difference between the two setups is the presence of extra Doppler shift in the moving heterodyne channel. This Doppler shift can be large enough to introduce a complete mismatch between the heterodyne channel and the radar channel. Hence, one needs to compensate the relative motion between transmitter and receiver.

First of all, we consider an instantaneous bistatic triangle formed by the stationary heterodyne channel, shown in Figure 10(a). The three arms of the bistatic triangle are transmitter-to-receiver path (represented by B), transmitter-to-target path (R_T), and target-to-receiver (R_R). Also, the bistatic angle is denoted by β, the transmitter elevation angle by φ, and the angle between B and R_T by θ_{Tr}. For our experimentation with flight imitator we considered targets at short ranges (maximum target range 600 m). The typical transmitter-to-receiver range for GLONASS is $\sim$ 20000 km. Therefore, the angular separation, θ_{Tr}, is negligible. Hence, for a stationary heterodyne channel, the Doppler shifts due to satellite motion (F_S) in the two paths are similar. The residual Doppler variation after range compression is present only due to receiver motion relative to target at R_R. This residual Doppler variation in the radar channel forms the azimuth signature of a target. In the imaging algorithm, an appropriate azimuth compression filter is designed for each range bin accordingly.

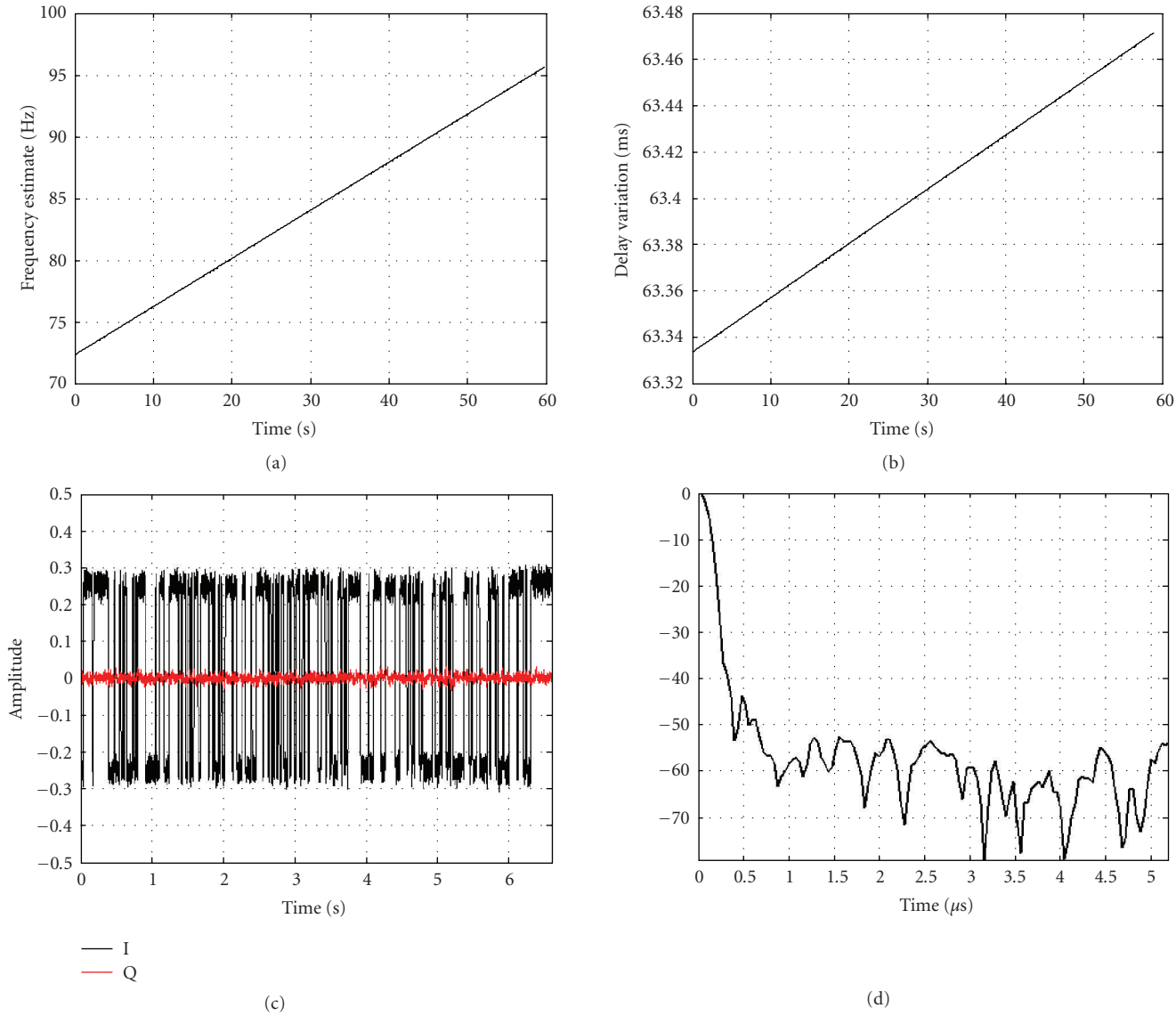

Figure 8: (a) Estimated frequency, (b) estimated delay variation (c), decoded navigation message, and (d) output of range compression algorithm.

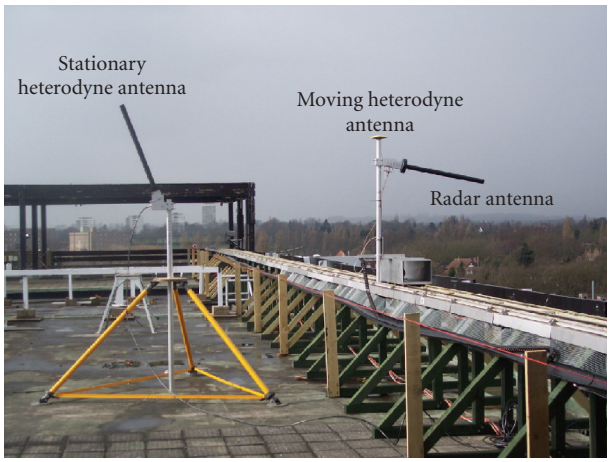

Figure 9: Experimental setups.

In a practical scenario, the heterodyne channel will be in motion as it is mounted on a real aircraft. Figure 10(b) shows the bistatic triangle for moving heterodyne channel. The only difference compared to the stationary case is the additional presence of Doppler variation (F_{RS}) due to receiver motion relative to the satellite in the heterodyne channel. It is clear from the figure that the residual Doppler variation is $F_{RS}+F_R$. The question whether F_{RS} can be ignored when designing the azimuth filter is discussed below.

For 20 seconds integration time, the maximum tolerable frequency difference between the designed azimuth signature and the actual received signal is $\sim$ 0.003 Hz (Considering $\pi/8$ phase difference over the integration time.). The value of F_{RS} can range from 10–100 Hz for an aircraft moving with a velocity of 30 m/sec. Hence, F_{RS} should be estimated and incorporated in the azimuth filter. It should be noted that this problem is not faced in a monostatic SAR as the transmitter

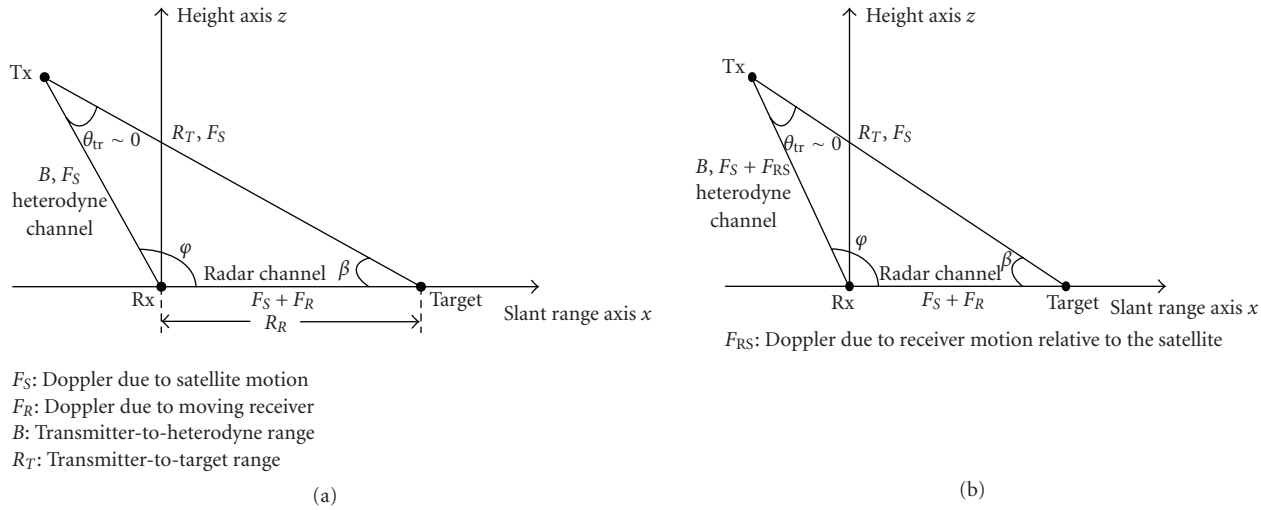

Figure 10: Bistatic triangle for (a) stationary heterodyne and (b) moving heterodyne.

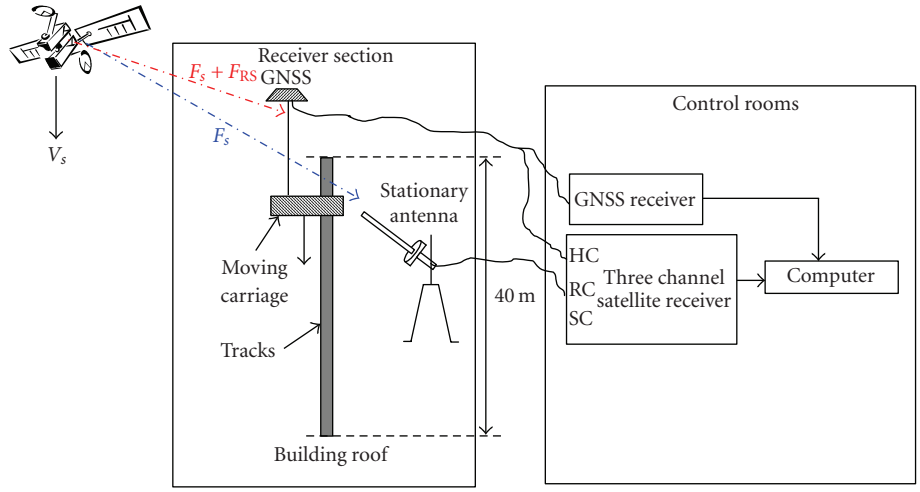

Figure 11: Experimental setup to calculate F_{RS}.

and receiver are colocated. The method we used to estimate F_{RS} is explained in the following section with the aid of an experimental setup.

6.1. Experimental setup to estimate F_{RS} and to verify moving heterodyne synchronisation

Figure 11 shows the experimental setup for collecting data from the GLONASS satellite to estimate F_{RS} and to verify the moving heterodyne synchronisation (We used GLONASS satellite as GALILEO was not available at the time of experimentation. However, this is a generic problem and the analysis can be extended to any transmitter used in SS-BSAR.). The signal from the satellite was directly received on two channels (moving and stationary). The moving channel antenna was an omnidirectional antenna and was separated by some 3 m from the stationary channel antenna. The moving channel corresponds to a moving heterodyne channel and we assume the stationary antenna to be a target at "zero range." In this experiment, we are ignoring the radar channel as the sole aim of the experimentation is to verify whether we can correctly estimate the F_{RS}.

The two channels were simultaneously fed to a microwave receiver that down-converts the received signal through appropriate filtering and amplification. The base-band signal was then stored on a PC for off-line processing. The output of the moving channel is also fed to a second "GNSS receiver." This receiver stores the navigation message of the GPS/GLONASS satellite and receiver observation data. An algorithm was developed that extracts the satellite and the moving antenna positions from the stored data. From this information we calculated the F_{RS}, that is, Doppler variation due to receiver motion relative to the satellite.

To test that whether we have correctly estimated the F_{RS}, first of all we correlated the moving and the stationary channel without compensating F_{RS} from the moving channel. Due to presence of Doppler difference (F_{RS}) between the two channels, one can expect degradation of correlation

function and rise in sidelobe level. Figure 12(a) shows the degradation of correlation function and Figure 12(c) shows a rise in the sidelobe level (dotted line). Figure 12(b) shows the correlations of the two channels after we have removed the F_{RS} from the moving channel. It is seen that after removing the residual Doppler we obtain a good correlation function. As expected, the width (first null) of the main lobe is 0.2 microsecond and the RMS sidelobe level of −64 dB for 35 seconds integration time (Figure 12(c)). Hence, our estimate of F_{RS} is correct.

7. SS-BSAR IMAGING

In this section, a conceptual description of the algorithm used for SS-BSAR image formation will be provided, along with some experimental results. A specific configuration is assumed, where the transmitter is a GNSS satellite and the receiver is airborne. A full description of the algorithm can be found in [12, 13], along with detailed descriptions of algorithms designed for other SS-BSAR configurations. Results of our research in this area can also be found in [14–17].

7.1. Algorithm description

Before proceeding into an explanation of the algorithm, it is perhaps useful to state problems associated with SS-BSAR image formation first. Traditional monostatic SAR algorithms exploit similarities in echo returns from different targets within the illuminated scene in order to reduce the signal processing load. These similarities are usually present in the range or azimuth target signatures and allow efficient processing in the frequency domain. In BSAR, and particularly SS-BSAR, these similarities do not exist. Moreover, the exact relationship between the azimuth-time signature (a chirp signal) of a target and its Doppler frequency spectrum is yet to be calculated analytically (at least without some approximation). These features are impediments to the derivation of efficient and accurate image formation algorithms operating in the frequency domain.

A block diagram of the generalised SS-BSAR image formation algorithm is shown in Figure 13. It may be noticed that it is a modification of the standard Range-Doppler algorithm, widely used in monostatic SAR image formation, and thoroughly described in [18].

The first step in the algorithm is to equalize the Range and Doppler histories of targets residing at the same range from the receiver. This is achieved by applying a single correction function to the SS-BSAR data, which removes the time delay and associated phase due to the transmitter-to-receiver range at each azimuth-time instant. The correction function is integrated with the range compression step, hence the term "modified range compression." The modified range compression is performed in the range-frequency, azimuth-time domain. At the output of this step, the Range and Doppler histories of targets at the same range, but different cross-range becomes very similar for a wide range of possible geometries. Since the transmitter-to-target and receiver-to-target ranges can normally be

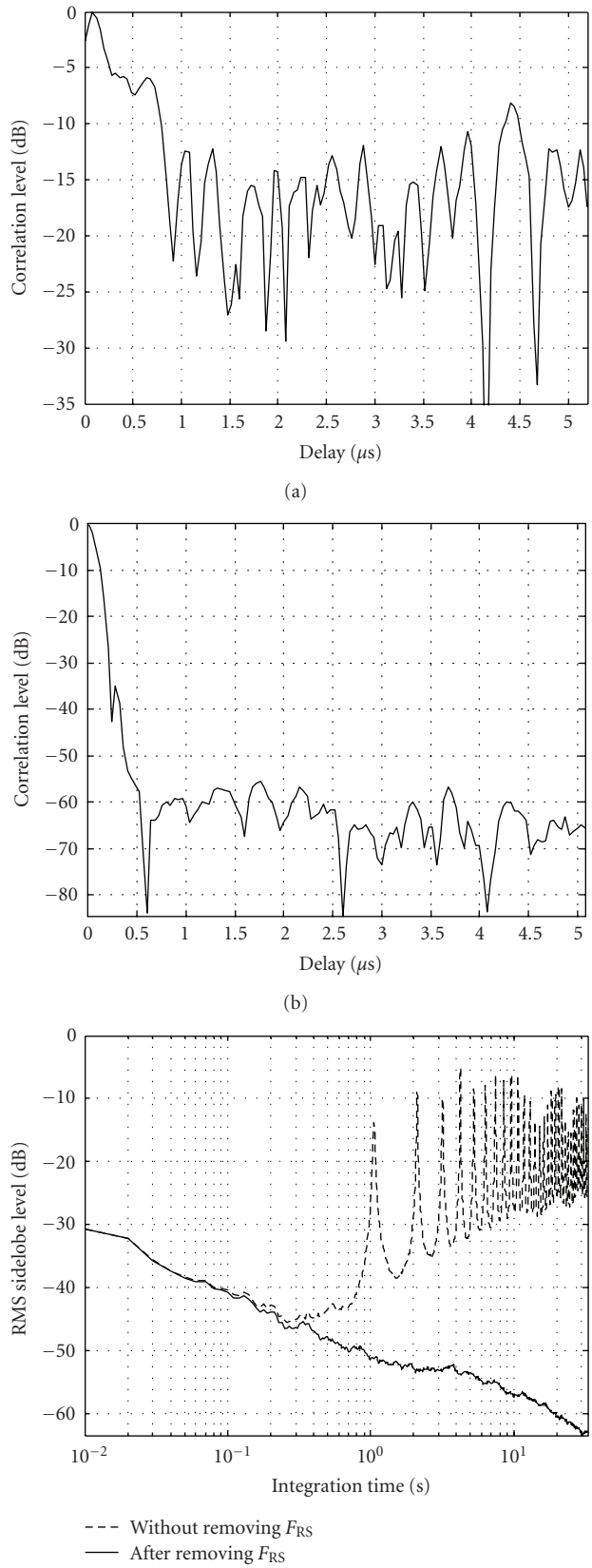

Figure 12: (a) Correlation without removing F_{RS}, (b) correlation after removing F_{RS}, and (c) RMS sidelobe level versus integration time (log scale).

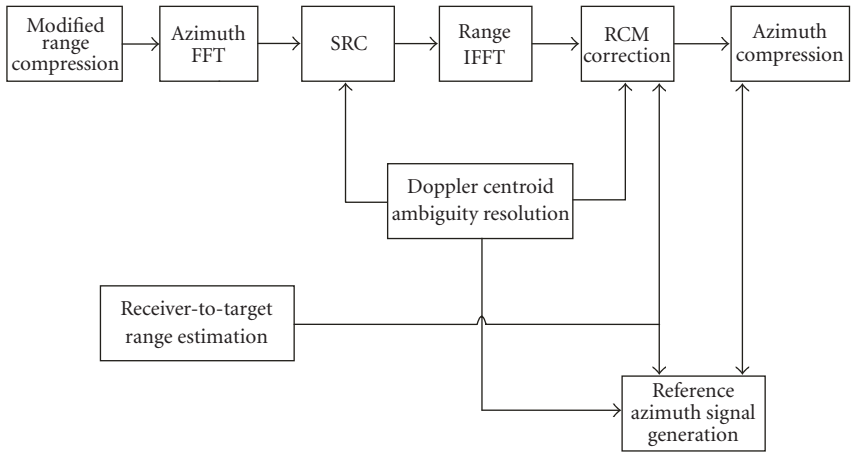

Figure 13: Block diagram of SS-BSAR image formation algorithm.

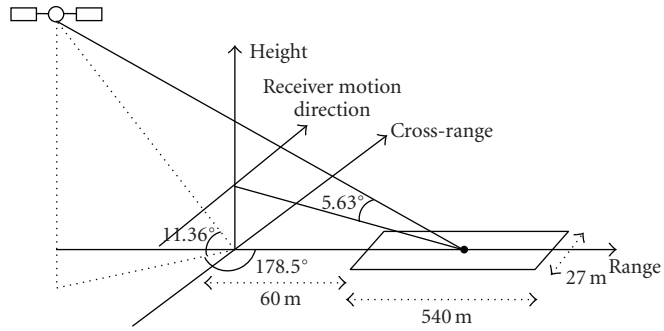

Figure 14: SS-BSAR experiment geometry.

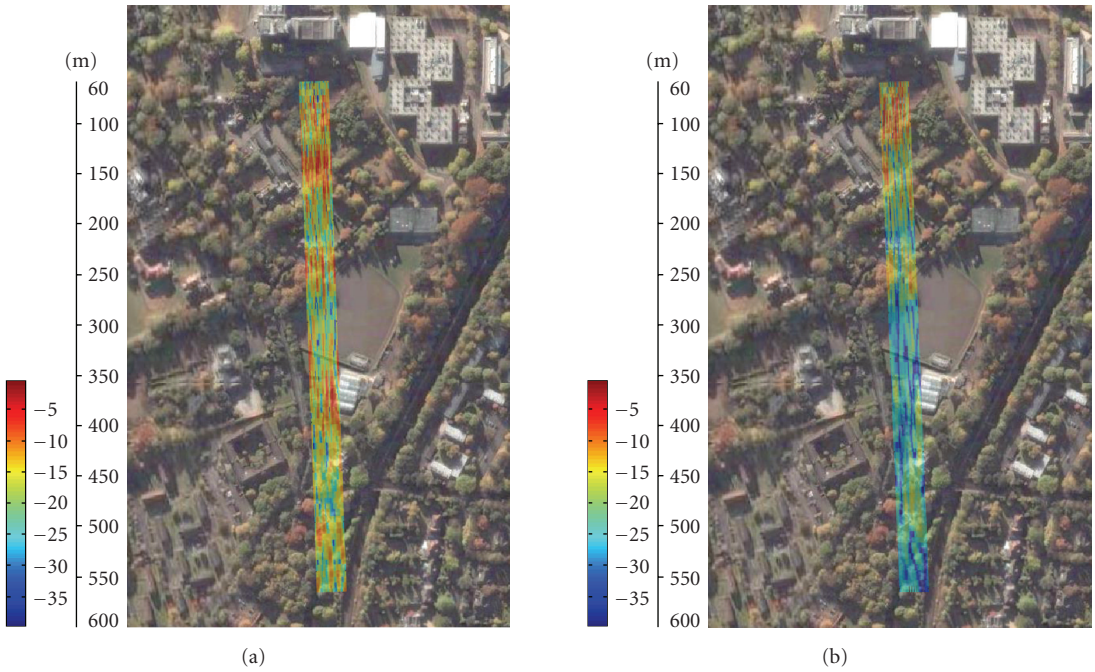

Figure 15: SS-BSAR image for (a) stationary heterodyne and (b) moving heterodyne.

Table 3: Experimental parameters.

Parameter	Stationary heterodyne	Moving heterodyne
GLONASS satellite	COSMOS 2394	COSMOS 2418
Carrier frequency (MHz)	1603.125	1603.125
Signal bandwidth (MHz)	5.11	5.11
Satellite's azimuth angle (degree)	178.49	182
Satellite's elevation angle (degree)	11.36	38
Bistatic angle (degree)	5.63	38
Receiver velocity (m/sec)	0.6	0.6
Receiver's height above the ground (m)	~25	~25
Receiver's aperture length (m)	27	27
Integration time (s)	45	45

approximated using second-order Taylor series expansions in SS-BSAR, it is also possible to derive signal expressions in the frequency domain. Therefore, use of a modification of the Range-Doppler algorithm is a convenient method to form the image of an observation area. A secondary range compression (SRC) is performed in the two-dimensional frequency domain to compensate for the cross-coupling between the range and azimuth frequencies. Before this operation is executed, the Doppler ambiguity is resolved (i.e., because the target azimuth signature could contain a large Doppler centroid outside the range of sampled azimuth frequencies). Range cell migration (RCM) is corrected in the range-time, azimuth-frequency (or Range, Doppler) domain, after RCM components due to the receiver motion and residual RCM after the modified range compression are calculated. For this operation, it is proposed to estimate the receiver-to-target range from the range sum (the difference between the total range history and the transmitter-to-receiver range history) in order to identify the individual RCM components mentioned above. Finally, azimuth compression is performed in the range, Doppler domain.

7.2. Experimental results

In this section, we present the SS-BSAR images obtained by applying the proposed algorithm on experimental data collected from the experimental setups shown in Figure 7. A detailed description of our experimental hardware (including the flight imitator) can be found in [19]. The experimental parameters are shown in Table 3. The geometry of the first experiment is shown in Figure 14.

Figure 15(a) shows the SS-BSAR image obtained for a stationary heterodyne channel (5.63° bistatic angle). The image obtained from the observation area is superimposed on a satellite photograph of the area. The color-scale is in dB, where 0 dB represents the highest processed echo intensity. It is important to note that the heterodyne channel was stationary, so there was no need for the motion compensation described in Section 6. However, the signal synchronisation described in Section 5 was required. Estimates of the satellite's instantaneous Doppler frequency and time delay with respect to the heterodyne antenna (provided by the synchronisation algorithm) were used for the modified range compression. We can see from Figure 15(a) that the intensity variation in the SS-BSAR image obtained corresponds to the variation in the strength of echoes from the observed area. More analysis and verification on the obtained image can be found in [20].

Figure 15(b) shows the SS-BSAR image obtained for moving heterodyne channel (38° bistatic angle). Therefore, all the algorithms described in previous sections (synchronisation, motion compensation, and imaging) were applied to the acquired data. The experimental parameters are also included in Table 3.

Comparing Figures 15(a) with 15(b) shows high level of similarity. Strong reflections at the near field are observed in both images. Also, targets at the range of 240 m, 350 m, 500 m are visible in both images. Figures 16(b) and 16(c) show the strong reflections from the building at 240 m in both images. The dynamic range is almost same in both images, although the signal strength in second image is lower than the first one. This is due to possible bistatic RCS reduction.

Figure 17 shows cross-sections of the building shown in Figure 16(a), taken along the azimuth direction for each of the SS-BSAR images. It is observed that even though the physical characteristics of the building have not changed, image reflectivity has changed. This can be because the imaging geometry between the two acquisitions is different.

8. CONCLUSIONS

This paper gave an overview of the research carried out by University of Birmingham in the area of SS-BSAR, utilising microwave emissions from GNSS transmitters as the ranging signal. GLONASS satellite was used for experimentation.

In the paper, different GNSS transmitters (GPS, GLONASS, and GALILEO) were compared on the basis of resolution and power budget. It was highlighted that GALILEO and the new GPS satellite are the most prospective candidate for SS-BSAR. GALILEO E5 signal has potential range resolution of 3–8 m and can detect targets with 50 m^2 RCS at a range of approximately 5 km. On the other hand, the new GPS signal can also provide the same range resolution, but has 10 times more detection range compared to GALILEO.

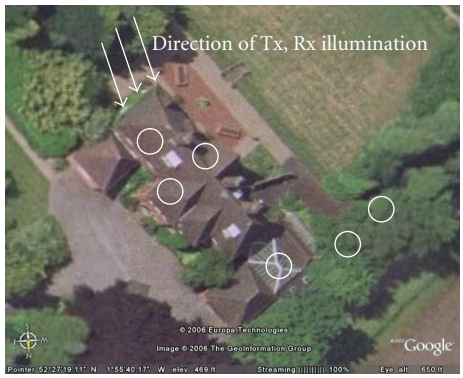

(a)

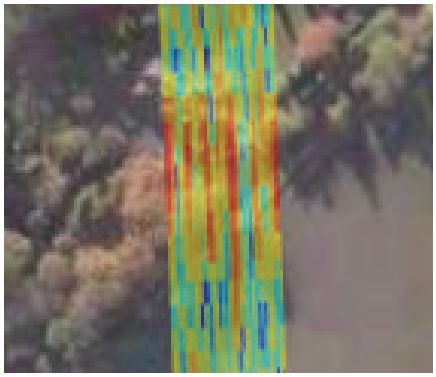

(b)

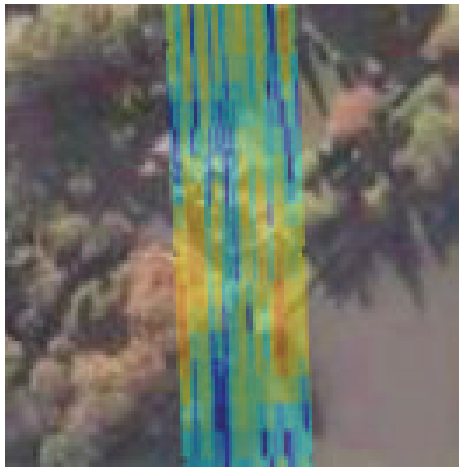

(c)

Figure 16: (a) Aerial photo of building at 240 m, (b) enlargement of image area around the building at 240 m for 10° bistatic angle, and (c) enlargement of image area around the building at 240 m for 40° bistatic angle.

Some of the practical problems (such as interference, signal structure, synchronisation) were also briefly discussed. One of the important problems was moving heterodyne channel. It was discussed that the motion of the heterodyne channel introduces a Doppler shift. This Doppler shift needs to be estimated and incorporated in the azimuth compression filter design. A method to estimate this Doppler shift was described and experimentally verified.

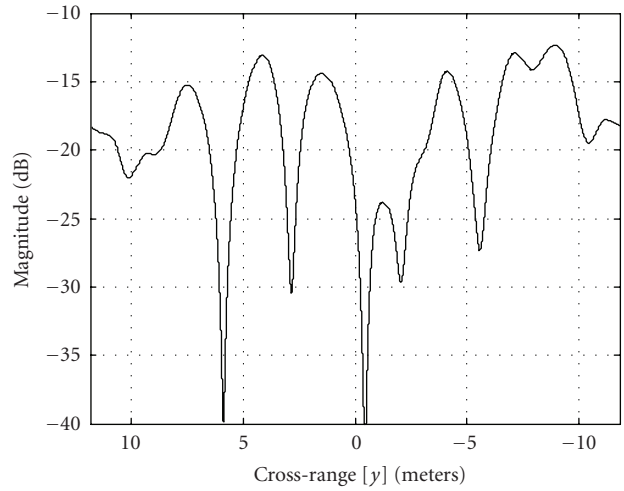

(a)

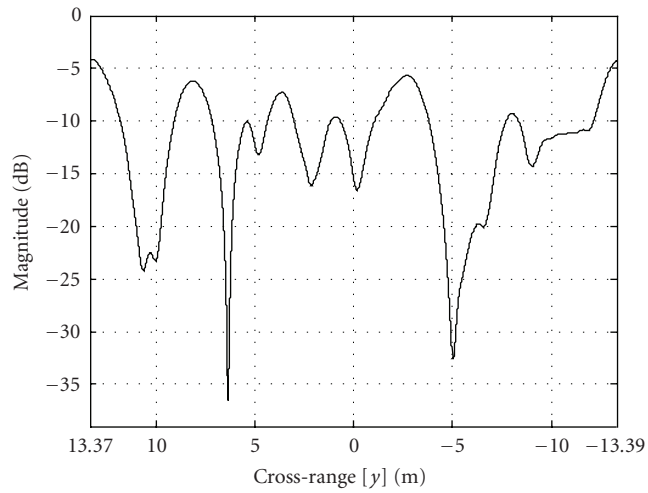

(b)

Figure 17: Azimuth cross-sections taken along the building at 240 m for the (a) moving heterodyne and (b) stationary heterodyne images.

An imaging algorithm for SS-BSAR was briefly discussed and experimentally tested. Using the flight imitator, bistatic images were successfully obtained for moving and stationary heterodyne channel. These images were also briefly analysed. Comparison of moving heterodyne image with that of stationary heterodyne channel showed high level of similarity, suggesting our new (moving heterodyne) configuration is functioning properly. Finally, we can conclude that we can obtain an SS-BSAR image for a moving heterodyne channel. The next stage of our work will concentrate on obtaining image using a real aircraft.

ACKNOWLEDGMENT

The work reported in this paper was funded by the Electro-Magnetic Remote Sensing (EMRS) Defence Technology Centre, established by the UK Ministry of Defence and run

by a consortium of SELEX Sensors and Airborne Systems, Thales Defence, Roke Manor Research, and Filtronic. Project no. 1/27.

REFERENCES

[1] P. Dubois-Fernandez, H. Cantalloube, B. Vaizan, et al., "ONERA-DLR bistatic SAR campaign: planning, data acquisition, and first analysis of bistatic scattering behaviour of natural and urban targets," *IEE Proceedings: Radar, Sonar and Navigation*, vol. 153, no. 3, pp. 214–223, 2006.

[2] I. Walterscheid, J. H. G. Ender, A. R. Brenner, and O. Loffeld, "Bistatic SAR processing and experiments," *IEEE Transactions on Geoscience and Remote Sensing*, vol. 44, no. 10, pp. 2710–2717, 2006.

[3] A. Moccia, N. Chiacchio, and A. Capone, "Spaceborne bistatic synthetic aperture radar for remote sensing applications," *International Journal of Remote Sensing*, vol. 21, no. 18, pp. 3395–3414, 2000.

[4] M. Younis, R. Metzig, and G. Krieger, "Performance prediction of a phase synchronization link for bistatic SAR," *IEEE Geoscience and Remote Sensing Letters*, vol. 3, no. 3, pp. 429–433, 2006.

[5] M. Cherniakov, "Space-surface bistatic synthetic aperture radar—prospective and problems," in *Proceedings of the IEEE International Radar Conference*, no. 490, pp. 22–25, Edinburgh, UK, October 2002.

[6] http://www.en.wilkipedia.org/wiki/GPS_modernization.

[7] M. Cherniakov, R. Saini, M. Antoniou, R. Zuo, and J. Edwards, "SS-BSAR with transmitter of opportunity—practical aspects," in *Proceedings of the 3rd EMRS DTC Technical Conference*, Edinburgh, UK, July 2006.

[8] X. He, M. Cherniakov, and T. Zeng, "Signal detectability in SS-BSAR with GNSS non-cooperative transmitter," *IEE Proceedings: Radar, Sonar and Navigation*, vol. 152, no. 3, pp. 124–132, 2005.

[9] X. He, T. Zeng, and M. Cherniakov, "Interference level evaluation in SS-BSAR with GNSS non-cooperative transmitter," *Electronics Letters*, vol. 40, no. 19, pp. 1222–1224, 2004.

[10] U. Roßbach, *Positioning and navigation using the Russian satellite system GLONASS*, Ph.D. thesis, Universität der Bundeswehr München, Munchen, Germany, 2000.

[11] J. B.-Y. Tsui, *Fundamentals of Global Positioning System Receivers: A Software Approach*, John Wiley & Sons, New York, NY, USA, 2000.

[12] M. Antoniou, *Image formation algorithms for space-surface bistatic SAR*, Ph.D. thesis, University of Birmingham, Birmingham, UK, 2007.

[13] M. Antoniou, M. Cherniakov, and C. Hu, "Space-surface BSAR image formation algorithms," submitted to *IEEE Transactions in Geoscience and Remote Sensing*.

[14] M. Cherniakov, M. Antoniou, R. Saini, R. Zuo, and J. Edwards, "Space-surface BSAR—analytical and experimental study," in *Proceedings of the 6th European Conference on Synthetic Aperture Radar (EUSAR '06)*, Dresden, Germany, May 2006.

[15] M. Antoniou, R. Saini, and M. Cherniakov, "Results of a space-surface bistatic SAR image formation algorithm," *IEEE Transactions on Geoscience and Remote Sensing*, vol. 45, no. 11, pp. 3359–3371, 2007.

[16] M. Antoniou, R. Saini, R. Zuo, and M. Cherniakov, "Image formation algorithm for space-surface BSAR," in *Proceedings of the 4th European Radar Conference (EuRAD '07)*, pp. 413–416, Munich, Germany, October 2007.

[17] M. Antoniou, R. Saini, R. Zuo, and M. Cherniakov, "Space-surface bistatic SAR topology and its impact on image formation," in *Proceedings of the 7th European Conference on Synthetic Aperture Radar (EUSAR '08)*, Friedrichshafen, Germany, June 2008.

[18] I. G. Cumming and F. H. Wong, *Digital Processing of Synthetic Aperture Radar Data: Algorithms and Implementation*, Artech House, Norwood, Mass, USA, 2005.

[19] R. Zuo, *Test bed development for space-surface bistatic SAR investigation*, M.S. thesis, University of Birmingham, Birmingham, UK, October 2005.

[20] M. Cherniakov, R. Saini, R. Zuo, and M. Antoniou, "Space-surface bistatic synthetic aperture radar with global navigation satellite system transmitter of opportunity-experimental results," *IET Radar, Sonar & Navigation*, vol. 1, no. 6, pp. 447–458, 2007.

Hindawi Publishing Corporation
International Journal of Navigation and Observation
Volume 2008, Article ID 810816, 11 pages
doi:10.1155/2008/810816

Research Article

Enhanced Radar Imaging in Uncertain Environment: A Descriptive Experiment Design Regularization Approach

Yuriy Shkvarko,[1] Hector Perez-Meana,[1] and Alejandro Castillo-Atoche[2]

[1] *ESIME, Unidad Culhuacan, Avenida Santa Ana no. 1000, Colonia San Francisco Culhuacan, México D.F., C.P. 04430, Mexico*
[2] *CINVESTAV, Unidad Guadalajara, Avenida Científica no. 1145, Colonia El Bajío, Zapopan, Jalisco, C.P. 45015, Mexico*

Correspondence should be addressed to Alejandro Castillo-Atoche, acastill@uady.mx

Received 4 February 2008; Accepted 29 May 2008

Recommended by M. Greco

A new robust technique for high-resolution reconstructive imaging is developed as required for enhanced remote sensing (RS) with imaging array radar or/and synthetic aperture radar (SAR) operating in an uncertain RS environment. The operational scenario uncertainties are associated with the unknown statistics of perturbations of the signal formation operator (SFO) in turbulent medium, imperfect array calibration, finite dimensionality of measurements, uncontrolled antenna vibrations, and random carrier trajectory deviations in the case of SAR. We propose new descriptive experiment design regularization (DEDR) approach to treat the uncertain radar image enhancement/reconstruction problems. The proposed DEDR incorporates into the minimum risk (MR) nonparametric estimation strategy the experiment design-motivated operational constraints algorithmically coupled with the worst-case statistical performance (WCSP) optimization-based regularization. The MR objective functional is constrained by the WCSP information, and the robust DEDR image reconstruction operator applicable to the scenarios with the low-rank uncertain estimated data correlation matrices is found. We report and discuss some simulation results related to enhancement of the uncertain SAR imagery indicative of the significantly increased performance efficiency gained with the developed approach.

1. INTRODUCTION

Modern applied theory of reconstructive radar imaging is now a mature and well-developed research field, presented and detailed in many works (see, e.g., [1, 2] and references therein). The classical imaging with array radar or SAR implies application of a method called "matched spatial filtering" to process the recorded data signals [1, 3, 4]. Stated formally [1], such a method implies application of the adjoint signal formation operator (SFO) to the recorded data, squared detection of the filter outputs, and their averaging over the actually recorded samples (the so-called snapshots [5]) of the independent data observations. Although a number of authors have proposed different linear and nonlinear postprocessing approaches to enhance the images formed using such matched estimator (see, e.g., [3, 5–8]), all those are not a direct inference from the Bayesian statistically optimal estimation theory [4]. Other approaches had focused primarily on designing the constrained regularization techniques for improving the resolution of the closely spaced components in the power spatial spectrum pattern (SSP) obtained by ways different from the matched spatial filtering [9–12], but again without aggregating the regularization principles with the minimum risk estimation strategy. Although the existing theory offers a manifold of statistical and descriptive regularization techniques for reconstructive imaging, in many application areas there still remain some unresolved crucial theoretical and processing problems related to large scale sensor array radar/SAR reconstructive imaging in *uncertain* operational scenarios.

The predominant challenge of this study is to solve the SSP reconstruction problem in context of the uncertain environment. Thus, the problem of enhanced imaging of the extended large-scale scenes remotely sensed with an array radar/SAR operating in the *uncertain* remote sensing (RS) environment is stated and treated as an ill-conditioned statistical nonlinear inverse problem. The operational uncertainties are associated with the unknown statistics of perturbations of the SFO in the turbulent medium, imperfect array calibration, finite dimensionality of measurements, uncontrolled antenna vibrations, and random carrier trajectory deviations in the case of SAR. New descriptive experiment

design regularization (DEDR) approach to radar imaging in the uncertain environment is addressed to perform the enhanced reconstruction of the power spatial spectrum pattern (SSP) of the scattered wavefield from the uncertain data measurements. The proposed DEDR incorporates into the minimum risk (MR) nonparametric estimation strategy the DEDR-motivated constraints of the observability of the initial scene scattering wavefield algorithmically coupled with the worst-case statistical performance (WCSP) optimization-based regularization. The MR objective function is constrained by the WCSP information, and the DEDR technique for robust image reconstruction applicable to the scenarios with the low-rank uncertain estimated data correlation matrices is found. Pursuing such an approach, we establish a family of the robust DEDR-related estimators that encompass a manifold of the imaging techniques ranging from traditional array matched spatial filtering to new DEDR-related robust adaptive array beamforming. We also present the robust DEDR-related imaging algorithms that manifest enhanced resolution of the reconstructed array images with substantially decreased computational load. The efficiency of two general DEDR-related algorithms (the robust spatial filtering (RSF) algorithm and the robust adaptive spatial filtering (RASF) algorithm) is illustrated through computer simulations of reconstructing the digital images provided with the SAR operating in some typical uncertain remote sensing scenarios.

2. DESCRIPTIVE EXPERIMENT DESIGN REGULARIZATION FORMALISM

2.1. Problem model

Consider a coherent RS experiment in a random medium and the narrowband assumption [1, 4, 6] that enables us to model the extended object backscattered field by imposing its time invariant complex scattering (backscattering) function $e(\mathbf{x})$ in the scene domain (scattering surface) $X \ni \mathbf{x}$. The measurement data wavefield $u(\mathbf{y}) = s(\mathbf{y}) + n(\mathbf{y})$ consists of the echo signals s and additive noise n and is available for observations and recordings within the prescribed time-space observation domain $Y = T \times P$, where $\mathbf{y} = (t, \mathbf{p})^{\mathrm{T}}$ defines the time-space points in Y. The model of the observation wavefield u is defined by specifying the stochastic equation of observation (EO) of an operator form [1, 13]: $u = \widetilde{S}e + n$; $e \in \mathrm{E}$; $u, n \in \mathrm{U}$; $\widetilde{S} : \mathrm{E} \to \mathrm{U}$, in the Hilbert signal spaces E and U with the metrics structures induced by the inner products, $[u_1, u_2]_{\mathrm{U}} = \int_Y u_1(\mathbf{y}) u_2^*(\mathbf{y}) d\mathbf{y}$ and $[e_1, e_2]_{\mathrm{E}} = \int_X e_1(\mathbf{x}) e_2^*(\mathbf{x}) d\mathbf{x}$, respectively. The operator model of the stochastic EO in the conventional integral form [1, 13] may be written as

$$u(\mathbf{y}) = (\widetilde{S}e(\mathbf{x}))(\mathbf{y}) + n(\mathbf{y}) = \int_X \widetilde{S}(\mathbf{y}, \mathbf{x}) e(\mathbf{x}) d\mathbf{x} + n(\mathbf{y}). \quad (1)$$

The random functional kernel $\widetilde{S}(\mathbf{y}, \mathbf{x})$ of the stochastic integral SFO $\widetilde{S}$ given by (1) defines the signal wavefield formation model. Its mean, $S(\mathbf{y}, \mathbf{x}) = \langle \widetilde{S}(\mathbf{y}, \mathbf{x}) \rangle$, is referred to as the nominal SFO in the RS measurement channel specified by the time-space modulation of signals employed in a particular radar system [3, 8] and the variations about the mean $\delta S(\mathbf{y}, \mathbf{x}) = \widetilde{S}(\mathbf{y}, \mathbf{x}) - S(\mathbf{y}, \mathbf{x})$ model the model uncertainties and random perturbations of the wavefield at different propagation paths (the so-called extended Rytov's model [1]).

We assume an incoherent nature of the backscattered field $e(\mathbf{x})$. This is naturally inherent to the RS experiments and leads to the δ-form of the object field correlation function, $R_e(\mathbf{x}, \mathbf{x}') = b(\mathbf{x})\delta(\mathbf{x} - \mathbf{x}')$, where $e(\mathbf{x})$ and $b(\mathbf{x}) = \langle |e(\mathbf{x})|^2 \rangle$ are referred to as the scene random complex scattering function and its average power scattering function or spatial spectrum pattern (SSP), respectively. The radar imaging problem is to derive an estimate $\widehat{b}(\mathbf{x})$ of the SSP

$$b(\mathbf{x}) = (\mathcal{B}e)(\mathbf{x}) = \mathrm{Aver}^{(2)}\{e(\mathbf{x})\} = \langle e(\mathbf{x}) e^*(\mathbf{x}) \rangle \quad (2)$$

(referred to as the desired RS image) by processing the available finite dimensional array radar/SAR measurements of the data wavefield $u(\mathbf{y})$, where $\mathcal{B}$ defines the second-order statistical averaging operator.

2.2. Projection formalism for data representation

Viewing it as an approximation problem leads one to a projection concept for a reduction of the data field $u(\mathbf{y})$ to the M-D spatial-temporal data recordings:

$$\mathbf{u} = \underset{m}{\mathrm{vec}}\{u_m = [u, h_m]_{\mathrm{U}};\ m = 1, \ldots, M\} \quad (3)$$

composed of the expansion/decomposition coefficients $\{u_m = [u, h_m]_{\mathrm{U}};\ m = 1, \ldots, M\}$, where $\{h_m(\mathbf{y})\}$ defines the set of orthogonal normalized basis functions in the M-D data approximation subspace $\mathrm{U}_{(M)} = P_{\mathrm{U}(M)}\mathrm{U}$ [13]. These are defined via corresponding compositions of the calibrated antenna array tapering functions and sampling filters that explicitly specify the corresponding data projection operator $P_{\mathrm{U}(M)}$ (see [13–15] for details).

In analogy to (3), one can define now the K-D vector-form approximation of the scene random scattering function as follows:

$$\mathbf{e} = \underset{k}{\mathrm{vec}}\{e_k = [e, g_k]_{\mathrm{E}};\ k = 1, \ldots, K\}. \quad (4)$$

The elements of vector (4) are composed of the decomposition coefficients $\{e_k = [e, g_k]_{\mathrm{E}};\ k = 1, \ldots, K\}$ with respect to some chosen normalized orthogonal set of expansion functions $\{g_k(\mathbf{x})\}$ that span such K-D signal approximation subspace $\mathrm{E}_{(K)} = P_{\mathrm{E}(K)}\mathrm{E}$ and specify the corresponding scene wavefield projection operator $P_{\mathrm{E}(K)}$.

The descriptive experiment design (DED) aspects of the SSP reconstruction problem involving the analysis of how to choose the basis functions $\{g_k(\mathbf{x})\}$ that span the signal representation subspace $\mathrm{E}_{(K)} = P_{\mathrm{E}(K)}\mathrm{E} = \mathrm{Span}\{g_k\}$ for a given observation subspace $\mathrm{U}_{(M)} = \mathrm{Span}\{h_m\}$ were investigated in more details in the previous studies [13, 15]. Following [15], in the rest of this study, we consider the conventional (i.e., ordinary rectangular pixel format) representation basis over a $K_{x2} \times K_{x1}$ regular pixel-formatted lattice [14, 16],

where K_{x1} defines the dimension of the rectangular grid over the horizontal (azimuth) coordinate x_1, and K_{x2} defines its dimension over the orthogonal (range) coordinate x_2 (the number of the slant range gates projected onto the scene frame). Such regular lattice of points is next specified by the ordered multi-index $k = (k_{x1}, k_{x2})$; $k_{x1} = 1, \ldots, K_{x1}$; $k_{x2} = 1, \ldots, K_{x2}$; $k = 1, \ldots, K = K_{x1} \times K_{x2}$.

2.3. Uncertain finite-dimensional observations

In the DED formalism, an imperfect calibration of the array (due to displacements of some array elements with respect to the presumed nominal positions, as well as distorted antennas shapes [4, 9]) is attributed to the unknown disturbances $\{\delta h_m; m = 1, \ldots, M\}$ in the decomposition functions $\{\widetilde{h}_m = h_m + \delta h_m\}$ in (3). In imaging SAR applications, such disturbances incorporate the deviations of a carrier from the nominal trajectory and antenna vibration [3, 17]. These disturbances and propagation perturbations result in the uncertain SFO matrix:

$$\widetilde{\mathbf{S}} = \mathbf{S} + \mathbf{\Delta}. \tag{5}$$

In (5), the nominal $M \times K$ SFO matrix $\mathbf{S}$ is composed of the elements $\{S_{mk} = [Sg_k, h_m]_U\}$, while all problem model uncertainties are attributed to the distortion term, in which the elements of the uncertainty matrix $\mathbf{\Delta}$ are treated as unknown values (realizations of random variables) with an unknown probability density function (pdf) $p(\mathbf{\Delta})$.

2.4. Vector-form equation of observation

Now, we proceed from the stochastic integral-form EO (1) to its finite-dimensional approximation (vector) form:

$$\mathbf{u} = \widetilde{\mathbf{S}}\mathbf{e} + \mathbf{n} = \mathbf{S}\mathbf{e} + \mathbf{\Delta}\mathbf{e} + \mathbf{n}, \tag{6}$$

in which the disturbed SFO matrix is defined by (5), and $\mathbf{e}$, $\mathbf{n}$, $\mathbf{u}$ represent zero-mean vectors composed of the decomposition coefficients e_k, n_m, and u_m, respectively. These vectors are characterized by the correlation matrices: $\mathbf{R_e} = \mathbf{D} = \mathbf{D}(\mathbf{b}) = \mathrm{diag}\{\mathbf{b}\}$ (a diagonal matrix with vector $\mathbf{b}$ at its principal diagonal), $\mathbf{R_n}$, and $\mathbf{R_u} = \langle \widetilde{\mathbf{S}}\mathbf{R_e}\widetilde{\mathbf{S}}^{+} \rangle_{p(\Delta)} + \mathbf{R_n}$, respectively, where $\langle \cdot \rangle_{p(\Delta)}$ defines the averaging performed over the randomness of $\mathbf{\Delta}$ characterized by the *unknown* probability density function $p(\mathbf{\Delta})$. Vector $\mathbf{b}$ is composed of the elements, $b_k = \mathcal{B}(e_k) = \langle e_k e_k^* \rangle = \langle |e_k|^2 \rangle$; $k = 1, \ldots, K$ and is referred to as a K-D vector-form representation of the SSP.

We refer to the estimate, $\widehat{\mathbf{b}}$, as a discrete-form representation of the desired SSP, that is, the brightness image of the wavefield sources distributed over the pixel-formatted object scene remotely sensed with an employed array radar/SAR. Thus, the uncertain SSP reconstruction problem can be reformulated now as follows: to derive an estimator for reconstructing the K-D approximation:

$$\widehat{b}_{(K)}(\mathbf{x}) = \sum_{k=1}^{K} \widehat{b}_k \left| g_k(\mathbf{x}) \right|^2 = \mathbf{g}^T(\mathbf{x}) \mathrm{diag}\{\widehat{\mathbf{b}}\} \mathbf{g}(\mathbf{x}) \tag{7}$$

of the SSP distribution in the environment $X \ni \mathbf{x}$. Note that in applications, we employ the ordinary pixel expansion format [16], while all theoretical results are valid also for any feasible decomposition function basis, $\mathbf{g}(\mathbf{x}) = \underset{k}{\mathrm{vec}}\{g_k(\mathbf{x})\}$, in (7).

3. DEDR STRATEGY

3.1. Formulation of DEDR estimation strategy

In the descriptive statistical formalism, the desired SSP vector $\widehat{\mathbf{b}}$ is recognized to be a vector of the principal diagonal of an estimate of the correlation matrix $\mathbf{R_e}(\mathbf{b})$, that is, $\widehat{\mathbf{b}} = \{\widehat{\mathbf{R}}_\mathbf{e}\}_{\mathrm{diag}}$. Thus, one can seek to estimate the desired SSP $\widehat{b}_{(K)}(\mathbf{x}) = \mathbf{g}^T(\mathbf{x}) \mathrm{diag}\{\widehat{\mathbf{b}}\} \mathbf{g}(\mathbf{x})$ given the data correlation matrix $\mathbf{R_u}$ pre-estimated via averaging of some J independent sampled correlations [6]:

$$\mathbf{Y} = \widehat{\mathbf{R}}_\mathbf{u} = \underset{j \in J}{\mathrm{aver}}\{\mathbf{u}_{(j)}\mathbf{u}_{(j)}^{+}\} = \frac{1}{J}\sum_{j=1}^{J} \mathbf{u}_{(j)}\mathbf{u}_{(j)}^{+}, \tag{8}$$

and determining the solution operator (SO) $\mathbf{F}$ such that

$$\widehat{b}_{(K)}(\mathbf{x}) = \mathbf{g}^T(\mathbf{x}) \mathrm{diag}\{\{\mathbf{F}\mathbf{Y}\mathbf{F}^{+}\}_{\mathrm{diag}}\} \mathbf{g}(\mathbf{x}). \tag{9}$$

To optimize the search for the desired SO $\mathbf{F}$, we formulate here the following DEDR strategy:

$$\mathbf{F} = \arg\min_{\mathbf{F}} \{\mathfrak{R}(\mathbf{F})\} \tag{10}$$

$$\text{subject to} \quad \left\langle \|\mathbf{\Delta}\|^2 \right\rangle_{p(\Delta)} \le \delta, \tag{11}$$

where the conditioning term represents the worst-case statistical performance (WCSP) regularizing constraint imposed on the unknown second-order statistics $\langle \|\mathbf{\Delta}\|^2 \rangle_{p(\Delta)}$ of the random distortion component $\mathbf{\Delta}$ of the SFO matrix (5), and the DEDR "generalized risk" function is defined as

$$\mathfrak{R}(\mathbf{F}) = \mathrm{tr}\left\{ \left\langle (\mathbf{F}\widetilde{\mathbf{S}} - \mathbf{I})\mathbf{A}(\mathbf{F}\widetilde{\mathbf{S}} - \mathbf{I})^{+} \right\rangle_{p(\Delta)} \right\} + \alpha \mathrm{tr}\{\mathbf{F}\mathbf{R_n}\mathbf{F}^{+}\}, \tag{12}$$

where superscript + defines conjugate transpose. The DEDR strategy (10), (11) implies the minimization of the α-weighted sum of the systematic error measure (specified by the first term in the risk function (12)) and noise error (specified by the second term in the risk function (12)) in the desired RSS estimate (9), in which the unknown disturbances of the SFO are treated through the WCSP bounding constraint (11) imposed onto the averaged squared norm of $\mathbf{\Delta}$. The selections (adjustments) of the regularization parameter α and the diagonal-form weight matrix $\mathbf{A}$ (the so-called metrics inducing matrix [13, 16]) with the diagonal composed of positive numbers $\{a_{kk} > 0; k = 1, \ldots, K\}$ provide the additional DEDR "degrees of freedom" assigning the weights a_{kk} to the particular SSP vector components b_k. These weights $\{a_{kk}\}$ are the user-defined parameters that may incorporate any descriptive metrics properties of a solution [7, 8, 16]. In the simplest case of no preference

to reconstruction of particular SSP components over the observation scene frame, the uniform metrics is typically induced by setting $\mathbf{A} = \mathbf{I}$, that is, the identity matrix. In Section 3.2, we will consider the adaptive DEDR case and specify the corresponding solution-dependent $\mathbf{A}$. Nevertheless, independent on any feasible choice of α, $\mathbf{A}$ in the risk function (12), the conditional optimization problem (10), (11) can be reformulated as

$$\mathbf{F} = \arg\min_{\mathbf{F}} \max_{\langle \|\boldsymbol{\Delta}\|^2 \rangle_{p(\Delta)} \le \delta} \{\Re(\mathbf{F})\}. \tag{13}$$

3.2. Decomposition of DEDR risk

To proceed with the derivation of the estimator (9), (13), we now decompose the risk (12) incorporating directly the WCSP uncertainty constraint into the DEDR strategy. The first term in the risk function (12) specifies the systematic error component as it measures "how far" the desired SO $\mathbf{F}$ is from the pseudoinverse of $\widetilde{\mathbf{S}}$ in the averaged operator metrics. We next, decompose this term into the following:

$$\mathrm{tr}\left\{\left\langle (\mathbf{F}\widetilde{\mathbf{S}} - \mathbf{I})\mathbf{A}(\mathbf{F}\widetilde{\mathbf{S}} - \mathbf{I})^{+}\right\rangle_{p(\Delta)}\right\} = \|\mathbf{FS} - \mathbf{I}\|_{\mathbf{A}}^2 + \langle \|\mathbf{F}\boldsymbol{\Delta}\|_{\mathbf{A}}^2 \rangle_{p(\Delta)}, \tag{14}$$

where $\|\mathbf{C}\|_{\mathbf{A}}^2 = \mathrm{tr}\{\mathbf{CAC}^{+}\}$ denotes the $\mathbf{A}$-weighted squared operator norm of a matrix, $\mathbf{C}$. The second term in (14) has the statistical meaning of the average noise energy in the resulting solution (9); hence it specifies the fluctuation error measure. This term can be bounded applying the Loewner ordering [16] of the weight matrix $\mathbf{A} \le \gamma\mathbf{I}$ with the Loewner ordering factor $\gamma = \min\{\overline{\gamma} : \mathbf{A} \le \overline{\gamma}\mathbf{I}\} > 0$ that yields

$$\langle \|\mathbf{F}\boldsymbol{\Delta}\|_{\mathbf{A}}^2 \rangle \le \gamma \langle \|\mathbf{F}\boldsymbol{\Delta}\|^2 \rangle \le \gamma \|\mathbf{F}\|^2 \langle \|\boldsymbol{\Delta}\|^2 \rangle, \tag{15}$$

where the second inequality follows from the Cauchy-Schwarz inequality [16], and $\|\mathbf{C}\|^2 = \|\mathbf{C}\|_{\mathbf{I}}^2 = \mathrm{tr}\{\mathbf{CC}^{+}\}$ defines a conventional squared norm of a matrix, $\mathbf{C}$. Using the constraint (11), we next evaluate the maximum value that may take the last term in the inequality (15), that is,

$$\max_{\langle \|\boldsymbol{\Delta}\|^2 \rangle_{p(\Delta)} \le \delta} \left\{\gamma \|\mathbf{F}\|^2 \langle \|\boldsymbol{\Delta}\|^2 \rangle_{p(\Delta)}\right\} = \varepsilon \|\mathbf{F}\|^2 \tag{16}$$

valid for any given bounding factor $\varepsilon = \delta\gamma \ge 0$. With this evaluation (16), the WCSP-constrained DEDR strategy (13) is transformed into the following nonconstrained optimization problem:

$$\mathbf{F} = \arg\min_{\mathbf{F}} \{\Re_{\mathrm{DEDR}}(\mathbf{F})\} \tag{17}$$

with the *aggregated* DEDR risk functional:

$$\{\Re_{\mathrm{DEDR}}(\mathbf{F})\} = \mathrm{tr}\{(\mathbf{FS} - \mathbf{I})\mathbf{A}(\mathbf{FS} - \mathbf{I})^{+}\} + \alpha \mathrm{tr}\{\mathbf{F}\mathbf{R}_{\Sigma}\mathbf{F}^{+}\}, \tag{18}$$

where

$$\mathbf{R}_{\Sigma} = \mathbf{R}_{\Sigma}(\beta) = (\mathbf{R}_{\mathbf{n}} + \beta\mathbf{I}); \quad \beta = \frac{\varepsilon}{\alpha} \ge 0. \tag{19}$$

4. DEDR ESTIMATORS OF SSP

4.1. General-form SSP estimator

Routinely solving the minimization problem (17), we obtain the desired DEDR-optimal SO:

$$\mathbf{F}_{\mathrm{DEDR}} = \mathbf{K}_{\mathbf{A},\alpha,\beta}\mathbf{S}^{+}\mathbf{R}_{\Sigma}^{-1} \tag{20}$$

with the self-adjoint robust reconstruction operator:

$$\mathbf{K}_{\mathbf{A},\alpha,\beta} = \left(\mathbf{S}^{+}\mathbf{R}_{\Sigma}^{-1}(\beta)\mathbf{S} + \alpha\mathbf{A}^{-1}\right)^{-1} \tag{21}$$

dependent on three degrees of freedom: α, β, and $\mathbf{A}$.

Note, that the derived robust SO (20) involves the Hermitian conjugate $\mathbf{S}^{+}$ of the regular SFO $\mathbf{S}$ (i.e., it satisfies the DED-observability requirements [15]) and does not involve the inversion of $\mathbf{Y}$ (i.e., it is applicable to the reconstructive SAR imaging problems with only one-recorded realization of the trajectory data signal available for further processing, $J = 1$).

The general-form DEDR-optimal SO (20) enables us now to derive the corresponding general-form robust SSP estimator putting (20) into (9) that yields

$$\begin{aligned}\widehat{b}_{(K)}(\mathbf{x}) &= \widehat{b}_{(K)}(\mathbf{x} \mid \mathbf{A}, \alpha, \beta) \\ &= \mathbf{g}^{T}(\mathbf{x})\mathrm{diag}\left\{\{\mathbf{K}_{\mathbf{A},\alpha,\beta}\mathbf{S}^{+}\mathbf{R}_{\Sigma}^{-1}(\beta)\mathbf{Y}\mathbf{R}_{\Sigma}^{-1}(\beta)\mathbf{S}\mathbf{K}_{\mathbf{A},\alpha,\beta}\}_{\mathrm{diag}}\right\}\mathbf{g}(\mathbf{x}).\end{aligned} \tag{22}$$

This general-form DEDR estimator for the SSP can also be represented in the alternative form as

$$\widehat{b}_{(K)}(\mathbf{x}) = \mathbf{g}^{T}(\mathbf{x})\mathrm{diag}\left\{\left\{\mathbf{K}_{\mathbf{A},\alpha,\beta}\operatorname*{aver}_{j\in J}\{\mathbf{q}_{(j)}\mathbf{q}_{(j)}^{+}\}\mathbf{K}_{\mathbf{A},\alpha,\beta}\right\}_{\mathrm{diag}}\right\}\mathbf{g}(\mathbf{x}), \tag{23}$$

where $\mathbf{q}_{(j)} = \mathbf{S}^{+}\mathbf{R}_{\Sigma}^{-1}\mathbf{u}_{(j)}$ is recognized to be an output of the DEDR-regularized matched spatial processing algorithm with noise whitening that assumes the given composed correlation matrix, $\mathbf{R}_{\Sigma} = \mathbf{R}_{\Sigma}(\beta)$. In practical RS scenarios, it is a common practice [3–5, 14] to accept the robust white observation noise model, that is, $\mathbf{R}_{\mathbf{n}}^{-1} = (1/N_0)\mathbf{I}$ and treat the noise intensity N_0 together with the uncertainty factor β in the composed model of $\mathbf{R}_{\Sigma}$ defined by (19).

4.2. Family of the DEDR-related algorithms

A family of the DEDR-related algorithms for estimating the SSP can be derived now from (22) via controlling the regularization parameters α, β, and the weight matrix $\mathbf{A}$ that constitute the degrees of freedom of the developed DEDR method.

4.2.1. Robust spatial filtering algorithm

Consider the white zero-mean noise in observations and no preference to any prior model information, that is, putting $\mathbf{A} = \mathbf{I}$. Let the regularization parameter be adjusted as the

Table 1: IOSNR gained with different DEDR-related reconstruction algorithms (results are reported for the first uncertain operational scenario and second scene).

Scenario 1: $\Delta\Psi_a^{(1)}(x_1) = 10$; $\Delta\Psi_r(x_2) = 3$; $k_\Delta = \beta/N_0 = 0.1$				
μ [dB]	Nonconstrained RSF IOSNR$^{(2)}$	Constrained RSF IOSNR$^{(3)}$	Nonconstrained RASF IOSNR$^{(4)}$	Constrained RASF (WCSP-optimized) IOSNR$^{(5)}$
5	1.85	2.158	2.2	2.45
10	2.4	2.68	2.32	2.89
15	2.56	2.76	2.67	3.4
20	2.73	3.37	3.02	4.2
25	3.47	4.23	3.1	5.32
30	3.85	4.95	3.64	5.46

Table 2: IOSNR gained with different DEDR-related reconstruction algorithms (results are reported for the second uncertain operational scenario and second scene).

Scenario 2: $\Delta\Psi_a^{(1)}(x_1) = 14$; $\Delta\Psi_r(x_2) = 6$; $k_\Delta = \beta/N_0 = 0.05$				
μ [dB]	Nonconstrained RSF IOSNR$^{(2)}$	Constrained RSF IOSNR$^{(3)}$	Nonconstrained RASF IOSNR$^{(4)}$	Constrained RASF (WCSP-optimized) IOSNR$^{(5)}$
5	1.71	2.17	1.9	2.41
10	1.85	2.61	1.92	2.88
15	1.9	2.9	2.2	3.45
20	1.93	3.4	2.18	4.16
25	2.01	3.78	2.6	4.56
30	2.11	4.3	3.08	5.32

inverse of the signal-to-noise ratio (SNR), that is, $\alpha = (N_0 + \beta)/b_0$, where b_0 is the prior average gray level of the SSP, and the uncertainty factor β is attributed to α. In that case, the SO $\mathbf{F}$ is recognized to be the Tikhonov-type robust spatial filter (RSF):

$$\mathbf{F}_{\mathrm{RSF}} = \left(\mathbf{S}^{+}\mathbf{S} + \left((N_0 + \beta)/b_0\right)\mathbf{I}\right)^{-1}\mathbf{S}^{+}. \tag{24}$$

4.2.2. Matched spatial filtering algorithm

Consider the model from the previous example for an assumption, $\alpha \gg \|\mathbf{S}^{+}\mathbf{S}\|$, that is, the case of a priority of the second error measure (suppression of noise) over the systematic error in the optimization problem (17). In this case, we can roughly approximate (20), (24) as the matched spatial filter (MSF):

$$\mathbf{F}_{\mathrm{MSF}} \approx \text{const. } \mathbf{S}^{+}, \tag{25}$$

where the normalizing constant is irrelevant as it specifies the constant image scaling factor that does not influence the overall reconstructed image pattern.

4.2.3. Robust adaptive spatial filtering algorithm

Consider the case of an arbitrary zero-mean noise with the composed correlation matrix $\mathbf{R}_\Sigma$, equal importance of two error measures in (18), that is, $\alpha = 1$, and the solution-dependent weight matrix $\mathbf{A} = \widehat{\mathbf{D}} = \mathrm{diag}\{\widehat{\mathbf{b}}\}$. In this case, the SO becomes the robust adaptive (i.e., solution-dependent) spatial filter (RASF) operator:

$$\mathbf{F}_{\mathrm{RASF}} = \left(\mathbf{S}^{+}\mathbf{R}_\Sigma^{-1}\mathbf{S} + \widehat{\mathbf{D}}^{-1}\right)^{-1}\mathbf{S}^{+}\mathbf{R}_\Sigma^{-1}. \tag{26}$$

The three SSP reconstruction techniques that employ the SOs (24), (25), and (26) compose the family of the DEDR-related estimators:

$$\widehat{b}_{(K)}^{(p)}(\mathbf{x}) = \mathbf{g}^{T}(\mathbf{x})\mathrm{diag}\left\{\left\{\mathbf{F}^{(p)}\mathbf{Y}\mathbf{F}^{(p)+}\right\}_{\mathrm{diag}}\right\}\mathbf{g}(\mathbf{x}), \quad p = 1, 2, 3 \tag{27}$$

with $\mathbf{F}^{(1)} = \mathbf{F}_{\mathrm{MSF}}$, $\mathbf{F}^{(2)} = \mathbf{F}_{\mathrm{RSF}}$, and $\mathbf{F}^{(3)} = \mathbf{F}_{\mathrm{RASF}}$, respectively. Any other feasible adjustments of the DEDR degrees of freedom (the regularization parameters α, β, and the weight matrix $\mathbf{A}$) provide other possible DEDR-related SSP reconstruction techniques numbered further on as $p = 4, \ldots$. As an important example, in the sequential subsection, we show that such DEDR family encompasses also the celebrated minimum variance distortionless response (MVDR) beamforming method transformed into the high-resolution RSS estimation technique with the proper MVDR SO $\mathbf{F}_{\mathrm{MVDR}} = \mathbf{F}^{(4)}$ specified further on by (31).

4.3. Relationship with the robust MVDR beamformer

The conventional MVDR beamformer [7] "reconstructs" the RS image by minimizing the power or variance of the adaptive array output for all search directions, $k = 1, \ldots, K$, under the constraint that the gain in the particular look

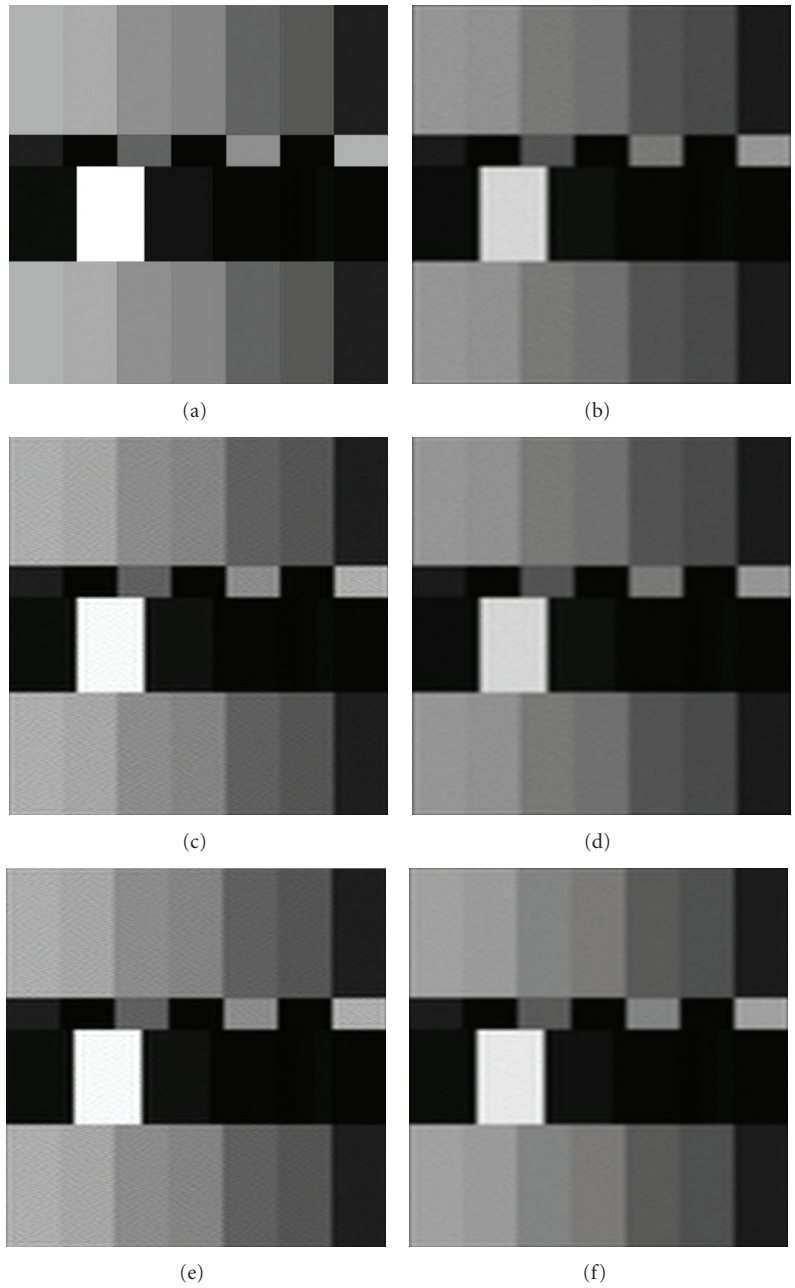

Figure 1: First operational scenario, first scene ($\mu = 20$ dB): (a) artificially synthesized original scene; (b) degraded uncertain scene image formed applying the MSF method; (c) image reconstructed applying the nonconstrained RSF algorithm; (d) image reconstructed with the constrained RSF algorithm; (e) image reconstructed applying the nonconstrained RASF algorithm; and (f) image reconstructed applying the constrained RASF (WCSP-optimized) algorithm.

direction is equal to a constant (one, for simplicity). This results in the well-known conventional MVDR algorithm [7, 10]:

$$\widehat{b}_k = \left(\mathbf{s}_k^{+}\mathbf{Y}^{-1}\mathbf{s}_k\right)^{-1}; \quad k = 1, \ldots, K, \tag{28}$$

where $\mathbf{s}_k$ represents the so-called "steering vector" for the kth look direction, which in our notations is essentially the kth column vector of the nominal SFO matrix $\mathbf{S}$.

For the purposes of establishing a relationship between the MVDR beamformer and the DEDR-related SSP estimators (27), we now rewrite the conventional MVDR algorithm (28) as

$$\widehat{\mathbf{b}}_{\mathrm{MVDR}} = \left\{\left[\mathrm{diag}\left\{\left\{\mathbf{S}^{+}\mathbf{Y}^{-1}\mathbf{S}\right\}_{\mathrm{diag}}\right\}\right]^{-1}\right\}_{\mathrm{diag}} \tag{29}$$

that can be considered as a solution to the equation, $\widehat{\mathbf{D}} = \widehat{\mathbf{D}}\mathbf{S}^{+}\mathbf{Y}^{-1}\mathbf{S}\widehat{\mathbf{D}}$. Expressing now $\mathbf{Y}^{-1} = \mathbf{Y}^{-1}\mathbf{Y}\mathbf{Y}^{-1}$ and using the

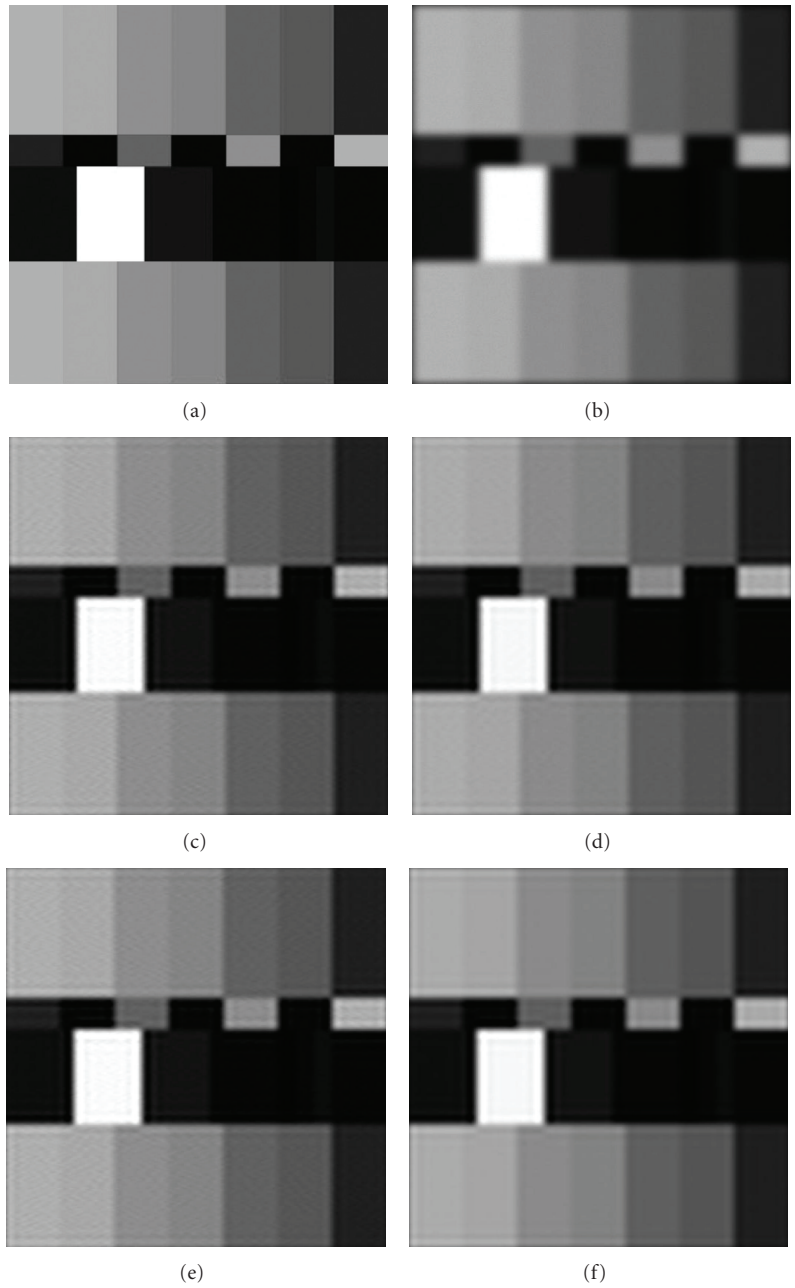

FIGURE 2: Second operational scenario, first scene ($\mu = 20$ dB): (a) artificially synthesized original scene; (b) degraded uncertain scene image formed applying the MSF method; (c) image reconstructed applying the nonconstrained RSF algorithm; (d) image reconstructed with the constrained RSF algorithm; (e) image reconstructed applying the nonconstrained RASF algorithm; and (f) image reconstructed applying the constrained RASF (WCSP-optimized) algorithm.

second-form representation [15] for the operator, $\widehat{\mathbf{D}}\mathbf{S}^{+}\mathbf{Y}^{-1} = \left(\mathbf{S}^{+}\mathbf{R}_{\mathbf{n}}^{-1}\mathbf{S} + \widehat{\mathbf{D}}^{-1}\right)^{-1}\mathbf{S}^{+}\mathbf{R}_{\mathbf{n}}^{-1}$, we obtain the alternative representation form for the MVDR algorithm (28), that is,

$$\widehat{\mathbf{b}}_{\mathrm{MVDR}} = \left\{\mathbf{F}_{\mathrm{MVDR}}\mathbf{Y}\mathbf{F}_{\mathrm{MVDR}}^{+}\right\}_{\mathrm{diag}} \tag{30}$$

with

$$\mathbf{F}_{\mathrm{MVDR}} = \mathbf{F}^{(4)} = \widehat{\mathbf{D}}\mathbf{S}^{+}\mathbf{Y}^{-1} = \left(\mathbf{S}^{+}\mathbf{R}_{\mathbf{n}}^{-1}\mathbf{S} + \widehat{\mathbf{D}}^{-1}\right)^{-1}\mathbf{S}^{+}\mathbf{R}_{\mathbf{n}}^{-1}. \tag{31}$$

Examining the formulae (20), (21), and (31), one may deduce that $\mathbf{F}_{\mathrm{MVDR}} = \mathbf{F}^{(4)}$ coincides with $\mathbf{F}_{\mathrm{DEDR}}$ for the nonrobust adaptive case, that is, $\beta = 0$, $\mathbf{A} = \widehat{\mathbf{D}}$.

5. SIMULATIONS AND DISCUSSIONS

We simulated a conventional side-looking SAR with the fractionally synthesized aperture, that is, the array was synthesized by the moving antenna. The regular SFO of such

SAR is factored along two axes in the image plane [17, 18]: the azimuth or cross-range coordinate (horizontal axis, x_1) and the slant range (vertical axis, x_2). In the simulations, we considered the conventional triangular SAR range ambiguity function (AF) $\Psi_r(x_2)$ and two approximations of the SAR azimuth AF: (i) "sinc" approximation, $\Psi_a^{(1)}(x_1) = |\mathrm{sinc}(x_1/a)|$, and (ii) Gaussian "bell" approximation, $\Psi_a^{(2)}(x_1) = \exp(-(x_1)^2/a^2)$, with the adjustable fractional parameters a [15]. Note that in the imaging radar theory [3, 8], the AF is referred to as the continuous-form approximation of the ambiguity operator matrix $\mathbf{\Psi} = \mathbf{S}^+\mathbf{S}$ and serves as an equivalent to the point spread function in the conventional image processing terminology [16, 19]. In this paper, we present the simulations performed with two characteristic scenes. The fist one of the 512-by-512 pixel format was artificially generated. The second one of the same 512-by-512 pixel format was borrowed from the real world high-resolution terrain SAR imagery (south-west Guadalajara region, Mexico [20]). The first scene was used as a test for adjustment of the degrees of freedom of the developed RSF and RASF algorithms to attain the desired improvement in the image enhancement performances (the IOSNR defined below). In the reported simulations, the representation formats along the x_2 (slant range) and x_1 (cross range, i.e., azimuth) directions were adjusted to the same effective pixel width. In the x_1 direction, the fractional parameter a was controlled to adjust different effective widths $\Delta\Psi_a(x_1)$ of the azimuth AF. The corresponding adjustment of different effective width of the range AF $\Delta\Psi_r(x_2)$ was performed over the slant range direction (x_2).

For the purpose of objectively testing the performances of different DEDR-related SSP estimation algorithms, a quantitative evaluation of the improvement in the SSP estimates (gained due to applying the DEDR-related reconstructive solution operators $\mathbf{F}^{(p)}$; $p = 2, \ldots$, instead of the MSF, i.e., the adjoint operator $\mathbf{F}^{(1)} = \mathbf{S}^+$) was accomplished. In analogy to image reconstruction quality metrics [16, 19], we adopt here the quality metric defined as an improvement in the output signal-to-noise ratio (IOSNR):

$$\mathrm{IOSNR}^{(p)} = 10\log_{10}\frac{\sum_{k=1}^{K}\left(\hat{b}_k^{(\mathrm{MSF})} - b_k\right)^2}{\sum_{k=1}^{K}\left(\hat{b}_k^{(p)} - b_k\right)^2}, \quad p = 2, 3, 4, 5, \tag{32}$$

where b_k represents a value of the kth element (pixel) of the original SSP $\mathbf{b}$, $\hat{b}_k^{(\mathrm{MSF})}$ represents a pixel value of the kth element (pixel) of the rough SSP estimate $\hat{\mathbf{b}}_{\mathrm{MSF}}$ formed applying the matched spatial filtering technique (conventional matched beamformer with $\mathbf{F}^{(1)} = \mathbf{S}^+$), and $\hat{b}_k^{(p)}$ represents a value of the kth pixel of the SSP reconstructed from the matched $\hat{\mathbf{b}}_{\mathrm{MSF}}$ applying one of the particular developed DEDR-related SOs. In the simulation studies, four different DEDR-related estimators were tested, renumbered here as $p = 2$, 3, 4, and 5. The $\mathbf{F}^{(2)}$ corresponds to the nonconstrained $\mathbf{F}_{\mathrm{RSF}}$, that is, to the RSF method adjusted incorrectly to the scenario assuming no uncertainties in the data ($\beta = 0$). The $\mathbf{F}^{(3)}$ corresponds to the constrained $\mathbf{F}_{\mathrm{RSF}}$ with the SFO uncertainty factor $k_\Delta = \beta/N_0$ correctly adjusted to two different uncertain scenarios (as specified in Tables 1 and 2). The $\mathbf{F}^{(4)}$ corresponds to the nonconstrained RASF, that is, the RASF method adjusted incorrectly to the scenario with no uncertainties in the data ($\beta = 0$). Last, the $\mathbf{F}^{(5)}$ corresponds to the constrained $\mathbf{F}_{\mathrm{RASF}}$ with the SFO uncertainty factor $k_\Delta = \beta/N_0$ correctly adjusted to two different uncertain scenarios (as specified in Tables 1 and 2), that is, the WCSP-optimized DEDR estimator. According to the quality metric (32), the higher the IOSNR, the better the improvement in the SSP estimate is, that is, the closer the estimate is to the original SSP.

In this section, we report the qualitative simulation results and the relevant quantitative performances evaluated via the IOSNRs (32) (in the dB scale) gained with these four robust DEDR-related estimators, in particular: $\mathrm{IOSNR}^{(2)}$ gained using the nonconstrained RSF in the uncertain scenario; $\mathrm{IOSNR}^{(3)}$ gained applying the constrained RSF in the same uncertain scenario; $\mathrm{IOSNR}^{(4)}$ gained using the nonconstrained RASF; and $\mathrm{IOSNR}^{(5)}$ gained applying the constrained RASF (WCSP-optimized estimator) in the same uncertain scenario. The simulation experiments were run for two typical SAR systems that operate under different SNRs levels $\mu = b_0/N_0$, different fractionally synthesized apertures (characterized by the width of the azimuth AFs $\Delta\Psi_a(x_1)$), and different uncertainty factors $k_\Delta = \beta/N_0$ (as specified in Tables 1 and 2) that bound via (11), (19) the impact of the uncertainty SFO term. In particular, the simulated scenarios are specified as follows.

(i) First uncertain operational scenario (simulation experiment specifications):

   (a) fractional azimuth AF width, $\Delta\Psi_a^{(1)}(x_1) = 10$ pixels of the 512×512 scene pixel format (at the 0.5 from the peak value of the "sinc-type" AF, $\Psi_a^{(1)}(x_1) = |\mathrm{sinc}(x_1/a)|$);
   (b) range AF width, $\Delta\Psi_r(x_2) = 3$ pixels (at the 0.5 from the peak value of the triangular $\Psi_r(x_2)$);
   (c) SNRs range, $\mu = b_0/N_0 = 5\,\mathrm{dB}, \ldots, 30\,\mathrm{dB}$;
   (d) SFO uncertainty factor, $k_\Delta = \beta/N_0 = 0.1$.

(ii) Second uncertain operational scenario (simulation experiment specifications):

   (a) fractional azimuth AF width, $\Delta\Psi_a^{(2)}(x_1) = 14$ pixels (at the 0.5 from the peak value of the "bell-type" AF, $\Psi_a^{(2)}(x_1) = \exp(-(x_1)^2/a^2)$);
   (b) range AF width, $\Delta\Psi_r(x_2) = 6$ pixels (at the 0.5 from the peak value of the triangular $\Psi_r(x_2)$);
   (c) SNRs range, $\mu = b_0/N_0 = 5\,\mathrm{dB}, \ldots, 30\,\mathrm{dB}$;
   (d) SFO uncertainty factor, $k_\Delta = \beta/N_0 = 0.05$.

These specifications correspond to two typical uncertain scenarios with airborne SAR sensor trajectory deviations modelled in [17].

Figures 1(a) and 2(a) show the same artificially synthesized test scene. Figures 3(a) and 4(a) show the second tested original scene (borrowed from the real world high-resolution

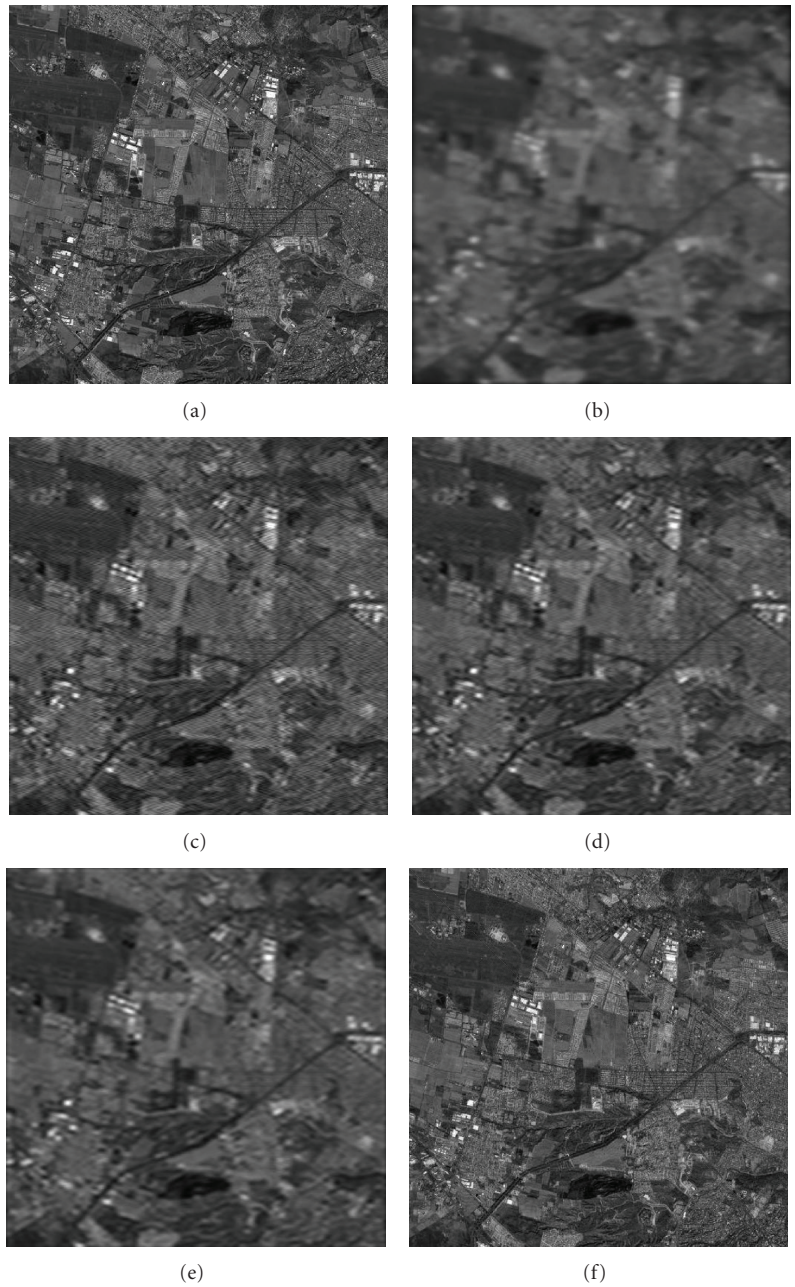

(a) (b) (c) (d) (e) (f)

Figure 3: First operational scenario, second scene ($\mu = 20$ dB): (a) original scene; (b) degraded uncertain scene image formed applying the MSF method; (c) image reconstructed applying the nonconstrained RSF algorithm; (d) image reconstructed with the constrained RSF algorithm; (e) image reconstructed applying the nonconstrained RASF algorithm; and (f) image reconstructed applying the constrained RASF (WCSP-optimized) algorithm.

SAR imagery [20]). The remaining images of Figure 1 through Figure 4 present the results of image formation applying different DEDR-related SSP estimators as specified in the figure captions. Figures 1(b) through 4(b) demonstrate the images formed applying the conventional MSF for the uncertain fractionally synthesized SAR scenarios. According to the EO (6), the overall uncertain data degradations $\tilde{\mathbf{n}} = \mathbf{\Delta e} + \mathbf{n}$ were composed of a mixture of conventional white additive observation noise $\mathbf{n}$ and correlated (scene-dependent) multiplicative noise $\mathbf{\Delta e}$. Following the DEDR methodology (detailed in Section 3), the SFO uncertainty cannot be factorized into separate terms caused by the environmental perturbations, SAR trajectory deviations, or antenna vibrations. Thus, the composed multiplicative degradation effect was modeled via simulating the MSF scene image corrupted by the speckle noise via incorporating into (9) with the SO (25), the uncertain operational scenario factors, in particular, the uncertain data model correlation matrix $\mathbf{Y}$ that corresponds to the degraded EO (6) with the diagonal loaded noise augmented correlation matrix (19). Figures 1(c) through 4(c) show the enhanced images formed applying the unconstrained RSF, that is, the RSF

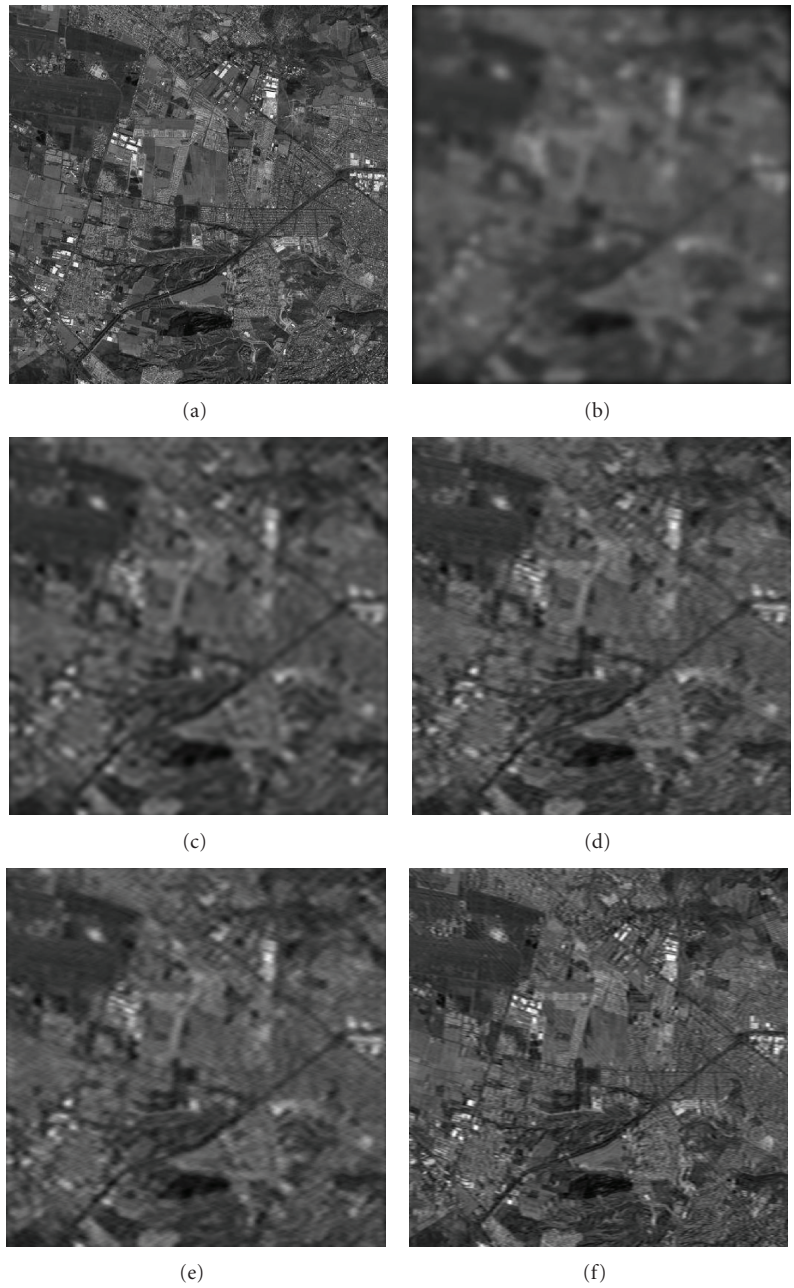

FIGURE 4: Second operational scenario, second scene ($\mu = 20$ dB): (a) original scene; (b) degraded uncertain scene image formed applying the MSF method; (c) image reconstructed applying the nonconstrained RSF algorithm; (d) image reconstructed with the constrained RSF algorithm; (e) image reconstructed applying the nonconstrained RASF algorithm; and (f) image reconstructed applying the constrained RASF (WCSP-optimized) algorithm.

incorrectly adjusted to the uncertain scenario via ignoring the uncertainty factor ($\beta = 0$). Figures 1(d) through 4(d) present the enhanced images formed using the constrained RSF properly adjusted to the particular uncertain scenario ($k_\Delta = \beta/N_0 = 0.1$ for the first scenario, and $k_\Delta = \beta/N_0 = 0.05$ for the second scenario, respectively). The images enhanced with the unconstrained RASF ($\beta = 0$) are shown in Figures 1(e)–4(e), and the corresponding images reconstructed with the constrained RASF (WCSP-optimized method) are presented in Figures 1(f)–4(f), respectively.

From the presented simulation results, the advantage of the well-designed imaging experiments (constrained RSF and WCSP-optimized RASF) over the case of badly designed experiment (nonrobust MSF and unconstrained RSF) is evident. Due to the performed regularized inversions, the resolution was substantially improved in all simulated scenarios (as reported in Tables 1 and 2). The higher values of $\text{IOSNR}^{(3)} > \text{IOSNR}^{(2)}$ as well as $\text{IOSNR}^{(5)} > \text{IOSNR}^{(4)}$ were obtained with the constrained DEDR-related estimators, that is, with the DEDR techniques adopted to the uncertain

scenarios. Note that IOSNR (32) is basically a square-type error metric. Thus, it does not qualify quantitatively the "delicate" visual features in the reconstructed images; hence, small differences in the corresponding IOSNRs reported in Tables 1 and 2. In addition, both enhanced robust estimators manifest the higher IOSNRs in the case of more smooth azimuth AFs (larger $\Delta\Psi_a(x_1)$) and higher SNRs μ. For the DEDR-optimized RASF method, in addition, the ringing (image speckle) effect was substantially reduced, while the nonadaptive constrained RSF estimator requires considerably less computational load. These results qualitatively demonstrate that with proper adjustment of the degrees of freedom in the developed DEDR estimators (24), (27), one could approach the quality of the DEDR-optimal image formation method (22) avoiding the cumbersome adaptive computations required to implement the DEDR-optimal algorithm [10, 15].

6. CONCLUSION

New descriptive experiment design regularization (DEDR) approach for estimation of the spatial spectrum pattern (SSP) of the wavefield power distribution in the uncertain remotely sensed environment has been proposed as required for the conventional array imaging radar, side-looking airborne radar, and SAR. Unifying the DEDR and the worst-case statistical performance (WCSP) optimization into the aggregated WCSP-constrained minimum risk technique, the inverse problem ill-posedness has been alleviated in a statistically grounded fashion. The derived general-form DEDR estimator does not involve the inversion of the estimated data correlation matrix. This principal algorithmic-level result of the undertaken study constitutes the crucial advantage of the developed family of the DEDR-related estimators that makes them applicable to the uncertain operational scenarios with ill-conditioned (e.g., low-rank) estimates of the array data correlation matrices, in particular, to the SAR imaging scenarios where only one realization of the trajectory data signal degraded due to the uncontrolled random carrier trajectory deviation and antenna vibration is available for further processing. Being nonlinear and solution-dependent, the DEDR-optimal robust adaptive spatial filtering (RASF) estimator requires rather complex signal processing. The computational complexity arises due to the necessity to perform simultaneously the solution-dependent operator inversion operations and adaptive adjustments of the degrees of freedom of the overall RASF technique. To reduce the computational load, the simplified constrained robust spatial filtering (RSF) algorithm was proposed and employed, which manifests almost the same reconstruction performances as the RASF in typical uncertain operational scenarios that was verified in the simulation experiment.

REFERENCES

[1] S. E. Falkovich, V. I. Ponomaryov, and Y. Shkvarko, *Optimal Reception of Space-Time Signals in Channels with Scattering*, Radio i Sviaz,Moscow, Russia, 1989.

[2] G. T. Capraro, A. Farina, H. Griffiths, and M. C. Wicks, "Knowledge-based radar signal and data processing: a tutorial review," *IEEE Signal Processing Magazine*, vol. 23, no. 1, pp. 18–29, 2006.

[3] D. R. Wehner, *High-Resolution Radar*, Artech House, Boston, Mass, USA, 2nd edition, 1994.

[4] H. L. Van Trees, *Detection, Estimation and Modulation Theory, Part IV, Optimum Array Processing*, Wiley-Interscience, New York, NY, USA, 2002.

[5] S. M. Kay, *Modern Spectral Estimation*, Prentice-Hall, Englewood Cliffs, NJ, USA, 1988.

[6] S. Haykin and A. Steinhardt, Eds., *Adaptive Radar Detection and Estimation*, John Willey & Sons, New York, NY, USA, 1992.

[7] P. Stoica and R. L. Moses, *Introduction to Spectral Analysis*, Prentice-Hall, Englewood Cliffs, NJ, USA, 1997.

[8] F. M. Henderson and A. V. Lewis, Eds., *Principles and Applications of Imaging Radar*, vol. 2 of *Manual of Remote Sensing*, John Willey & Sons, New York, NY, USA, 3rd edition, 1998.

[9] S. A. Vorobyov, A. B. Gershman, and Z.-Q. Luo, "Robust adaptive beamforming using worst-case performance optimization: a solution to the signal mismatch problem," *IEEE Transactions on Signal Processing*, vol. 51, no. 2, pp. 313–324, 2003.

[10] A. B. Gershman, "Robustness issues in adaptive beamforming and high-resolution direction finding," in *High-Resolution and Robust Signal Processing*, Y. Hua, A. B. Gershman, and Q. Cheng, Eds., pp. 63–100, Marcel Dekker, New York, NY, USA, 2004.

[11] D. W. Rieken and D. R. Fuhrmann, "Generalizing MUSIC and MVDR for multiple noncoherent arrays," *IEEE Transactions on Signal Processing*, vol. 52, no. 9, pp. 2396–2406, 2004.

[12] J. Li, P. Stoica, and Z. Wang, "Doubly constrained robust Capon beamformer," *IEEE Transactions on Signal Processing*, vol. 52, no. 9, pp. 2407–2423, 2004.

[13] Y. Shkvarko, "Estimation of wavefield power distribution in the remotely sensed environment: Bayesian maximum entropy approach," *IEEE Transactions on Signal Processing*, vol. 50, no. 9, pp. 2333–2346, 2002.

[14] Y. Shkvarko, "Unifying regularization and Bayesian estimation methods for enhanced imaging with remotely sensed data—part II: implementation and performance issues," *IEEE Transactions on Geoscience and Remote Sensing*, vol. 42, no. 5, pp. 932–940, 2004.

[15] Y. Shkvarko, "From matched spatial filtering towards the fused statistical descriptive regularization method for enhanced radar imaging," *EURASIP Journal on Applied Signal Processing*, vol. 2006, Article ID 39657, 9 pages, 2006.

[16] H. H. Barrett and K. J. Myers, *Foundations of Image Science*, Wiley-Interscience, New York, NY, USA, 2004.

[17] G. Franceschetti, A. Iodice, S. Perna, and D. Riccio, "SAR sensor trajectory deviations: Fourier domain formulation and extended scene simulation of raw signal," *IEEE Transactions on Geoscience and Remote Sensing*, vol. 44, no. 9, pp. 2323–2334, 2006.

[18] M. S. Greco and F. Gini, "Statistical analysis of high-resolution SAR ground clutter data," *IEEE Transactions on Geoscience and Remote Sensing*, vol. 45, no. 3, pp. 566–575, 2007.

[19] V. Ponomaryov, A. Rosales, F. Gallegos, and I. Loboda, "Adaptive vector directional filters to process multichannel images," *IEICE Transactions on Communications*, vol. E90-B, no. 2, pp. 429–430, 2007.

[20] Space Imaging, GeoEye Inc., 2007, http://www.geoeye.com/.

Hindawi Publishing Corporation
International Journal of Navigation and Observation
Volume 2008, Article ID 762378, 8 pages
doi:10.1155/2008/762378

Research Article

Damage Detection from SAR Imagery: Application to the 2003 Algeria and 2007 Peru Earthquakes

Giovanna Trianni[1] and Paolo Gamba[2]

[1] *Department of Electronics, University of Pavia, via Ferrata 1, 27100 Pavia, Italy*
[2] *EO Science and Applications Department D/EOP-SEP, SERCO, c/o ESA/ESRIN, Via Galileo Galilei, Casella Postale 64, 00044 Frascati, Rome, Italy*

Correspondence should be addressed to Paolo Gamba, paolo.gamba@unipv.it

Received 25 January 2008; Accepted 4 June 2008

Recommended by Simon Watts

This paper is focused on the improvement and further validation of a recently proposed approach for the joint use of radar satellite imagery of an area affected by a major disaster and ancillary data. The study was carried out at different sites on imagery of two different earthquakes occurred one in the Mediterranean coast of Algeria on May 21st, 2003, which severely affected the city of Boumerdes, and one in the Pacific Coast of Peru on August, 15th, 2007. The combination of different radar-extracted features results in very fuzzy classification of the damage patterns, far less detailed than what available using optical imagery. However, focused results using the above-mentioned ancillary data provide enough detail and precision to be comparable with them. In particular, quantized damage level at the block level is achieved at enough detail using ALOS/PALSAR data and thus validates the original idea.

1. INTRODUCTION

One of the most important issues in disaster damage detection is time, and map timeliness is as important as precision. As a consequence of that, every kind of data available is used in order to provide information to emergency operators [1]. To this aim, remotely sensed imagery can be instrumental, as well as geographical information system (GIS) layers, printed maps, and historical datasets. However, while the use of this kind of imagery has been constantly growing in the past few years, image interpretation tools, though fast and efficient even if not highly accurate, are still not used in many applications.

Damage assessment is actually a big challenge, being impossible to get the right data at the right time. For this reason, the organizations such as the International Charter on "Space and Major Disasters" are forced to consider a wide range of sources. The need of rapid damage pattern estimate requires information extraction about damages using quick and possibly efficient approaches suited to the decided spatial scale and the available data. So, the scale at which the analysis can be carried out is determined by the spatial resolution of the available data; for example, while SAR data can be useful to extract damage information only at a parcel level, it should be possible to recognize the single collapsed buildings from HR images.

The aim of this work is to understand the viability of radar satellite approaches to damage patterns by analyzing many different disasters all around the world, looking also at different scales of work. SAR data are becoming widely available with more and more fine spatial resolution, and thus with larger usability for urban area management. This improvement actually allows a better match between the growing requests for focused analysis in these areas (due to the concentration of population) with the enhanced availability of dataset. Still, approaches to disaster management in urban areas using SAR data are very limited, due to the problems in data interpretation and the lack of automated or semiautomated tools.

2. DAMAGE PATTERN ESTIMATE FROM SAR DATA

In recent technical literature, some works have already suggested that multitemporal SAR data may provide, at

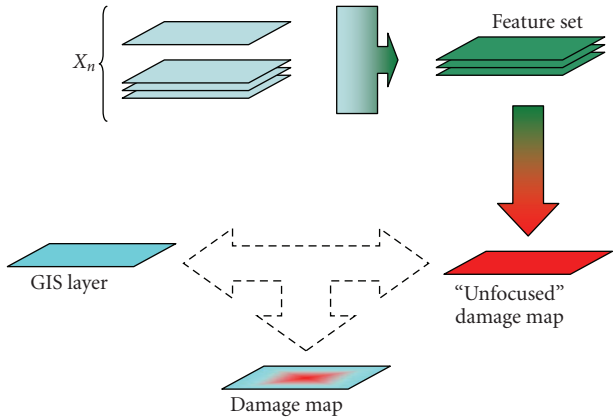

Figure 1: Overall structure of the damage mapping procedure.

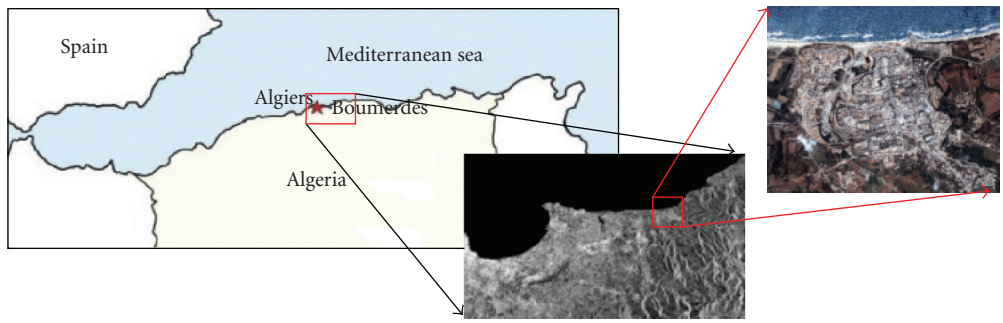

Figure 2: Location of the urban area of Boumerdes in Algeria.

Table 1: Overall accuracy for maps in Figures 5–9.

	Overall accuracy	O.A. (4 classes)
Figure 5 MRF + GIS	56.51%	45.71%
Figure 5 FA + GIS	**75.66**%	
Figure 6 MRF + GIS	66.98%	
Figure 6 FA + GIS	65.08%	
Figure 7 MRF + GIS	**70.16**%	44.44 %
Figure 7 FA + GIS	67.62%	
Figure 8 MRF + GIS	69.84%	
Figure 8 FA + GIS	68.25%	

a proper temporal and spatial scale, interesting information about disaster like earthquakes and floods. Most of these works concerning earthquakes need data coming from ground surveys to validate but also to initiate the process of information extraction. For this reason, these strategies are very useful in order to correlate damage patterns with ground displacements and soil properties [2, 3], or to provide precise 3D changes of the earth crusts [4], but offer very poor results in terms of damage assessment and rapid damage mapping of an affected area. However, it is important to say that classification and change detection methodologies solely used cannot provide immediately usable results to the final user. Instead, these methods integrated with some kind of ancillary data allow obtaining more precise and understandable results. Moreover, damage analysis is almost uniquely required in urban areas and human settlements in general, where it is often easily feasible to collect layers of Geographic Information System (GIS) data.

In this work, we apply a technique recently proposed in [5] for the two test cases of the Bam (Iran) [6] and of the Golcük (Turkey) earthquakes. The first aim of this work is indeed to show that the proposed approach is valid in other situations and produces useful results fro damage assessment in different areas in the world. As a second objective, this paper reports the results of an investigations about the robustness of the approach to the lack of some of the features originally used in the cited papers.

The overall methodologyof the data analysis is proposed in Figure 1, even if, for sake of brevity, we do not recall here all the details of the algorithm. The procedure involves first of all the extraction of a suitable set of features from the original multitemporal dataset comprising pre- and postevent SAR imagery of the area under test. This feature set is then input to a multiband supervised classifier, whose output is a multiple class change detection map. Finally, a postclassification fusion step is performed at the end of the procedure involving the use of the above mentioned ancillary data.

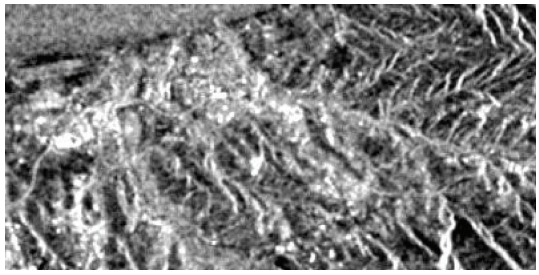

(a)

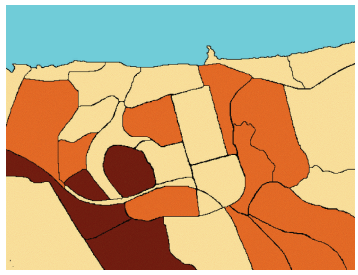

(b)

FIGURE 3: Postevent SAR image (left) and available damage map (right), where brown refers to highly damaged areas, orange to medium damaged areas, and off-white to undamaged areas.

The set of feature extracted from the multitemporal SAR images of the area under test depends on the trivial assumption that radar returns in damaged areas are quite different than in the original "undisturbed" configuration of the buildings. There are studies showing that urban areas show a remarkably strong coherence in complex return values and correlation in amplitude/intensity values during time. It is interesting therefore to use as hint to damages the change in the complex coherence and in the intensity correlation. In particular, intensity correlation has been tested in technical literature for the Hyogoken-nambu (Japan) and Bam (Iran) earthquakes. Following the paper where this was originally proposed [2], each (complex) SAR image of the available data sequence X_n, $n = 1, 2, \ldots$, is prefiltered with a Lee filter, and intensity correlation r_i between the ith image and the previous one in the temporal sequence is computed according to the formula

$$r_i = \frac{\sum_W x_i x_{i-1} - N\overline{x}_i\overline{x}_{i-1}}{\sqrt{\left(\sum_W x_i^2 - N\overline{x}_i^2\right)\left(\sum_W x_{i-1}^2 - N\overline{x}_{i-1}^2\right)}}, \quad (1)$$

where $x_i = \|X_i\|$ (recall that SAR data are complex values), the $\sum_W(\cdot)$ notation means that computation is done for each image element in a window $W = N \times X$ around it, and finally the mean value $\overline{x}_i$ is similarly computed in W.

Along with intensity correlation, another valuable input feature is the difference between the logarithmic value of the mean prefiltered data intensity $d_i = 10\log_{10}(\overline{x_i}) - 10\log_{10}(\overline{x_{i-1}})$, and the feature set is completed by the original pre- and postevent pointwise intensities.

	53.08%	534	177	295	0
	55.84%	749	2362	1119	0
	59.32%	968	2512	5205	89
	100%	0	0	0	1992
		23.72%	46.76%	78.64%	95.72%

(a) Overall accuracy: **63.07**%

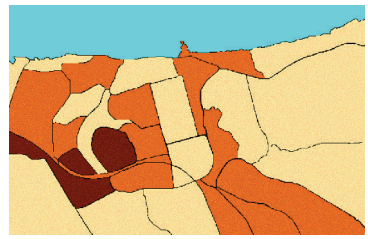

	75%	3	0	1	0
	90%	0	9	1	0
	76.47%	0	4	13	0
	100%	0	0	0	1
		100%	69.23%	86.67%	100%

(b) Overall accuracy: **81.25**%

FIGURE 4: Damage maps for the Boumerdes area: (a) using remotely sensed data and change detection algorithm; (b) introducing the GIS information about parcel borders in the urban area.

Of course, according to the dimension of the window W and thus to the geographic area of computation of the spatial features, multiple scales of analysis of the data can be enhanced. A convenient value for the window size, according to our past experience, depends on the ground spatial resolution of the data and the mean dimension of a meaningful block of buildings in the human settlement under test. In all the considered cases, a value of N between 15 and 21 is equally valuable, when the SAR images have spatial resolution in the 10 meters' range.

The second step of the approach, as shown in Figure 1, is a multiband classification, performed in this work comparing two different approaches: a neuro-fuzzy per-pixel Fuzzy ARTMAP (FA) classifier [7], and a contextual classifier based on the assumption of a Markov random field (MRF) spatial model [8]. Generally speaking, the neuro-fuzzy classifier has been chosen because of its proven capability to provide good

(a)

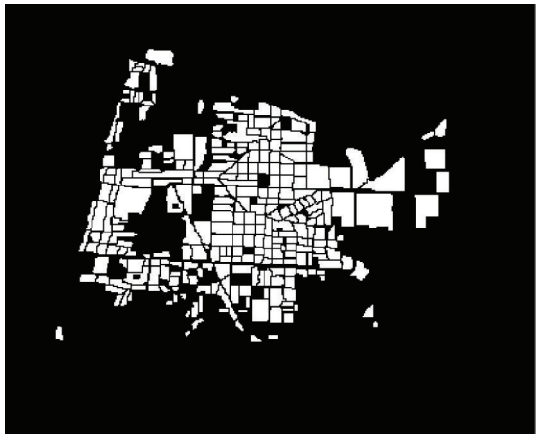

(b)

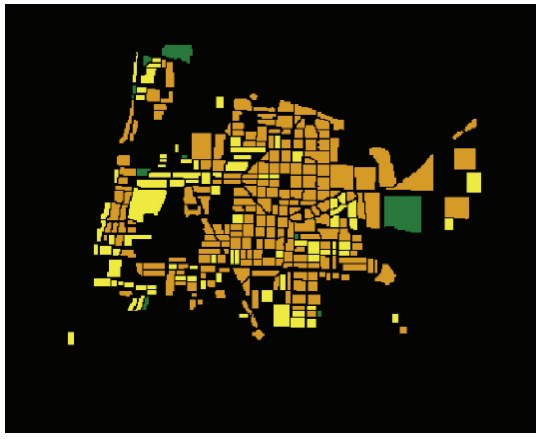

(c)

Figure 5: Postevent pan-sharpened image of the town of Pisco (a) and GIS information (b) about the blocks in the town and (c) damage map with three classes (from [9]): green (untouched), yellow (light damage), and orange (medium/high damage).

results when performing a multiband per pixel classification, while the MRF approach allows a spatially joint analysis. Both algorithms are supervised, and as such a minimal knowledge about the damages on the ground, their locations, and level is required.

After classification, and due to the complex interactions between radar waves and the urban environment, either damaged or undamaged, it is very likely that the damage classification map has a "blurred" or "fuzzy" appearance. To improve the results, and to meaningfully focus the damage map at a spatial scale of interest to the final user, a fusion step between the map results and ancillary GIS data is performed. To this aim, the best results between the two classification methods are used to make a decision, by means of a decision fusion process, about each of the areas detailed by the GIS ancillary information. This processing step involves a data fusion procedure which has been detailed in [5] and in this work will be degraded to the simplest situation, that is, majority voting. This basically means that the most voted damage class in each block individuated by the GIS layer is considered as representative of the whole block.

Following this procedure, in next section two different testcases will be considered, referring to very different countries in different parts of the world. Moreover, different SAR sensors are considered, and thus different scale of analysis and data availability. With the results of the following section we want to stress how much the simple procedure presented here can be helpful in real situations, and compare how much and how well different choices of the input feature set can highlight the damage patterns in the area. The goal of having more test cases and comparing with the originally studied Bam (Iran) and Golcük (Turkey) cases is also a way to check for the best combination (if any) for all of them.

3. APPLICATIVE TEST CASES

In order to test the proposed methodology, the aim of our tests was to consider different SAR datasets, coming from sensors on board of different satellites. The combination of different bands of work, spatial resolution, polarization information, availability or not of phase information was meant to provide a method to test the robustness of the approach and find where it has to be adapted. Moreover, the very diverse damage patterns, connected to the original spatial urban patterns and the effect of the earthquake, make the two test site analyzed in the following. (in addition to the 2003 Bam test case in [5] and the 1999 Turkey case in [6] a definitely valid series of applicative results.)

3.1. *First test site: Boumerdes (2003 Algeria earthquake)*

The first results refer to the magnitude 6.8 earthquake occurred in northern Algeria on May 21st, 2003. Centered on the Boumerdes province (Figure 2) some 50 km east of Algiers, the worst affected urban areas included the cities of Boumerdes, Zemmouri, Thenia, Belouizdad, Rouiba, and Reghaia. For this event, many different remotely sensed data are available; in this work the analysis will be concentrated in the urban area of Boumerdes, for which two ERS-2 have been acquired, one pre-event acquired on July 27th, 2002, and one postevent acquired on June 7th, 2003.

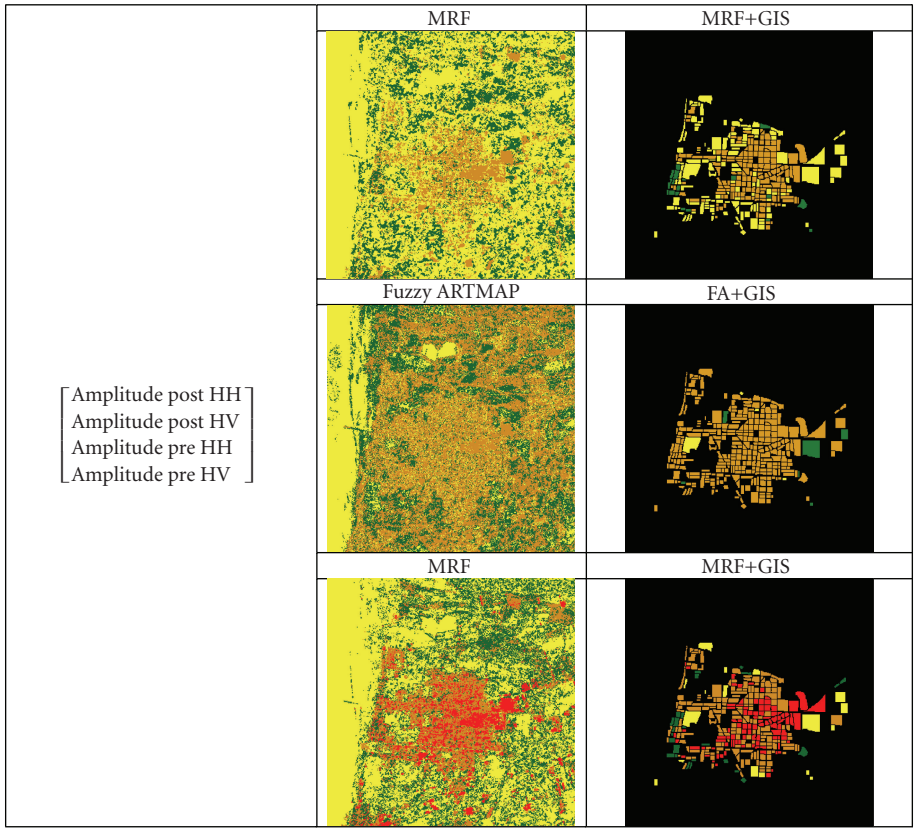

Figure 6: Per-pixel damage maps and focused damage map using ancillary information for both the MRF and FA case. The input multiband/multitemporal dataset is detailed on the left.

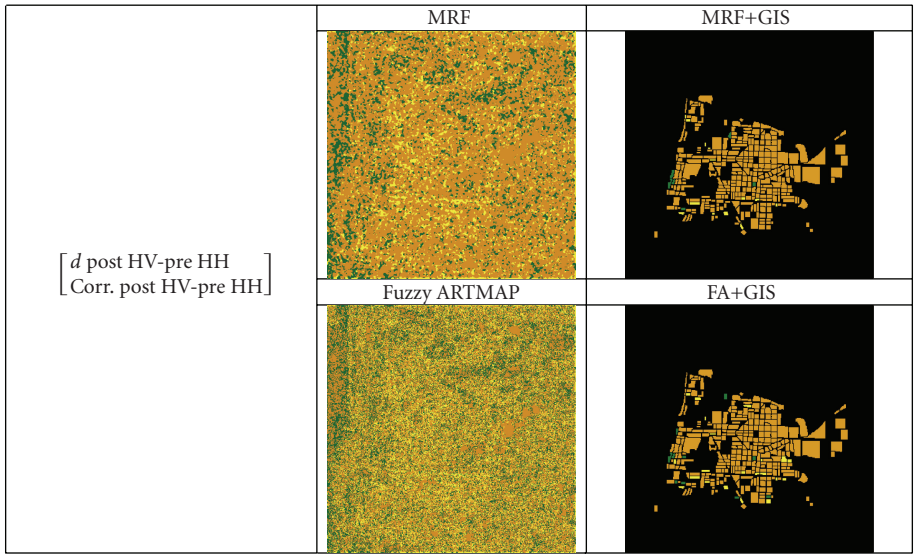

Figure 7: Per-pixel damage maps and focused damage map using ancillary information for both the MRF and FA case. The input multiband/multitemporal dataset is detailed on the left.

3.2. *Second test site: Pisco (2007 Peru earthquake)*

The second example refers to the test case of Peru, whose central coast was stricken by a 7.9-magnitude earthquake on August 15th, 2007. Among the affected cities, the city of Pisco has been considered because it appears in two ALOS/PALSAR fine beam double polarization (HH/HV) Precision images, provided in geocorrected form and 12.5 meters posting. The two images were acquired before (on August, 12th, 2007) and after (on August 27th, 2007) the earthquake. Ancillary data

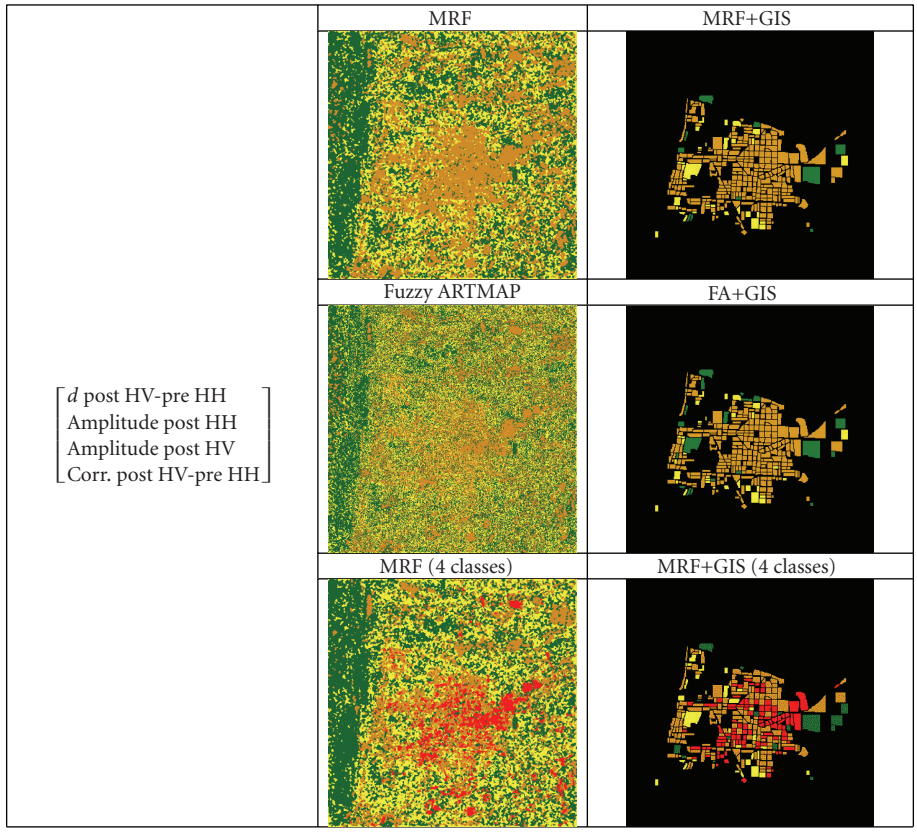

Figure 8: Per-pixel damage maps and focused damage map using ancillary information for both the MRF and FA case. The input multiband/multitemporal dataset is detailed on the left.

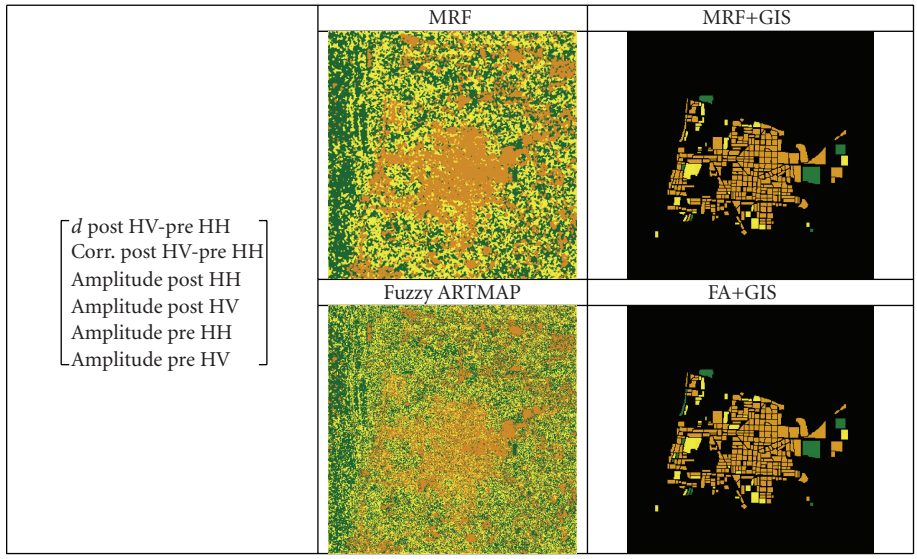

Figure 9: Per-pixel damage maps and focused damage map using ancillary information for both the MRF and FA case. The input multiband/multitemporal dataset is detailed on the left.

consist of a GIS layer depicting the borders of the parcels in the urban area, and were obtained by manual digitalization of the information in [9], and validated by comparison with the same SPOT pre-event image used in that paper. From the same paper, also the information related to damaged areas obtained by in situ measurements was extracted (see Figure 5).

Since the data have been provided as amplitude images, no phase information could have been considered. This prevents us from using the bands which were considered as

the best choice in [5] for the problem of damage detection, that is, pre- and postevent intensity, pre-post coherence and difference between pre-post and pre-pre coherence. Instead, from the available images only some intensity features have been extracted, in particular the intensity correlation r and the backscattering coefficient d and taking into account the different spatial resolution of the ALOS/PALSAR scene than the ERS and JERS data used in all the works on the same subject so far. Other considered features are the pre- and postevent intensities, computed from the original data after despeckling with a 5×5 Gamma filter. As in the first test case the first classification by means of the above neuro-fuzzy per-pixel classifier or the context-aware MRF classifier is followed by a fusion with the GIS layer, where each parcel of the GIS is assigned to the class to which the majority of mapped pixels belong.

For this test case, a wider range of classification maps is proposed in Figures 6–9 to allow a better comparison of the combinations of features and classifiers, as well as to appreciate the improvement in understanding the results by using the data fusion final step. The need for this extended result analysis is connected to the different spatial resolution of ALOS/PALSAR with respect to the ERS/JERS data used so far. This makes the classification map more precise at the per-pixel level and allows defining spatial units smaller than in the previous test site (compare Figures 5(b) with 3(b)). Moreover, the lack of original complex data does not allow computing the phase coherence, one of the most important bands for the multiband/multitemporal damage assessment classification step according to [5]. We thus intend to analyze which, among the computed features, are the most viable ones to get a rapid damage map in this situation.

Finally, Table 1 reports the overall accuracy for the maps in the rightmost column in Figures 6–9 and allows to improve the visual comparison with a quantitative assessment.

A first comment to the results is that the information fusion step is really mandatory to achieve results not only with a decent mapping accuracy, but also understandable to anyone looking to the map. A second comment is that the accuracy values are in the same range as the one reported for the first test case, the Algeria earthquake. Although the ground truth in the present case is more detailed, the higher spatial resolution of the SAR data allow matching the accuracy values obtained from Boumerdes' images.

According to the maps and the accuracy values, the best result is obtained by using a combination of the amplitude pre-event image (both polarizations HH and HV) and the amplitude postevent image (again with both polarizations), and the second best approach is the use of the backscattering and the correlation computed between the pre-event image (HH polarization) and the postevent image (HV polarization), and the postevent image (with both polarizations).

Since the ALOS/PALSAR image pre- and postevent image pairs are alternate polarization (AP) images, it was also possible to compare the effect of polarization with respect to damage mapping task using the proposed approach. However, it was found that no particular choice can be made, and the problems in mapping the damage to the right extent in some portion of the area are equally in place suing one or the other of the two polarizations, or even a combination of both.

A last comment is driven by the fact that the damage maps in [9] involve four classes, instead of the three used in our validation. In Figure 9, in fact, medium and high damages were considered as a single class, in orange. The reason is that previous trials attempting to obtain maps with high level of damage discrimination did fail. The highest accuracy values, as reported in Table 1 for sake of completeness, were around 45% at their best. The corresponding maps, where a high level of damage is depicted in red, are reported in the last row of Figures 6 and 8. Apparently, thereare limits inherent to the structure of the artificial elements of the landscape, the typology of earthquake, and the spatial resolution that prevent the 7 m ALOS/PALSAR to be enough for this precise recognition task.

4. CONCLUSIONS

In this paper, a rapid damage mapping approach is proposed, based on the exploitation and interpretation of satellite SAR data. The approach proves to be robust and useful to detect the damage patterns. It is however imprecise with respect to accuracy and needs improvements.

More specifically, although semiautomatic SAR data interpretation in urban areas is an open research issue, this paper shows that a combination (fusion) of remotely sensed data and geographical databases may lead to a real improvement in this interpretation, making the data more useful for the end-user. Accuracy and robustness of the procedure, together with its affordability, were proved by the analysis of extreme events (notably, earthquakes) in many different parts of the world.

There are some commonalities among the choices of input features used in the cases presented in this work, and the combination of the pre- and postevent intensity data with the intensity correlation and the difference of the logarithmic means achieves always better results. The possibility to incorporate some phase information by means of coherence, not exploited in this work but proposed in the original paper [5], leads apparently to the best among these multiple possible choices.

Very interesting and still open issues are those connected to the analysis of additional spatial feature and the correlation between the maps and the features itself to the actual, on site generated, damage map.

ACKNOWLEDGMENTS

The first part of this work has been carried out during the stay of G. Trianni at the John A. Blume Earthquake Engineering Center, Stanford University, Calif, USA, as a visiting researcher. The authors would like to thank Professor Anne Kiremidjian and Dr. Pooya Sarabandi for their hospitality and M. Matsuoka and Professor F. Yamazaki for providing the SAR dataset and the damage map for the Boumerdes test site. The PALSAR satellite data over Peru were provided by

JAXA via the European Distribution Node for ALOS data, operated by ESA. The pre-event SPOT image was instead provided by INDECI, Instituto Nacional de Defensa Civil, Lima, Peru. Finally, G. Lisini is gratefully acknowledged for developing and maintaining the GIS fusion software.

REFERENCES

[1] B. Allenbach, R. Andreoli, S. Battiston, et al., "Rapid EO disaster mapping service: added value, feedback and perspectives after 4 years of charter actions," in *Proceedings of the IEEE International Geoscience and Remote Sensing Symposium (IGARSS '05)*, vol. 6, pp. 4373–4378, Seoul, Korea, July 2005.

[2] M. Matsuoka and F. Yamazaki, "Building damage mapping of the 2003 Bam, Iran, earthquake using Envisat/ASAR intensity imagery," *Earthquake Spectra*, vol. 21, supplement 1, pp. S285–S294, 2005.

[3] C. Yonezawa and S. Takeuchi, "Decorrelation of SAR data by urban damages caused by the 1995 Hyogoken-nanbu earthquake," *International Journal of Remote Sensing*, vol. 22, no. 8, pp. 1585–1600, 2001.

[4] S. Stramondo, M. Moro, C. Tolomei, F. R. Cinti, and F. Doumaz, "InSAR surface displacement field and fault modelling for the 2003 Bam earthquake (southeastern Iran)," *Journal of Geodynamics*, vol. 40, no. 2-3, pp. 347–353, 2005.

[5] P. Gamba, F. Dell'Acqua, and G. Trianni, "Rapid damage detection in the Bam area using multitemporal SAR and exploiting ancillary data," *IEEE Transactions on Geoscience and Remote Sensing*, vol. 45, no. 6, pp. 1582–1589, 2007.

[6] P. Gamba, F. Dell'Acqua, G. Trianni, and M. Stasolla, "GIS and remote sensing for disaster assessment in urban areas," in *Proceedings of the Urban Remote Sensing Joint Event*, pp. 1–5, Paris, France, April 2007.

[7] P. Gamba and F. Dell'Acqua, "Increased accuracy multiband urban classification using a neuro-fuzzy classifier," *International Journal of Remote Sensing*, vol. 24, no. 4, pp. 827–834, 2003.

[8] G. Trianni and P. Gamba, "A novel Markov random field model for multisource data fusion in urban areas," in *Proceedings of 28th General Assembly of International Union of Radio Science*, New Delhi, India, October 2005.

[9] A. R. Zambrano, G. C. Henriquez, and K. Gonzales, "Contribucion de la teledeccion y los sistemas de informacion geografica en la evaluacio de los danos producidos en la ciuddad de Pisco por el terremoto del 15 de agosto del 2007," (in Spanish), Direccion de Sismologia, Instituto Geofisico del Peru, vol. especial, preprint.

Hindawi Publishing Corporation
International Journal of Navigation and Observation
Volume 2008, Article ID 347518, 14 pages
doi:10.1155/2008/347518

Research Article

An Analysis of X-Band Calibrated Sea Clutter and Small Boat Reflectivity at Medium-to-Low Grazing Angles

P. L. Herselman,[1] C. J. Baker,[2] and H. J. de Wind[1]

[1] *CSIR Defence, Peace, Safety and Security, P.O. Box 395, Pretoria 0001, South Africa*
[2] *Department of Electronic and Electrical Engineering, University College London, Torrington Place, London WC1E 7JE, UK*

Correspondence should be addressed to P. L. Herselman, pherselman@csir.co.za

Received 15 February 2008; Accepted 4 June 2008

Recommended by Simon Watts

The coherent temporal characteristics of medium-to-low grazing angle sea clutter and small boat reflectivity are considered for different radar waveforms under a range of environmental conditions and geometrical configurations. Accurate empirical modelling of sea clutter enables the inference of the local sea conditions from radar returns, pertinent for port safety and navigation. Understanding the dynamics and associated reflectivity of small boats, in addition to empirical sea clutter models, allows the development of advanced detection and tracking algorithms, which will improve the performance of surveillance and marine navigation radar against small boats. Work presented is based on the empirical analysis of data recorded with two calibrated, coherent, pulsed radar systems at X-band frequencies. Specifically, target echoes from small boats are included in the datasets and subsequent analysis.

1. INTRODUCTION

There is a growing need for accurate, real-time instrumentation of the sea surface for safe navigation of vessels in and around harbours and shipping lanes. A commercial product, wave and surface current monitoring system (WaMoS) [1], can be connected to a conventional X-band marine radar. WaMoS II processes the unfiltered sea clutter to estimate the wave and surface current parameters in near real-time. According to the manufacturers the instrumented range is 0.1–3 km. At X-band operating frequencies, the main scattering mechanism is that of Bragg scattering, associated with the resonant capillary waves [2]. Capillary waves, in turn, are generated by the local near-surface wind and do not propagate beyond the breeze area. Only in a fully developed sea can the wave height be directly related to the present wind speed and can the significant wave height H_s be accurately inferred from the average sea clutter reflectivity [3]. In transient sea conditions, the best fit for the Georgia Institute of Technology (GIT) mean sea clutter reflectivity model [4] is found if the sea state is related to the local mean wind speed rather than H_s [5, 6]. It can therefore be deduced that it is possible to also infer local wind conditions from X-band sea clutter. This article investigates the temporal characteristics of coherent sea clutter, with specific interest in the Doppler characteristics of sea clutter and the relationship thereof to the local wind and wave conditions (e.g., average wind speed, wind direction, and wind gusts).

The significant increase in sea clutter reflectivity in rough seas with strong winds, together with relatively small radar cross section (RCS) of small boats (e.g., yachts, ski boats, and rigid inflatable boats (RIBs)), has often been blamed for disasters at sea where large ships collided with these small boats [7]. In certain cases, the marine radar could not discern the boat signature from the clutter, while in other cases there were too many false tracks established leading to the subsequent disabling of the automatic tracker. For safe navigation it is pertinent that the detection capabilities of marine radar in adverse conditions are improved. With the introduction of cheaper, solid-sate, coherent marine radar [8] a whole new class of coherent detection algorithms has become applicable to marine navigation radar, for example, [9–11]. Theoretical and first-order empirical analysis suggest subclutter visibility [11]. Little work has been presented on the performance of this class of detectors (often referred

to as asymptotically optimal) on measured data of small boats [12]. No reference is made to the performance as a function of the type of manoeuvring of the boat and the influence of the boat on the surrounding sea surface. This article investigates the performance of the adaptive linear quadratic (ALQ) detector [11] under different boat manoeuvres for different types of RIBs, including the 4.2 m pencilduck type that is often used for watersport racing. This boat has a very small RCS, but since it has a racing speed of up to 40 kts the local disturbance of the sea surface often exceeds the boat RCS by up to 10 dB. With improved subclutter visibility, the problem arises that first detections are declared not only for small boats, but also for large birds such as seagulls, with a typical RCS of 0.01–0.1 m^2 [3], and angels (flocks of birds flying together). Effective algorithms to discard tracks established on birds have to be developed [13].

Typical scanning surveillance systems (including maritime radar) have to declare a detection using only a limited number of pulses. Due to the long decorrelation time of sea clutter [14] and the more often than not spiky amplitude statistics [15], detection is quite difficult due to the short dwell time. Persistent, ubiquitous surveillance has become a top priority internationally. Typical entities of interest range from small recreational watercraft to large tanker ships. One of the characteristics of such systems, *for instance,* AwareNet [16], is the ability to employ long dwell times at specific areas of interest through the utilization of multiple, electronically steered receiver channels. Improved discernibility of small boats with long dwell times is therefore investigated in this article.

Two sea clutter and boat reflectivity measurement trials were conducted in 2006 and 2007 on the south western coast of South Africa. The aim of these trials was firstly to record datasets of sea clutter returns at different frequencies, range resolutions, grazing angles, look angles, and environmental conditions to validate current sea clutter models. Secondly, the aim was to record boat reflectivity datasets for a number of small boats to investigate its detectability with open literature detectors that will hopefully lead to the development of improved detection algorithms for radar systems employing adaptive dwell times.

The layout of the article is as follows. Section 2 presents an overview of the two measurement trials. The results presented in this article were obtained from the analysis of the data recorded during these trials. A description is given of the different radar systems, the experimental set-up, as well as the system and data integrity verification procedures. Section 3 investigates a subset of the sea clutter measurements, focusing on the amplitude statistics and temporal characteristics for fixed frequency and frequency agile waveforms. The RCS and temporal fluctuation of a variety of small boats are investigated in Section 4 for different manoeuvres. Of particular interest is the effect of the boat manoeuvring on the local sea surface and its subsequent reflectivity. Section 5 presents an analysis of the detectability of these small boats, seagulls, as well as angels.

Figure 1: Fynmeet deployed at OTB.

Figure 2: Radar deployed on Signal Hill with open view of sea.

2. OVERVIEW OF MEASUREMENT TRIALS

The first measurement trial was conducted with the Fynmeet dynamic RCS measurement facility (Figure 1) at the Overberg Test Range (OTB). The site provided azimuth coverage of 135° predominantly up-swell with well-developed waves and with a significant variation in wind direction. Sea clutter at grazing angles 0.3–3° were recorded. The second measurement trial was conducted with an experimental, monopulse, X-band radar (Figure 5) deployed on top of Signal Hill in Cape Town. This site provided azimuth coverage of 140° from up- to cross-swell, but with only two predominant wind directions for the duration of the trial. The sea was more representative of open sea conditions. Sea clutter and littoral clutter at grazing angles 0.3–10° were recorded. The experimental radar uses pulse compression to increase the system gain and subsequently yields extended range capabilities compared to Fynmeet.

2.1. Overberg test range 2006 trial

2.1.1. Radar and experimental set-up

The radar was deployed at OTB at location 34°36′56.52″S, 20°17′17.46″E, 67 m above mean sea level (AMSL). The shortest distance to the coastline was 1.2 km due south. A plan overview of the deployment site is depicted in Figure 2. The important specifications of Fynmeet are listed in Table 1.

Local wind speed and direction (Figure 4(a)) were logged with two weather stations separated by 1 km. The local wave direction ϕ_{wave}, significant wave height H_s, maximum wave height $H_{\max}$ and wave period T_{wave} (Figure 4(b)) were logged

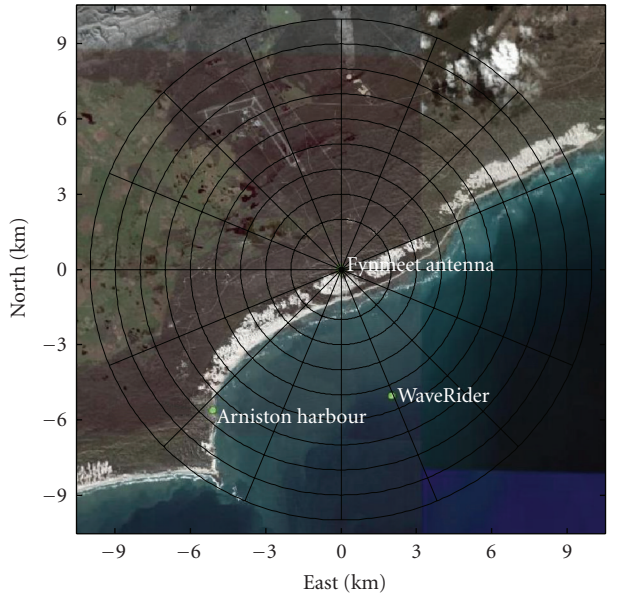

Figure 3: Plan overview of Fynmeet deployment site.

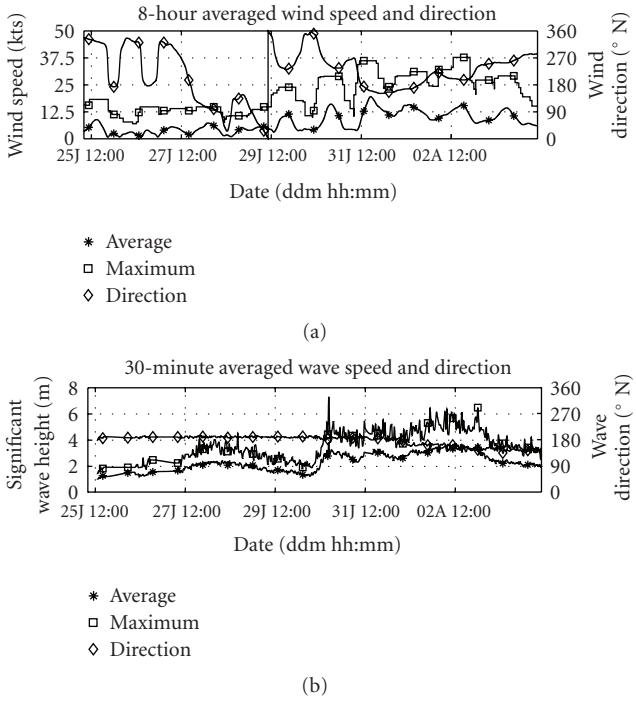

Figure 4: Environmental conditions during OTB trial: (a) wind, and (b) wave.

with a directional recording wave buoy. The local wave structure is influenced greatly by significant weather patterns from the south west and further perturbed by the diffraction patterns due to the cape, southwest of the deployment site which is located in a small bay area with a sea bed depth varying between 10–30 m at ranges of 3–10 km. The ground truth tracks of the boats were estimated using a differential processing global positioning system (GPS) receiver.

Table 1: Fynmeet system and performance specifications.

Transmitter	Frequency range	6.5–17.5 GHz
	Peak power	2 kW
	PRF range	0–30 kHz
	Waveforms	100 and 300 ns pulsed Continuous Wave (CW), fixed/pulse-to-pulse frequency agile (500 MHz)
Antenna	Type	Dual offset reflector
	Gain	≥30 dB
	Beam width	≤2° (3 dB beam width)
	Side lobes	≤ −25 dB
Receiver	Dynamic range	60 dB (instantaneous)/120 dB (total)
	Capture range	200 m–15 km
	Range gates	1–64; $\Delta R = 15$ m or 45 m
	Sampler type	I/Q intermediate frequency sampler
	Image rejection	≤ −41 dBc

2.1.2. System and data integrity verification

For absolute RCS calibration the response from a sphere suspended below a helicopter, tracked in range with a typical $\alpha - \beta$ tracker and in angle with a video centroid tracker, was measured and the calibration coefficient was calculated as

$$C_{\text{cal}} = 20 \log_{10}\left(\frac{1}{N}\sum_{n=1}^{N}\left|\sum_{m=M(n)-1}^{M(n)+1} x(n,m)\right|\frac{AR^4}{\sigma_{\text{cs}}}\right), \quad (1)$$

where N is the number of pulses transmitted, $M(n)$ the range gate with maximum return for the nth pulse, A the receiver attenuation, and σ_{cs} the sphere RCS. A standard deviation of 1 dB was achieved. Daily stability verification measurements were done with a corner reflector, exhibiting variations in the order of about 1 dB across the measurement period.

Linearity of the quadrature receiver channels were ascertained by the analysis of calibrated noise source, receiver noise, and blue sky measurements taken throughout the trial. This analysis included the estimation of channel skewness, kurtosis as well as the 2nd to 4th normalized intensity moments, $I_2 - I_4$. The amplitude and phase imbalance of the quadrature channels were estimated as 0.03 dB and 1° resulting in a negative Doppler image of ≤−41dBc. Additionally, there were also harmonically related spurious responses at a level of ≤ −50dBc. A 5 MHz leak-through signal was identified and removed from the data. The signal phase was nondeterministic and therefore the amplitude and phase were estimated from the dataset itself. Sea clutter with a strong steady state component biases this estimate and the best results were obtained by using a censored mean level technique in the estimation process. The percentage of the dataset censored was chosen such that the resultant estimate yielded the lowest variance. Applying the discrete fourier transform (DFT) to the corrected data, a 0 Hz frequency bin with a comparable power density to adjacent frequency

(a) (b) (c)

Figure 5: Boats deployed during OTB trial: (a) 5.7 m RIB, (b) ski boat, and (c) chokka fishing vessel.

bins was obtained without suppressing the steady state clutter response.

2.1.3. Trial summary

Sea clutter datasets were recorded over a period of 11 days, with 112 fixed frequency and 38 stepped frequency datasets centred at four transmit (Tx) frequencies over an azimuth angle range from 90°N to 225°N and a grazing angle range 0.3–3°. The local weather pattern may be described as roughly following a 6-day cycle [17] as cold front systems pass by from the west to the east. Over the trial period, the average wind speed ranged between 1–20 kts, with a maximum gust of 40 kts. Wind direction spanned 360°, but the high wind speeds were mainly from the south west. H_s varied between 1–3.8 m, with a maximum recorded wave height of 7.31 m. The wave direction was roughly 180°N, and slowly changed direction toward the end of the trial to 135°N.

Even with a low wind speed of 1 kt, the significant wave height was ≥1 m. This is due to the strong incoming south westerly swell combined with the diffraction patterns of the close-by cape and the reduction in sea depth. The illuminated sea area can therefore not be defined as a fully developed sea [3] and the standard tables relating wind speed and wave height to sea state do not apply. In terms of the average wind speed, sea states 1 to a low 5 were observed. In terms of the wave height, sea states from a high 2 to a high 5 were observed.

A 5.7 m RIB, a glass fibre ski boat and a wooden chokka fishing vessel (Figure 4) were deployed on 4 days with conditions ranging from calm to rough seas. The boats sailed a number of manoeuvres at different ranges and azimuth angles. A total of 55 fixed frequency and 43 stepped frequency datasets were recorded centred at four Tx frequencies.

The recorded datasets have been made available to the international research community. For information on the available datasets and how to access these datasets, refer to http://www.csir.co.za/small_boat_detection/.

2.2. Signal hill 2007 trial

2.2.1. Radar and experimental set-up

The experimental, X-band, monopulse radar was deployed on Signal Hill at location 33°55′15.62″S, 18°23′53.76″E, 308 m AMSL, as indicated on the plan view in Figure 6. The shortest distance to the coast line was 1250 m at a bearing of 288°N. The site provided 140° azimuth coverage from 240°N

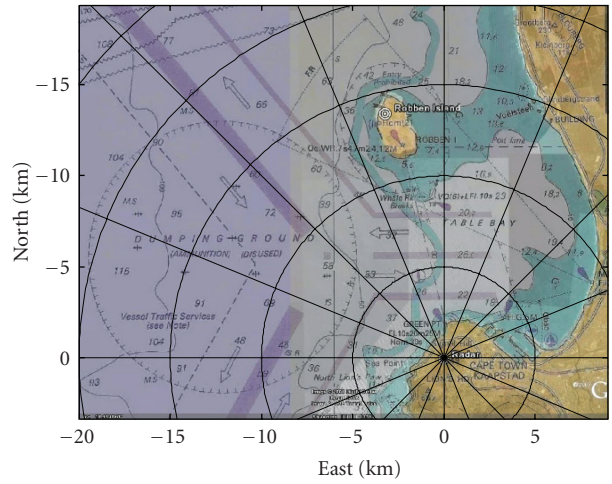

Figure 6: Plan overview of radar deployment site.

to 20°N, of which a large sector spanned open sea whilst the remainder looked towards the West Coast coastline from the direction of the open sea. The radar had an open view of Robben Island at a distance of 11 km. Grazing angles ranging from 10° at the coastline to 0.3° at the radar instrumented range of 60 km were obtained.

Local wind conditions (Figure 8(a)) were measured at the radar, Robben Island, Cape Town Harbour as well as Slangkop (south-southwest of the radar). The local wave conditions (Figure 8(b)) were measured with a seabed-based wave sensor at Camp's Bay and a directional wave buoy at Cape Point whilst numerically modelled at eight other locations in Table Bay and around Robben Island. The tracks of the instrumented boats (Figure 8) were estimated using a differential-processing GPS receiver.

2.2.2. System and data integrity verification

Due to the similarity of the two radar systems, similar system and data integrity verification process were followed as for the Fynmeet radar described in Section 2.1.2. The experimental radar employs matched filter pulse compression, where pulse compression codes c_{pc} are designed to yield a specific pulse compression gain, sidelobe levels and blind range. In the calibration procedure the height and range of the helicopter carrying the calibration sphere over the sea were restricted. The above-mentioned restrictions result in not all codes being calibrated. It is possible however, to estimate C_{cal} for the uncalibrated codes from the calibrated codes by adding the relative pulse compression gain for the uncalibrated code

$$G_{\text{pc}} = \frac{\sum_{n=1}^{N} \left| c_{\text{pc}}(\text{uncal}, n) \right|^2}{\sum_{k=1}^{K} \left| c_{\text{pc}}(\text{cal}, k) \right|^2}, \tag{2}$$

where N is the uncalibrated and K the calibrated code lengths. Equation (2) is valid for a matched filter with unit noise gain. Similarly, the Doppler processing gain

(a) (b) (c) (d)

Figure 7: Boats deployed during Signal Hill trial: (a) Nadine Gordimer, (b) Rotary Endeavour, (c) pencilduck, and (d) SANParks RIB.

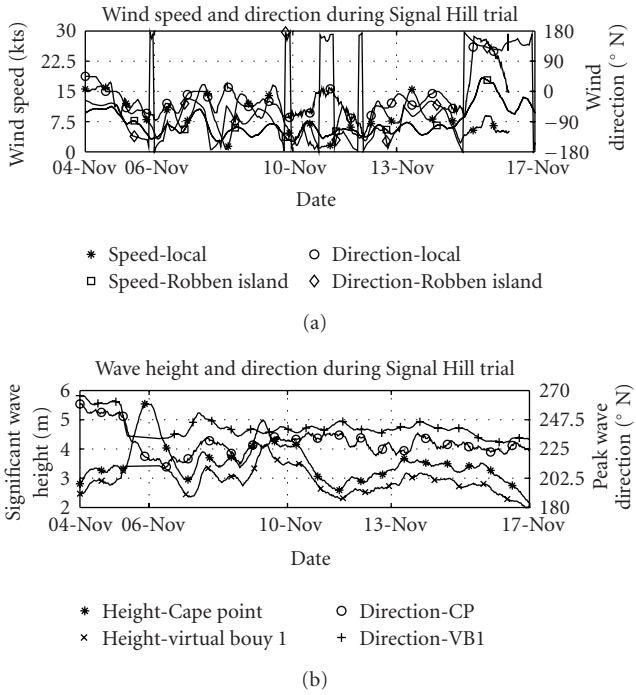

Figure 8: Environmental conditions during Signal Hill trial: (a) wind, and (b) wave.

can be estimated for the uncalibrated Doppler processing coefficients c_{dp},

$$G_{\mathrm{dp}} = \frac{\left[\sum_{l=1}^{L} c_{\mathrm{dp}}(\mathrm{cal}, l)^2\right]\left[\sum_{m=1}^{M} c_{\mathrm{dp}}(\mathrm{uncal}, m)\right]^2}{\left[\sum_{l=1}^{L} c_{\mathrm{dp}}(\mathrm{cal}, l)\right]^2\left[\sum_{m=1}^{M} c_{\mathrm{dp}}(\mathrm{uncal}, m)^2\right]}, \quad (3)$$

where M is the uncalibrated and L the calibrated Doppler processing coefficient lengths. For the experimental radar, the image rejection and spurious response is sufficiently below the noise floor. Pulse compression codes utilized during the measurement trial yielded range sidelobe levels in the order of −35 dB.

2.2.3. Trial summary

Sea clutter datasets were recorded on eight different days over a period of thirteen days. The predominant wind direction was northwestern, but with southeastern intervals. The average wind speed varied between 0 kts and 40 kts, with a maximum gust of 60 kts. The significant wave height ranged in 1–4.5 m, whilst the swell direction varied between 230°N and 270°N.

Datasets of the instrumented boats depicted in Figure 8 were recorded on five different days.

The Nadine Gordimer is a 10 m Class A deep sea rescue vessel with two MTU 1000 turbo diesel inboard motors and a range of communication antennas. The Rotary Endeavour is a Class 3 5.5 m RIB with two 60 hp Yamaha outboard motors and a single VHF antenna. The South African National Parks (SANParks) RIB is a 4.8 m RIB with a 60 hp Yamaha outboard motor. The 4.2 m pencilduck has a single 50 hp outboard motor with no antennas. In addition, datasets were recorded for a large variety of noncooperative boats of opportunity. Recordings were made using a range of fixed frequency and stepped frequency waveforms.

3. SEA CLUTTER ANALYSIS

Various statistical properties are evaluated in this section for seven sea clutter datasets recorded during the OTB 2006 measurement trial. These datasets represent low and high sea states at grazing angles 1° and 0.5° for a single Tx frequency and pulse widths of 100 nanoseconds and 300 nanoseconds. The range-time intensity plot for the high sea state, 1°, 100 nanoseconds dataset *CFC16-001* is presented in Figure 9.

The strong underlying modulation caused by the well developed waves is clearly visible for this up-swell configuration dataset. For cross-swell configurations and further ranges coupling between the waves and the underlying modulation becomes less pronounced as multiple waves are contained within a resolution cell, which is defined by the azimuth beamwidth and radar range resolution at low grazing angles. The underlying modulation also becomes less pronounced in weaker swell conditions.

3.1. Mean reflectivity and amplitude statistics

The mean reflectivity σ_0 and clutter-to-noise ratio (CNR) for the different OTB 2006 datasets are tabulated in Table 2 and compared to the GIT and the hybrid (HYB) models [4]. In both models the sea state S was derived from the mean wind speed v_{wind} using the empirical relation

$$v_{\mathrm{wind}} = 3.16S^{0.8}. \quad (4)$$

From Table 2 it can be concluded that there is good agreement between empirical $\hat{\sigma}_0$ and the HYB model, with values generally between that of the HYB and the GIT. The GIT typically underestimates σ_0 at low grazing angles for low sea states by a significant margin, as discussed in detail in [4]. Of particular interest is the good fit found by matching

Table 2: Empirical reflectivity [dBm^2/m^2] and CNR [dB].

Sea state	Low	Low	Low	Low	High	High
Grazing angle	1°	0.5°	1°	0.5°	1°	0.5°
Resolution [m]	15	15	45	45	15	15
CNR [dB]	11	−3	17	5	21	7
Reflectivity [dBm^2/m^2]	−48	−51	−51	−52	−39	−41
GIT model [dBm^2/m^2]	−101	−115	−101	−115	−35	−39
HYB model [dBm^2/m^2]	−47	−53	−47	−53	−36	−39

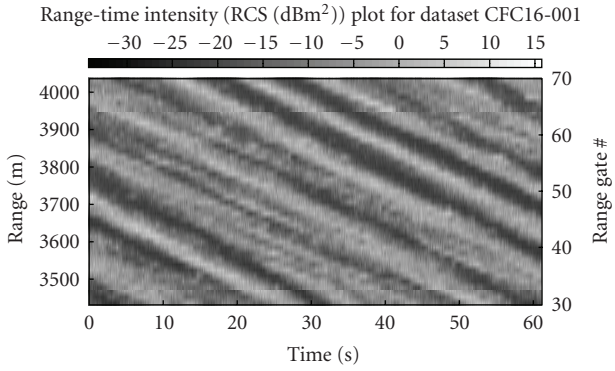

Figure 9: Range-time intensity plot for dataset *CFC16-001*.

Table 3: Empirical versus model amplitude statistics.

Sea state	Low	Low	High	High
Grazing angle	1°	0.5°	1°	0.5°
I_2	3.57	2.27	6.05	4.61
I_3	24.88	9.47	72.32	63.75
I_4	261.9	66.88	1238.6	1629.6
$\hat{\nu}$	1.18	2	0.57	1.22
ν_{model}	1.88	1.79	0.92	0.88

sea state to local wind speed rather than H_s in transient sea conditions (not fully developed).

The 2nd to 4th normalised intensity moments $I_2 - I_4$ and the estimated shape parameter $\hat{\nu}$ are tabulated in Table 3, assuming a k-distributed envelope process and compared to the shape parameter model ν_{model} [15]. In this estimation, the theoretical relationship between the actual shape parameter $\hat{\nu}$ and the effective shape parameter $\hat{\nu}_{\text{eff}}$ in the presence of noise is used [18]:

$$\hat{\nu}_{\text{eff}} = \hat{\nu}\left(1 + \frac{1}{\text{CNR}}\right)^2. \tag{5}$$

The non-Rayleigh envelope statistics is evident. Theoretically spikiness should increase with a decrease in grazing angle. However, this is contradicted in the empirical analysis where a decrease in spikiness is observed with a decrease in grazing angle. This may be due to well-developed waves located closer to the radar (3 km) at the high grazing angles yielding increased spikiness, with less developed waves at the far-out ranges (8 km) where the low-grazing-angle sea clutter data was recorded.

These observations are indicative of the highly complex scattering environment and illustrate a still incomplete understanding of sea clutter.

3.2. Average doppler characteristics

As the capillary waves are the main scattering mechanisms at X-band and they are directly influenced by the near-surface local wind [2], it can be expected that the Doppler and autocorrelation properties of sea clutter are directly influenced by the local wind. The sea clutter speckle autocorrelation $r(\tau)$ [14] is plotted in Figure 10 for four different datasets. From the magnitude response it is evident that the speckle decorrelation time is 10–20 milliseconds, which is consistent with literature [14]. It also indicates that the decorrelation time is affected by sea state, where the decorrelation time decreases as the sea state (roughness of the sea) increases. An explanation for this may be the more rapid deformation of the capillary waves in rough seas. The complex autocorrelation is strongly coupled to the Doppler characteristics of the sea clutter. Evaluation of the real and imaginary components of $r(\tau)$ reveals that the second zero-crossing of $\Im\{r(\tau)\}$ approximates 1/2 of the mean projected Doppler period,

$$f_d(\phi_{\text{wind}}) \approx \left[2\tau|_{(\tau>0,\Im\{r(\tau)\}=0)}\right]^{-1}. \tag{6}$$

This together with the empirical model [3]

$$f_d(\phi_{\text{wind}}) \approx \frac{2\nu_{\text{wind}}\cos(\phi_{\text{wind}})f_0}{4c} \tag{7}$$

enables the estimation of the local projected wind speed from an analysis of the estimated autocorrelation. With a complete azimuth scan of the radar it would be possible to infer both wind speed and direction. This lies outside the scope of this paper and will be the subject of future research.

3.3. Spectrally inhomogeneous sea clutter

Section 3.2 provided empirical evidence that the average wind speed can be inferred from the sea clutter speckle autocorrelation, which is strongly correlated to the average Doppler response thereof. Experimental data suggests however that the sea clutter spectrum is inhomogeneous in both range and time in general. High Doppler resolution spectrograms of three different geometrical configurations and environmental conditions are presented in Figures 11–13. In addition to the spectrograms I_2 is plotted as a function

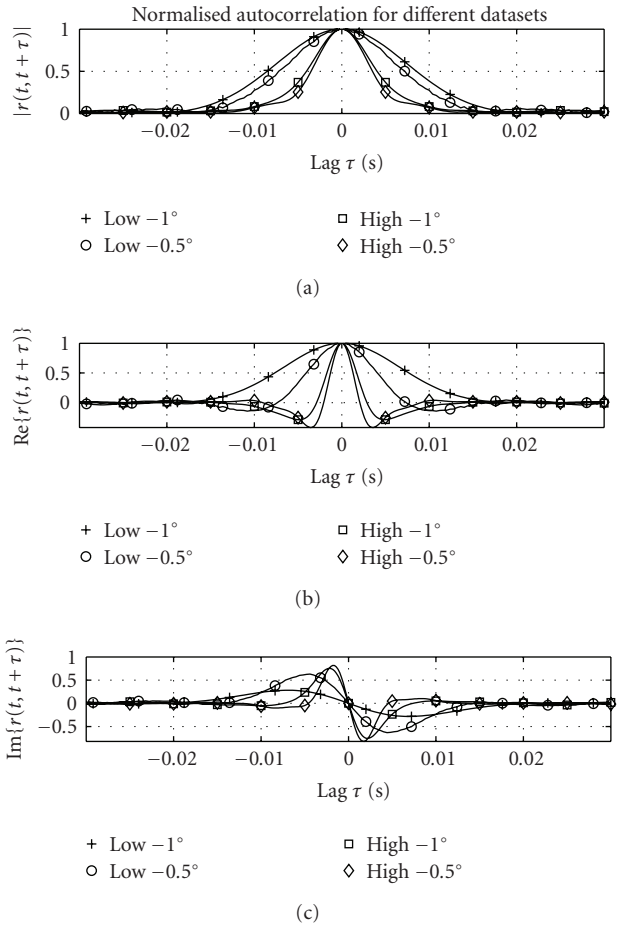

FIGURE 10: Speckle autocorrelation for different datasets: (a) magnitude, (b) real, and (c) imaginary.

of Doppler frequency, yielding an indication of the spikiness per Doppler resolution cell. The spectrogram in Figure 11 is representative of an up-swell sea (H_s = 3.4 m) with strongly developed waves and up-wind (v_{wind} = 15 kts) configuration at a range of 3.8 km. From the spectrogram the different individual waves can be distinguished as they are propagating through the given range cell. The different individual waves have very different Doppler spectra, which results in a significantly raised I_2 at the Doppler velocities associated with localised wind gusts. Thus in the Doppler domain these echoes will compete with those of real targets and hence may have an adverse effect on the false alarm rate. Since the individual waves are resolved, I_2 is also higher than 2 at the mean Doppler frequency. The spectrogram in Figure 12 is representative of a 70° cross-swell sea (H_s = 2.8 m) and down-wind (v_{wind} = 15 kts) configuration at a range of 5.3 km. The sea was more representative of open sea conditions. From the spectrogram it is clear that the short-time Doppler spectrum is much more homogeneous and it is impossible to distinguish individual waves or events. At the mean Doppler frequency I_2 tends to the theoretical value of 2 and is only slightly raised at the average Doppler spectrum edges. The spectrogram in Figure 13 is representative of a 20° up-swell sea (H_s = 2.5 m) and up-wind (v_{wind} = 7 kts) configuration at a range of 5.6 km. Once again the sea was representative of open sea conditions. For this dataset the short-time Doppler spectrum is inhomogeneous compared to the previous dataset, but not as severe as the first dataset analysed in this subsection. For this up-swell configuration there is evidence of individual waves propagating through the range cell, but it is clear that more than one wave are contained within the resolution cell. The events associated with the broadened Doppler response may be associated with whitecaps blown off the top of the waves by the higher wind and/or gusts. The spikiness at the Doppler frequencies associated with the local maximum wind speed is confirmed by a significant raise in I_2.

This brief analysis of the sea clutter Doppler spectrum and $I_2(f_d)$ suggests that it is possible to also infer the existence and severity of whitecaps from the sea clutter.

3.4. Frequency agility

It is generally accepted that sea clutter speckle decorrelates with frequency agility when the frequency step size exceeds the pulse bandwidth, $\Delta f_c \geq B$ [3]. The correlation coefficient $\rho(f_0, f_n)$ is plotted for a coherent processing interval (CPI) of 100 milliseconds at a fixed range cell over a period of 60 seconds—depicting the correlation between the base Tx frequency f_0 and an offset frequency of up to f_0 + 130 MHz for a pulse bandwidth of 10 MHz. From Figure 14 it can be concluded that in general the sea clutter speckle decorrelates whenever $\Delta f_c \geq B$. However, there are a number of CPIs where the speckle only decorrelates after a step size of 40 MHz. Discrete spike events can also be identified where there is strong correlation for a step size of up to 130 MHz. Most radar detection mechanisms will declare these spikes as targets. It is important to note that these discrete spike events have a typical lifetime of 0.5–2 seconds.

Thus, overall these observations show broad agreement with those reported elsewhere and with the GIT and HYB models. They also re-emphasise the complexity of the scattering environment in which a target is required to be detected. This aspect is examined further in the following two sections.

4. SMALL BOAT REFLECTIVITY ANALYSIS

This section presents the results of the analysis of a range of small instrumented boats deployed during the two trials detailed in Section 2.

4.1. Small boat RCS and amplitude statistics

The mean RCS of the small boats, averaged over aspect angle, have been estimated from the measured data and tabulated in Table 4. Isolation of the boat signature from the sea clutter was obtained by Doppler filtering, using the GPS-estimated Doppler frequency as input. The responses of the three-range cells closest to the GPS range were coherently added to counter range-gate straddling losses. The effects of multipath fading from smooth sea surfaces and of shadowing of the

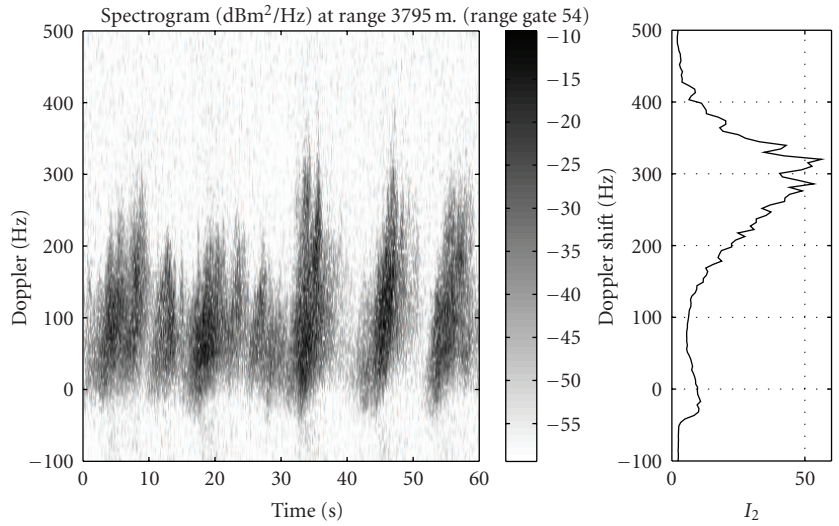

Figure 11: Spectrogram and I_2 for OTB dataset CFC16-001.

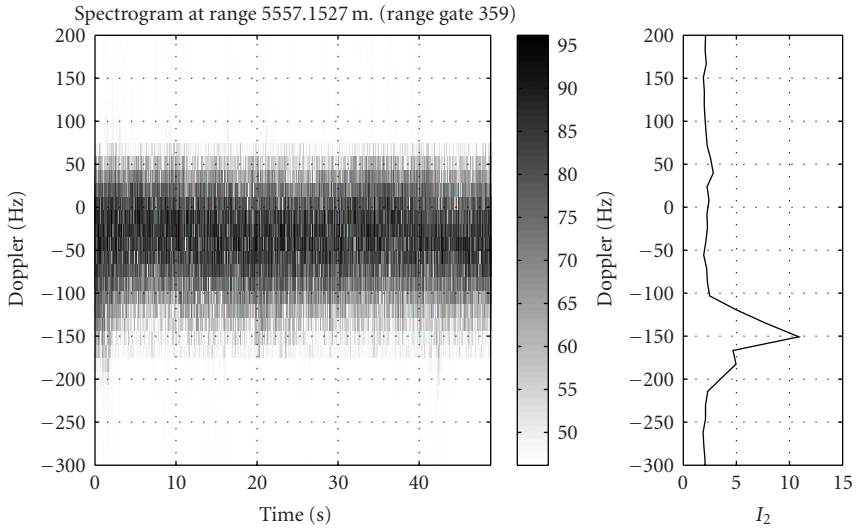

Figure 12: Spectrogram and I_2 for spectrally homogeneous Signal Hill dataset.

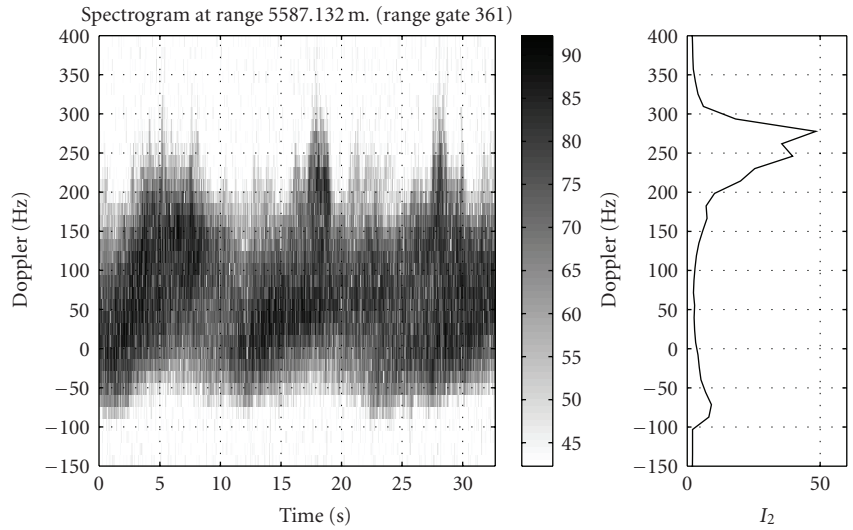

Figure 13: Spectrogram and I_2 for spectrally inhomogeneous Signal Hill dataset.

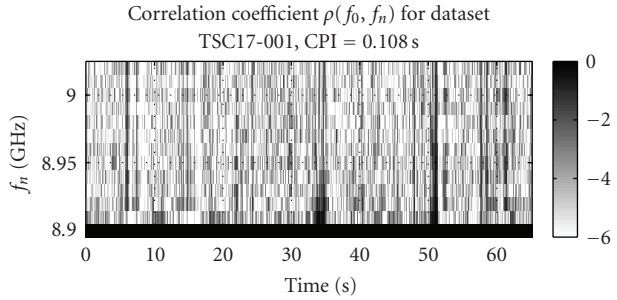

Figure 14: Sea clutter frequency agility decorrelation in the presence of discrete spikes.

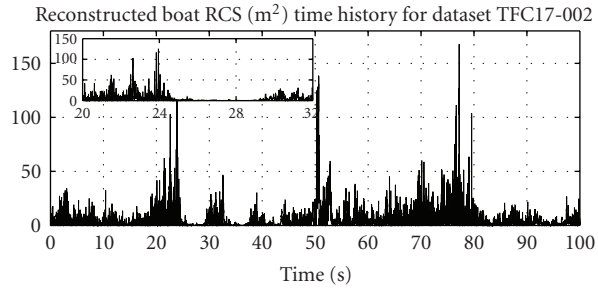

Figure 15: Reconstructed chokka fishing vessel RCS signature.

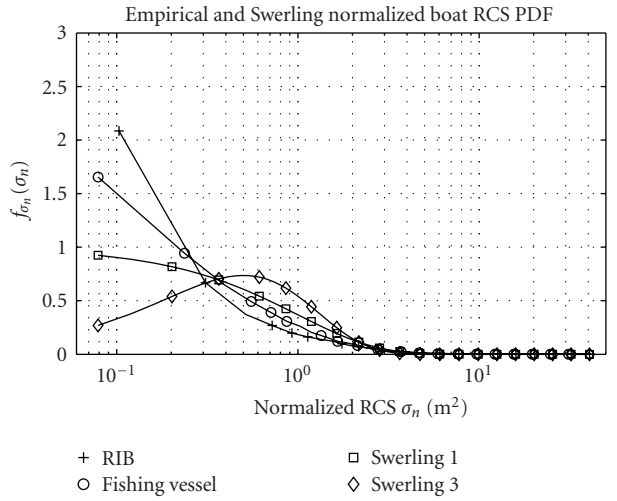

Figure 16: Empirical PDF of chokka fishing vessel and WaveRider RIB compared to Swerling models 1 and 3.

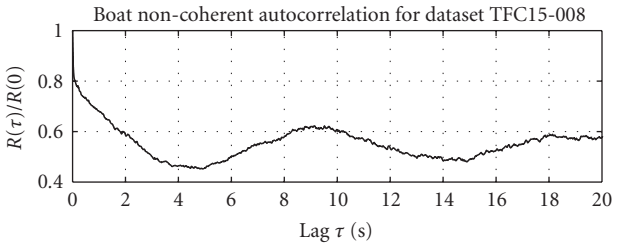

Figure 17: RIB non-coherent autocorrelation showing strong correlation with sea waves.

Table 4: Small boat RCS [dBm^2].

Boat description	Length	Width	Engines	RCS (m^2)
Pencilduck	4.2 m	1.6 m	1×50 hp	≈ 1
SANParks RIB	4.8 m	1.8 m	1×60 hp	1–3
WaveRider RIB	6.5 m	2 m	2×85 hp	1–5
Ski Boat	5.2 m	1.8 m	2×85 hp	4–15
Chokka Fishing Vessel	6.2 m	2 m	$1 \times$ inboard	5–16

boat in higher sea states on the RCS values were not corrected for in the results presented in Table 4.

From Table 4 it is clear that the RCS of an RIB is related to its physical size and ranges between 1–5 m^2. The RCS of solid boats are larger in general, with the mean RCS of the chokka fishing vessel up to 16 m^2. In addition to the mean RCS of the small boat it is also critical for detection performance calculation to have a good model for its RCS fluctuation. The isolated boat RCS signature for the chokka fishing vessel is plotted in Figure 15, with the empirical probability density function (PDF) plotted for both the chokka fishing vessel and the WaveRider RIB in Figure 16.

Slight differences between the PDFs of the two boats are visible as well as the inability of the Swerling models to accurately describe their amplitude distributions. A characteristic of small boats in heavy sea is the fading of the RCS as the boat steers into the troughs of the waves, as indicated by the close-up view about 25–29 seconds in Figure 15. This suggests a strong correlation of boat RCS with the local sea waves and explains the poor fit of the empirical PDFs to the Swerling models at low RCS values. The noncoherent autocorrelation of a boat steering directly into the waves (Figure 17) shows periodicity with the same period as the mean sea wave period. This correlation of boat RCS and sea clutter echo strength further complicates an already challenging detection problem.

4.2. Small boat doppler bandwidth

The Doppler bandwidth of a target is an important design parameter for optimal coherent detection. Coherent processing gain is only achieved by an increase in the CPI whilst it still remains less than or equal to the inverse of the target Doppler bandwidth. High Doppler resolution spectrograms have been computed for the different small boats, with the results for CPI's of 10 milliseconds and 200 milliseconds plotted in Figure 18 for the WaveRider RIB.

The Doppler bandwidth for the WaveRider RIB can be observed from the high-resolution spectrogram. As for most of the other small boats, this is approximately 10 Hz. This yields an optimal CPI ranging between 100–200 milliseconds. As the CPI increases beyond this value, the boat energy will start to spread over multiple Doppler resolution cells, yielding no additional coherent processing gain. This is a key consideration in the design of an optimal detector.

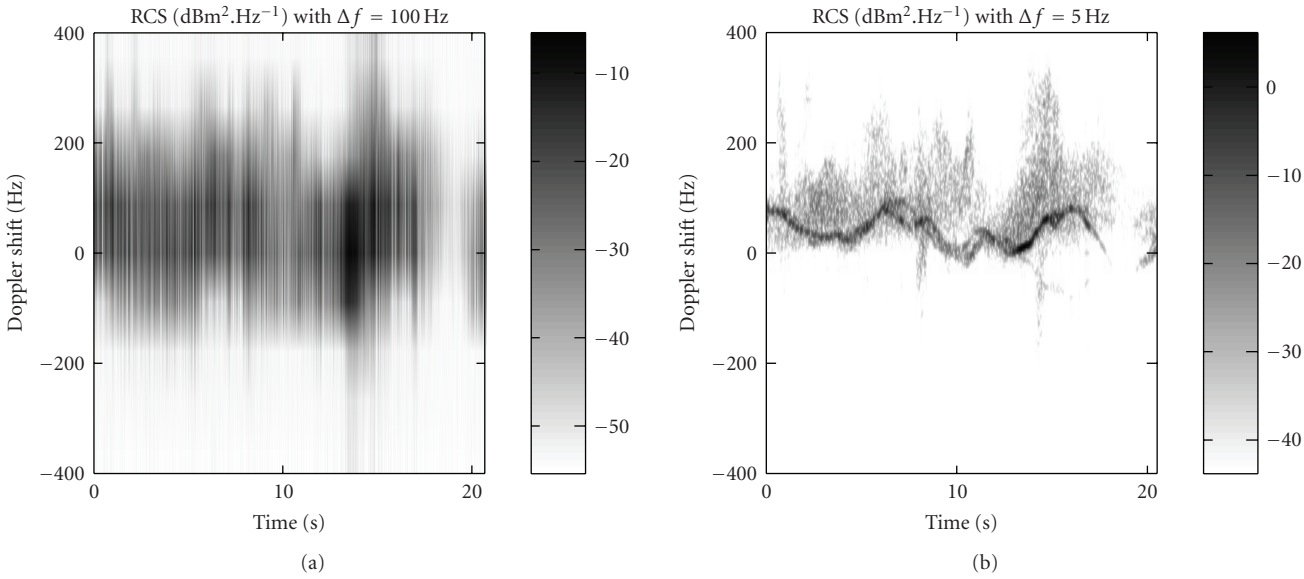

Figure 18: High Doppler resolution spectrograms for different CPI's: (a) 10 milliseconds, and (b) 200 milliseconds.

4.3. Highly manoeuverable small boats

Due to its small size, light weight and powerful engines, the RIB class of small boats is highly manoeuvrable with the ability to reach speeds of up to 40 kts for even the small 4.2 m pencilduck. Especially in the design of coherent detection and tracking algorithms, it is important to have a good understanding of the anticipated manoeuvrability of the target. In addition, the disturbance of the manoeuvring boat on the local sea surface may also greatly influence its detectability either adversely or positively. The high Doppler resolution spectrograms of two different RIB's are plotted in Figure 19–21 for three different manoeuvres. The narrow Doppler response of the drifting pencilduck (Figure 19) is evident, as well as the slight movement of the pencilduck due to the local waves. The drifting pencilduck caused little disturbance on the local sea surface. The WaveRider RIB steering radially outbound at a speed of about 10 kts (Figure 20) had a narrow Doppler response, with a local disturbance of the sea surface visible when the RIB was crashing through the crests of the waves. This local disturbance is observed as quite broad Doppler bandwidth noise with Doppler velocities ranging from slightly higher than the speed of the boat down to the Doppler velocity of the local sea clutter speckle. The spectral density of the disturbance is 20 dB lower than the boat signature. The pencilduck racing at 40 kts radially outbound (Figure 21) still had a narrow Doppler response for the body of the boat, but caused a significant local disturbance of the sea water (e.g., splashing waves and water spray by the propeller), decreasing the localised signal-to-interference ratio (SIR) to less than −10 dB. With such a low SIR, it becomes increasingly difficult to detect the boat with clutter suppression algorithms, even though the local disturbance of the sea surface may be detected by a basic envelope thresholding detector. However, there is still ample Doppler separation between the boat and interference, and in principal a long dwell time range-Doppler detector could be constructed that will consistently declare detections for this fast moving boat. Also of interest is the case where the boat is racing cross-range. This still yields strong self-induced interference, but the Doppler response of the body of the boat will be buried within the interference and it will become extremely difficult to detect.

From this subsection it can be concluded that the exact manoeuvre of the small boat has a great influence on its detectability, especially due to its potential disturbance to the local sea surface. It is also clear that not only the speed, but also the heading of small boats has to be modelled for accurate performance prediction.

4.4. Frequency agility correlation for small boats

Theoretically the correlation coefficient $\rho(f_0, f_n)$ for the RCS of a point scatterer for different frequencies should be unity. For a target that can be approximated as a point scatterer it is assumed that $|\rho(f_0, f_n)| \to 1$. In the presence of clutter and multipath fading, the correlation will be adversely effected. $\rho(f_0, f_n)$ is plotted in Figure 22 for a CPI of 100 milliseconds for the two range cells containing most of the energy for the chokka fishing vessel.

The frequency agility correlation for the boat exceeded 0.5 with $\Delta f_c = 100$ MHz for 84% of the total time period, compared to only 10% for sea clutter only as represented in Figure 14. There were time periods when the correlation coefficient dropped to similar levels as the sea clutter, which coincided with low levels of SCR and/or SNR. For a 10 MHz pulse bandwidth empirical evidence suggest that small boats exhibit significant frequency agility correlation for frequency step sizes up to and beyond 130 MHz. It is possible to design a detection algorithm that uses $\rho(f_0, f_n)$ as the basis for its

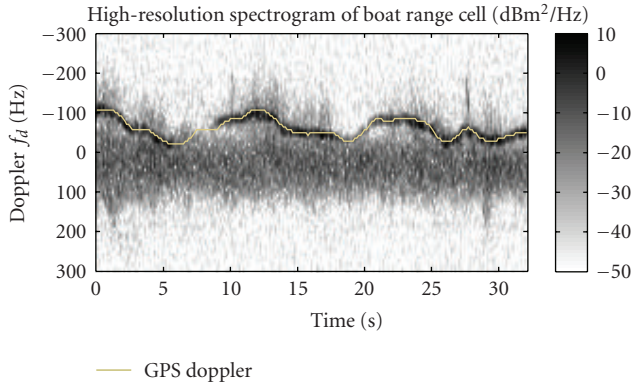

Figure 19: High Doppler resolution spectrogram for drifting pencilduck.

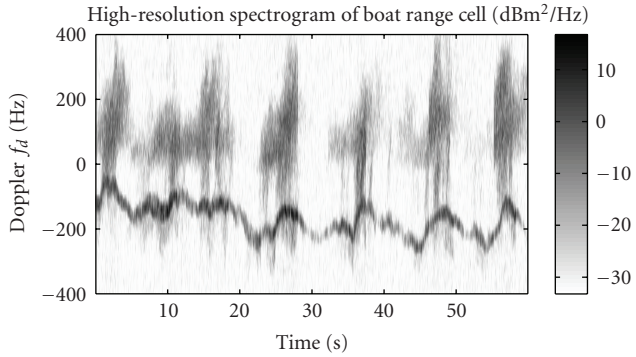

Figure 20: High Doppler resolution spectrogram for radial outbound WaveRider RIB.

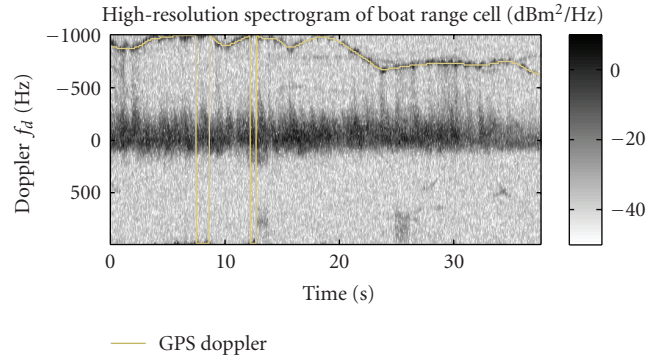

Figure 21: High Doppler resolution spectrogram for pencilduck racing at 40 kts radially outbound.

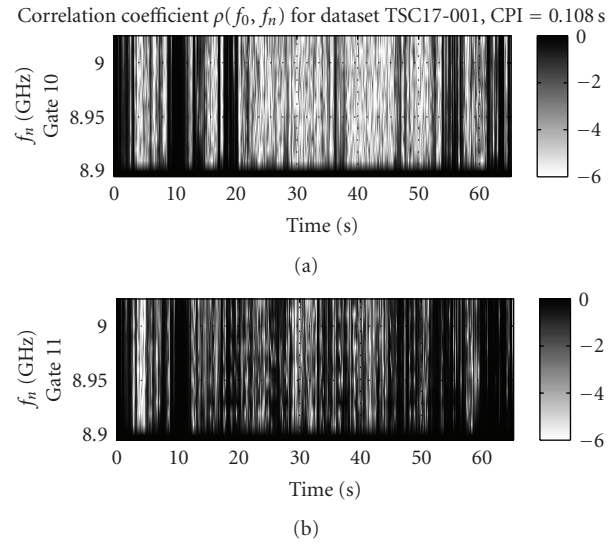

Figure 22: Frequency agility correlation for chokka fishing vessel: (a) gate 10, and (b) gate 11.

test statistics. This detector may still detect discrete spikes, since they have similar characteristics as the small boats (e.g., at $t \in (6, 51)$ s in Figure 14). Once again, these discrete spikes only have a limited lifetime of less than 2 seconds.

5. DETECTABILITY OF SMALL BOATS

This section presents the detectability of small boats undergoing different manoeuvres using the ALQ detector as an example of the asymptotically optimal class of detectors.

5.1. Overview of the ALQ detector

The ALQ detector is designed by extending the generalized likelihood ratio test approach, as suggested by Kelly [9] for Gaussian interference, to the spherically invariant random process model for non-Gaussian interference [19]. Assume that the radar transmits a coherent train of m pulses. The associated m received complex samples can be constructed as a vector $\mathbf{z} = [z(1), \ldots, z(m)]^T$. Under the assumption that $\mathbf{M}$ is known exactly, the ALQ detector can be expressed mathematically as

$$\frac{\left|\mathbf{p}^H \mathbf{M}^{-1} \mathbf{z}\right|^2}{\left(\mathbf{p}^H \mathbf{M}^{-1} \mathbf{p}\right)\left(\mathbf{z}^H \mathbf{M}^{-1} \mathbf{z}\right)} \underset{H0}{\overset{H1}{\gtrless}} \chi_t, \tag{8}$$

where $\mathbf{p}$ is the steering vector typically constructed with elements $p_i = e^{j2\pi i f_d T}$ [20], T the radar PRI and f_d the target Doppler frequency [11]. It is generally accepted that $\mathbf{M}$ is highly dependent on the radar configuration, geometry, and the environmental conditions and has to be estimated from adjacent range gates that are not contaminated by the boat itself. Various estimation techniques have been proposed [21]. Gini and Greco [11] describe one such technique that makes a good compromise between detection losses and hardware processing requirements:

$$\widehat{\mathbf{M}}_{\mathrm{AML}}(i+1) = \frac{1}{K} \sum_{k=1}^{K} \frac{m \cdot \mathbf{z}_k \mathbf{z}_k^H}{\mathbf{z}_k^H \widehat{\mathbf{M}}_{\mathrm{AML}}(i)^{-1} \mathbf{z}_k}, \tag{9}$$

for $i = 0, 1, 2, \ldots, N_{\mathrm{it}}$. During each iteration the approximately maximum likelihood (AML) estimation is normalized such that its trace is equal to m. Since the ALQ detector involves inversion of $\mathbf{M}$, care has to be taken to ensure that the matrix does not become singular. This can be ensured by setting the number of independent sea clutter time vectors

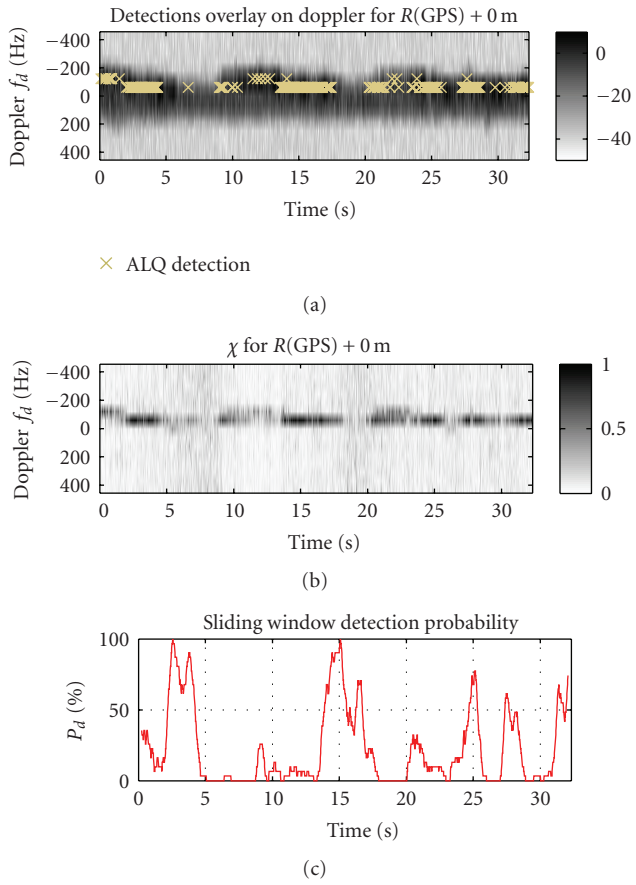

Figure 23: ALQ performance for drifting pencilduck: (a) spectrogram with detections, (b) test statistic χ, and (c) sliding window P_d.

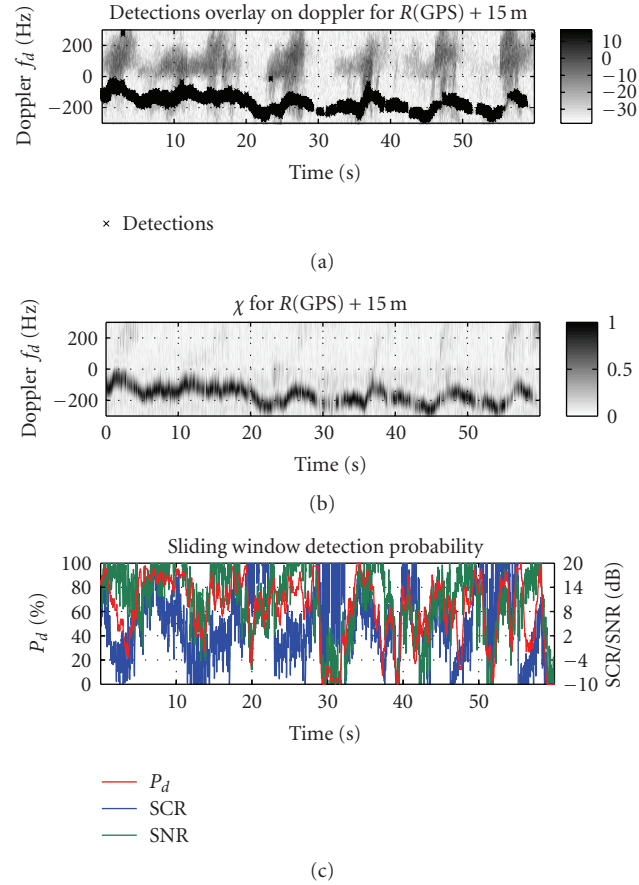

Figure 24: ALQ performance for 10 kts WaveRider RIB: (a) spectrogram with detections, (b) test statistic χ, and (c) sliding window P_d.

at different range gates k equal to at least the length of the test vector m, $k \geq m$ [9]. Detectability can be improved by increasing this ratio, but at the expense of increased hardware processing requirements.

5.2. ALQ performance for different RIB manoeuvres

In the first dataset evaluated, the 4.2 m pencilduck was floating close the southwestern shore of Robben Island, with $H_s = 3$ m and $v_{\text{wind}} = 6$ kts NE. The radar look angle was 343°N at range $R = 11$ km with grazing angle $\theta = 1.5°$. SCR and CNR were 6 dB and 24 dB, respectively. Figure 23(a) plots the spectrogram with a dwell time equal to that of the ALQ detector with the Doppler-dependent thresholding detections overlaid for $P_{\text{FA}} = 10^{-4}$. Figure 23(b) plots the test statistic χ. Figure 23(c) plots the sliding window P_d with window length $L = 31$, with $E\{P_d\} = 23\%$. For such a low SIR this is rather significant. The ability of the detector to whiten the sea clutter is clear in Figure 23(b), whilst the boat signature shows very little evidence of decorrelation. The fading in target signature and the subsequent fading in detectability may very well be due to shadowing of the boat by the sea waves.

In the second dataset, the WaveRider RIB was steering away from the radar into the well-developed waves at a speed of 10 kts at range $R = 3.3$ km. The radar look angle was 166°N, whilst $H_s = 3.2$ m and $v_{\text{wind}} = 16$ kts SSE. SCR and CNR were 4 dB and 17 dB, respectively. The performance of the ALQ detector for $P_{\text{FA}} = 10^{-4}$ is plotted in Figure 24, with $E\{P_d\} = 62\%$. Even though the SCR is lower than in the previous case, a significant increase in P_d is observed. This is most probably due to the increased Doppler separation. Figure 24(c) indicates that low P_d is in general associated with low SCR and/or low SNR.

With the observed increase in sensitivity with an increase in Doppler separation, it can be expected that detectability will increase even further for the high-speed pencilduck. The performance of the ALQ detector is plotted in Figure 25 for the pencilduck racing at 40 kts radially outbound at a range of 21.5 km. Even though the boat can be distinguished in the high Doppler resolution spectrogram (Figure 21) the ALQ detector only manages very intermittent detections. The sea clutter and localised disturbance are whitened over all Doppler, effectively masking the boat. In this case the ALQ cannot be classified as an asymptotically optimal, since a range-Doppler cell-averaging CFAR detector can be configured to steadily detect the boat due to the separation in Doppler of the interference and the boat signature and its narrow Doppler spectrum.

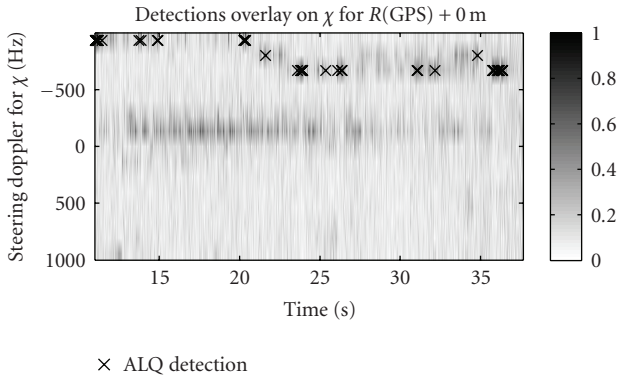

Figure 25: ALQ masking of fast moving pencilduck.

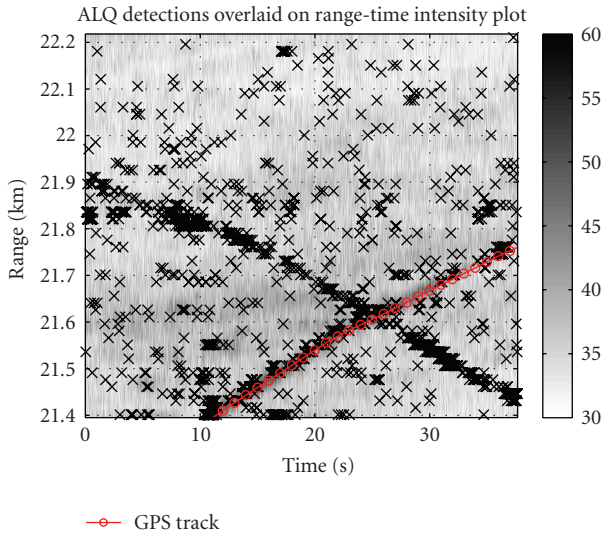

Figure 26: Detection of seagulls and an angel with the ALQ detector.

5.3. *Detection of seagulls and angels*

With improved subclutter visibility, the problem arises that first detections are declared not only for small boats, but also for large birds such as seagulls. ALQ detections for the last dataset in Section 5.2 are overlaid on the range-time intensity plot in Figure 26. Even though only intermittent detections were declared for the racing pencilduck, a large number of detections were declared for the entire dataset. Examination of these detections reveals that they coincide with scatterers yielding an RCS of approximately 0.01–0.1 m^2 and a narrow Doppler spectrum with very fast acceleration. Comparing this to the Doppler signatures of birds in [13] and observation by the copilot of the pencilduck led to the conclusion that these scatterers are indeed seagulls.

Of particular interest in Figure 26 is the consistent detections declared from a range of 21.9 km at $t = 0$ second closing in to a range of 21.4 km. Closer inspection revealed that this was a flock of about 6 seagulls flying in formation. The combined RCS of this "angel" was 10 dB lower than the pencilduck, but still yielded significantly higher P_d. The main reason for this is the Doppler separation and that the seagulls caused no local disturbance of the sea surface. The resultant SIR for the angel was indeed higher than for the pencilduck. As radar sensitivity is increased, this will become a more and more significant problem.

6. CONCLUSIONS

Current commercial products provide near real-time estimation of basic wave and surface current parameters using the video output of standard X-band marine radar. This paper investigated sea clutter and small boat reflectivity in the littoral and proved that sea clutter reflectivity is related to v_{wind} rather than H_s. Temporal characteristics of sea clutter were investigated, with empirical results suggesting that v_{wind} and ϕ_{wind} can be estimated from the sea clutter speckle autocorrelation. The spectral inhomogeneity of sea clutter was investigated for different sea conditions. The brief analysis of the sea clutter Doppler spectrum and $I_2(f_d)$ suggested that it is possible to also infer the existence and severity of whitecaps from the sea clutter. Discrete spikes in sea clutter were clearly visible when the frequency agility decorrelation was estimated.

For safe navigation, it is pertinent that the detection capabilities of marine radar in adverse conditions are improved, especially for small boats. This requires an in-depth understanding of the dynamics and associated reflectivity of these boats. The absolute RCS, amplitude statistics, and temporal characteristics of a range of small boats have been analysed using a comprehensive set of recorded datasets. Of particular interest were the dependency of the boat reflectivity on the local sea, deviation from the Swerling RCS models, the perceived persistence of reflectivity for short periods of time and the distinguishable pulse-to-pulse frequency agility correlation properties of small boats. It was shown using real data that the ALQ detector can, under certain conditions, be subject to self-masking. A definite contribution to the knowledgebase is the importance of not only modelling the sea clutter and boat reflectivity accurately, but also to model the local disturbance caused by small boats, especially during fast manoeuvring.

ACKNOWLEDGMENTS

The authors acknowledge the CSIR team for their contribution in the planning and execution of the trial; the South African Department of Defence, the South African National Parks Board, the National Sea Rescue Institute, and the South African Weather Services for their contribution to the execution and funding of the measurement trials; as well as the Armaments Corporation of South Africa and the South African Air Force for permission to use the Fynmeet radar. The research was cofunded by the South African Department of Science and Technology, the South African Department of Defence and the Royal Society.

REFERENCES

[1] K. Reichert, K. Hessner, and B. Lund, "Coastal applications of X-band radar to achieve spatial and temporal surface wave monitoring," in *Proceedings of the OCEANS Europe Conference*, K. Hessner, Ed., pp. 1–6, Aberdeen, Scotland, June 2007.

[2] J. N. Briggs, *Target Detection by Marine Radar*, vol. 16 of *IEE Radar, Sonar and Navigation Series*, The Institution of Electrical Engineers, London, UK, 2004.

[3] F. E. Nathanson, *Radar Design Principles: Signal Processing and the Environment*, SciTech, Mendham, NJ, USA, 1999.

[4] J. P. Reilly and G. D. Dockery, "Influence of evaporation ducts on radar sea return," *IEE Proceedings Part F*, vol. 137, no. 2, pp. 80–88, 1990.

[5] K. D. Ward, R. J. A. Tough, and S. Watts, *Sea Clutter: Scattering, the K Distribution and Radar Performance*, vol. 20 of *IET Radar, Sonar and Navigation Series*, IET, London, UK, 2006.

[6] P. L. Herselman and C. J. Baker, "Analysis of calibrated sea clutter and boat reflectivity data at C- and X-band in South African coastal waters," in *The IET International Conference on Radar Systems (RADAR '07)*, p. 5, Edinburgh, UK, October 2007.

[7] "Report on the investigation of the loss of the sailing yacht ouzo and her three crew south of the isle of wight during the night of 20/21 august 2006," Investigation Report 7/2007, Marine Accident Investigation Branch, Southampton, UK, April 2007.

[8] B. Wade, "Sharpeye: a new technology marine radar," in *The IET International Conference on Radar Systems (RADAR '07)*, Edinburgh, UK, October 2007.

[9] E. J. Kelly, "An adaptive detection algorithm," *IEEE Transactions on Aerospace and Electronic Systems*, vol. 22, no. 2, pp. 115–127, 1986.

[10] F. Gini, M. V. Greco, K. J. Sangston, and A. Farina, "Coherent adaptive radar detection in non-Gaussian clutter," in *Proceedings of the 31st Asilomar Conference on Signals, Systems & Computers*, vol. 1, pp. 255–259, Pacific Grove, Calif, USA, November 1997.

[11] F. Gini and M. Greco, "Covariance matrix estimation for CFAR detection in correlated heavy tailed clutter," *Signal Processing*, vol. 82, no. 12, pp. 1847–1859, 2002.

[12] M. McDonald and S. Lycett, "Fast versus slow scan radar operation for coherent small target detection in sea clutter," *IEE Proceedings: Radar, Sonar and Navigation*, vol. 152, no. 6, pp. 429–435, 2005.

[13] W. L. Flock and J. L. Green, "The detection and identification of birds in flight, using coherent and noncoherent radars," *Proceedings of the IEEE*, vol. 62, no. 6, pp. 745–753, 1974.

[14] A. Farina, F. Gini, M. V. Greco, and L. Verrazzani, "High resolution sea clutter data: statistical analysis of recorded live data," *IEE Proceedings: Radar, Sonar and Navigation*, vol. 144, no. 3, pp. 121–130, 1997.

[15] K. D. Ward, C. J. Baker, and S. Watts, "Maritime surveillance radar—part 1: radar scattering from the ocean surface," *IEE Proceedings Part F*, vol. 137, no. 2, pp. 51–62, 1990.

[16] F. Anderson, "Awarenet: persistent, ubiquitous surveillance technologies for enhanced national security," Brochure, CSIR, Pretoria, South Africa, October 2007, http://www.csir.co.za/dpss/brochures.html.

[17] R. Hamann, "Wind climatology of the south western cape," January 2006, http://www.windsurfingafrica.org/Articles/tabid/285/Default.aspx.

[18] S. Watts, "Radar detection prediction in K-distributed sea clutter and thermal noise," *IEEE Transactions on Aerospace and Electronic Systems*, vol. 23, no. 1, pp. 40–45, 1987.

[19] E. Conte and M. Longo, "Characterisation of radar clutter as a spherically invariant random process," *IEE Proceedings Part F*, vol. 134, no. 2, pp. 191–197, 1987.

[20] F. Gini, "Sub-optimum coherent radar detection in a mixture of K-distributed and Gaussian clutter," *IEE Proceedings: Radar, Sonar and Navigation*, vol. 144, no. 1, pp. 39–48, 1997.

[21] F. Gini, "Performance analysis of two structured covariance matrix estimators in compound-Gaussian clutter," *Signal Processing*, vol. 80, no. 2, pp. 365–371, 2000.

Hindawi Publishing Corporation
International Journal of Navigation and Observation
Volume 2008, Article ID 863129, 7 pages
doi:10.1155/2008/863129

Research Article

Nonlinear Dynamics of Sea Clutter

Timothy R. Field and Simon Haykin

Departments of Electrical and Computer Engineering and Mathematics, McMaster University, 1280 Main Street West, Hamilton, ON, Canada L8S 4K1

Correspondence should be addressed to Timothy R. Field, field@mcmaster.ca

Received 26 February 2008; Revised 10 June 2008; Accepted 13 September 2008

Recommended by M. Greco

We review experimental evidence for the nonlinearity of sea clutter and the role of the z-parameter or Mann-Whitney rank-sum statistic in quantifying this nonlinear behavior in the context of a hybrid AM/FM model for sea clutter, viewed as a cyclostationary process. An independent theoretical derivation of the stochastic dynamics of radar scattering in a sea clutter environment, in terms of a pair of coupled stochastic differential equations for the received envelope and radar cross-section (RCS), enables the identification of nonlinearity in terms of the shape parameter for the RCS. We are led to conclude that, from both experimental and theoretical points of view, the dynamics of sea clutter are nonlinear with a consistent degree of nonlinearity that is determined by the sea state.

1. INTRODUCTION

Haykin et al. [1] advocated a state-space formalism for the processing of radar signals in the presence of sea clutter (i.e., radar backscatter from an ocean surface). Such a model not only accounts for the temporal dimension of sea clutter in an explicit manner but also for its statistical characterization. Basic to this formalism is whether the underlying dynamics of sea clutter are linear or nonlinear.

In the detailed experimental study reported in Haykin et al., [1] it was also demonstrated that sea clutter is a nonlinear dynamic process, with the degree of nonlinearity increasing as the "sea state" becomes higher. The conclusion reached on the nonlinearity of sea clutter was based on two premises, using real-life data collected with an instrument-quality coherent radar system.

(1) The characterization of sea clutter embodies two forms of continuous-wave modulation:

(i) amplitude modulation (AM), which is linear, and

(ii) frequency modulation (FM), which is nonlinear.

The latter phenomenon is responsible for the nonlinearity of sea clutter.

(2) The z-parameter, denoting the Mann-Whitney rank-sum statistic, is less than the special value -3, which is a strong indicator of nonlinearity.

With regards to point 1, it is also noteworthy that in another study that focussed on the spectral characterization of sea clutter using the Loève transform [2], it was discovered for the first time that sea clutter is a cyclostationary process. Cyclostationarity is ordinarily associated with modulation. But knowing that sea clutter is cyclostationary, it does not tell us the type of modulation involved in the characterization of its waveform.

In this paper, we expand on the characterization of sea clutter as a nonlinear dynamic process, using a principled theoretical approach. In particular, the approach is rooted in stochastic differential equation (SDE) theory. The issue of the dynamics of radar scattering in a sea clutter environment has been addressed in the literature independently from both theoretical and experimental points of view. Perhaps most notably in the former case, Field & Tough [3, 4] develop a theoretical basis for the dynamics which is demonstrated to agree with experimental data to a remarkable degree of accuracy. In the latter case, Haykin et al. [1] study experimental data to motivate a line of argument leading to the conclusion that sea clutter is inherently nonlinear (and indeed possibly chaotic). In the current paper, we bring these two independent lines of development together in a consistent way in order to establish the nonlinear nature of sea clutter from both physical and mathematical viewpoints. More precisely, the scattering dynamics can be derived from

first principles in terms of a pair of stochastic differential equations (SDEs) for the received envelope and the radar cross-section (RCS) that feature a nonlinear coupling and encode the statistical character of the sea state in terms of a certain "shape parameter." Examination of the differentiable parts in this system of SDEs reveals a corresponding "noise-free skeleton," that is, a nonlinear vector process, with a degree of nonlinearity dependent on the shape parameter in a manner consistent with that shown experimentally by Haykin and coworkers. This significant development affirms the case for the nonlinear character of radar sea clutter.

The paper is organized as follows. Section 2 provides a summary of the experimental study that led to the formulation of a hybrid AM/FM model, and the conclusion that sea clutter is a nonlinear dynamic process. Section 3 summarizes the essential ingredients of SDE theory necessary for the basic interpretation of the SDE dynamics of radar sea clutter. In Section 4 we apply this formalism to establish the nonlinear character of the stochastic dynamics of the vector process consisting of the radar cross-section (RCS) and resultant back-scattered amplitude or "received envelope." This is achieved from first principles via an extended random walk model. The extent of the nonlinearity in the resulting SDE description is quantified in terms of a certain "shape parameter" (the relative variance in the RCS, minus one) that encodes the sea state. We conclude in Section 5 with a discussion of the interplay between the two independent lines of enquiry that lead to the common conclusions concerning the nonlinear character of radar sea clutter. We also indicate how our results may suggest which types of experiments to perform to further substantiate and enhance the theoretical framework, and discuss future prospects for the investigation of chaotic dynamics.

We refer the reader also to the recent book by Haykin [5], where the experimental results of the current paper are mentioned in the broader context of adaptive radar signal processing.

2. THE HYBRID AM/FM MODEL OF SEA CLUTTER

In an independent study reported in Gini & Greco [6], sea clutter was viewed as a fast "speckle" process multiplied by a "texture" component that represents the slowly varying power level of the sea clutter signal; such a model is perceptually satisfying. This is known as the K-distribution model and is widely used in the literature. It is the model that we will be concerned with in our dynamical description of sea clutter throughout the paper. The slow variation of the sea clutter power level was attributed to the large ocean waves passing through the observed ocean patch. The speckle was modeled as a stationary compound complex Gaussian process, and the texture was modeled as a harmonic process.

Inspired by the Gino-Greco model of sea clutter, Haykin and coworkers carried out an extensive physical study of sea clutter collected by the instrument quality coherent IPIX radar, where the radar data were recorded on the East Coast of Canada [1]. In that paper, it was demonstrated that amplitude modulation and frequency modulation play important roles in the waveform description of sea clutter. The hybrid AM/FM model of sea clutter has been substantiated further in Greco & Gini [7].

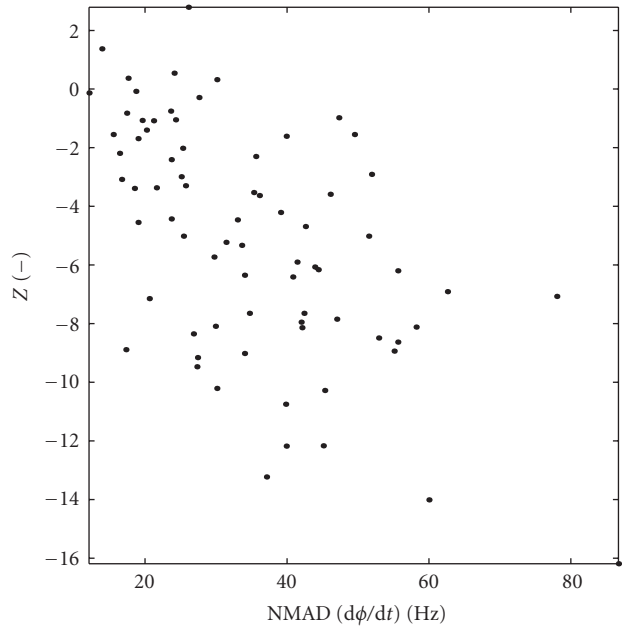

Figure 1: Z value versus NMAD ($\dot{\phi}$), computed for 78 data sets measured by the IPIX radar at various experimental conditions.

To explain the physical presence of modulation in sea clutter, we observe that when a large wave passes across a patch of the ocean surface, it will first accelerate and then decelerate the water's motion on the ocean surface. The continuous tilting of the ocean surface by the waves gives rise to amplitude modulation.

Moreover, the ocean wave will cause a cyclic motion of the instantaneous velocity of scatterers on the ocean surface, thereby giving rise to frequency modulation as another characteristic of the sea clutter waveform. When the mean velocity of the scatterers is high at a given instant of time, then the spectral spread (i.e., the bandwidth occupied by the frequency modulation) around that mean is correspondingly high, which is in perfect accord with modulation theory.

It is well known that, unlike amplitude modulation, frequency modulation is a nonlinear process [8]. Therefore, the presence of frequency modulation in the physical behavior of the sea clutter waveform leads us to hypothesize that sea clutter is a nonlinear dynamic process. To validate this hypothesis, Haykin et al. use 78 different coherent radar data sets to compute the z-parameter, which denotes the Mann-Whitney rank-sum statistic [9]. The results of this test are reproduced in Figure 1, where the z-parameter is plotted against the spectral width modulation.

A value of z less than -3 is considered to be a strong reason for rejecting the null hypothesis that the sea clutter data under test can be described by linearly correlated noise. In Figure 1, we clearly see that the large majority of the experimental points lie below $z = -3$. Those points were in actual fact representative of high sea states. Based on these experimental results, Haykin et al. concluded that sea clutter

is indeed a nonlinear dynamic process, with the degree of nonlinearity increasing with increasing sea state.

3. ELEMENTS OF SDE THEORY

Stochastic differential equation (SDE) theory has significant implications for statistical signal processing. It has recently proven successful in this context in the application to radar sea clutter [3, 4, 10]. In a more general physical context, including optical propagation, the stochastic calculus has led to substantial new theoretical developments in the subject of electromagnetic scattering from random media [11–13].

More recently, SDE techniques have been applied to wireless channel modelling [14] to include the effects of phase fluctuations in multipath reception. The fact that similar techniques are applicable to both the radar backscattering and wireless propagation problems stems from the fact that each is multipath in nature, with the only essential difference being that for radar the receiver and transmitter are colocated. This latter feature, however, does not affect the structure of the mathematical model used to describe the resulting amplitude signal.

In this paper, we will consider the RCS and received envelope processes to evolve according to the dynamics governed by a stochastic differential equation (SDE). In the context of the radar cross-section, such dynamics arise from taking the continuum limit of a generic population dynamic model for the (discrete) number of component scatterers. For the scattered radiation, the origin of the SDE dynamics lies in the behavior of the component phases which are taken to evolve in time according to a Wiener process W_t [15] on a suitable (Rayleigh) timescale. Thus, as we will see explicitly in Section 3, we are able to represent the essential ingredients of the radar back-scatter temporally, in the form of a set of continuous time SDEs, the basic mathematics of which we now introduce. Consider an arbitrary continuous time stochastic process, say q_t, which evolves in time according to

$$\mathrm{d}q_t = b_t \mathrm{d}t + \sigma_t \mathrm{d}W_t. \tag{1}$$

Herein, b_t is a random process referred to as the "drift," and represents the ordinary time derivative of the process q_t in the case that σ vanishes. The quantity σ_t, on the other hand, is the amplitude of the noise or fluctuating part of q_t, in general a random process, and referred to as the "stochastic volatility" of q_t. In the cases we study, it will become apparent that $b_t = b(t, q_t)$ and $\sigma_t = \sigma(t, q_t)$ for some specific functions b, σ, and accordingly the process q_t is called a "diffusion."

In contrast to the part of $\mathrm{d}q_t$ containing b_t, the σ_t term contributes an essential part to q_t that is not differentiable, in the ordinary sense that $\mathrm{d}\mathrm{d}t$ is well-defined. Nevertheless, the (Ito) stochastic differential of q_t can be well defined.

In the engineering physics literature, one is perhaps more familiar with the "Langevin" equation for the time derivative

$$\frac{\mathrm{d}q}{\mathrm{d}t} = b_t + \sigma_t \Gamma_t \tag{2}$$

in which Γ_t is the familiar white noise process and Γ_t has the autocorrelation property $\langle \Gamma_t \Gamma_{t'} = \delta(t - t') \rangle$. For our purposes, it will be sufficient to understand and interpret from the dynamical equations for the RCS and the received radar amplitude that, in a discrete-time setting,

$$\delta q_{t_i} = b_{t_i} \delta t + \sigma_{t_i} n_{t_i} \delta t^{1/2}, \tag{3}$$

where $\{t_i\}$ is a discrete set of observation times, $\delta t = t_{i+1} - t_i$, and $\{n_{t_i}\}$ are a collection of independent $\mathcal{N}(0, 1)$ random variables. Thus, in terms of the Wiener process, we make the discrete time identification $\delta W_{t_i} = n_{t_i} \delta t^{1/2}$. Moving from (2) to (3), the same drift and volatility coefficients become sampled at this discrete set of times.

Then the above properties of q and its time derivative are evident. The essential distinguishing feature of the Ito stochastic differential is that it refers to an integration of (3) in which the volatility is to be evaluated at the left most point of each time subinterval (see [15] for a detailed rigourous account).

The essence of the approach taken is therefore to postulate the exact dynamics in continuous time, and then sample at a discrete set of times corresponding to the physical measurements. This procedure is inevitably more precise than an attempt at a model that is fundamentally discrete time in nature, since the physical observables are not quantized in time.

4. NONLINEAR DYNAMICS FROM SDE THEORY

We will assume the (dynamical extension of the) random walk model for the resultant back-scattered amplitude or "received envelope"

$$\mathcal{E}_t^{(N)} = \sum_{j=1}^{N} \overbrace{a_j \exp[i\varphi_t^{(j)}]}^{s^{(j)}} \tag{4}$$

with (fluctuating) population size N, random phasor step $s^{(j)}$, "form factors" a_j, and component phases $\varphi^{(j)}$, wherein the collection $\{N, a_j, \varphi^{(j)}\}$ is assumed to be mutually independent. Our basic dynamical assumption is that the component phases $\varphi_t^{(j)}$ evolve according to a Wiener process on a suitable (Rayleigh) timescale, that is, that $\mathrm{d}\varphi_t^{(j)} = \mathcal{B}\mathrm{d}W_t^{(j)}$, which relation serves to define the constant $\mathcal{B}$.

The key result of relevance to our discussion is obtained by taking the (Ito) stochastic differential of (4), in the limit that N, the number of component scatterers becomes large. Accordingly we introduce the normalized amplitude process $\Psi_t = \mathcal{E}_t^{(N)}/N^{1/2}$, and a continuous valued RCS x_t via $N = \overline{N}x$, where $\overline{N}$ denotes the mean of the discrete scattering population size. In terms of these quantities, we now provide the following coupled stochastic dynamics of the RCS and scattered amplitude/received envelope. (We can express $\Psi_t = I_t + jQ_t$ ($j = \sqrt{-1}$), the familiar sum of its "in-phase" and "quadrature phase" components.)

Proposition 1. *The dynamics of the RCS and received envelope for radar sea clutter, with shape parameter $\nu = \alpha - 1$, are*

given by the following set of nonlinearly coupled SDEs:

$$\mathrm{d}x_t = \mathcal{A}(\alpha - x_t)\mathrm{d}t + (2\mathcal{A}x_t)^{1/2}\mathrm{d}W_t^{(x)}, \tag{5}$$

$$\frac{\mathrm{d}\Psi_t}{\Psi_t} = \left[\mathcal{A}\left(\frac{2(\alpha - x_t) - 1}{4x_t}\right) - \frac{1}{2}\mathcal{B}\right]\mathrm{d}t + \left(\frac{\mathcal{A}}{2x_t}\right)^{1/2}\mathrm{d}W_t^{(x)} + \frac{\mathcal{B}^{1/2}}{\gamma_t}\mathrm{d}\xi_t, \tag{6}$$

in which γ_t is a unit power Rayleigh process, whose dynamics are obtained by setting x_t equal to a constant of unity and $\mathcal{A} = 0$ in the above system.

This result pertains to (the simulation of) sea clutter from a generic radar system.

Thus, in terms of the familiar K-distribution model for sea clutter, the fast-speckle component is represented by γ_t (or its modulus squared) which is multiplied by a "texture" component, the RCS x_t, according to the product representation $\Psi_t = x_t^{1/2}\gamma_t$. Incidentally, the separation of the radar scattering process into the RCS and received amplitude (or intensity) components in this manner is introduced in a statistical context in Jakeman [16], Jakeman & Tough [17] and developed in a stochastic dynamical context in Field & Tough [3, 4]. (The original proof of this result appears as [4, Proposition 2.1], and we will omit the details of this mathematical derivation which are outside the scope of this paper.)

It is beneficial at this point, in relation to the above proposition, to explain the roles of the various quantities that occur in more familiar radar terminology. The shape parameter ν used in the SDE model is the same as that familiar from the standard K-distribution statistical model of sea clutter. The quantity Ψ is the total radar backscattered *amplitude*, or received envelope, incorporating both speckle and texture components; its modulus squared is equal to the total backscattered intensity, that is taken to be K-distributed. The RCS or texture component is represented by the correlated process x_t.

Thus, the nonlinear SDE for Ψ_t is derived theoretically from first principles beginning with the random walk model for the scattered electric field under the assumption of a uniform phase distribution. (The assumption of a uniform phase distribution can be relaxed, and a corresponding detailed dynamical description in terms of SDEs has been given in [11].) An immediate consequence of this dynamical equation is the "noise-free skeleton", obtained by setting the volatility coefficients of the fluctuating Wiener terms, that is, those containing W_t, equal to zero. Accordingly, the randomness of the process is eliminated and the residual dynamics are deterministic and differentiable. Physically, this corresponds to an evolution conditioned on the current state of the system and then averaged over an ensemble. (In other words, for an Ito process q_t with SDE $\mathrm{d}q_t = b_t\mathrm{d}t + \sigma_t\mathrm{d}W_t$, the ensemble average evolution is determined by $\mathbf{E}|_\mathbf{t}[\mathrm{d}q_t] = b_t\mathrm{d}t$, where $\mathbf{E}|_\mathbf{t}$ denotes the expectation conditional on information at time t.) The concept of the residual noise-free part is explored further below.

This set of coupled stochastic dynamical equations is manifestly *nonlinear* by virtue of the reciprocal term in x_t appearing in the amplitude equation, and only reduces to linear dynamics in the special case that $\mathcal{A}$ vanishes, that is, the scattering cross-section is constant (Rayleigh scattering). It turns out that a natural quantifier of this nonlinearity, in the context of the SDE model for K-distributed noise, is the parameter α appearing in the coupled system of Proposition 1, as discussed below and illustrated in Figure 2.

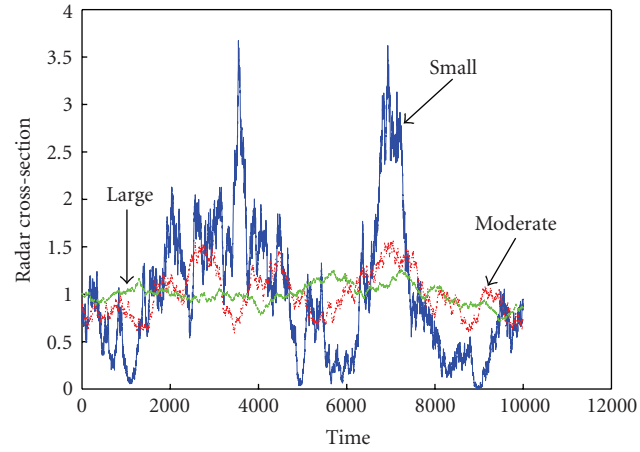

Figure 2: Normalized RCS time-series for low/moderate/high values of the shape parameter; simulated data with $\mathcal{A}\delta t = 0.001$, $\alpha = 1, 10, 100$.

4.1. Radar parameters

In the present context, it is worth remarking on some of the key salient features of the SDE theory, in relation to the sensitivity analysis of sea clutter to certain radar parameters. Most notably, this kind of description is illuminating in respect of the following issues.

4.1.1. Correlation

The constants $\mathcal{A}, \mathcal{B}$ in (5), (6) have the physical dimension of frequency, so that their reciprocals represent correlation timescales for the RCS modulation (texture) and unit power Rayleigh (speckle) components, respectively. The constant $\mathcal{B}$ is electromagnetic in origin with a value $\mathcal{B} \sim c|\mathbf{k}|$, where $\mathbf{k}$ is the wave vector of the carrier and c is the speed of light. In radar situations, the illuminating radiation is such that $\mathcal{A} \ll \mathcal{B}$, with the value of $\mathcal{A}$ being determined as an intrinsic property of the statistics of the scattering surface, independent of the electromagnetic wave. Accordingly, in radar, the correlation time for the RCS is much longer than that of the Rayleigh speckle (cf. also the discussion of amplitude and frequency modulation in Section 5). The pulse frequency of the radar is the reciprocal of δt in the discrete implementation of the coupled system of Proposition 1, and is assumed small compared to the Rayleigh correlation timescale $\mathcal{B}^{-1}$, which amounts to the dimensionless criterion $\mathcal{B}\delta t \ll 1$.

4.1.2. Superposition

In light of the SDE theory, we may argue that the SDE of sea clutter is independent of the amplitude profile of a transmitted pulse, provided the transmit energy is maintained constant. This property, which is derived explicitly in Field [12], is related to the fact that the form factors (i.e., the amplitude weightings) in (4) may be taken as a unity for an asymptotically large population (cf. also [17] where the emergent statistical properties are independent of the choice of form factors).

For a radar pulse of constant amplitude, suppose that the two halves of the pulse have transmit frequencies ω_1 and ω_2. Then we may consider the correlation between the SDE of sea clutter for the two portions as frequency ω_1 increases relative to ω_2. The transmit frequencies are proportional to the Rayleigh constant $\mathcal{B}$ appearing in (6) ($\mathcal{B}\sim c|\mathbf{k}|$, as explained above), and the relationship between the two SDEs, for the two different transmit frequencies, is through (6). The two terms involving the constant $\mathcal{A}$ are the same for both SDEs. On the other hand, the terms involving the Rayleigh constant have different $\mathcal{B}$ values corresponding to the two transmit frequencies. Nevertheless, on physical grounds, the two complex Wiener processes ξ_t for each transmit frequency should be considered perfectly correlated. The reason for this correlation is that the physical origin of the component phase fluctuations $\phi^{(j)}$ is (microscopic) Doppler—the Doppler frequency ratio ω_1/ω_2 is a function of the radial velocity of the jth member of the population, so the micro-Doppler phase shift scales with the transmit frequency; the ξ_t process is the same for any transmit frequency (assuming that these are transmitted simultaneously) as this depends only on the behavior of the component scatterer.

In a similar fashion, consider the simultaneous transmission of two pulses of constant amplitude, with two different frequencies as above, and the resulting SDE of sea clutter received by a common antenna. Since Maxwell's equations of electromagnetism are linear, the resulting Ψ is a linear superposition $\Psi = \kappa_1^{1/2}\Psi^{(1)} + \kappa_2^{1/2}\Psi^{(2)}$, where κ_1, κ_2 are the relative intensities of the two transmit waveforms, normalized so that $\kappa_1 + \kappa_2 = 1$, and $\Psi^{(i)}$ are the constituent complex amplitude processes, both satisfying the SDE (6), with different Rayleigh constants $\mathcal{B}$ corresponding to the two transmit frequencies. Since the beams are simultaneous, the ξ processes are perfectly correlated, with the remaining parts of (6) involving the constant $\mathcal{A}$, the same for both transmit frequencies. Thus, the nonlinear dynamics do not infringe the principle of superposition inherent in Maxwell's equations. (It is necessary to assume here that the scattering populations $N^{(1)}$ and $N^{(2)}$ pertaining to the different transmit frequencies are equal.)

4.1.3. Sea state and polarization

Next, consider the two different copolarizations "HH" and "VV." The SDE theory conveniently represents the spikiness in the RCS of sea clutter due to "HH," versus the noise-like character due to "VV," as follows.

The cross-section SDE (5) emerges as a large N limit of an underlying discrete-valued model for the scattering population, the so-called birth-death-immigration (BDI) model [18], in which α occurs as the ratio of the immigration and birth rates. A property of the continuum limit of this population model, as represented by the SDE (5), is that the distribution of x_t is (univariate) gamma, with parameter α. As a consequence, since the distribution of the modulus amplitude for a given value of the RCS is Rayleigh (as follows from (4) for fixed N), the intensity emerges as being K-distributed (also parameterized by α). Thus, the BDI population model is appropriate to an RCS that generates K-distributed data. Now, for this gamma distribution, we have $\mathrm{Var}[x] = \mathbf{E}[x] = \alpha$. So the absolute magnitude of fluctuations in the RCS, that give rise to the K-distribution for the intensity (as opposed to the Rayleigh "noise-like" distribution), becomes more appreciable as α increases. However, the appropriate theoretical measure of "spikiness" is the *relative* variance R given by

$$R = \frac{\mathrm{Var}[x]}{(\mathbf{E}[x])^2}, \tag{7}$$

($\mathbf{E}$ denotes the expectation functional) which is the physical parameter of interest since it is dimensionless and invariant under rescaling of the RCS. In the case of K-scattering that we consider, R is equal to $1/\alpha$, and therefore the horizontal copolarization "HH" has small α, with larger α for vertical copolarization "VV." The SDE theory explains that if the ratio α of the immigration to birth rates is small, then the sea clutter possesses spikes. It is therefore a natural mathematical, as opposed to a detailed phenomenological, way of encoding this physical property of the sea surface. (However, the SDE theory does not explain why for "HH" polarization one should expect the population to behave this way, the phenomenological reasons for which we do not describe here.) Correspondingly, there are two different K-distributions for the intensity, indexed by different values of the shape parameter $\nu = \alpha - 1$, for the respective polarizations, where α is the SDE parameter appearing in Proposition 1.

The situation as regards the extent of the temporal fluctuations in the RCS for low/moderate/high values of the shape parameter is illustrated in Figure 2, which has been generated independently via a direct numerical integration of (5) according to (3), for various values of the shape encoding parameter α. The figure demonstrates the extreme departures from the mean value for large R, which represents in physical terms sea spikes or glints in the scattering surface. As the sea state settles down to a low value, the (normalized) RCS has small fluctuations away from its mean (unity), so that there is no significant modulation of the Rayleigh scattering time series—in other words, the scattering is of constant local power. We remark also that spikiness should also be more apparent at low grazing angles, represented by corresponding small values of the shape parameter.

As the sea state diminishes, correspondingly in terms of the SDE dynamics, the parameter $\alpha \to \infty$ and the relative variance in the RCS tend to zero. Thus in Figure 2 the nonlinear term becomes less pronounced. Accordingly, as we

have seen in Section 2, so does the degree of nonlinearity as measured by the z-parameter, which further substantiates the experimental findings reported in Haykin et al. [1].

Our analysis therefore establishes the precise relationship between the radar shape parameter, its statistical interpretation, and the dynamical SDE theory, via the explicit appearance of α in the coupled system of Proposition 1.

5. DISCUSSION

We have described a detailed analysis of radar sea clutter data, whose primary purpose is to address the presence of nonlinearity, from real experimental data. A natural quantifier for this nonlinearity is the z-parameter or Mann-Whitney rank-sum statistic, which has been successfully applied in the context of a hybrid AM/FM model for sea clutter. The SDE dynamical model of radar sea clutter has also been verified previously to a remarkable degree of accuracy, in terms of real experimental data (see [3, Section 4(b)]). Moreover, an independent theoretical account for such a model was provided in Field & Tough [4], and has served as the basis for other significant developments [11, 12]. As we have seen in Section 4, this stochastic dynamic behavior is inherently nonlinear, due to the broader timescale fluctuations in the RCS. The extent of nonlinearity arises naturally in the SDE description through the relative variance or shape parameter, which encodes the sea state. Thus, from an SDE dynamical perspective, the nonlinear character of radar sea clutter is firmly established, both theoretically and experimentally.

Calculation of the z-parameter is from real data *containing* noise, the latter being akin to the stochastic fluctuating terms present in (5), (6). However, z has the stochastic element removed, that is, it is not a random variable. Accordingly, some ensemble averaging takes place in the calculation of z, and for this purpose, the statistical properties of ergodicity and stationarity are assumed, legitimate over realistic short timescales. In terms of the parameter $\mathcal{A}$ of (5), such timescales are short enough that the assumption of constant $\mathcal{A}$ is valid. Nevertheless, they should be long enough (of the order of $\mathcal{A}^{-1}$) for the fluctuations in the RCS (or equivalently, as we elucidate below, the frequency modulation effect) to be appreciable so that nonlinearity can indeed be detected.

From an engineering physics perspective, the dynamics of sea clutter are perhaps more naturally viewed in terms of amplitude (AM) and frequency modulation (FM). Studies have indicated that the degree of nonlinearity is governed by the extent of FM which, in turn, is more noticeable for higher sea states (i.e., the shape parameter ν is large). To relate this further to the SDE description of Section 4, it is convenient to view the resultant amplitude process Ψ_t in the product representation $\Psi = x^{1/2}y$, in which x is the RCS and y is a unit power Rayleigh process. Then, the AM consists of the fluctuations of y_t (Rayleigh "speckle") which is "frequency" modulated by the RCS process x_t over a much broader timescale. The FM/AM contributions therefore have characteristic frequencies determined by $\mathcal{A}$, $\mathcal{B}$, respectively. With zero FM, that is, x_t constant, the dynamics of the resultant amplitude are rendered linear, according to Proposition 1.

It is worth emphasizing that the roles of α and $\mathcal{A}$, $\mathcal{B}$ are essentially different, both theoretically and in terms of their radar significance. The parameter α determines the associated gamma distribution for the RCS and corresponding intensity K-distribution, and provides a scale invariant measure of the spikiness of the backscatter. On the other hand, the frequency constants $\mathcal{A}$ and $\mathcal{B}$ set the fluctuation timescales of the respective texture and speckle processes, and thus leave the (asymptotic) statistics invariant. In terms of Figure 2, the adjustment of $\mathcal{A}$ can be considered as an amplitude preserving dilation of the time series along the temporal axis, with smaller values of $\mathcal{A}$ yielding longer duration between peaks in the texture component.

Observe that, whereas the FM/AM characteristics of the received envelope do not map to unique stochastic dynamics, conversely the SDE description allows for explicit extraction of both the FM/AM constituents (see [12]), and therefore the SDE description is more fundamental than the spectral one. Indeed, given the SDE dynamics, we are able to extract all higher order statistical information through the propagators obtained as solutions of the associated Fokker-Planck equations [4, 19]. In this way, the SDE description of sea clutter should be viewed as the most complete dynamical description, which preserves the inherent randomness in the physical processes involved.

We have seen that independent lines of enquiry, from theoretical and experimental perspectives, lead to the common conclusion that radar sea clutter is nonlinear over appreciable timescales such that the temporal variation in the RCS is significant. The degree of nonlinearity is determined by the sea state, which is represented by a certain "shape parameter" ν that features in the SDE for the RCS. (More precisely, $\nu = \alpha - 1$, where α is the parameter in the SDE for the RCS, and $\alpha \geq 0$ arises from the parameters in the scattering population model.) Consistently, the nonlinearity is also determined by the extent of frequency modulation which, in terms of real experimental data, has been quantified in terms of a certain z-parameter representing the Mann-Whitney rank-sum statistic.

From a theoretical point of view, the deterministic part of the stochastic dynamics (5), (6) is nonlinear, and is augmented with the addition of fluctuating Wiener terms in the description of real experimental data, which is inherently noisy (cf. the discussion of chaos surrounding [20, Figure 2], and also [21, 22].) We recommend that further studies be made on the noise-free skeleton of the coupled system (5), (6), which is manifestly nonlinear, to establish the existence or otherwise of an underlying deterministic chaotic behavior. If chaos is present, then this system of nonlinearly coupled SDEs is an instance of "stochastic chaos." We remark in this respect that the presence of the Wiener fluctuating terms in the system has the effect of stabilizing the system, so that any chaotic behavior may no longer be observable experimentally. These issues will be pursued in a subsequent paper.

It is worth emphasizing again that the SDE theory of sea clutter is experimentally valid, in its own terms (see

[3, Section 4(b)]), and has also succeeded in practical applications, such as radar anomaly detection, to a remarkable degree of accuracy. The theory also provides a way of generating synthetic data, over which we have direct control, in terms of its dependence on the sea state. Thus, in principle, we could measure the z-parameter for a data set simulated using SDEs, for which the shape parameter is known, and thereby develop the precise relationship between the z-parameter and shape parameter quantifiers of nonlinearity. It may, indeed, also be possible to relate the two parameters in purely theoretical terms. We can also generate data with and without noise, which forms the basis for further experiment. We suggest that these two lines of enquiry could form the basis of future developments in the investigation of the nonlinear properties of radar scattering dynamics.

The novelty of the current paper can be summarized as follows. In Haykin's paper, it was experimentally demonstrated that sea clutter becomes increasingly nonlinear as the sea state increases. In this new paper, for the first time, theoretical justification of this important result has been presented based on the earlier results of Field.

ACKNOWLEDGMENT

T. R. Field and S. Haykin acknowledge the Award of Discovery Grants from the Natural Sciences and Engineering Research Council of Canada.

REFERENCES

[1] S. Haykin, R. Barker, and B. W. Currie, "Uncovering nonlinear dynamics—the case study of sea clutter," *Proceedings of the IEEE*, vol. 90, no. 5, pp. 860–881, 2002.

[2] S. Haykin and D. J. Thomson, "Signal detection in a nonstationary environment reformulated as an adaptive pattern classification problem," *Proceedings of the IEEE*, vol. 86, no. 11, pp. 2325–2344, 1998.

[3] T. R. Field and R. J. A. Tough, "Diffusion processes in electromagnetic scattering generating K-distributed noise," *Proceedings of the Royal Society A*, vol. 459, no. 2037, pp. 2169–2193, 2003.

[4] T. R. Field and R. J. A. Tough, "Stochastic dynamics of the scattering amplitude generating K-distributed noise," *Journal of Mathematical Physics*, vol. 44, no. 11, pp. 5212–5223, 2003.

[5] S. Haykin, Ed., *Adaptive Radar Signal Processing*, chapter 4, John Wiley & Sons, New York, NY, USA, 2006.

[6] F. Gini and M. Greco, "Texture modeling and validation using recorded high resolution sea clutter data," in *Proceedings of IEEE National Radar Conference (NRC '01)*, pp. 387–392, Atlanta, Ga, USA, May 2001.

[7] M. Greco and F. Gini, "Sea clutter nonstationarity: the influence of long waves," in *Adaptive Radar Signal Processing*, S. Haykin, Ed., chapter 5, pp. 159–191, John Wiley & Sons, New York, NY, USA, 2007.

[8] S. Haykin, *Communication Systems*, John Wiley & Sons, New York, NY, USA, 4th edition, 2001.

[9] A. Siegel, *Nonparametric Statistics for the Behavioral Sciences*, McGraw-Hill, New York, NY, USA, 1956.

[10] T. R. Field, "Stochastic differential equations and their application to the characterization of sea clutter," October 2002, Invited Lectures at Adaptive Systems Laboratory, McMaster University.

[11] T. R. Field and R. J. A. Tough, "Dynamical models of weak scattering," *Journal of Mathematical Physics*, vol. 46, no. 1, Article ID 013302, pp. 1–19, 2005.

[12] T. R. Field, "Observability of the scattering cross-section through phase decoherence," *Journal of Mathematical Physics*, vol. 46, no. 6, Article ID 063305, pp. 1–8, 2005.

[13] T. R. Field, *Electromagnetic Scattering from Random Media*, Oxford International Series of Monographs on Physics, Oxford University Press, Oxford, UK, 2008.

[14] T. Feng, T. R. Field, and S. Haykin, "Stochastic differential equation theory applied to wireless channels," *IEEE Transactions on Communications*, vol. 55, no. 8, pp. 1478–1483, 2007.

[15] B. Oksendal, *Stochastic Differential Equations: An Introduction with Applications*, Springer, New York, NY, USA, 5th edition, 1998.

[16] E. Jakeman, "On the statistics of K-distributed noise," *Journal of Physics A*, vol. 13, no. 1, pp. 31–48, 1980.

[17] E. Jakeman and R. J. A. Tough, "Non-Gaussian models for the statistics of scattered waves," *Advances in Physics*, vol. 37, no. 5, pp. 471–529, 1988.

[18] M. S. Bartlett, *An Introduction to Stochastic Processes*, chapter 3, Cambridge University Press, Cambridge, UK, 1966.

[19] H. Risken, *The Fokker-Planck Equation*, Springer, New York, NY, USA, 2nd edition, 1989.

[20] G. Sugihara, "Nonlinear forecasting for the classification of natural time series," *Philosophical Transactions of the Royal Society of London. Series A*, vol. 348, pp. 477–495, 1994.

[21] L. Stone, "Coloured noise or low-dimensional chaos?" *Proceedings of the Royal Society B*, vol. 250, no. 1327, pp. 77–81, 1992.

[22] G. Sugihara and R. M. May, "Nonlinear forecasting as a way of distinguishing chaos from measurement error in time series," *Nature*, vol. 344, no. 6268, pp. 734–741, 1990.